UNIVERSIDAD CARLOS III DE MADRID

ESCUELA POLITÉCNICA SUPERIOR

DEPARTAMENTO DE TEORÍA DE LA SEÑAL Y COMUNICACIONES

TESIS DOCTORAL

Contributions to the Development of Microwave Active Circuits: Metamaterial Dual-Band Active Filters and Broadband Differential Low-Noise Amplifiers

Autor:
Óscar Alberto García Pérez

Directores:
Daniel Segovia Vargas
Vicente González Posadas

Leganés, Madrid, Junio de 2011

TESIS DOCTORAL

Contributions to the Development of Microwave Active Circuits: Metamaterial Dual-Band Active Filters and Broadband Differential Low-Noise Amplifiers

Autor: **Óscar Alberto García Pérez**

Directores: **Daniel Segovia Vargas** y **Vicente González Posadas**

FIRMA DEL TRIBUNAL CALIFICADOR:

Presidente:

Vocal:

Vocal:

Vocal:

Secretario:

Calificación:

Leganés, a de de .

Contents

Agradecimientos

En primer lugar me gustaría dar las gracias a mis directores de tesis, Daniel Segovia y Vicente González, por su supervisión durante todos estos años y por darme la oportunidad de realizar el trabajo de investigación que finalmente se ha materializado en este libro. También quisiera dar las gracias a Enrique García, cuya supervisión ha sido también de mucha ayuda en gran parte del trabajo realizado para esta tesis.

Me gustaría agradecer de manera especial a José Antonio López Fernández, por darme la oportunidad de trabajar en una institución tan prestigiosa como el Centro Astronómico de Yebes, y por confiar en mí para colaborar en un proyecto tan importante como el proyecto SKA. También quisiera dar las gracias a José Manuel Serna y a Tim Finn por su ayuda en dicho proyecto.

I also wish to thank The Netherlands Institute for Radio Astronomy (ASTRON), and especially Jan Geralt Bij de Vaate, for giving me the opportunity to work at this prestigious institution for three months. It was a rewarding experience in which I learned a lot, and some of the results presented in this thesis where developed there. I am also very thankful to Roel Witvers, Juergen Morawietz, Rob Maaskant, Michel Arts and Marianna Ivashina, for their helpful discussions and suggestions.

I would like to thank Jan Macháč and Christophe Craeye for reviewing this thesis. They have provided very constructive suggestions to improve the overall quality of the manuscript.

No quisiera olvidarme de mis compañeros de laboratorio (Óscar Quevedo, Rosa, Javier Herraiz, Eduardo Ugarte, Daniel Doñoro, Belén, Javier Montero y Nacho), con los que he compartido grandes momentos durante los años que ha durado esta tesis. También quisiera agradecer al resto de amigos en el departamento, con los que he pasado tantas comidas y sobremesas agradables en la Universidad.

Me gustaría agradecer toda la ayuda recibida de mi familia, especialmente de mi madre y mis hermanos, porque sin su inestimable apoyo este trabajo no

hubiera sido posible.

Por último, aunque no por ello menos importante, me gustaría agradecer con mucho cariño a mi novia Lorena, por haber estado a mi lado durante todo este tiempo.

Acronyms

AF	Array factor
BECA	Bunny Ear Combline Antenna
BJT	Bipolar junction transistor
CMOS	Complementary metal-oxide semiconductor
CMRR	Common mode rejection ratio
CRLH	Composite right/left-handed
DC	Direct current
DUT	Device-under-test
EMBRACE	Electronic Multi-Beam Radio Astronomy ConcEpt
FET	Field-effect transistor
FIDA3	FG-IGN Differential Active Antenna Array
FLOWPAD3	Foil-based LOW-cost PAcman Differential Dual-polarized Demonstrator
GaAs	Gallium arsenide
HBT	Heterojunction bipolar transistor
HEMT	High electron mobility transistor
IGN	Instituto Geográfico Nacional
InP	Indium phosphide
JFET	Junction field-effect transistor
LH	Left-handed
LNA	Low noise amplifier
MESFET	Metal-semiconductor field-effect transistor
MIC	Microwave integrated circuit
MMIC	Monolithic microwave integrated circuit
MOSFET	Metal-oxide field-effect transistor
NIC	Negative impedance converter
ORA	Octagon Ring Antennas
RF	Radio frequency

RFI	Radio frequency interference
RH	Right-handed
Si	Silicon
SKA	Square Kilometre Array
SKADS	Square Kilometre Array Design Studies
SRR	Split-ring resonator
THEA	THousand Element Array
TL	Transmission line
TSA	Tapered-slot antenna
UC3M	Carlos III University
VALARRY	Vivaldi ALuminium ARRaY
VSWR	Voltage standing wave ratio

"If you take a bale of hay and tie it to the tail of a mule and then strike a match and set the bale of hay on fire, and if you then compare the energy expended shortly thereafter by the mule with the energy expended by yourself in the striking of the match, you will understand the concept of amplification."

William Shockley
Inventor of the transistor

Preface

New telecommunication systems require electronic components with increasing performance. Microwave active circuits are not an exception. In fact, these active devices (such as amplifiers, active filters, oscillators, mixers, switches, modulators, etc.) are a key part of any modern communication device and, in many cases, the components that greatly limit the overall system performance. During the last decades, engineers have been improving the performance and operation capabilities of such active components, in order to satisfy the new requirements that novel communication services were demanding. This development has taken place in two distinct lines of action. The first line deals with the optimization of the fabrication process of the transistors, which are the basic components in most active circuits. This physical improvement usually translates into higher transconductance, lower noise figure or operation at higher frequencies. The other line is related with the circuit topology in which the transistor is embedded. This second aspect handles the interaction of the transistor with other additional components or transmission lines and provides the desired operation (e.g., amplification, oscillation, etc.). This thesis is more related with the last aspect, in which the use of novel active circuit topologies is investigated. Two main research lines are presented. In the first line, novel dual-band active filter topologies are proposed. This multiband response is achieved by the use of metamaterial structures. In the second one, the use of differential low noise amplifiers is proposed for the design of active antenna arrays. The intended application is the development of a broadband active antenna array demonstrator for radio-astronomy applications.

The design of microwave active filters with metamaterial transmission lines is presented in Chapter 2. This work has been developed for the project TEC2006-13248-C04-04 of the Spanish Government, in which the Carlos III University (UC3M) participates. The aim of this project is the development of new materials, devices and radiating systems to improve the performance in radio frequency (RF) front-ends. One of the main research lines followed by UC3M consists in the design of new components based on the so-called metamaterial lines. Metama-

terials are artificial structures engineered to provide properties that may not be readily available in nature. This technology is one of the main developments of the last decade, and involves several disciplines, such as optics, optoelectronics, electromagnetics, material sciences or microwave and antenna engineering. Some preliminary work developed by UC3M was done to achieve compactness and multiband operation, mainly focused on the design of passive components and antennas. The following two recent theses are a significant representation of this work:

- F. J. Herraiz-Martinez, "Metamaterial-loaded printed antennas: design and application," Ph.D. dissertation, Carlos III University, Leganes, Spain, 2010.
- O. Quevedo-Teruel, "Innovative electromagnetic designs making use of periodic structures and advanced optimization tools," Ph.D. dissertation, Carlos III University, Leganes, Spain, 2010.

At the beginning of the realization of the present thesis, there were many references of metamaterial-based microwave components and antennas, providing compact designs, multiband operation or improved radiation properties. Although some works predicted the potentiality of hypothetical microwave active devices with metamaterial particles, the fact was that the published practical examples about this topic were anecdotic. We early noticed this technological niche, and tried to combine metamaterial transmission lines in active circuit structures. In concrete, the aim of this work was to achieve dual-band performance with recursive active filter topologies. In this case the motivation was double, since there were no previous references on microwave active filters providing two arbitrary pass-bands, not only based on metamaterials but in any other technology.

The work developed in Chapter 2 is pioneering in the design of multiband microwave active filters. The use of a recursive structure allows using metamaterial transmission lines as feedback block, whose inherent non-linear phase response is used to achieve the desired dual-band operation. First designs were based on simple first-order designs, in which dual-band hybrids were used to combine the signals. The desired dual-band performance was successfully proved with this approach. However, this design presented some limitations in the transmission response. An improved design based on ring structures was developed to overcome this limitation, as well as it facilitated the implementation of higher-order structures. This allowed a better control on both the shape of the filter and its selectivity. First-, second-, and third-order prototypes were fabricated using this approach. Finally, another active filter design with two independent frequency-tunable pass-bands was also proposed. The main contributions related with Chapter 2 have been published or presented in 3 journal papers, 1 book chapter and 7 conferences.

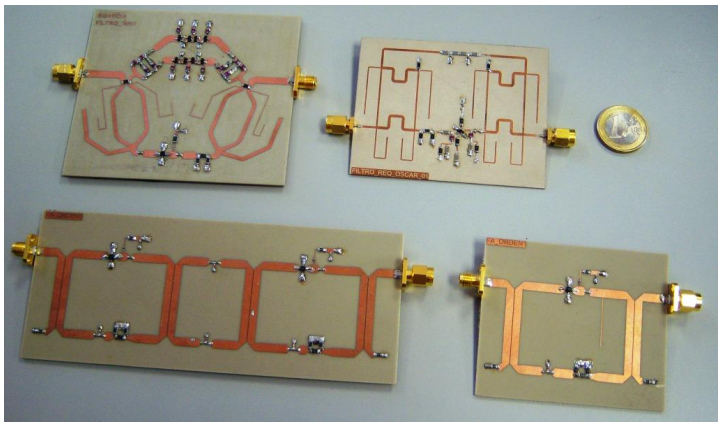

Figure 1: Manufactured active filters based on metamaterial lines.

The second part of the thesis is devoted to the design of differential low noise amplifiers for active antenna arrays, which is presented in Chapter 3. This work was carried out for the European project Square Kilometre Array Design Studies (SKADS), in which the UC3M collaborated with the Instituto Geográfico Nacional (IGN). SKADS is a consortium formed by 31 institutions, and it was conceived "to investigate and develop technologies which will enable us to build an enormous radio-astronomy telescope with a million square meters of collecting area". This great instrument is known as Square Kilometre Array (SKA), and breaks with the classical concept of radio-telescope known up to date. Unlike traditional radio-telescopes, mainly based on large parabolic reflectors, SKA will be based on arrays of millions of small antennas and receivers, in order to scan the sky with sensitivity 100 times greater than current telescopes. This array is intended to cover a wide bandwidth, between 70 MHz and 20 GHz. The first observations are projected by 2019 and full operation by 2024.

To operate in the entire bandwidth, different antenna technologies will be used in three different sub-bands. The work carried out by UC3M-IGN is focused on the intermediate band, between 300 MHz and 1 GHz. This sub-band will be covered by using active phased arrays of planar balanced antennas. Our main task was the design and implementation of an active phased array prototype, called FG-IGN Differential Active Antenna Array (FIDA3), whose technology is a potential candidate for the cited frequency band in the final implementation of SKA. This thesis is focused on the design and measurement of the differential low noise amplifiers (LNAs) needed for the receivers of FIDA3, as well as in the measurement process of the complete array system. These results complement the design process of the radiating structure of FIDA3, which can be found in one of the chapters of the following thesis:

- E. Lera-Acedo, "Ultra-wideband phased array antennas for low-frequency radio astronomy", Ph.D. dissertation, Carlos III University, Leganes, Spain, 2010.

Many technology challenges are raised in this project. Previous approaches used in the design of current radio-telescopes can not be considered in this case. With respect to the LNAs, one of the main limitations is that the use of cryogenic amplifiers is not feasible, due to the large number of active antenna elements needed for this application. Thus, noise temperatures of some tens of Kelvins should be provided by active devices working at ambient temperature. Unlike other solutions based on conventional single-ended amplifiers attached to the antenna elements by means of any kind of balancing circuit (balun), our proposal is based on a direct connection of a differential amplifier at the two connectors of the balanced antenna. This differential antenna-LNA design was one of the innovative points of our prototype. Despite the evident advantages provided by this approach, in which the losses (and noise increase) of a passive balun is avoided, the use of differential amplifiers in this frequency range is not trivial. Although differential circuits are very common in low frequency electronics, the design and measurement processes at microwave frequencies still present some difficulties. Our first task was the study of accurate measurement methods to characterize differential active devices at microwave frequencies. Thus, one of the main contributions presented in this chapter is the use of source-pull methods to obtain the gain and noise circles of differential amplifiers. Next step was the design and characterization of a differential LNA prototype for the FIDA3 antenna array prototype, with which noise temperatures around 50 K were achieved with the device alone. These LNAs were integrated with the antennas, and the complete antenna array system was also characterized. Later, other differential LNA designs were developed, demonstrating measured noise temperatures lower than

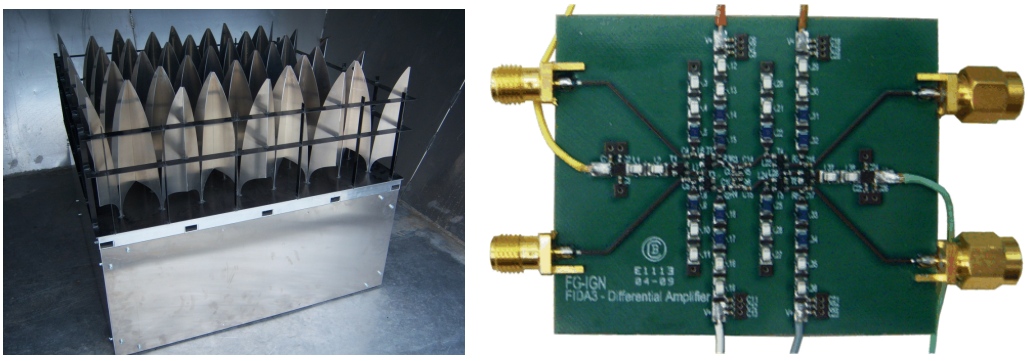

(a) (b)

Figure 2: FIDA3 antenna array prototype (a) and a differential LNA board (b).

30 K in the band of interest. The main contributions related with Chapter 3 have been published or presented in 2 journal papers and 9 conferences.

Finally, the main conclusions and future working lines are presented in Chapter 4. The complete list of contributions resulting from the development of this thesis is shown in the *Publications* section at the end of this book.

Chapter 1

Introduction to Microwave Active Circuits

More than one century ago, primitive amplifying devices were developed to regenerate the signals in the transoceanic telecommunication systems. Nowadays, despite the apparent maturity of this technology, active devices are in continuous evolution due to the increasingly strong requirements imposed by the new communication services. These include higher frequency operation, broader bandwidth, multiband operation, higher gain, lower noise figure, more efficient power consumption, etc. One of the main revolutions in electronics was given by the invention of the transistor. In fact, most modern electronic devices and systems are inconceivable without the use of solid-state transistors. This chapter begins with a historical perspective of the evolution of the amplifiers along the last decades. A description of the main existent solid-state technologies is given in Section 1.2. Finally, some important figures of merit in the design of microwave amplifiers are defined in Section 1.3. The aim with this chapter is to give a general overview on the development of microwave active circuits, as well as to introduce some general terms and concepts that will be used in subsequent chapters.

1.1 Historical Background

1.1.1 Cable relays and magnifiers

The transistor is considered as one of the most important developments of the 20th century. In fact, this component is the basic element of many integrated circuits, which are indispensable in the implementation of most modern electronic devices. However, the amplification of low power signals was a necessity in many telecommunication systems, even before the invention of the transistor. During the late 19th century, supersensitive cable relays were developed for the automatic signal regeneration and retransmission in the first transoceanic submarine telegraph cables [1]. In 1899, the electrical engineer S. G. Brown patented his drum relay, which was used in many cable stations until the development of electronic amplifiers (Fig. 1.1). This relay was an instrument of the D'Arsonval galvanometer type, with 'on' or 'off' states depending on whether the signal voltage excited or not the instrument. Other cable relays were developed during this period, providing similar on/off operation.

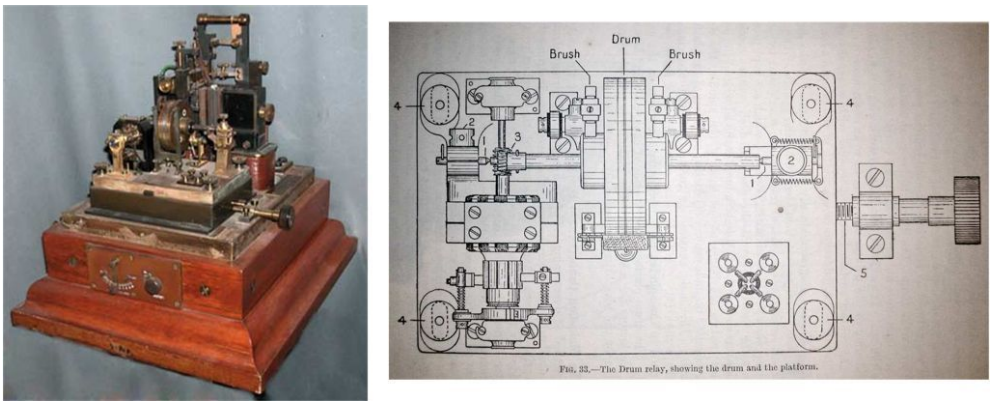

Figure 1.1: Brown drum cable relay, GB Patent no. 1434 (1899) [1].

Unlike the cable relays, which converted the weak input voltages into digital on/off or mark/space output signals, the magnifier was the first device that was able to obtain an amplified copy of the input signal [2]. One of the most ingenious magnifiers was invented by E. S. Heurtley in 1911 (Fig. 1.2). It consisted of two thin wires with high thermal conduction, connected to a galvanometer coil by two non-conductive fibres. These two wires and two equal resistors formed the four arms of a Wheatstone bridge. An air pump was used to equally cool both arms of the bridge. However, the current changes excited the galvanometer, displacing the position of the wires in the cooling stream, changing their temperature and,

therefore, their resistance. Thus, the effect was that small currents through the coil generated much larger currents at the output. Many other types of magnifiers were developed until the decade of 1930.

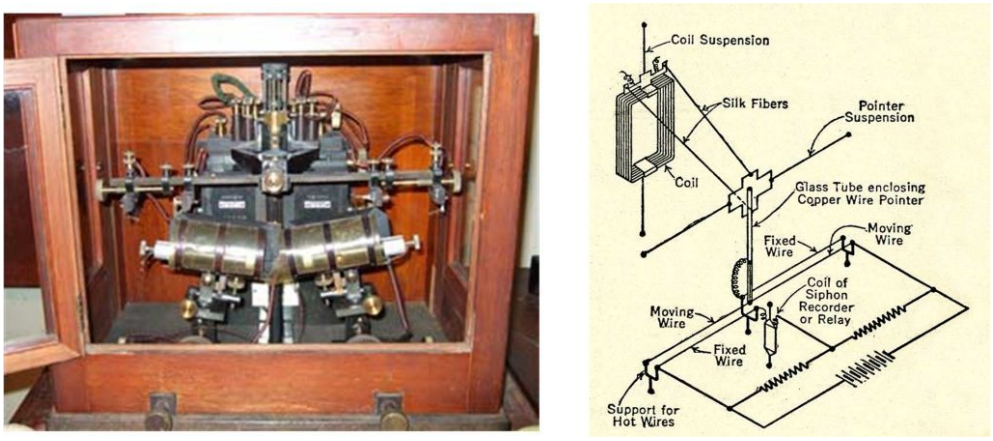

Figure 1.2: Heurtley magnifier, GB Patent no. 8397 (1911) [1].

1.1.2 Vacuum tubes

One of the main advances in electronics corresponds to the invention of the vacuum tube diode by J. A. Fleming in 1904. This device is based on the thermionic effect, which was firstly investigated by T. A. Edison in 1884. Edison tried to find the way of avoiding the black spots in the glass envelope of the light bulbs caused by the coal filament. Thus, he introduced a conductive plate inside the bulb. When the plate (anode) received a more negative voltage than the filament (cathode), no electron flowed between the filament and the plate. However, when the plate was connected to a more positive voltage than the filament, a flux of electrons could be observed through the vacuum, between the filament and the plate. This thermionic effect was caused when the electrons of the atoms in the filament received a great amount of energy from the plate in form of heat and they escaped from the nucleus. The described effect is the well-known operation of a diode, which can conduct the current only in one direction, from the anode to the cathode. Although Edison patented this research, he did not understand all the potential of his discovery. It was in the early 20th century when J. A. Fleming and others found their application in radio detectors and in the first telephone amplifiers.

In 1908, L. D. Forest developed the triode, a novel device similar to the vacuum tube diode, but including a control grid between the plate and the filament

(Fig. 1.3). If a negative voltage was applied to the grid, then the grid repelled some of the electrons back to the cathode. The larger the voltage applied to the grid, the smaller the current flowing to the plate. Thus, as a primitive version of modern transistors, if an alternating current signal excited the control grid, the same signal appeared amplified in the plate. The triodes were used in many radio receivers and transmitters. However, it was found that they tended to oscillate due to the parasitic capacitance between the anode and the grid. In the decade of 1920, this problem was solved by adding a screen grid between the control grid and the plate. This second grid completely decoupled the anode and the control grid and avoided any oscillation in the circuit. This four-terminal device was known as tetrode. Although the problem with the parasitic feedback was solved, this device presented some limitations. When the main current of electrons knocked over the plate, a secondary flow of electrons was generated. In the triode, this secondary flow is not very energetic, so it does not reach the plate. However, in the tetrode, it can reach the secondary grid, reducing the current in the device, even when increasing the voltage. Furthermore, the current flowing through the secondary plate could cause overheat and destroy the tube. This problem was again solved by adding a suppressor grid, whose negative voltage repelled the secondary flow of electrons back toward the plate. This new device was known as pentode, and it was invented by B. D. H. Tellegen in 1928.

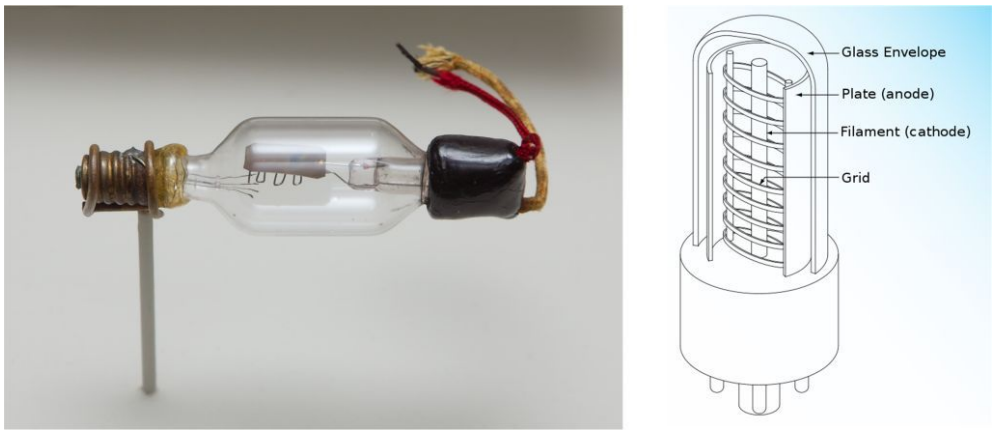

Figure 1.3: Triode tube developed by L. D. Forest in 1908.

Vacuum tube devices were critical in the development and expansion of many communication equipments, such as radio broadcasting, television, radar, telephone networks, etc. Nowadays, vacuum tubes have been mostly replaced by solid-state transistors and diodes. However, they are still in use for some specific applications [3]. Their robustness and linearity with high signal voltages makes vacuum tubes be useful for high-power RF emitters. Furthermore, they

are less sensitive to electromagnetic pulses or explosions, so they are widely used in many military applications. Moreover, they are also very appreciated in audio amplification.

1.1.3 Transistors

The substitute of vacuum tube components was the transistor, which was invented in 1947 by J. Bardeen, W. H. Brattain and W. B. Shockley, all of them working for AT&T Bell Laboratories (Fig. 1.4). The invention received the Nobel Prize in Physics in 1956. This novel device presented many interesting advantages compared with thermionic valves, such as compactness, durability, reliability, efficiency, cost, etc. Furthermore, they do not operate in vacuum like the valves, but in solid state (e.g., silicon), so they do not need extremely high voltage levels to work.

Figure 1.4: Replica created by Lucent Technologies in 1997 to commemorate the 50th anniversary of the first transistor developed by Bell Labs in 1957.

The bipolar junction transistor (BJT) appeared in 1949, and was formed by three sections of doped semiconductor materials. The nomenclature bipolar is related with their operation nature based on the movement of both electrons and holes. The doped regions provide higher concentration of electrons (N) or holes (P), giving two different transistor configurations (NPN or PNP), depending on the configuration of the three semiconductor sections. The heterojunction bipolar transistor (HBT) is an improvement of the classical BJT, which was developed in 1951 with the aim of operating at very high frequencies. Nowadays, HBT devices are very common in many high frequency circuits. Another family of

transistors are the field-effect transistors (FETs), which were firstly proposed in 1953, although they began to be manufactured in the 60's. In the FET, an electric field generates the current through the channel of one type of charge carrier in the semiconductor. Depending if a voltage or a lack of voltage generates the conductive channel, two different types of FETs are considered: P-channel and N-channel. There exist many different types of transistors inside the FET family, such as the junction field-effect transistors (JFETs), metal-oxide field-effect transistors (MOSFETs), metal-semiconductor field-effect transistors (MESFETs) or high electron mobility transistors (HEMTs). In general, this type of device is more suitable for low noise applications.

During the last decades, the industry has optimized the manufacturing process of the transistors, with a continuous reduction of the key device dimensions (e.g., submicron gate lengths), which yields to higher operation frequencies. Furthermore, novel techniques have been developed in order to obtain highly localized doping regions (e.g., molecular beam epitaxy), which increase the mobility of the electrons in the semiconductor and, therefore, also allow operating at higher frequencies. In parallel, microwave designers have been developing novel active circuit topologies in which integrate the transistors to obtain the desired performance, which include amplifiers, mixers, active filters, oscillators, etc.

1.2 Solid-State Technologies

RF and microwave transistors can be classified into two different groups: junction transistors (BJT, HBT) and field-effect transistors (JFET, MESFET, HEMT, MOSFET). Each type of transistor provides different characteristics. Thus, if attention is paid to the specifications of a particular active circuit implementation, the appropriate technology should be chosen according to aspects such as performance, availability or cost. Table 1.1 shows a list of solid-state technologies, with the suggested frequency range and main applications [4]. These technologies are described in detail in subsequent subsections. Table 1.2 shows a comparison of the two main substrate materials used in the fabrication of solid-state devices: silicon (Si) and gallium arsenide (GaAs) [5]. In the case of the Si, this material is very abundant in the Earth's crust and very cheap to process. In addition, the silicon oxide is a very good insulator that can be easily incorporated onto Si circuits. The lower $1/f$ noise makes Si be very used in the design of oscillators with low phase noise. Other advantage is the higher mobility of the holes compared with GaAs, allowing the design of faster P-channel FETs required for complementary metal-oxide semiconductor (CMOS) logic. Finally, the impurities in Si are lower than in GaAs, which allows building smaller structures. On the other hand, GaAs provides higher electron mobility, which allows transistors made on it to operate at much higher frequencies. Furthermore, GaAs generates less noise at higher frequencies, so they are more adequate for low noise devices. GaAs devices can manage higher power values, due to the higher breakdown field levels. Additionally, GaAs substrates are highly resistive, which provides high isolation between devices and components. Thus, it allows easily combining active and passive components on a single substrate slice in monolithic microwave integrated circuits.

1.2.1 Bipolar junction transistor

BJTs are widely used in many electronic applications in which low cost and modest performance is required. They are implemented only in silicon, in both monolithic and discrete forms, and can operate from DC up to the lower part of the microwave range (≈10 GHz). This technology is not suitable for GaAs or indium phosphide (InP), since the width of the P dopants (holes) region would be difficult to control, and the base necessary for high current gain would present a very high input resistance value.

BJTs can be analyzed as a PN-junction diode with an extra third terminal. The current in the PN junction is controlled by means of the voltage between these two terminals (base and emitter), and this current is collected in the third

Table 1.1: Solid state technologies and applications.

Device	**Frequency range**	**Characteristics and applications**
BJT	Usually below 10 GHz	Small signal amplifiers (not low noise) Fast digital circuits Power devices Oscillators
HBT	Up to 70 GHz	Power amplifiers Low noise oscillators
JFET	VHF/UHF	Amplifiers Oscillators Mixers Oscillators Switches
MESFET	Up to 45 GHz (HEMTs are preferable) at higher frequencies)	Low noise amplifiers Oscillators Mixers Modulators Multipliers
HEMT	Up to 300 GHz	The same applications than MESFETs, although at higher frequencies
MOSFET	Up to 10 GHz	Analog digital and RF silicon integrated circuits

Table 1.2: Comparison of Si and GaAs semiconductor technologies.

Property	**Silicon**	**GaAs**
Breakdown field (V/cm)	$\approx 3 \cdot 10^5$	$\approx 4 \cdot 10^5$
Electron mobility (cm^2/V·sec)	≈ 1500	≈ 8500
Hole mobility (cm^2/V·sec)	≈ 450	≈ 400
Thermal conductivity at 300 K (W/cm·°C)	≈ 1.45	≈ 0.45
Saturated electron drift velocity (@10^5 V/cm)	$\approx 10^7$	$\approx 10^7$
$1/f$ Noise corner frequency (Hz) BJT/HBT MOSFET/MESFET	 10-10^3 10^3-10^5	 10^4-10^6 10^6-10^8
Substrate resistivity (Ω·cm)	$\approx 10^3$	$\approx 10^8$

terminal (collector). Fig. 1.5 shows the simplified scheme of a planar NPN BJT. The emitter and the collector are N regions (excess of electrons) and the base is a P region (excess of holes). The P base is lightly doped and the N emitter is heavily doped, which implies that the current in the PN junction is basically due to electrons flowing from the emitter to the base. Since the base region is very thin, just a few electrons are able to recombine with holes in the base. The rest of electrons are swept into the collector, since it is usually biased with a relatively large positive voltage. Thus, it implies that the voltage applied between the base and the emitter generates a proportional current in the collector, resulting in amplification when a proper load is connected to the collector.

There are some limitations in the operation of BJTs. The base current is not zero due to the flux of holes into the emitter, and the recombination of electrons in the base region. This effect limits the current gain. On the other hand, the high impedance of the base combined with the high capacitance between the base and the emitter significantly deteriorate the performance of the transistor. Additionally, the parasitic elements caused by the capacitances in the junctions and the resistances in the ports have great effect in the performance of the device.

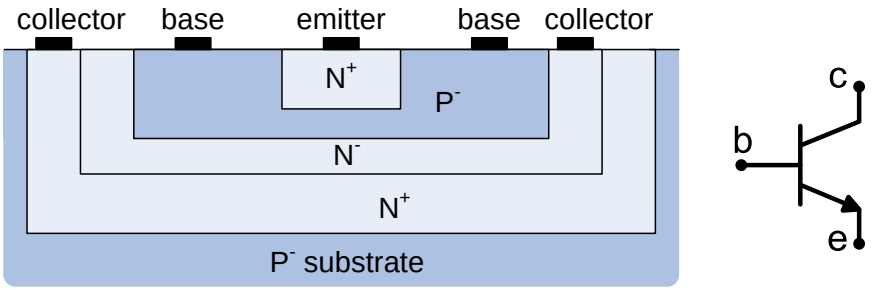

Figure 1.5: Simplified cross section of a planar NPN BJT.

1.2.2 Heterojunction bipolar transistor

HBTs are an improvement of the BJTs with the aim of working at higher frequencies. The main difference between both technologies is that HBTs use different materials for the base and emitter regions, creating the heterojunction. The effect is to limit the injection of holes from the base to the emitter, due to the high barrier generated by the heterojunction. Thus, unlike in BJT technology, the base of a HBT can be heavily doped in order to reduce the base resistance while maintaining the gain. Fig. 1.6 shows the scheme of an AlGaAs-GaAs HBT. The top part is the N emitter. It consists of a GaAs layer and an AlGaAs layer that form the base-emitter junction. The base is a layer of P GaAs, as thin as

possible in order to reduce the equivalent resistance. The collector is conventional, with a heavily doped region N^+ to reduce the collector resistance. HBT technology is suitable for high frequencies, up to the millimeter wave region. The noise figure is modest, although small-signal devices tend to present poor levels of intermodulation distortion.

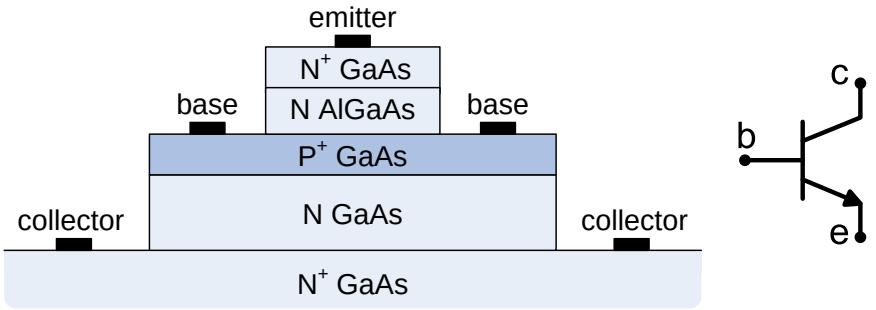

Figure 1.6: Simplified cross section of a NPN AlGaAs-GaAs HBT.

1.2.3 Junction field-effect transistor

The different types of FETs present some common properties. They have a conductive region called channel, in which the drain and source terminals are connected. The majority carriers, electrons in N-type or holes in P-type devices, travel through the channel between the source and the drain. The number of available carriers is controlled by the voltage applied between the third terminal, the gate, and the source terminal.

JFETs are the simplest form of a FET device and, therefore, they present limited performance. Fig. 1.7 shows the scheme of an N-channel junction FET. It is fabricated on a silicon P substrate. The channel is an N region diffused into the substrate. Highly doped N^+ regions are used for the contacts with the source and the drain terminals. The gate is a heavily doped P^+ region. The width of the channel is the dimension perpendicular to the plane shown in the figure, and it is usually larger than the length (distance between the drain and the source). A voltage applied between the gate and the source modifies the width of the depletion region present in the PN junction. A large enough voltage (pinch-off) applied between both terminals can completely deplete the channel, preventing the channel current. Another voltage applied between the drain and the source creates a current in the channel. When the drain-source voltage is low, the device acts as a resistor whose value is controlled by the gate-source voltage (linear range). For higher values of the drain voltage, the drain edge of the channel becomes narrower and therefore the current in the channel saturates.

JFET technology provides a low cost solution for low frequency applications up to some hundreds of MHz. The high-frequency operation is limited by several factors. The gate of the JFET is relatively long, due to the high tolerances during the diffusion process. Thus, the transit time is elevated, which degrades the transconductance and, therefore, the gain and noise properties, especially at high frequencies. Additionally, the high parasitic gate-channel capacitance also limits the frequency of operation. Finally, the electron mobility in N-silicon is small in comparison with other substrates, such as GaAs or InP. It results in high parasitic resistances, especially the source resistance.

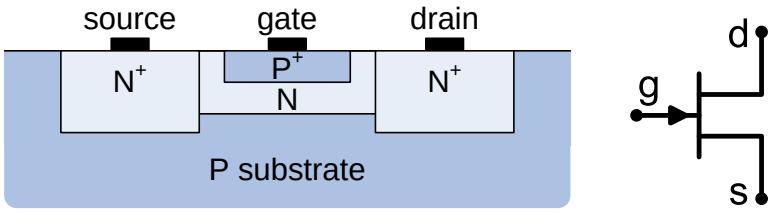

Figure 1.7: Simplified cross section of a N-channel JFET.

1.2.4 Metal-semiconductor field-effect transistor

GaAs MESFETs provide several improvements in comparison with with Si JFETs. The gate is a metal-semiconductor junction (Schottky), which avoids the diffusion process in the gate and therefore allows using a much shorter gate length. It allows reducing the gate-channel capacitance and the gate transit time. Furthermore, the dimensions of the channel can be accurately controlled by means of epitaxial process on a high-resistivity substrate. Additionally, other substrates such as GaAs can be used, which provides higher electron mobility. Fig. 1.8 shows the simplified scheme of a GaAs MESFET. The transistor is fabricated on a high-resistivity substrate. A relatively thick buffer region is grown over the substrate in order to reduce the impurities in the channel. A thin epitaxial layer is used for the channel, which is thinner in the region near to the gate terminal. Highly doped N regions are used close to the source and drain terminals. The operation of MESFETs is equivalent to JFETs.

GaAs MESFETs are widely used in a great variety of microwave applications, especially at microwave and lower millimeter-wave frequency ranges. For higher frequencies or lower noise performance HEMTs may be preferable. However, MESFETs are more adequate for power amplifiers due to the higher current capability.

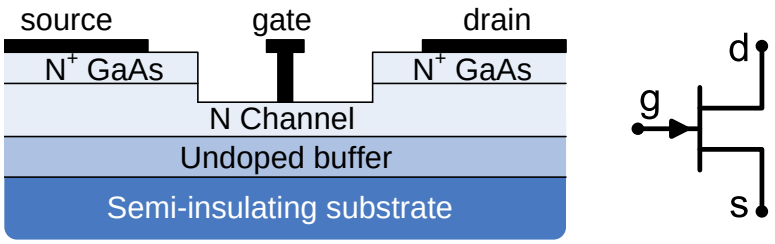

Figure 1.8: Simplified cross section of a GaAs MESFET.

1.2.5 High electron mobility transistor

HEMT technology has higher electron mobility than MESFET, which provides devices with higher transconductance, lower noise and higher frequency operation. It is achieved by using a heterojunction instead of a doped channel. Fig. 1.9 shows the cross section of a HEMT. The heterojunction consists on a doped layer of AlGaAs under the gate, a layer of undoped AlGaAs spacer, and a layer of undoped GaAs. The discontinuity in the band gaps of the AlGaAs and the GaAs generates a thin layer of electrons under the gate, between the spacer and the undoped GaAs. The electron concentration is modulated by means of the gate voltage, and therefore it varies the drain current. To improve the output power, several heterojunctions can be utilized. An extra InGaAs layer can be included between the undoped GaAs and the AlGaAs spacer to improve the output power and the transconductance (i.e., pseudomorphic HEMT). Unlike in MESFETs, HEMT technology provides many degrees of freedom in order to improve the performance of the device, including the materials or the dimensions of its many layers.

Most of the properties and applications of the MESFETs described in Section 1.2.4 can be extrapolated to HEMTs. Of course, HEMTs provide much better noise performance and are more adequate at higher frequencies, up to several hundreds of GHz.

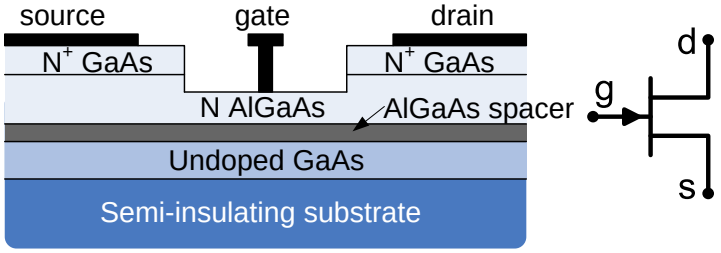

Figure 1.9: Simplified cross section of a HEMT.

1.2.6 Metal-oxide-semiconductor field-effect transistor

MOSFET technology uses an oxide layer to separate the gate and the channel, instead of a PN or a Schottky junction like in JFETs or MESFETs. The voltage applied in the gate is used to control the flux of electrons under the oxide. This electron layer creates the channel. As shown in Fig. 1.10, there are two types of MOSFETs, enhancement-mode and depletion-mode devices. Additionally, N- and P-channel can be fabricated, although the maximum frequency operation of the N-type is one order of magnitude higher than the P-type, due to the higher mobility of the electrons. The enhancement-mode transistor does not have a doped channel. The channel is created when a large enough positive voltage is applied to the gate (for the N-type), and the density of electrons is proportional to the voltage value. For the case of the depletion-mode transistor, there is a doped channel. The voltage applied to the gate controls the depth of the depletion region, as in the case of the JFET. In both cases, the oxide layer is as thin as possible, in order to increase the transconductance.

MOSFET devices provide a performance between JFETs and MESFETs. Although the operation of MOSFETs is quite similar to JFETs, the gate of a MOSFET can be fabricated more precisely and shorter than the diffused gate of a JFET. Thus, the performance of the MOSFETs is much better than of the JFETs, although somewhat poorer than the MESFETs. However, the cost of MOSFETs is considerably lower compared to MESFETs, and they provide quite acceptable performance up to some hundred of MHz.

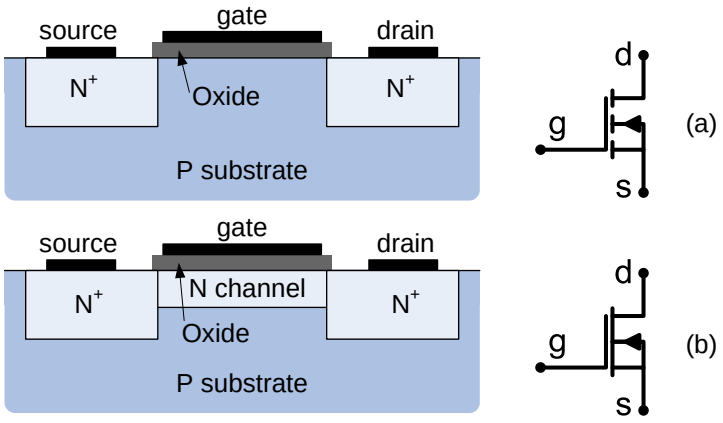

Figure 1.10: Simplified cross section of an enhancement-mode (a) and a depletion-mode (b) MOSFET.

1.3 Amplifier Characterization

Different design goals can be required when optimizing a microwave amplifier:

- Maximum transducer gain
- Minimum noise figure
- Stability
- Input and output voltage standing wave ratio (VSWR) as low as possible
- Flat gain over a specified bandwidth
- Etc.

All these objectives cannot be satisfied at the same time, so a trade-off between all the different properties is necessary. For example, gain is usually limited to ensure stability, or input power matching is sacrificed to minimize the noise.

Microwave circuits are commonly characterized by means of their scattering (S-) parameters matrix. It is particularly useful for the case of active devices, since the impedance (Z-) or admittance (Y-) parameters of a transistor cannot be directly measured. The S-parameters of an amplifier are usually measured by inserting the device into a 50 Ω test-fixture. It should be noticed that the S-parameters of an amplifier are dependent on the biasing voltages and currents and on the temperature. Moreover, they may differ from transistor to transistor, even if they share the same device number.

The properties of an amplifier are determined by the internal parameters of the active device (i.e., scattering and noise parameters), and by the source and/or load impedance conditions (Fig. 1.11). Table 1.3 shows a list of different amplifier parameters and their dependence on the source and load impedances [6].

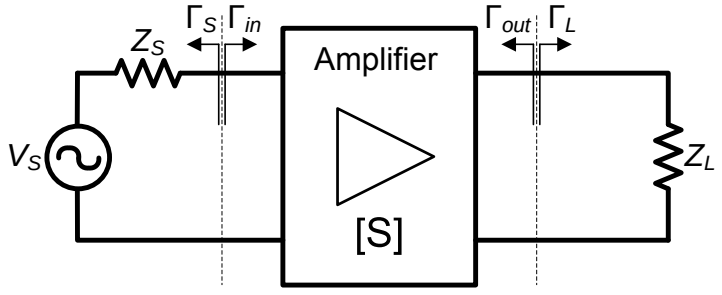

Figure 1.11: Simplified scheme of an amplifier with Γ_S and Γ_L loading conditions.

Table 1.3: Amplifier properties and their dependence with Γ_S or Γ_L.

Property		**Dependence on Γ_S**	**Dependence on Γ_L**
Gain	Power gain		X
	Available Gain	X	
	Transducer Gain	X	X
Impedance Matching	Input	X	
	Output		X
Stability	Input	X	
	Output		X
Noise Figure		X	

1.3.1 Gain

There are several definitions for the gain of a microwave amplifier:

$$\begin{aligned}
\text{Power gain} = G_P &= \frac{\text{power delivered to the load}}{\text{input power to the amplifier}} \\
\text{Available gain} = G_A &= \frac{\text{power available to the load}}{\text{power available from the source}} \\
\text{Transducer gain} = G_T &= \frac{\text{power delivered to the load}}{\text{power available from the source}}
\end{aligned} \tag{1.1}$$

When conjugate input and output impedance matching is simultaneously achieved (for an unconditionally stable transistor), the three gain values coincide, and are equal to the maximum gain value of the amplifier. When referring to gain in the following chapters, the transducer gain G_T definition will be used, since it includes both input and output mismatching effects (Table 1.3). The formula of the transducer gain can be obtained as:

$$G_T = \frac{1-|\Gamma_S|^2}{|1-\Gamma_{in}\Gamma_S|^2}|s_{21}|^2\frac{1-|\Gamma_L|^2}{|1-s_{22}\Gamma_L|^2} = \frac{1-|\Gamma_S|^2}{|1-s_{11}\Gamma_S|^2}|s_{21}|^2\frac{1-|\Gamma_L|^2}{|1-\Gamma_{out}\Gamma_L|^2} \tag{1.2}$$

where the input and output reflection coefficients of the amplifier are given by

$$\begin{aligned}
\Gamma_{in} &= s_{11} + \frac{s_{12}s_{21}\Gamma_L}{1-s_{22}\Gamma_L} \\
\Gamma_{out} &= s_{22} + \frac{s_{12}s_{21}\Gamma_S}{1-s_{11}\Gamma_S}
\end{aligned} \tag{1.3}$$

1.3.2 Input/output impedance matching

The general scheme of an amplifier with input and output matching networks is shown in Fig. 1.12. The aim of the matching networks is to transform from Z_0 impedance conditions to the desired Z_S and Z_L impedances.

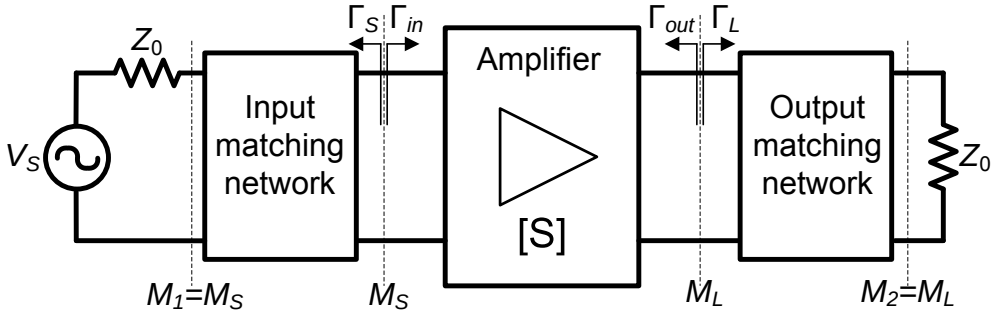

Figure 1.12: Amplifier with input and output matching networks.

Two mismatching coefficients M_S and M_L in the source and load planes can be defined. They represent the disagreement between Z_S and Z_{in}^* and between Z_L and Z_{out}^* respectively. These coefficients are given as

$$\begin{aligned} M_S &= \frac{4R_S R_{in}}{|Z_S + Z_{in}|^2} = \frac{(1-|\Gamma_{in}|^2)(1-|\Gamma_S|^2)}{|1-\Gamma_{in}\Gamma_S|^2} \\ M_L &= \frac{4R_L R_{out}}{|Z_L + Z_{out}|^2} = \frac{(1-|\Gamma_{out}|^2)(1-|\Gamma_L|^2)}{|1-\Gamma_{out}\Gamma_L|^2} \end{aligned} \tag{1.4}$$

It can be demonstrated that the mismatching factor before and after the lossless passive matching networks remains constant, that is $M_1 = M_S$ and $M_2 = M_L$ [7].

The module of the reflection coefficients at the input and output of the amplifier can be obtained from the mismatching factor as

$$\begin{aligned} |\Gamma_1| &= \sqrt{1-M_1} \\ |\Gamma_2| &= \sqrt{1-M_2} \end{aligned} \tag{1.5}$$

In general, it can be considered that a device is well matched if the input and output reflection coefficients are lower than -10 dB (less than 10 % of power reflected). For the case of active devices, a reflection coefficient below -6 dB (less than 25 % of power reflected) can be still acceptable. For low noise amplifiers, the input power matching can be sacrificed in order to minimize the noise figure, due the unavoidable trade-off between both properties.

1.3.3 Stability

For a two-port network, oscillations are possible when the module of either the input or output reflection coefficient is higher than unity. This is very critical in active devices due to the amplification and to the parasitic feedback effects

that are intrinsically present in the transistors. The stability requirements are characterized by

$$\begin{aligned} |\Gamma_{in}| &= \left| s_{11} + \frac{s_{12}s_{21}\Gamma_L}{1 - s_{22}\Gamma_L} \right| < 1 \\ |\Gamma_{out}| &= \left| s_{22} + \frac{s_{12}s_{21}\Gamma_S}{1 - s_{11}\Gamma_S} \right| < 1 \end{aligned} \tag{1.6}$$

If the previous expressions are taken to the limit, that is $|\Gamma_{in}| = 1$ and $|\Gamma_{out}| = 1$, two circles are defined in the Smith chart for the design conditions Γ_L and Γ_S. The center and radius of these circles are derived in [7]. Thus, concerning the stability performance of the amplifier, two different situations may appear

- Unconditionally stable amplifier: The amplifier is stable for any source and load impedance condition inside the Smith chart.
- Conditionally stable amplifier: There are some source or load impedances for which the amplifier becomes unstable.

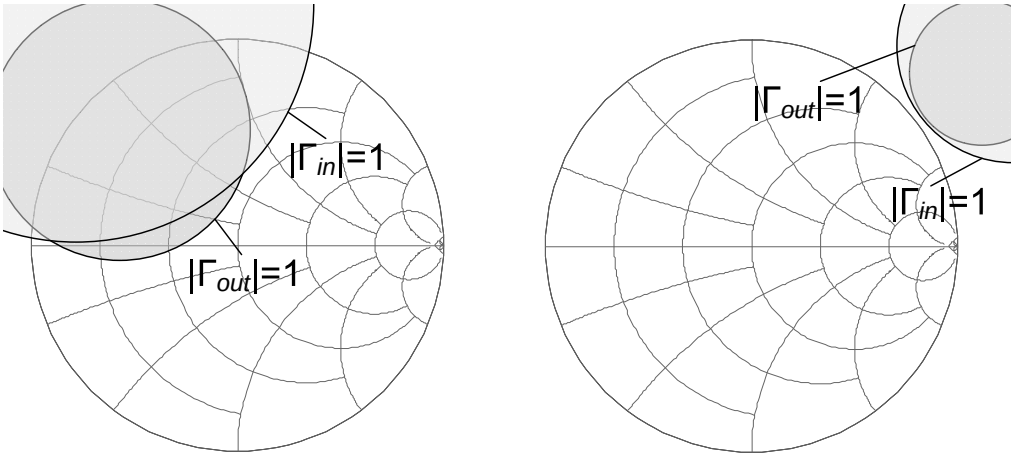

(a) (b)

Figure 1.13: Examples of the stability circles of a conditionally (a) and an unconditionally (b) stable amplifier (gray parts indicate $|\Gamma| > 1$).

Unconditional stability is typically determined by the stability factors K and B_1. These parameters can be obtained as a function of the S-parameters of the amplifier as

$$\begin{aligned} K &= \frac{1 - |s_{11}|^2 - |s_{22}|^2 + |\Delta|^2}{2 - |s_{12}s_{21}|} \\ B_1 &= 1 + |s_{11}|^2 - |s_{22}|^2 - |\Delta|^2 \end{aligned} \tag{1.7}$$

where $\Delta = s_{11}s_{22} - s_{12}s_{21}$. Thus, the necessary and sufficient conditions for unconditional stability are $K > 1$ and $B_1 > 0$.

Although the analysis with the set K-B_1 is mathematically consistent, this method cannot be utilized to compare the stability of two or more devices. Other stability criterion based on a single parameter can be utilized for this purpose, as the geometric stability factor [8]

$$\begin{aligned} \mu_1 &= \frac{1 - |s_{11}|^2}{|s_{22} - s_{11}^* \Delta| + |s_{12}s_{21}|} \\ \mu_2 &= \frac{1 - |s_{22}|^2}{|s_{11} - s_{22}^* \Delta| + |s_{21}s_{12}|} \end{aligned} \tag{1.8}$$

where μ_1 is obtained for the load plane, and μ_2 is obtained for the source plane. In this case, the unconditional stability is ensured when either $\mu_1 > 1$ or $\mu_2 > 1$. Additionally, larger values of the parameters imply greater stability in the corresponding plane. In practice, stability can be improved by adding series resistors at the input or output ports, although it also affects to other parameters as the noise and the gain of the amplifier.

1.3.4 Noise

Noise is usually generated by the random motion of charge carriers in materials and devices, which degrades the performance of any electronic circuit. There are three main contributions of noise in active devices:

- Thermal noise: generated by the resistive elements.
- Shot noise: due to the discrete motion of the charge carriers in the PN junctions.
- Flicker noise: due to a variety of effects, such as impurities in a conductive channel.

Flicker noise varies inversely with frequency ($1/f$), and is usually negligible compared with thermal and shot noise when working at frequencies higher than 100 MHz. Thermal and shot noise present flat spectral noise density. Shot noise in transistors can be reduced by biasing with low currents. However, it also reduces the transconductance, and therefore the gain. Thus, there is an optimum value of bias current that gives a compromise between low noise and gain.

Noise figure (F) is a measure of the degradation of the signal-to-noise ratio due to the electronic components of a RF signal chain. The definition of the noise

figure is

$$F = \frac{\text{signal-to-noise ratio at input}}{\text{signal-to-noise ratio at output}} \tag{1.9}$$

In amplifiers, the output noise comes from the amplification of the thermal noise generated by the source resistance combined with the noise produced by the amplifier. Thus, F gives a measure of the excess noise added by the amplifier. Sometimes, the noise of an amplifier is characterized by means of an equivalent noise temperature T_n. Assuming a noiseless version of the amplifier, T_n gives the hypothetical temperature of the source resistor which produces the same output noise power than the amplifier itself. The noise temperature can be given in terms of the noise figure as

$$T_n = T_0(F - 1) \tag{1.10}$$

where T_0 is the reference temperature (290 K). In the case of a passive attenuator, the noise figure of the circuit is directly given by its loss factor.

The noise figure of a transistor-based amplifier is usually given modeled as

$$\begin{aligned} F &= F_{min} + \frac{1}{R_n \mathrm{Re}\{Z_S\}} |Z_S - Z_{opt}|^2 \\ &= F_{min} + 4\frac{R_n}{Z_0} \frac{|\Gamma_S - \Gamma_{opt}|^2}{|1 + \Gamma_{opt}|^2 (1 - |\Gamma_S|^2)} \end{aligned} \tag{1.11}$$

where F_{min} is the minimum noise figure of the amplifier, R_n is the noise resistance parameter of the amplifier, Z_{opt} is the optimum noise impedance (at which F_{min} is achieved), and Z_S is the source impedance. It can also be expressed in terms of reflection coefficients, where Γ_S is the source reflection coefficient, Γ_{opt} is the optimal noise matching, and Z_0 is the reference impedance. As it can be seen, the noise figure of the amplifier depends on the intrinsic noise parameters of the amplifier (F_{min}, R_n and Z_{opt}), and on the source impedance Z_S. In order to minimize the noise, Z_S should be synthesized to be as close as possible to Z_{opt}.

When cascading different subsystems (Fig. 1.14), the noise figure of the overall system is given by the Friis formula as

$$F_{casc} = F_1 + \frac{F_2}{G_1} + \frac{F_3}{G_1 G_2} + \cdots + \frac{F_N}{G_1 G_2 \cdots G_{N-1}} \tag{1.12}$$

where F_i and G_i indicates the noise figure and gain of the subsystem i.

As it can be seen from (1.12), the noise figure of the first subsystem is more significant, since the noise of subsequent sections is attenuated by the gain factors of the precedent sections. This is the reason for which the first device after the antenna in a receiver chain is typically a low noise amplifier.

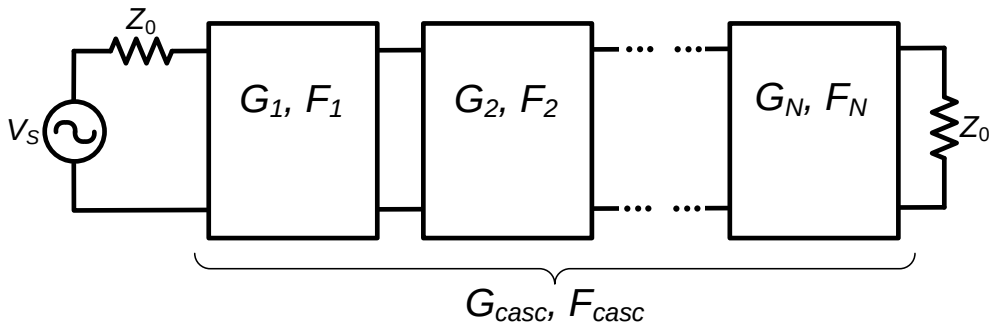

Figure 1.14: System formed by N cascaded devices. G_i and F_i indicate gain and noise figure respectively.

In theory, the noise figure of an amplifier could be obtained by measuring the output power for a matched load at 0 K. However, it is not practical since source impedance at 0 K cannot be achieved. Instead, a different technique known as Y-factor method is commonly used. It consists of using two different loads at two different temperatures (Fig. 1.15). If two source loads at temperatures T_1 and T_2 are used to feed an amplifier (or another two-port device), the corresponding output powers are given by

$$\begin{aligned} P_1 &= kGT_1B + kGT_nB \\ P_2 &= kGT_2B + kGT_nB \end{aligned} \tag{1.13}$$

where k is the Boltzmann constant (i.e., k=$1.38 \cdot 10^{-23}$ JK^{-1}), G and T_n are the gain and the noise temperature of the amplifier, and B is the bandwidth.

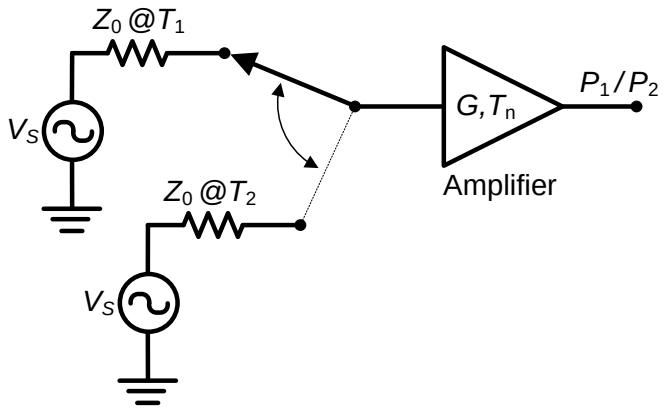

Figure 1.15: Description of the Y-factor method.

Assuming that $P_1 > P_2$, the Y-factor is defined as

$$Y = \frac{P_1}{P_2} \geq 1 \tag{1.14}$$

Finally, the noise temperature of the amplifier can be determined from (1.13) and (1.14) as

$$T_n = \frac{T_1 + YT_2}{Y - 1} \tag{1.15}$$

in which it is necessary to know the two source temperatures and the two measured output powers. It should be noticed that better accuracy is obtained for higher difference between the 'hot' and 'cold' temperatures.

1.4 References

[1] History of the Atlantic Cable & Undersea Communications: http://www.atlantic-cable.com/

[2] J. Moyle, "Amplifier before electronics - The magnifiers," *IEEE History of Telecommunication Conference*, pp. 136–141, Sep. 2008.

[3] R. H. Abrams, B. Levush, A. A. Mondelli, and R. K. Parker, "Vacuum electronics for the 21st century," *IEEE Microwave Magazine*, vol. 2, no. 3, pp. 61–72, Sep. 2001.

[4] S. A. Maas, *The RF and microwave circuit design cookbook*. Artech House Publishers, 1998.

[5] L. E. Larson, "Integrated circuit technology options for RFIC's - Present status and future directions," *IEEE Journal Solid-State Circuits*, vol. 33, no. 3, pp. 387–399, Mar. 1998.

[6] D. Segovia-Vargas, L. E. Garcia-Castillo, and A. Garcia-Lamperez, "Microondas y circuitos de alta frecuencia", Opencourseware, Leganes, Dec. 2009. [Online]. Available: http://ocw.uc3m.es/teoria-de-la-senal-y-comunicaciones/microondas-y-circuitos-de-alta-frecuencia/

[7] R. E. Collin, *Foundations for microwave engineering*. Wiley Interscience, 2nd ed., 2001.

[8] D. M. Pozar, *Microwave engineering*. John Wiley & Sons, 2nd ed., 1998.

Chapter 2

Dual-Band Active Filters Based on CRLH Transmission Lines

Modern wireless telecommunication equipments tend to provide several communication services into the same physical device (Fig. 2.1). Since each communication standard usually operates at a different carrier frequency, the use of multiband electronic components is a very efficient solution in the implementation of the RF front-ends for such devices. Recently, many efforts have been done in the design of RF components working at several frequencies, including antennas, amplifiers, filters, combiners, etc.

During the last years, the development of metamaterial-inspired microwave devices has led to significant progress in this field. In particular, engineers have taken advance of the non-linear phase response of the so-called composite right/left-handed (CRLH) transmission lines [1] for the implementation of many multiband antennas [2]-[4] and circuits [5]-[16]. Regarding to the last topic, although the list of references about passive devices is quite extensive, only a few examples that embed CRLH lines in active circuit topologies to achieve dual-band operation can be found. Apart of the work presented in this thesis [9]-[11], these other examples include the design of dual-band power amplifiers [12]-[15] and distributed amplifiers [16].

On the other hand, microwave designers have found active filters to be a very powerful solution in the design of modern telecommunication devices. Thus, different techniques have been developed, such as negative resistance elements [17], active inductors [18], actively coupled resonators [19], and transversal or recursive topologies [20]. Furthermore, active filters offer responses with high quality (Q) factors in a relatively compact size with respect to planar passive resonators. Surprisingly, although many dual-band and multiband passive resonators topologies

have been proposed in the literature (e.g. [21]-[23]), the design of active filters with multiple pass-bands was an almost unexplored field, in particular at RF and microwave frequencies.

The work presented in this chapter deals with the design of dual-band active filters based on CRLH transmission lines. By taking advantage of the feedback configuration of recursive active filter topologies [20], it is possible to achieve pass-bands at two arbitrary frequencies by placing CRLH transmission lines in some branches of the structure. It provides additional degrees of freedom in comparison with conventional lines, so that the phase response of such branches can be independently controlled at the two desired bandpass frequencies.

This chapter is structured as follows. Section 2.1 presents some introductory concepts related with microwave active filters. In addition, the operation principles of recursive active filters are analyzed. The main properties and applications of metamaterial transmission lines are described in Section 2.2. The novel structure based on embedding CRLH transmission lines in recursive active filter topologies to achieve dual-band bandpass operation is presented in Section 2.3. Furthermore, the different designs and implemented prototypes proposed in this thesis are also presented in this section. They include first-order topologies based on branch-line hybrids [9] (subsection 2.3.2), multiple-order filters based on coupled rings [10] (subsection 2.3.3) and tunable dual-band active filters [11] (subsection 2.3.4). Finally, the main conclusions of this chapter are exposed in Section 2.4.

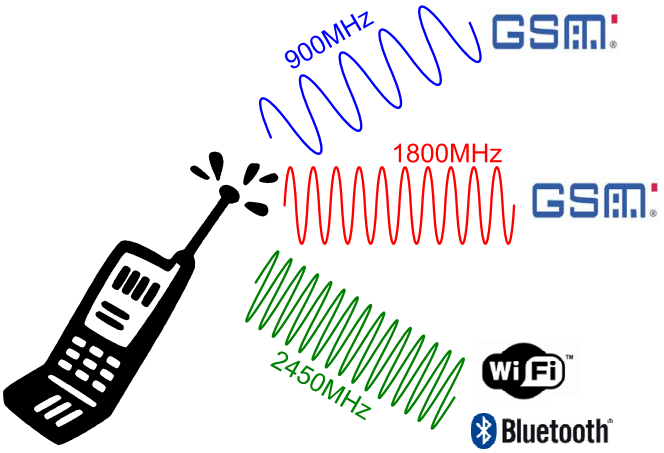

Figure 2.1: Example of a modern wireless terminal providing different services at several frequencies.

2.1 Microwave Active Filters

2.1.1 Introduction to active filters

Microwave filters are a fundamental part in any telecommunication system. They are used to preserve a determined frequency band and can be cataloged as low-pass, high-pass, band-pass or band-stop devices, depending on the range of transmitted/rejected frequencies. Classical microwave filter designs were widely based on waveguide approaches. However, due to the compact size and low weight required in many modern applications, the evolution toward planar solutions has been unavoidable. Passive planar filters can be firstly considered because of their simplicity and robustness. However, one of the main limitations of passive resonators is their constant product between insertion loss and bandwidth. Thus, the narrower the bandwidth in a filter of a given technology, the higher its loss. Therefore, the only way to reduce the insertion loss of a filter, for a given technology and bandwidth, is to increase the Q-factor of its resonant circuits. Generally, this means larger size and higher cost.

One option to overcome the previous drawbacks, especially losses compensation, consists in the integration of both active components and passive filtering structures. This active filter approach presents several advantages in comparison with passive resonators, as for example:

- High gain
- Improved selectivity
- Easy integration in MIC/MMIC technologies
- Small dimensions and weight

On the other hand, the use of active devices opens new considerations that must be taken into account:

- Noise figure increase
- Biasing power
- Dynamic range reduction
- Electrical stability
- Variation with external mechanical, climatic or electromagnetic conditions

At low frequencies, up to about 1 MHz, active filters based on lumped components and operational amplifiers have been developed during the last decades. At microwave frequencies, filters can still use distributed or discrete elements, but they can be quite bulky, especially in comparison with monolithic microwave integrated circuits (MMICs). The use of MMIC technology to implement microwave filters provides great performance-to-size ratio and, additionally, allows ease of integration with signal processing circuits. However, MMIC filters built with passive components alone provide poor selectivity and high losses, basically due to the undesired parasitic effects of their planar lumped components. For example, in [24], a passive LC bandpass filter on GaAs MMIC technology presents 6.7 dB of insertion losses at a center frequency of 3 GHz. The only way to improve this performance is by combining both lumped elements and transistors, where the gain of the active device can compensate the losses of the passive elements. At frequencies below 1 MHz, operational amplifiers can be considered almost ideal gain blocks, which facilitates the active filter design. Nevertheless, transistor parameters at higher frequencies are quite dependent on frequency, biasing or signal level. Therefore, the success of an active filter design in the microwave range requires using accurate modeling of both active and passive components.

2.1.2 Classification of active filters

Microwave active filters can be classified in different ways, depending on the circuit topology, the type of the passive or active components, the resonator configuration, the frequency band, etc. One of the classical classifications divides active filters into four groups: based on negative resistance elements, active inductors, actively coupled resonators and transversal/recursive filters. The main characteristics of each group and some practical examples will be described below. Special attention will be paid to the last approach, since the recursive topology will be the one used in Section 2.3 in the implementation of the proposed dual-band active filters.

2.1.2.1 Negative resistance elements

Several decades ago, negative impedance converters (NICs) were developed as an active circuit that provided an input impedance proportional to the negative of a certain load impedance [25]. In most cases, NICs are used for compensation of losses and resistive parts of passive circuits. They were originally conceived for low frequency applications, although they can be used at microwave frequencies if parasitics and transmission line effects are carefully taken into account. Two design examples of NICs are shown in Fig. 2.2 [26].

For the case of the design shown in Fig. 2.2(a), the input impedance is dependent on three load impedances (Z_1, Z_2 and Z_3) and requires two FETs (F_1 and F_2). The calculation of the input impedance is detailed below. The gate-to-source voltage of F_2 (i.e., V_{gs2}), can be obtained as a function of the gate-to-source voltage of F_1 (i.e., V_{gs1}), the transconductances of F_1 and F_2 (i.e., g_{m1} and g_{m2}), and the load impedances Z_1 and Z_2

$$\begin{aligned} V_{gs2} &= -g_{m1}V_{gs1}Z_1 - g_{m2}V_{gs2}Z_2 \\ \Rightarrow V_{gs2} &= -\frac{g_{m1}V_{gs1}Z_1}{1+g_{m2}Z_2} \end{aligned}$$

Now, both the input voltage and current, i.e., V_{in} and I_{in} respectively, can be obtained as

$$\begin{aligned} V_{in} &= -g_{m2}V_{gs2}Z_3 - V_{gs1} = \left(\frac{g_{m1}g_{m2}Z_1Z_3 - 1 - g_{m2}Z_2}{1+g_{m2}Z_2}\right)V_{gs1} \\ I_{in} &= -g_{m1}V_{gs1} \end{aligned}$$

The input impedance can be calculated as the the ratio between both values as

$$Z_{in} = \frac{V_{in}}{I_{in}} = -\frac{g_{m1}g_{m2}Z_1Z_3 - 1 - g_{m2}Z_2}{g_{m1} + g_{m1}g_{m2}Z_2}$$

Finally, if high-gain transistors are assumed, i.e., $g_m \to \infty$, the input impedance can be approximated to

$$Z_{in} \approx -\frac{Z_1Z_3}{Z_2} \tag{2.1}$$

Regarding to (2.1), it can be directly seen the negative impedance behavior of the circuit, whose input impedance is a negative version of a ratio given by the load impedances Z_1, Z_2 and Z_3.

For the case of the other circuit shown in Fig. 2.2(b), only one load impedance is used. The input impedance calculation is similar. The input voltage and current can be obtained as

$$\begin{aligned} V_{in} &= \frac{V_{gs2}}{g_{m1}Z_1} \\ I_{in} &= -g_{m2}V_{gs2} \end{aligned}$$

Therefore, the input impedance is given by

$$Z_{in} = \frac{V_{in}}{I_{in}} = -\frac{1}{g_{m1}g_{m2}Z_1} \tag{2.2}$$

In this second NIC, the negative input impedance is proportional to the inverse of the load impedance Z_1, and depends on the transconductances of both transistors.

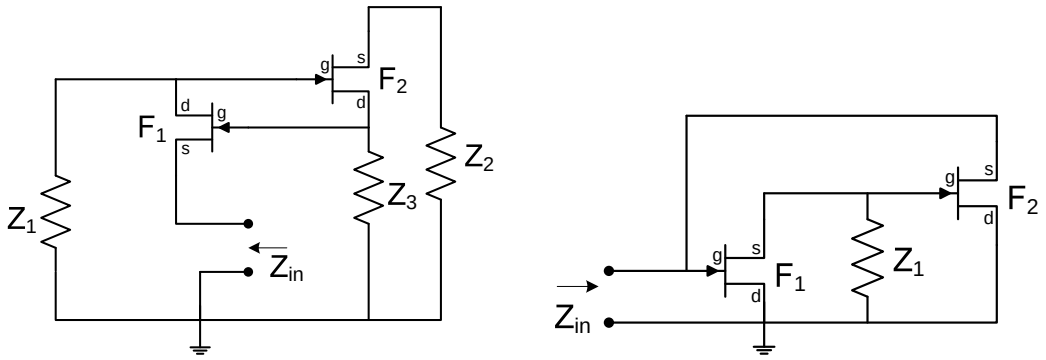

(a) (b)

Figure 2.2: Two examples of negative impedance converters [26].

A practical example of a bandpass active filter that makes use of a negative resistance is given in [17]. The unitary tank is shown in Fig. 2.3(a), and is based on a coupled shunt resonator. A negative resistance R_n is connected to the circuit in order to cancel out the intrinsic dissipating resistance of the tank, so a lossless tank can be obtained by properly adjusting the value of R_n. The filter response of a two pole implementation is shown in Fig. 2.3(b). This plot shows a comparison of the active filter with respect to an equivalent passive implementation. A significant improvement over the selectivity of the filter can be seen, as well as the insertion losses are reduced from 9 dB to almost 0 dB in the pass band.

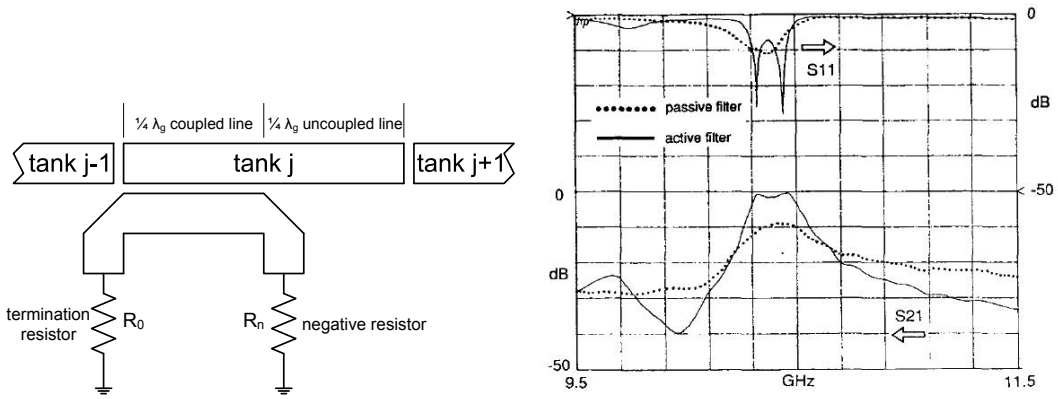

(a) (b)

Figure 2.3: Microstrip active tank (a) and measured performance (b) of a two pole filter using the coupled negative resistance method [17].

2.1.2.2 Active inductors

In MMIC designs, inductors are usually implemented by means of planar spirals. However, this kind of inductors presents high capacitive and resistive parasitics, which makes difficult the design of broadband inductances. Furthermore, high inductance values are also difficult to implement, since they would need large size. Thus, smaller-sized and broadband active inductors have been proposed in the literature to overcome all these problems. An example of an active inductor design proposed in [27] is shown in Fig. 2.4. A common source cascode configuration is fed back by using a common gate FET. The admittance Y seen from the input of this active circuit can be approximated by

$$Y = g_{mf}\left(1 - \frac{C_{gs2}g_{m1}}{C_{gs1}g_{m2}}\right) + \frac{g_{m1}g_{mf}}{j\omega C_{gs1}}$$

where sub-index 1 and 2 correspond to the FETs in the common source cascode, and sub-index f correspond to the common gate FET. When the common source cascode is composed by FETs with the same transconductance g_m and gate-to-source capacitance C_{gs}, the conductance of the previous expression is canceled. Therefore, the circuit acts as a lossless inductor whose impedance value is given by

$$Z = j\omega\frac{C_{gs}}{g_m g_{mf}} \tag{2.3}$$

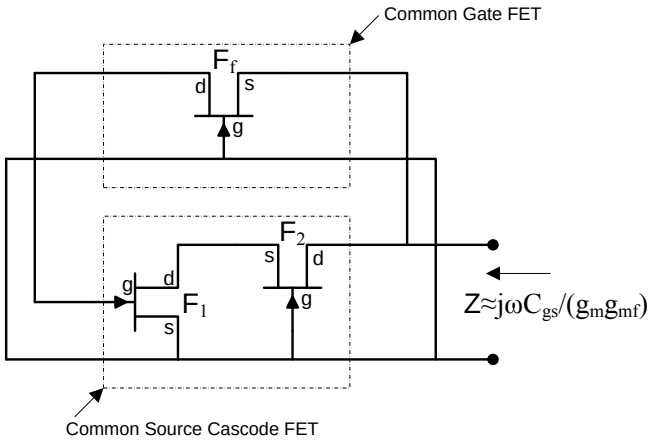

Figure 2.4: Example of an active inductor design [27].

A practical implementation of a filter is presented in [18]. In this case, the basic filter cell consists of a shunt LC resonator, as it can be seen in Fig. 2.5(a). The idea is to use a high-Q inductor, which can provide much lower resistive

parasitics than a planar inductor, and therefore the insertion losses of the filter can also be reduced. Different basic cells can be combined by means of series coupling capacitors, that is C_2 and C_3 in Fig. 2.5(a). The measured results of a bandpass filter centered at 2 GHz by using three cascaded resonators are shown in Fig. 2.5(b). The insertion losses at the center frequency are around 0.3 dB.

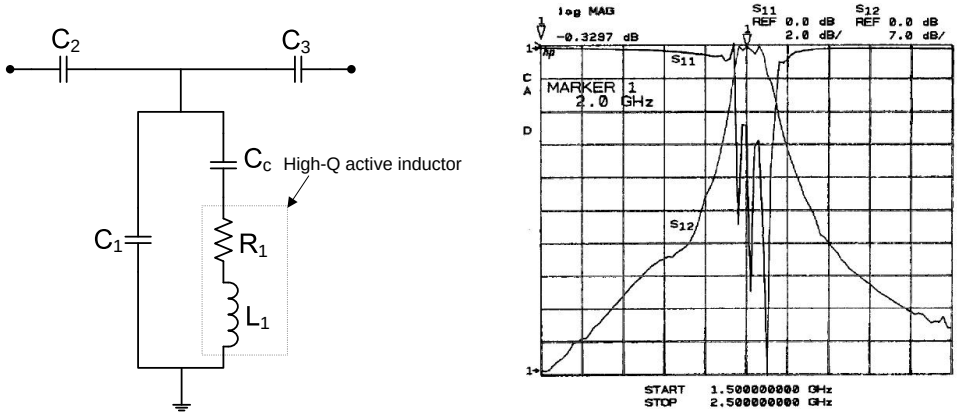

(a) (b)

Figure 2.5: Shunt resonator based on a high-Q active inductor (a) and measured response of a three resonator active filter implementation (b) [18].

2.1.2.3 Actively coupled resonators

Multiple-order filters are commonly implemented by using several passive resonators in cascade. However, due to the loading effects between the different stages, the performance of a N-order filter may differ with respect to the theoretical response obtained from concatenating N isolated stages. A technique to isolate the different stages and, therefore, reducing the circuit sensitivity to process tolerances consists on placing transistors between the different passive resonators. Additionally, the task of designing a high-order filter is reduced to simple low-order sections, since the pole positions of each resonator can be independently controlled. Although the transistors are not a part of the resonators, their parasitics must be considered during the design process, since they are not ideal unilateral gain sections. An example of the basic cell of an actively coupled resonator is shown in Fig. 2.6(a) [28]. It should be noticed that a single transistor is needed in each transition between the passive resonators. In this case, the resonator is formed by the conductance G_p, the inductance L_p and the capacitance C_p, where sub-index p denotes parallel. An equivalent representation of the unit cell taking into account the transistor parasitics is presented in Fig. 2.6(b).

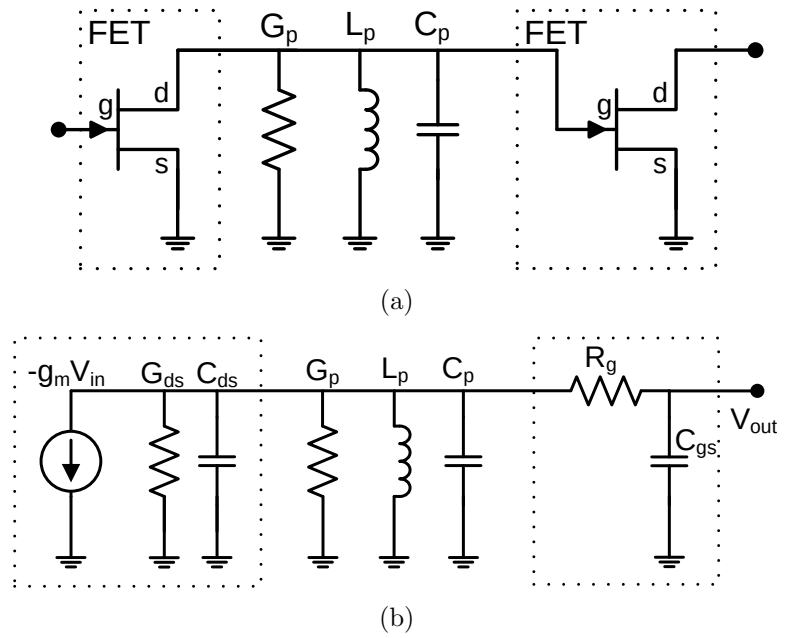

Figure 2.6: Example of a cell of an actively coupled resonator (a) and equivalent circuit representation including FET parasitics (b) [28].

The transfer function of the circuit in the frequency domain can be obtained as

$$H(\omega) = \frac{V_{out}}{V_{in}} = -\frac{g_m}{G + \frac{R_g C_{gs}}{L_p} R_g C C_{gs} \omega^2 + j \frac{L_p \omega^2 (C + C_{gs}(1 + R_g G)) - 1}{L_p \omega}} \tag{2.4}$$

where g_m is the transconductance of the transistor, C_{ds} and G_{ds} are the drain-to-source parasitic capacitance and conductance, R_g is the parasitic gate resistance, C_{gs} is the gate-to-source parasitic capacitance, $G = G_p + G_{ds}$, $C = C_p + C_{ds}$ and $\omega = 2\pi f$. This formula can be approximated to

$$H(\omega) \approx H(\omega_0) \frac{1}{1 + jQ\left(\frac{\omega}{\omega_0} - \frac{\omega_0}{\omega}\right)}$$

where Q is the quality factor of the cell and ω_0 is the resonant frequency (at which the transfer function is purely real). These two parameters can be calculated as

$$\omega_0 = \sqrt{\frac{1}{L_p}(C + C_{gs}(1 + R_g G))}$$
$$Q = \frac{1}{L_p \omega_0 (G + R_g C_{gs}^2 (1 + R_g G) \omega_0^2)}$$

As it can be seen from the previous analysis, if the parasitics of the transistors are properly considered, the performance of each cell can be ideally adjusted independently from the other cells, due to the unilateral response of the active devices. It must be noticed that a more complete analysis can be done by adding the feedback parasitic capacitance C_{gd}. For this case the transistors are no longer considered as unilateral.

A practical implementation of a MMIC active filter based on actively coupled resonators is presented in [19]. It consists of three LC resonators and two FETs, in the configuration that is shown in Fig. 2.7(a). The filter response is plotted in Fig 2.7(b), in which a gain higher than 10 dB is obtained at about 1900 MHz. With these filters it is more feasible to obtain gain values higher than 0 dB than with other active filter topologies, since the passive resonators do not feed power back between the two terminals of the amplifiers and, therefore, the risk of instabilities is lower.

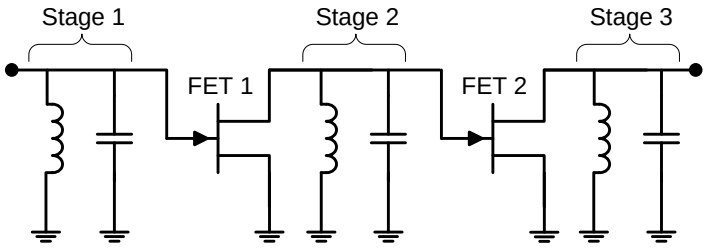

(a)

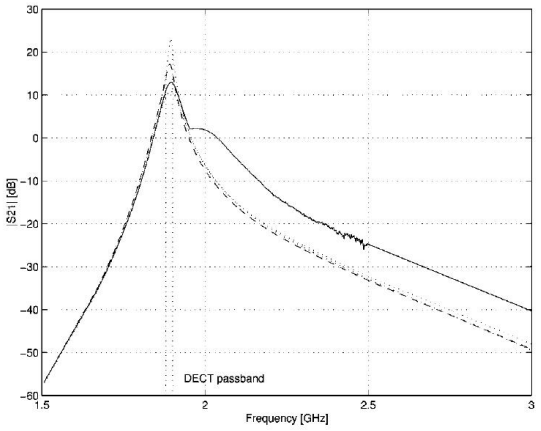

(b)

Figure 2.7: Circuit topology (a) and measured (solid) and simulated (dashed) response (b) of an active filter based on actively coupled resonators [19].

2.1.2.4 Transversal and recursive topologies

Transversal and recursive active filters are inspired by the filtering concepts used for low-frequency digital-domain filters. The filtering response of these distributed filters is based on the combination of different samples of the input signal along several paths through the output. Depending on the topology, two different filter categories can be considered: transversal and recursive. The transversal filter only presents feed-forward branches, as it can be seen in Fig. 2.8(a). This kind of structure is similar to the one used in distributed amplifiers. The difference is that, in the case of the amplifier, all the paths are identical and the signals combine in phase at every frequency. For the case of the transversal filter, the signals are combined in phase only at the desired bandpass frequency. On the other hand, recursive filters make use of both feed-forward and feedback branches, as it is shown in Fig. 2.8(b).

Transversal structures are usually simpler to design. However, the extra degree of freedom given by the feedback usually makes the recursive type need fewer branches than the transversal type to provide equivalent performance [20]. This fact translates into more compact implementations. Nevertheless, special considerations must be taken into account with the recursive topology in order to avoid instabilities due to the feedback lines.

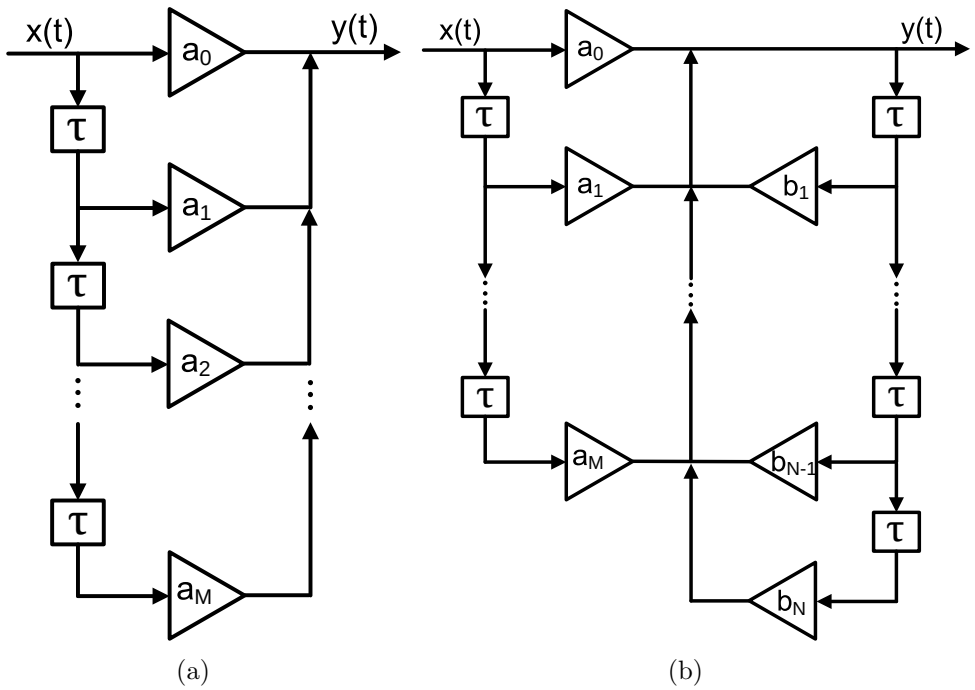

Figure 2.8: Flow graphs of a transversal (a) and a recursive (b) filter topologies.

The analysis of this kind of structures can be done in the time or in the frequency domain. In the case of the transversal filter shown in Fig. 2.8(a), the time-domain equation can be written as

$$y(t) = \sum_{m=0}^{M} a_m x(t - m\tau) \tag{2.5}$$

where $x(t)$ and $y(t)$ are the time-dependent input and output signals, a_m denotes the weights of the feed-forward branches, and τ represents a time delay. From (2.5), a frequency-dependent transfer function $H(f)$ can be easily obtained as

$$H(f) = \frac{Y(f)}{X(f)} = \sum_{m=0}^{M} a_m e^{-j2\pi f m\tau} \tag{2.6}$$

where $X(f)$ and $Y(f)$ are the frequency-dependent input and output signals. A similar analysis can be done with the recursive filter of Fig. 2.8(b), just by adding the feedback terms. Thus, the time-domain equation of the recursive filter can be written as

$$y(t) = \sum_{m=0}^{M} a_m x(t - m\tau) + \sum_{n=1}^{N} b_n y(t - n\tau) \tag{2.7}$$

where b_n are the weights of the feedback branches. Operating from (2.7), the transfer function of the recursive filter in the frequency domain can be written as

$$H(f) = \frac{Y(f)}{X(f)} = \frac{\sum_{m=0}^{M} a_m e^{-j2\pi f m\tau}}{1 - \sum_{n=1}^{N} b_n e^{-j2\pi f n\tau}} \tag{2.8}$$

The conventional notation for the order of the filter usually refers to the number of feed-forward and feedback branches (i.e., M and N values according to Fig. 2.8).

The microwave implementation of this types of filters usually requires transmission lines or lumped element cells for the time-delay blocks, amplifiers and/or attenuators for the weights, and power combiners to combine and split the signals in certain directions and avoid undesired feedback effects. It should be noticed that, unlike in the case of the ideal representation of Fig. 2.8, microwave components may present frequency-limited performance, which must be taken into account in the practical implementation.

The basic scheme of a first order filter ($M = 0$ and $N = 1$) and its implementation in microwave technology is shown in Fig. 2.9. Two microwave combiners have been connected at the input and output ports to properly control the power flux in the circuit. The weight of the direct branch (i.e., a_0) is controlled by means of the gain of an amplifier. The feedback weight (i.e., b_1) is given by the

combined amplitude parameters of the feedback transmission line and the upper branches of the power combiners. The lower branches of the combiners are effectively outside the loop, and they just act as two attenuators at the input and output of the filter. The phase delay in the loop can be controlled by modifying the length of the feedback transmission line. The operation principle is based on constructively combining the feedback power with the input signal at the desired bandpass frequency. This condition is equivalent to assume that the loop phase is multiple of 2π at such frequency, at which a maximum appears in the transfer function. During the design process, it should be taken into account not only the phase response of the feedback line, but also the phase delay introduced by the amplifier and the power combiners in the loop. A more detailed analysis about the performance of this topology is done later in subsection 2.1.3.

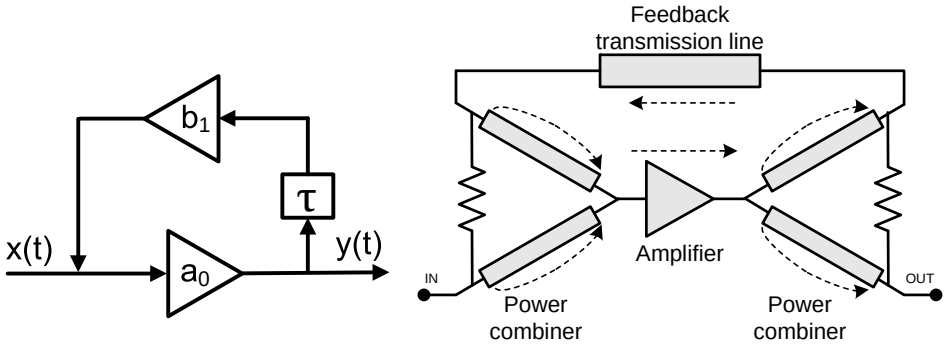

(a) (b)

Figure 2.9: Flow graph (a) and microwave implementation (b) of a first-order recursive active filter.

Several implementations of microwave recursive active filters are presented in the literature. In [29], a first-order MMIC implementation working at 10 GHz is presented. The circuit schematic is shown in Fig. 2.10(a). The signal combination is done by means of lumped-element Wilkinson hybrids. The direct branch is just formed by a series inductor. Both the delay and gain blocks are placed in the feedback line. The delay block is formed by inductors and capacitors, whose values are used to control the phase in the loop and, therefore, the desired center frequency. The measured transmission parameter is shown in Fig. 2.10(b). The gain value at the center frequency is about 8 dB.

The use of distributed power combiners can result in very voluminous filter implementations. As it was shown in [29], the use of lumped-elements solutions can be a feasible solution to reduce the size of the combiners. Another solution to guide the power in the desired directions and avoid undesired feedback effects is to use the unilateral response of the transistors. This second approach is known as

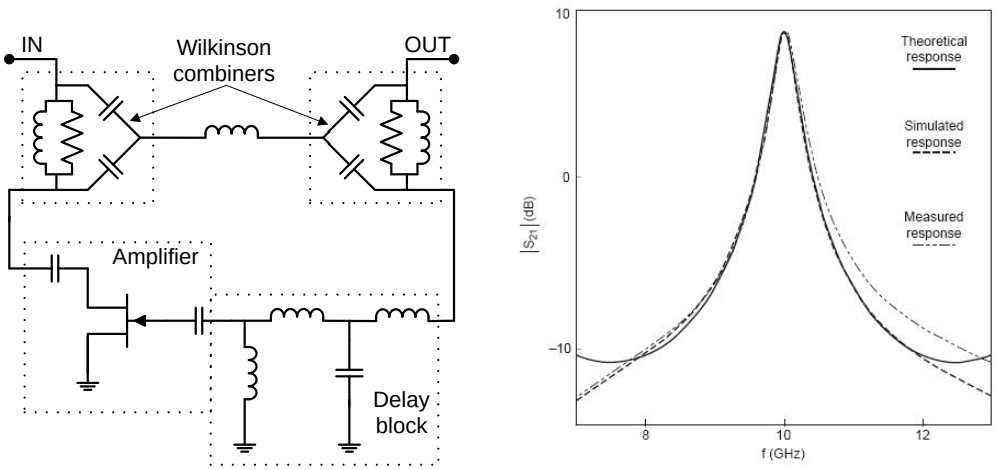

(a) (b)

Figure 2.10: Circuit schematic (a) and measured results (b) of a first-order recursive active filter based on Wilkinson combiners [29].

voltage matching technique [26] (in contrast with the power matching approach when using power combiners). An example of this technique is given in [30]. The circuit schematic is shown in Fig. 2.11(a). In this case, a common-gate and a common-drain transistor are placed at the input and output of the circuit respectively. The purpose of these two transistors is to improve the impedance matching of the filter as well as to avoid instability problems. A common-drain transistor is used as gain block in the direct branch, and a passive network is used as delay block in the feedback line. This implementation is also illustrative to see the tuning capabilities in recursive structures. Since the phase in the filter loop determines the bandpass frequency, just by including a phase shifter in either the direct or the feedback branch directly allows controlling the center frequency of the filter. In the circuit shown in Fig. 2.11(a), a variable capacitance is synthesized by means of a varactor diode, which allows modifying the phase response of the delay cell by means of a external voltage and, therefore, the center frequency of the filter. The measured results of this tunable filter are shown in Fig. 2.11(b). The center frequency is tuned from 7.2 GHz up to 9.5 GHz, while maintaining a constant gain of 3 dB.

Till now, previous recursive filter examples correspond to first-order structures. Of course, in order to satisfy certain requirements of selectivity, bandwidth or ripple, multiple-order resonators may be needed. A direct approach consists on cascading several first-order filtering structures. In [31], a filter based on four cascaded chips with a tunable version of the first-order filter shown in Fig. 2.10(a) is presented. The four poles of the filter are independently controlled to obtain

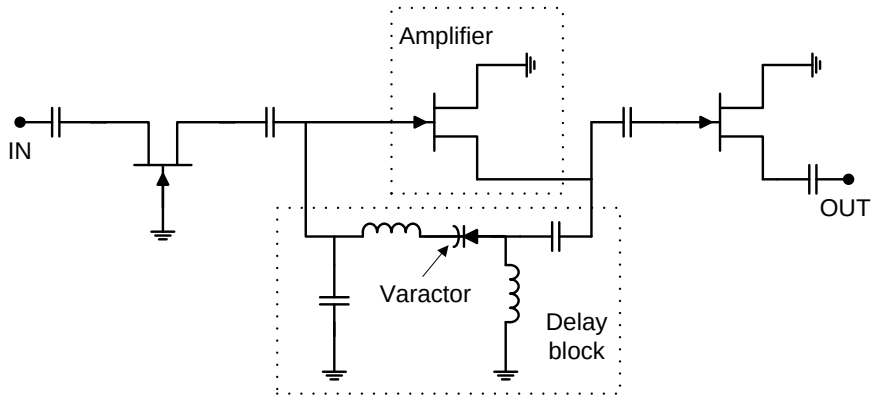

(a)

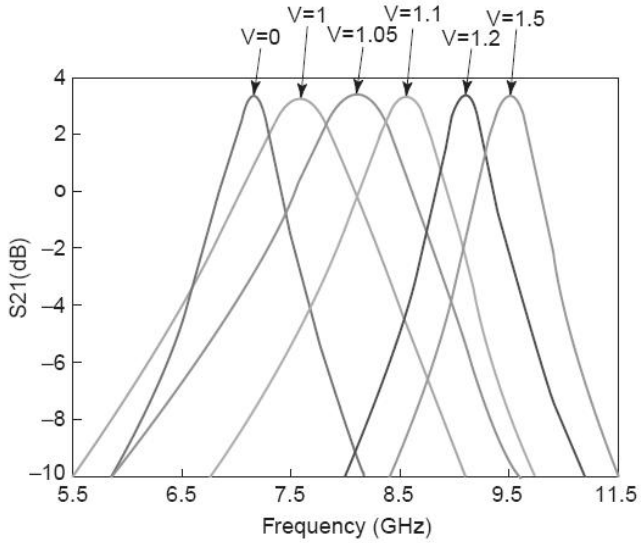

(b)

Figure 2.11: Circuit schematic (a) and measured results (b) of a tunable recursive active filter based on the voltage matching technique [30].

the desired trade-off between gain, selectivity and bandwidth. The measured parameters of the four-pole recursive active filter are plotted in Fig. 2.12. The poles have been fixed at 9.5, 9.85, 10.15 and 10.3 GHz respectively. The performance of the first-order filters alone are a gain close to 2.5 dB and out-of-band rejection better than 15 dB at 8 and 12 GHz. With the multiple-order implementation, the out-of-band rejection has been improved up to 50 dB and the gain has been increased up to near 6 dB. Other solutions based on using multiple feedback lines are also feasible. However, as pointed out in [31], they usually require more complex structures.

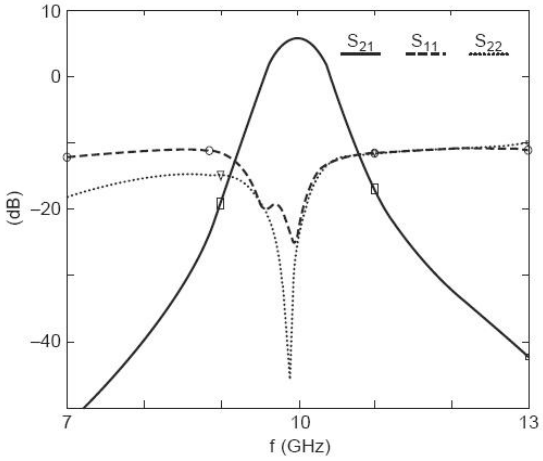

Figure 2.12: Measured results of a four-pole filter based on cascading multiple first-order recursive active filter implementations [31].

One of the main limitations when cascading several stages, and even when using several feedback branches, is that it may require the use of many power combiners and, therefore, the size of the circuit may become prohibitive. Additionally, the complexity of the filter may also be incremented. One solution to reduce the number and the size of the combiners in multiple-order recursive filters is to use coupled ring resonators. An example of this approach is given in [32]. The circuit schematic of a second-order active filter based on two active ring resonators is shown in Fig. 2.13(a). It consists of two coupled ring resonators. Two MMIC amplifiers are embedded in the structure, the first one in the feedback branch of the first ring and the second one in the direct branch of the second ring. In this case, the power is combined by means of combiners based on coupled lines. The improvement in terms of size when using these coupled lines instead of other power combiners (e.g., branch-line or Wilkinson) is evident. Firstly, it is a narrow structure, instead of the others that occupy great surface. Nevertheless, the main advantage is that a single combiner is needed in the interconnection

between the different stages, instead of the two that are needed when directly cascading conventional first-order recursive filters. Thus, in the case of a K-order filter, $2K$ combiners are needed with the approach of cascading K independent first-order filters, and only $K + 1$ combiners in the case of using coupled active rings. The measured results of the filter prototype are shown in Fig. 2.13(b). A gain value around 14 dB has been achieved at a center frequency of 4 GHz.

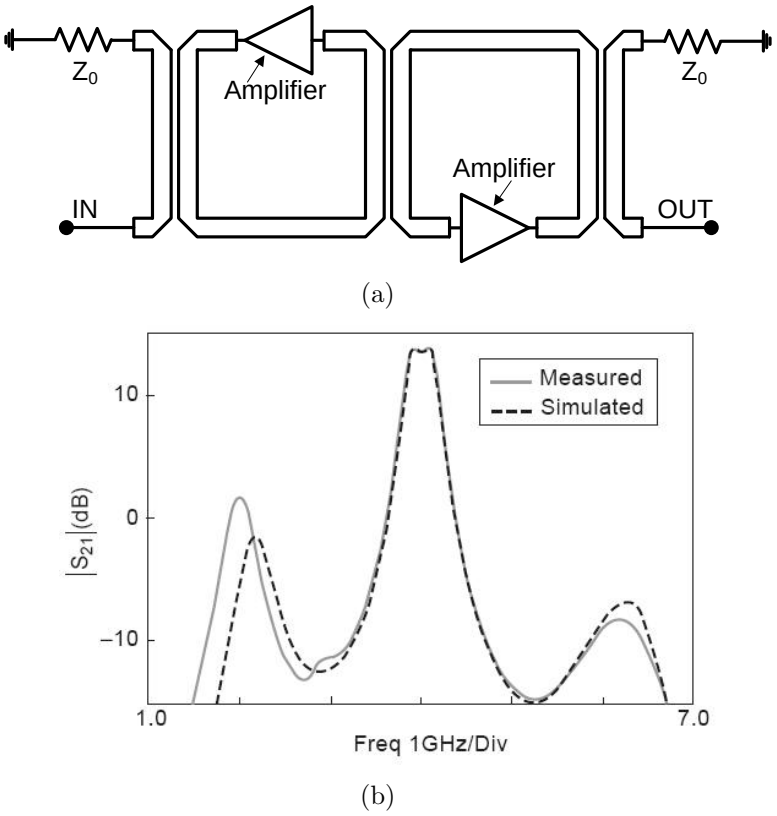

Figure 2.13: Circuit schematic (a) and measured results (b) of a second-order filter based on active ring resonators [32].

2.1.3 Analysis of recursive active filters

There are several characteristics that should be taken into account when designing and characterizing a microwave active filter and, more concretely, when designing a recursive active filter. Firstly, the gain of the active blocks will determine the gain of the filter at the bandpass frequencies. However, special care should be taken, since an excess of gain in the feedback structure may lead to instabilities in the circuit. On the other hand, the noise figure of the filter will be determined by

the noise performance of the gain block and the losses of the passive components. The main characteristics of the recursive active filter topologies will be analyzed in the subsequent subsections.

2.1.3.1 Gain

A general scheme of a first-order microwave recursive filter topology is shown in Fig. 2.14. It consists of two power combiners at the input and output of the circuit, which are represented by two branches. The transmission of the lower branches is characterized by the terms $\alpha_{1,2}$, and the transmission of the upper branches is characterized by the terms $\beta_{1,2}$. There are other two blocks, one in the direct branch and other one in the feedback branch, which are characterized by means of the terms A and B respectively. All the previous transmission parameters are assumed to be defined in terms of the scattering parameters (s_{21}), and they are frequency dependent. Thus, assuming perfect matching conditions between all the blocks of the circuit, the transfer function of the filter H can be obtained as

$$H(f) = s_{21}(f) = \frac{A\alpha_1\alpha_2}{1 - \beta_1\beta_2 AB} \tag{2.9}$$

where f denotes the frequency.

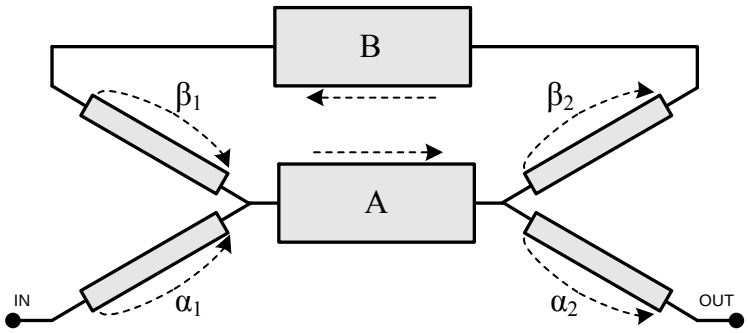

Figure 2.14: General schematic of a first-order recursive filter.

For stability reasons (see subsection 2.1.3.3), the gain in the loop should be bounded to be lower than one, i.e.,

$$|\beta_1\beta_2 AB| < 1 \tag{2.10}$$

If it is assumed that the modules of all the transmission parameters of the blocks in the filter are constant with respect to the frequency, the maximum of the module of the transfer function H is obtained when

$$\angle(\beta_1\beta_2 AB) = \angle(\beta_1) + \angle(\beta_2) + \angle(A) + \angle(B) = n2\pi \tag{2.11}$$

where $\angle(\bullet)$ denotes the angle and n is any integer number. Thus, from (2.11), it can be seen that the pass bands are given at the frequencies at which the sum of phases in the loop is a multiple of 2π. This condition implies that the signal traveling along the feedback block constructively combines with the signal coming from the input. In general, that condition can be satisfied at several frequencies simultaneously, which usually gives a response with multiple spurious.

In practice, blocks A and B can be implemented by means of amplifiers and transmission lines. Assuming that a single amplifier is used in the first-order filter implementation, two possible designs are possible, as it can be seen in Fig. 2.15. In the topology shown in Fig. 2.15(a), the amplifier is connected in the direct branch, and a transmission line is used as feedback block. The transfer function in this case can be calculated as

$$H_a(f) = \frac{\alpha_1 \alpha_2 A}{1 - \beta_1 \beta_2 A \gamma} = \frac{\alpha_1 \alpha_2 A}{1 - \beta_1 \beta_2 A e^{-j\beta_l l}} \tag{2.12}$$

where β_l and l denotes the phase constant and the physical length of the transmission line respectively. On the other hand, the topology shown in Fig. 2.15(b) represents the complementary structure, with the transmission line in the direct branch, and the amplifier in the feedback branch. In this second case the transfer function is calculated as

$$H_b(f) = \frac{\alpha_1 \alpha_2 \gamma}{1 - \beta_1 \beta_2 A \gamma} = \frac{\alpha_1 \alpha_2 e^{-j\beta_l l}}{1 - \beta_1 \beta_2 A e^{-j\beta_l l}} \tag{2.13}$$

The maximum gain of the filter is obtained at the frequencies at which condition (2.11) is fulfilled (pass bands). A representation of the gain of the filter as a function of the gain of the amplifier for the two topologies shown in Fig. 2.15 is given in Fig. 2.16. This curve has been obtained by assuming the use of 3-dB hybrids and ideal transmission lines. As it was stated in (2.10), the circuit is unstable if the gain in the loop is higher than the unit. In this case, it limits the practical range of values for $|A|$ below 6 dB. Just in the limit $|A|$=6 dB, there is an asymptote in the curve. However, even operating with amplifiers with gain limited below 6 dB, the corresponding range of gain values of the filter can theoretically take any value from 0 dB up to infinite. This property is given by the positive feedback, and is one of the main advantages of recursive filters. By using other approach, as for example using the same amplifier in cascade with a passive resonator, the maximum gain of the filter is always limited below the gain of the amplifier alone. This limit does not exist in the case of the recursive filters, in which the gain of the filter may be higher than the gain of the isolated amplifier. Finally, it should be noted that, since the amplifier usually presents gain $|A| > 1$, the filter configuration shown in Fig. 2.15(a) provides higher gain in the pass band than the configuration in Fig. 2.15(b) for a given set of components.

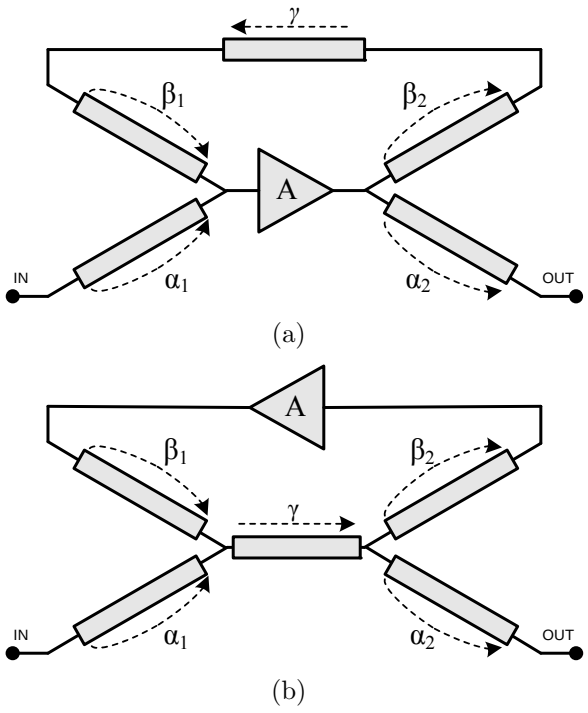

Figure 2.15: Two possible topologies of a first-order microwave recursive filter.

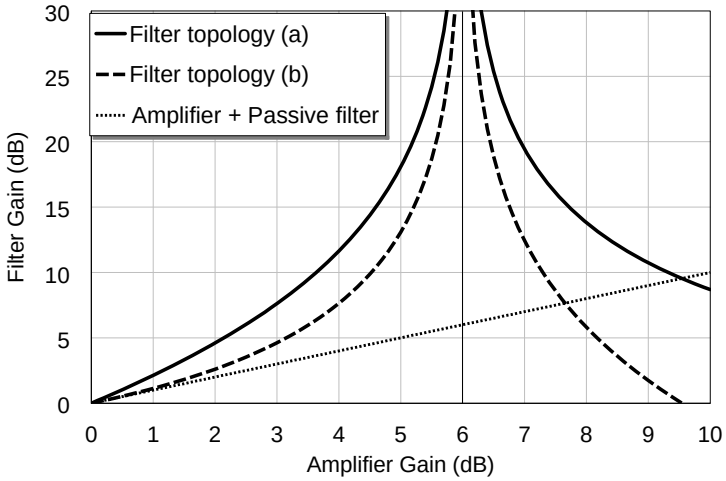

Figure 2.16: Gain of a first-order recursive filter as a function of the gain of the amplifier ($|A|$) for the two topologies shown in Fig. 2.15 and using 3-dB hybrids, and maximum gain achievable with the same amplifier in series with a passive resonator.

2.1.3.2 Multiple-order structures

Several topologies can be proposed in order to synthesize multiple-order recursive active filters. Some examples, all of them based on two-stage schemes, are shown in Fig. 2.17. For the case of the topology shown in Fig. 2.17(a), it consists on cascading several first-order stages. The transfer function of this scheme for a K-stages implementation is given by multiplying the transfer function of the individual stages, i.e.,

$$H_a^K = \prod_{k=1}^{K} \frac{A_k \alpha_{2k-1} \alpha_{2k}}{1 - \beta_{2k-1} \beta_{2k} A_k B_k} \tag{2.14}$$

For the case of the topology shown in Fig. 2.17(b), the structure provides several poles by using several feedback blocks. In this case, the transfer function for a scheme with K feedback lines can be obtained as

$$H_b^K = \frac{A_0 \alpha_1 \alpha_2}{1 - \beta_1 \beta_2 A_0 \gamma_{K-1}} \tag{2.15}$$

where

$$\gamma_i = \frac{A_i \alpha_{2i+1} \alpha_{2i+2}}{1 - \beta_{2i+1} \beta_{2i+2} A_i \gamma_{i-1}} \quad \text{, for } i > 0$$
$$\gamma_i = A_K \quad \text{, for } i = 0$$

As it was demonstrated in [31], the scheme shown in Fig. 2.17(b) may be more complex to implement, since it may require more branches than an equivalent cascaded filter based on the topology shown in Fig. 2.17(a).

Finally, the topology shown in Fig. 2.17(c) is very similar to the scheme shown in Fig. 2.17(a), but using coupled lines to combine the signals. The main advantage of using these 4-port combiners is that the number of combiners needed to achieve an equivalent response is lower compared with the conventional approach shown in Fig. 2.17(a). Thus, for a K-cell implementation, the conventional approach requires $2K$ combiners, whereas the coupled-lines approach requires only $K+1$ combiners. If the transmission along the lower branches of the combiners is much smaller than the transmission along the upper branches (i.e., $|\alpha_i| << |\beta_i|$), as it occurs with the coupled lines, the transfer function of a K-stages implementation can be approximated by

$$H_c^K = \prod_{i=1}^{K+1} \alpha_i \prod_{j=1}^{K} \frac{A_j}{1 - \beta_j \beta_{j+1} A_j B_j} \tag{2.16}$$

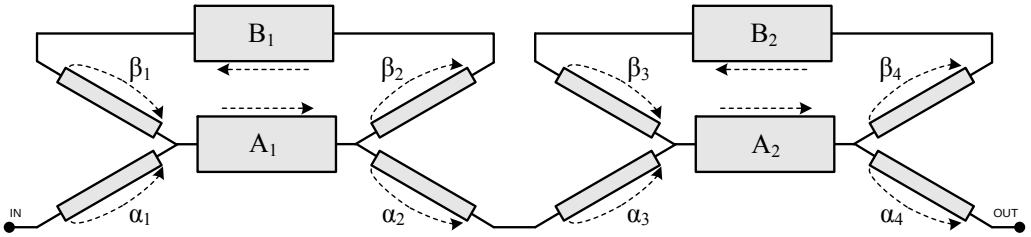

(a)

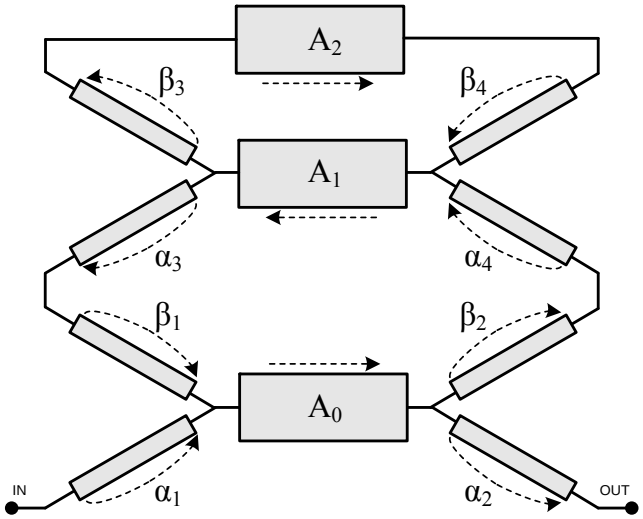

(b)

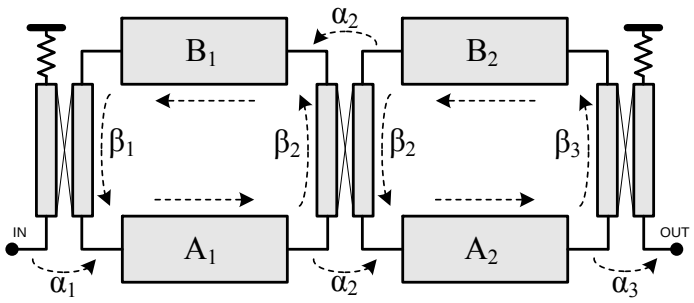

(c)

Figure 2.17: Three configurations for multiple-order recursive filters: based on multiple cascading stages (a), based on multiple feedback lines (b), and based on coupled rings (c).

2.1.3.3 Stability

Stability is one of the most important aspects that must be addressed in any active circuit and is especially critical for the case of the recursive active filters due to their feedback topology. The stability of a recursive filter topology can be studied by means of its transfer function (2.8). This expression can be written in terms of its Z-transform as

$$H(z) = \frac{\sum_{m=0}^{M} a_m z^{-m}}{1 - \sum_{n=1}^{N} b_n z^{-n}} = \sum_{k=0}^{+\infty} h_k z^{-k} \tag{2.17}$$

where $z = e^{j2\pi f\tau}$ and $\{h_k\}$ is the impulse response of the filter. The necessary and sufficient condition for a linear filter with response $\{h_k\}$ to be stable is that

$$|H(z)| \leq \sum_{k=0}^{+\infty} |h_k||z^{-k}| < \infty, \text{ for } |z| \geq 1 \tag{2.18}$$

Thus, the stability of the filter requires that the poles of $H(z)$ (zeros in the denominator) should be within the circle $|z| = 1$ [33]. In the case of the first-order scheme previously shown in Fig. 2.9(a), whose transfer function is given by

$$H(z) = \frac{a_0}{1 - a_0 b_1 z^{-1}} \tag{2.19}$$

the stability condition is satisfied when $|a_0 b_1| < 1$.

The previous analysis can be translated to the microwave domain. Assuming the first-order scheme shown in Fig. 2.14, the stability condition is directly given by (2.10). From this expression, it can be seen that it is necessary to operate with loop gain below one. In the particular cases shown in Fig. 2.15, the stability condition can be obtained from (2.12) and (2.13) as

$$|A\beta_1\beta_2| < 1 \tag{2.20}$$

Assuming a given implementation of the power combiners, the amplifier gain should be limited below a certain threshold to avoid stability problems. For example, in the case of using 3-dB combiners, the amplifier should necessarily provide a gain response lower than 6 dB, in order to operate below the asymptote in the filter response shown in Fig. 2.16. For practical implementations, this condition is more restrictive, due to the impedance mismatching between the components in the circuit, and the non perfect isolation of the power combiners in all the frequency range.

An example is shown in Fig. 2.18(a). A first-order recursive filter based on branch-line couplers and working at 1 GHz has been simulated. In order to

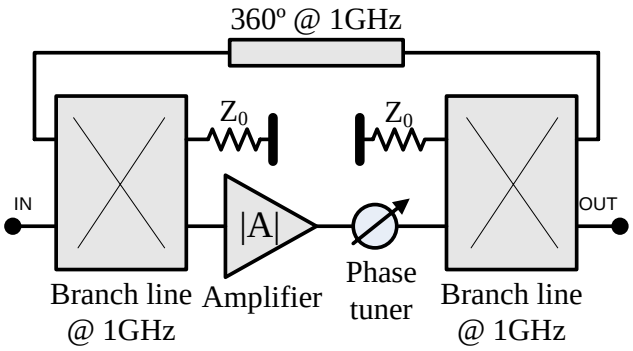

(a)

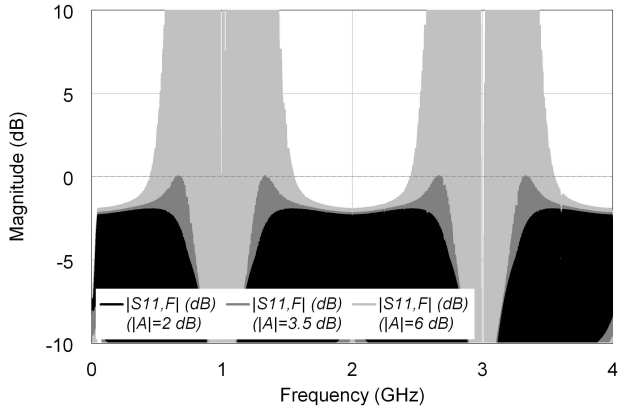

(b)

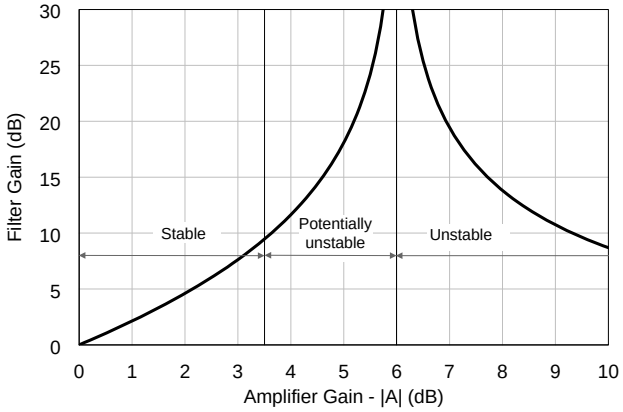

(c)

Figure 2.18: Stability analysis example: circuit schematic with a tunable phase shifter (a), reflection coefficient of the filter for a continuous sweep of the phase of the loop with three different amplifier gain values (b), and representation of the different stability regions of the filter (c).

synthesize all the possible phase conditions in the loop, a phase shifter has been placed in series with the amplifier in the direct branch. The reflection coefficient of the filter ($|s_{11,F}|$) for a parametric sweep of the phase in the loop and for three different values of the amplifier gain $|A|$ is shown in Fig. 2.18(b). It can be seen that for values of $|A|$ below 3.5 dB, the circuit is stable for any combination of phases in the loop. For values of $|A|$ between 3.5 dB and 6 dB, the circuit may oscillate ($|s_{11,F}|$ >0 dB) at some frequencies for some phase combinations in the loop. Finally, for gain values higher than 6 dB the circuit is unavoidably unstable, as it was concluded before, since the gain in the loop is higher than one. Thus, for this practical case the maximum gain of the filter may be limited to some dB below the theoretical threshold of 6 dB, due to the non-ideal behavior of the branch line combiners outside its center frequency. These results are summarized in Fig. 2.18(c), with the curve that represents the gain of the filter as a function of the gain of the amplifier when using 3-dB combiners. It is difficult to extract more general conclusions from this analysis, since it strongly depends on the particular implementation of the filter and its non-ideal components. It is the task of the circuit designer to ensure stability by controlling the gain of the amplifier for each particular filter design. Finally, it should be clarified that in this analysis it is assumed the use of 50 Ω input/output sources, and the factors that may affect the stability are not the impedance conditions of the circuit (as it is usually studied), but the different phase combinations in the loop.

2.1.3.4 Noise

One of the more limiting factors in recursive active filters is the noise figure. The presence of passive components around the gain block in the filter topology can make the noise figure of the filter be worse than the noise figure of the amplifier alone. The two different filter schemes previously presented in Fig. 2.15 will be considered in the subsequent analysis. Based on the noise wave technique developed in [34], the noise figure of the topology in Fig. 2.15(a) can be calculated as

$$F_a = 1 + \frac{1}{\alpha_1^2}(F_A - 1) + \left(\frac{\beta_2 - \beta_1 A\gamma}{\alpha_1 \alpha_2 A}\right)^2 \tag{2.21}$$

where F_A is the noise figure of the amplifier. On the other hand, the noise figure of the filter shown in Fig. 2.15(b) can be calculated as

$$F_b = 1 + \left(\frac{\beta_1 A}{\alpha_1}\right)^2 (F_A - 1) + \left(\frac{\beta_2 - \beta_1 A\gamma}{\alpha_1 \alpha_2 A}\right)^2 \tag{2.22}$$

As it can be seen from (2.21) and (2.22), the noise figure of the filter depends on the noise figure of the amplifier and on the transmission parameters of the

components in the circuit. Apart of using better noise performance amplifiers, one typical technique to reduce the noise figure of the filter is to choose a proper power balance (i.e., α and β) in the power combiners, especially the one at the input [34]. The noise performance of a first-order recursive filter (2.21) as a function of the noise figure of the amplifier (F_A) for different power balances in the combiners is shown in Fig. 2.19. It can be seen that reducing the factor $\alpha_{1,2}$ in the combiners allows reducing the overall noise figure of the filter. In practice, a trade-off value should also be found considering other aspects, such as the gain or the out-of-band rejection. Fig. 2.19 also represents the lower bound in the noise figure with this topology, since with the scheme shown in Fig. 2.15(a) the noise figure of the active filter is unavoidably worse than the noise of the amplifier alone [34].

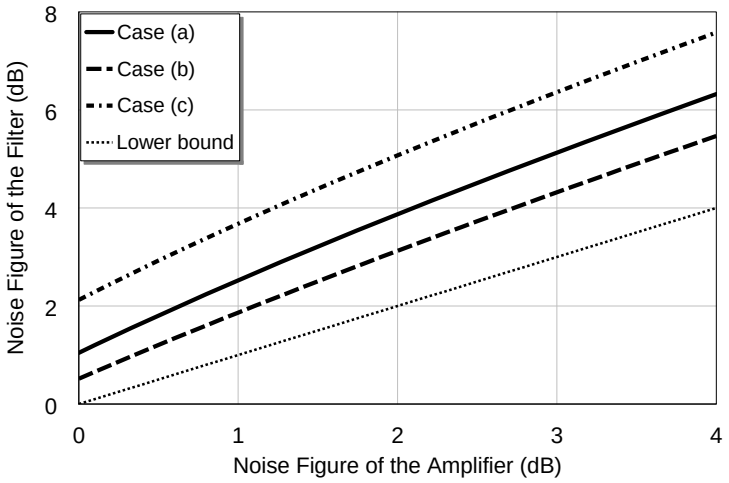

Figure 2.19: Noise figure of a first-order recursive filter as a function of the noise figure of the amplifier ($|A|$=4 dB) with different power combiners: α_1=α_2=β_1=β_2=-3 dB (case (a)); α_1=α_2=-2 dB and β_1=β_2=-4.3 dB (case (b)); and α_1=α_2=-4.3dB and β_1=β_2=-2 dB (case (c)).

2.2 Metamaterials and CRLH Transmission Lines

2.2.1 Introduction to metamaterials

Metamaterials are commonly defined as artificial electromagnetic structures with unusual properties not readily available in nature. In 1968, the extraordinary properties of materials with both negative electric permittivity (ϵ) and magnetic permeability (μ) were theoretically described by V. Veselago in his now-famous paper [35]. These phenomena include the reversal of some physical effects, such as the Doppler effect, the Vavilov-Cerenkov radiation, the Snell's law, etc. In addition, Veselago also demonstrated that these metamaterials support electromagnetic fields with anti-parallel phase and group velocities, which was defined as *backward-wave propagation*. This effect is associated with a negative index of refraction, and it implies that the energy flows away from the source, whereas the wavefronts travel toward the source. A diagram showing the different combinations of ϵ and μ, with the corresponding refractive index (n), is shown in Fig. 2.20. The quadrant I corresponds to conventional electromagnetic media, with both positive ϵ and μ. These materials are also known as right-handed (RH) materials, because of the right-handed triad formed by the electric field, the magnetic field and the wavevector. In this case, the corresponding refractive index, obtained as $n = \sqrt{\epsilon\mu}$, is positive and real, and conventional forward-wave propagation occurs. The Veselago's materials, with both negative ϵ and μ, are situated in the quadrant III. These media are known as left-handed (LH) materials since, in this case, the wavevector and the electric and the magnetic fields form a left-handed triad. In addition, the refractive index is negative and real, and backward-wave propagation occurs. Quadrants II and IV correspond to electromagnetic media with only one ϵ or μ negative. For this last case, the refractive index is imaginary, so propagation is not possible because the waves are evanescent.

Veselago already discussed about the difficulty to implement LH materials. In fact, during the next decades LH materials were only a theoretical speculation without any experimental validation. More than 30 years after the publication of the Veselago's paper, first experimental demonstrations of LH structures were presented. In the late 90's, J. B. Pendry presented a negative-ϵ structure based on thin wires [36]. Some time later he presented a negative-μ structure based on split-ring resonators (SRRs) [37]. In 2000, D. R. Smith et al. presented the first LH material, i.e. both negative ϵ and μ, combining both the thin wires and the SRRs previously proposed by Pendry in a single structure [38]. This structure, which is shown in Fig. 2.21, has average unit cell size smaller than the wavelength and, therefore, can be considered as an effectively homogeneous medium.

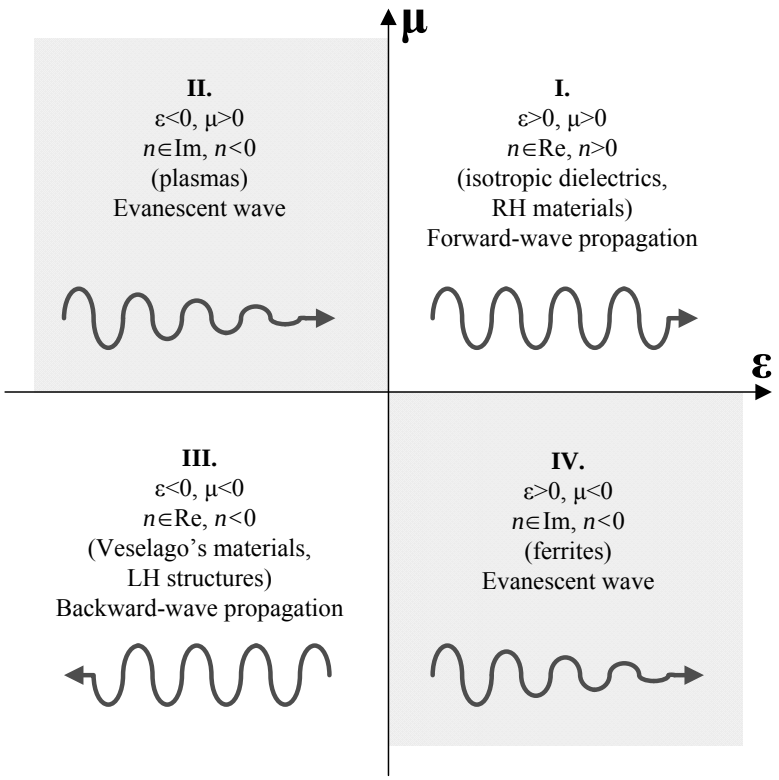

Figure 2.20: Permittivity-permeability (ϵ-μ) and refractive index (n) diagram [41].

Figure 2.21: First LH structure based on split-ring resonators and thin wires proposed by Smith et al. in 2000 [38].

A classification of some metamaterial-inspired microwave structures is shown in Fig. 2.22. This classification is done concerning the homogeneity and the resonant behavior of the structure. As it was mentioned before, the structure proposed by Smith is formed by unitary cells significantly smaller than the wavelength, so it can be considered as quasi-homogeneous. However, one of its main drawbacks is the resonant nature of its components, which limits the LH response of the circuit to a very narrow frequency range. Apart from SRR-based structures, equivalent performance to that of the structure proposed by Smith can be achieved by using other topologies, such as structures based on mushrooms [39], lumped components [40], or interdigital capacitors and shunt stub inductors [41]. These types of quasi-homogeneous and resonant LH structures are utilized in a variety of practical microwave applications, such as negative refractive index structures [39], anisotropic structures [42], unusual reflectors [43], frequency selective surfaces and antenna superstrates [44], and full-space scanning two-dimensional antennas [45].

On the other hand, the same resonant particles that form the previous quasi-homogeneous LH topologies can also be utilized in other non-periodic configurations to provide improved performance in guided-wave and radiated-wave circuits. Thus, SRR and mushroom particles are being used in the design of compact filters [46], elimination of spurious [47], compact antennas [48], multi-frequency and multi-mode antennas [3], dual-band transmission lines [49], or lines with extreme impedance values [50].

In order to overcome the attenuation and bandwidth limitations of the previous resonant LH devices, non-resonant LH transmission line approaches have been proposed in the literature, which can provide lower losses and wider bandwidths [1]. Researchers early realized that practical implementations of LH transmission lines unavoidably present an inherent RH response due to the parasitics, leading to a combined LH/RH response. Thus, this kind of metamaterial lines are commonly known as *composite right/left-handed* (CRLH) transmission lines. One of the classical CRLH transmission line implementations consists on interdigital capacitors and shunt stub inductors [51]. This approach has been utilized in the design of multiple variations of leaky-wave structures, such as backfire-to-endfire antennas [52], electronically scanned antennas [53], or reflecto-directive systems [54]. The same CRLH line implementation has been used in the design of other guided-wave applications, such as directional couplers with arbitrary coupling level [55]. Alternatively, other quasi-homogeneous microstrip CRLH transmission line topologies have been presented in the literature [56].

For some specific applications, such as leaky-wave antennas or couplers, the signals should flow along effectively homogeneous transmission lines in order to provide uniform propagation, and therefore the desired radiation or coupling

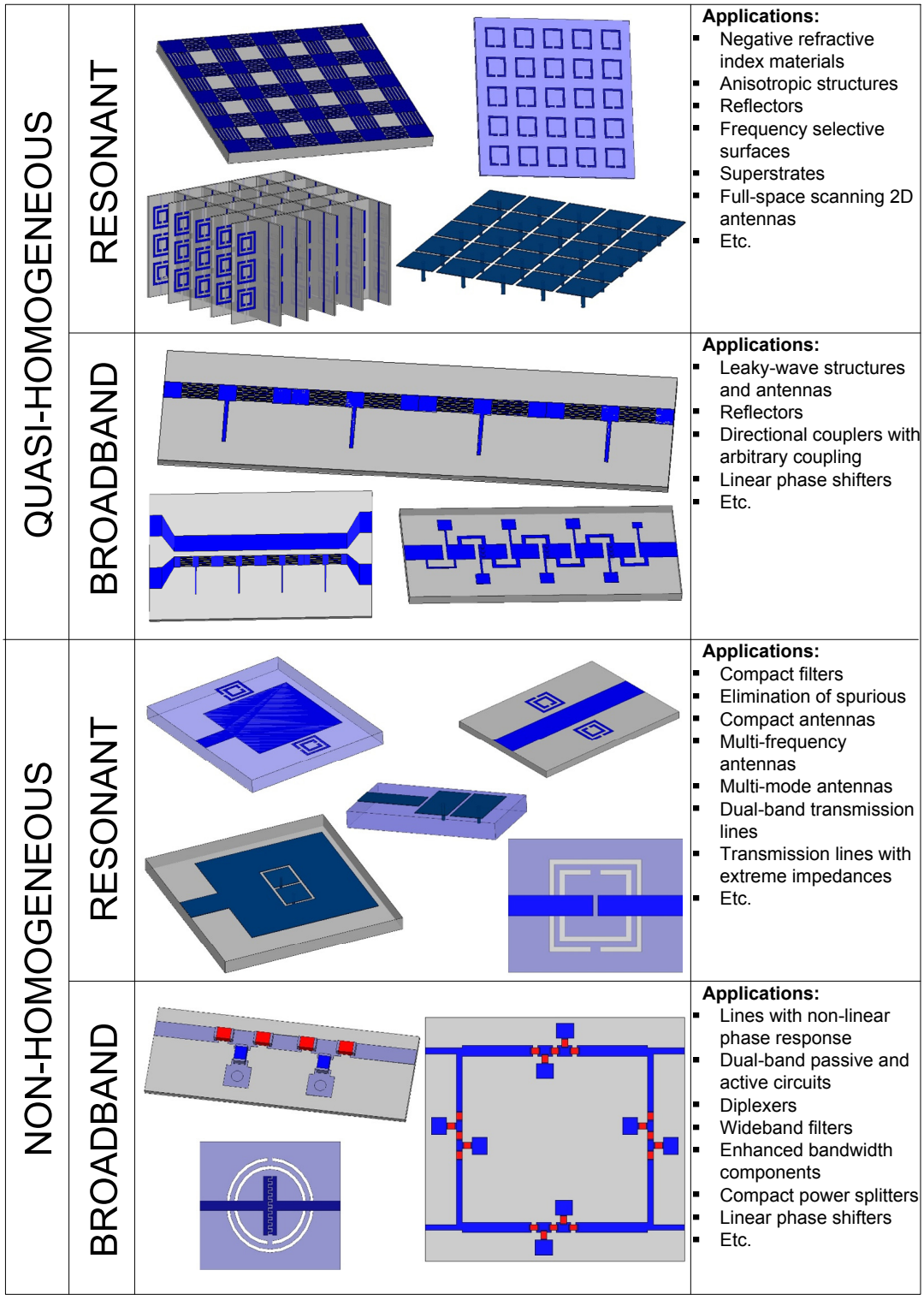

Figure 2.22: Classification of metamaterial-inspired microwave devices.

properties. However, for other applications homogeneity has been found not indispensable. This is the case of the dual-band guided-wave circuits based on CRLH transmission lines. In these circuits, CRLH transmission lines are synthesized as circuit blocks with certain impedance and phase values at two arbitrary frequencies, but in which the power does not need to flow along an uniform or homogeneous structure. In [5], 90-deg CRLH transmission lines are designed to implement branch-line and rat-race couplers with dual-band operation. These CRLH lines are synthesized by combining the effect of conventional transmission lines (RH response) and lumped capacitors and inductors (LH response). This structure cannot be considered homogeneous, since only two or three LH cells are used and the structure is not periodic. Nevertheless, these lines may provide a broadband impedance response and the possibility of adjusting any phase value (e.g., 90 deg in the previous case) at two arbitrary frequencies. The same transmission line approach has also been utilized to synthesize dual-band stubs for power amplifiers [12], to provide enhanced-bandwidth in passive components [57], or to design compact diplexers [58]. More recently, the improvement of SRR-based transmission lines to provide continuous transition between the LH and RH bands (i.e. balanced case) has allowed the implementation of broadband and compact CRLH transmission lines, which may be used, for instance, in the design of wideband filters [59]. The main advantage of all these non-homogeneous implementations is that only a few (or even a single) cells can be used, which translates into much simpler designs.

2.2.2 CRLH transmission lines

Transmission lines are commonly modeled as an infinite cascaded combination of infinitesimal (i.e., $\Delta z \rightarrow 0$) lumped-element unit cells, as it is shown in Fig. 2.23. For the general case, the unit cells are formed by a series per-unit length impedance Z_S (Ω/m) and a shunt per-unit length admittance Y_P (S/m). From this model, the corresponding parameters of the transmission line can be calculated. Firstly, the propagation constant can be calculated as

$$\gamma_0 = \alpha + j\beta = \sqrt{Z_S Y_P} \tag{2.23}$$

and secondly, the characteristic impedance can be obtained from

$$Z_0 = \sqrt{\frac{Z_S}{Y_P}} \tag{2.24}$$

In the particular case of a conventional transmission line, also known as RH transmission line, the unit cell corresponds to the one shown in Fig. 2.24(a).

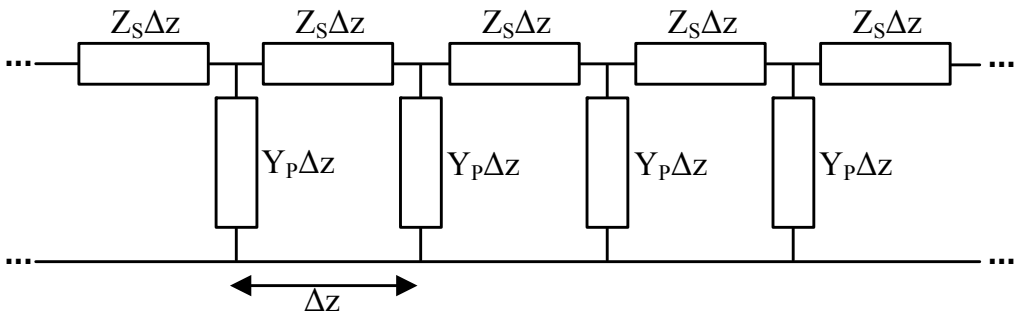

Figure 2.23: Equivalent circuit of a general transmission line.

Thus, the propagation constant of a RH transmission line can be obtained by applying (2.23) as

$$\gamma_{RH} = j\omega\sqrt{L_R C_R} \tag{2.25}$$

where ω is the angular frequency, and L_R and C_R are the series per-unit length inductance and the shunt per-unit length capacitance of the equivalent model of the RH transmission line. In an equivalent way, the characteristic impedance can be calculated from (2.24) as

$$Z_{RH} = \sqrt{\frac{L_R}{C_R}} \tag{2.26}$$

On the other hand, the unit cell of the equivalent circuit of a LH transmission line is the one shown in Fig. 2.24(b). It represents the dual part of the RH cell, and is formed by a series times-unit length capacitance C_L and a shunt times-unit length inductance L_L. Consequently, the propagation constant of the LH transmission line is obtained as

$$\gamma_{LH} = -j\frac{1}{\omega\sqrt{L_L C_L}} \tag{2.27}$$

and the characteristic impedance is calculated as

$$Z_{LH} = \sqrt{\frac{L_L}{C_L}} \tag{2.28}$$

Since LH materials do not exist in nature, engineers tried to synthesize LH media by replicating their equivalent circuit, i.e., by cascading series capacitors and shunt inductors. However, they early found that implementing this circuit in any microwave technology led to undesired parasitic effects associated with conventional RH media. Any LH transmission line implementation unavoidably has a combined LH and RH behavior and, therefore, what one has in practice is

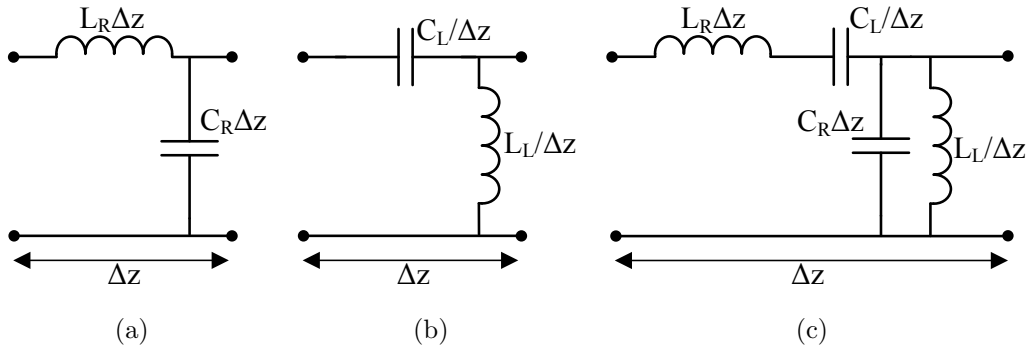

Figure 2.24: Unit cells of the equivalent model of a RH (a), LH (b), and CRLH (c) transmission lines.

a CRLH transmission line. This CRLH transmission line can also be represented by an equivalent lumped-element model, whose unit cell is the one shown in Fig. 2.24(c). It just consists on a combination of both RH and LH unit cells. Regarding to the general transmission line model shown in Fig. 2.23, the series impedance and the shunt admittance of a CRLH transmission line are given by

$$\begin{aligned} Z_S^{CRLH} &= j\left(\omega L_R - \frac{1}{\omega C_L}\right) \\ Y_P^{CRLH} &= j\left(\omega C_R - \frac{1}{\omega L_L}\right) \end{aligned} \tag{2.29}$$

There are two associated resonant frequencies at which the terms Z_S^{CRLH} and Y_P^{CRLH} are canceled. These two frequencies are defined as

$$\begin{aligned} \omega_{c1} &= \frac{1}{\sqrt{L_R C_L}} \\ \omega_{c2} &= \frac{1}{\sqrt{L_L C_R}} \end{aligned} \tag{2.30}$$

and they divide the dispersion diagram into three separated zones. Thus, the propagation constant of the CRLH transmission line can be calculated as

$$\gamma_{CRLH} = s(\omega)\sqrt{\left(\omega L_R - \frac{1}{\omega C_L}\right)\left(\omega C_R - \frac{1}{\omega L_L}\right)} \tag{2.31}$$

where

$$s(\omega) = \begin{cases} -j, \text{ for } \omega < min(\omega_{c1}, \omega_{c2}) \\ +1, \text{ for } min(\omega_{c1}, \omega_{c2}) < \omega < max(\omega_{c1}, \omega_{c2}) \\ +j, \text{ for } \omega > max(\omega_{c1}, \omega_{c2}) \end{cases}$$

and the characteristic impedance is given by

$$Z_{CRLH} = \sqrt{\frac{\omega L_R - 1/(\omega C_L)}{\omega C_R - 1/(\omega L_L)}} \tag{2.32}$$

With regard to (2.31), it can be seen that in the lower and upper sub-bands, the propagation constant is purely imaginary and, therefore, propagation is possible. However, in the mid sub-band between the two resonant frequencies there is a forbidden band in which the propagation constant is purely real and, therefore, the waves are evanescent. The representation of the typical dispersion diagrams of a RH, LH and CRLH transmission lines are presented in Fig. 2.25. From these curves, the group velocity v_g and the phase velocity v_p of these transmission lines can be inferred from

$$\begin{aligned} v_g &= \partial\omega/\partial\beta \\ v_p &= \omega/\beta \end{aligned} \tag{2.33}$$

It can be seen from the phase constant (β) response of a purely RH line that v_g and v_p are both positive and, therefore, parallel. In the case of a purely LH line, v_g is positive whereas v_p is negative, which provides the well-known anti-parallelism between v_g and v_p of the LH transmission lines. Finally, the CRLH transmission lines present anti-parallel v_g and v_p below the first resonant frequency (LH region), and present parallel v_g and v_p above the second resonant frequency (RH region).

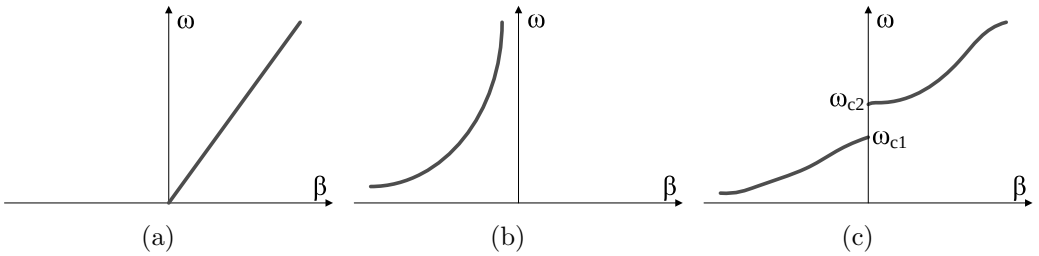

Figure 2.25: Dispersion diagrams (phase constant (β) vs. frequency (ω)) of a RH (a), LH (b), and CRLH (c) transmission lines.

It was seen before that CRLH transmission lines may present a characteristic stop-band, which is not present in either RH or LH transmission lines. This stop-band appears in the general case in which the series resonance (ω_{C1}) and the shunt resonance (ω_{C2}) are different (unbalanced case). When the two resonances coincide, this intermediate stop-band does not appear (balanced case). This particular balanced case occurs when

$$L_R C_L = L_L C_R \tag{2.34}$$

Therefore, the formula of the propagation constant can be simplified to

$$\gamma_{CRLH} \overset{balanced}{=} \gamma_{RH} + \gamma_{LH} = j\omega\sqrt{L_R C_R} - j\frac{1}{\omega\sqrt{L_L C_L}} \tag{2.35}$$

in which there are two separated RH and LH contributions. The equivalent circuit model can also be simplified into two separated RH and LH cells, as it is shown in Fig 2.26(a). The dispersion diagram of the balanced CRLH transmission line is represented in Fig 2.26(b). In this case, the transition between the LH and the RH regions is continuous, and it occurs at

$$\omega_0 = \frac{1}{\sqrt[4]{L_R C_R L_L C_L}} = \frac{1}{\sqrt{LC}} \tag{2.36}$$

where ω_0 is the transition frequency. For this case the propagation constant is purely imaginary and there is not a stop-band in the frequency response.

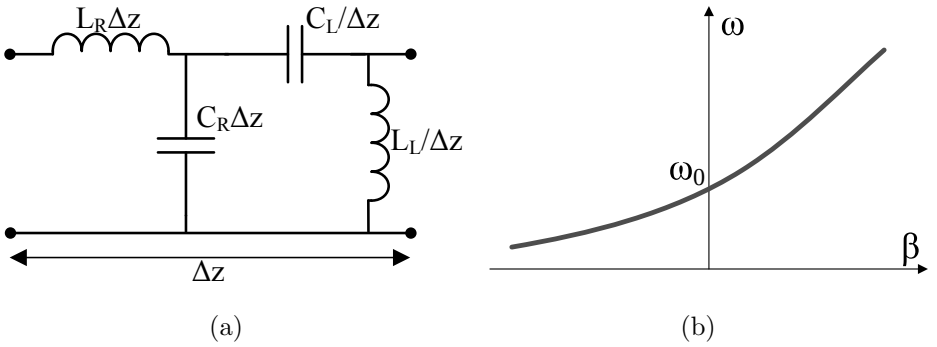

Figure 2.26: Unit cell (a) and dispersion diagram (b) of a balanced CRLH transmission line.

Multiple CRLH transmission line implementations have been proposed during the last decade. They basically consist on replicating the lumped-element equivalent circuit of such lines based on LH (Fig. 2.24(b)) or CRLH unit cells (Fig. 2.24(c)). A microstrip planar implementation of a CRLH transmission line is shown in Fig. 2.27(a) [51]. The interdigital capacitors and the shunt stubs connected to ground provide the series capacitance and shunt inductance of the LH cell respectively. In addition, the parasitic voltage gradients and currents provide the series inductance and shunt capacitance associated with a RH cell, resulting in a CRLH structure. Due to the distributed nature of this implementation, this solution can be used in radiated-wave or coupled-lines based circuits. Another CRLH transmission line implementation is shown in Fig. 2.27(b) [5]. This last case is based on lumped components. The series capacitors and the shunt inductors provide the LH behavior, whereas the connecting transmission lines provide

the RH behavior, resulting in an overall CRLH response. Since the LH cell and the RH line are separated, this topology is intrinsically balanced and does not present an intermediate band-gap. This implementation provides an easier control over the circuit parameters (inductances and capacitances) than the previous case. Other solutions replicating with lumped components the complete CRLH unit cell instead of only the LH cell are also feasible. Finally, other structures based on SRRs have also been proposed, as the one shown in Fig. 2.27(c) [59]. In the upper layer, the transmission line provides a series inductance and the intermediate gap provides a series capacitor. The bottom layer consists on a complementary SRR (shunt capacitor and shunt inductor) coupled to the upper line. Despite the resonant behavior of the SRR, if the parameters are properly adjusted to provide a balanced configuration (i.e., equation (2.34) is satisfied) this solution can provide a broadband response.

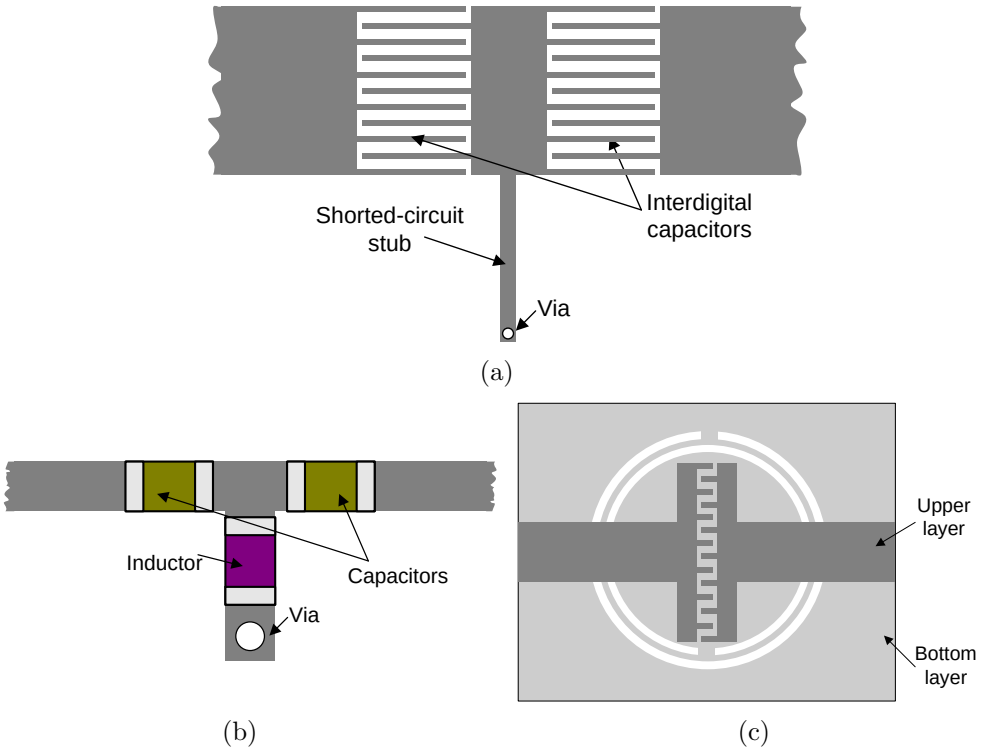

Figure 2.27: Some microstrip implementations of CRLH transmission lines: based on interdigital capacitors and shunt stubs [51] (a), based on lumped components and conventional transmission lines [5] (b), and based on transmission lines with coupled complementary SRRs [59] (c).

2.2.3 Applications of CRLH transmission lines

This subsection describes some devices based on CRLH transmission lines that have been presented in the literature and shows some of the potentialities of the CRLH transmission lines in the design of microwave components. It is focused on the implementation of dual-band and/or of active circuits due to the nature of the dual-band active filter topology proposed later in Section 2.3.

2.2.3.1 Dual-band passive components

Many passive circuits can operate at a certain design frequency (f_1) and, unavoidably, at other harmonic frequencies (i.e., $2f_1$, $3f_1$, etc.). This is because of the linear phase response provided by conventional transmission lines. For example, branch line couplers can operate at a certain design frequency f_1 and at its odd harmonics $3f_1$, $5f_1$, etc. However, this is not practical for many multi-band systems since, in general, they work at arbitrary non-harmonic separated frequencies. To overcome this problem, dual-band performance can be achieved just by replacing the conventional transmission lines with CRLH transmission lines in many well-known passive circuit topologies. As it was discussed in subsection 2.2.2, the phase response of a CRLH transmission line is non-linear, and it provides enough degrees of freedom to adjust two different phase values at any two arbitrary frequencies. The general phase response of a RH and a CRLH transmission line are compared in Fig. 2.28. In the case of a branch-line coupler design, this circuit requires ±90-deg transmission lines with characteristic impedances Z_0 and $Z_0/\sqrt{(2)}$ at the operation frequencies. They can be implemented with conventional transmission lines at a certain frequency f_1 and, unavoidably, they also work at the odd harmonics of f_1. Instead, 90-deg phase response can be simultaneously achieved with a CRLH transmission line at two arbitrary frequencies f_1 and f_2.

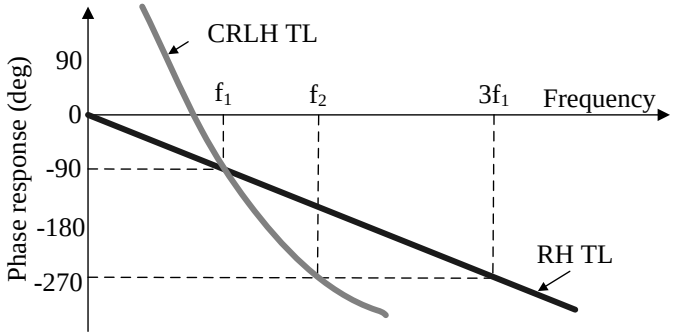

Figure 2.28: Phase responses of a RH and a CRLH 90-deg transmission line.

Several dual-band passive components based on this technique are presented in [5]. They make use of the CRLH transmission line implementation shown in Fig. 2.27(b). The schematic of a dual-band branch-line coupler developed with this technique is shown in Fig. 2.29(a). The transmission lines provide the required characteristic impedance of a classical branch-line coupler and the phase response of each line is equivalent to the one shown in Fig. 2.28, which provides -90 deg at f_1 and -270 deg at f_2. The measured results with a prototype working at 900 and 1800 MHz are shown in Fig. 2.29(b). This response is very similar to the one provided by a conventional branch-line but frequency-scaled to operate at non-harmonic frequencies. A dual-band rat-race coupler is also demonstrated in [5].

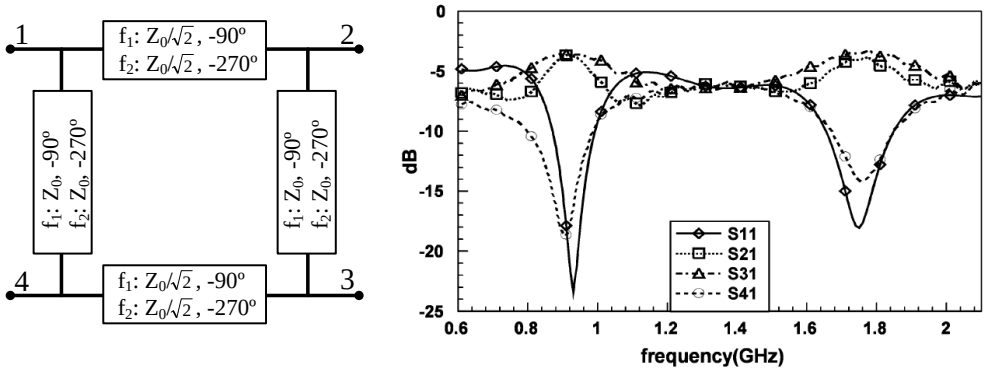

(a) (b)

Figure 2.29: Conceptual schematic of the dual-band branch-line coupler (a), and measured S-parameters (b) [5].

2.2.3.2 Improved power amplifiers

Several approaches make use of CRLH transmission lines to improve the performance of different power amplifier topologies. One example of a class-F amplifier is presented in [12]. It consists on a class-AB topology, but eliminating some undesired harmonics at its output. The network used to eliminate the harmonics is typically based on stubs, which should fulfill some requirements of phase and impedance in order to avoid impedance mismatching effects in the amplifier. The idea is that in class-F amplifiers, even-harmonics should appear as short-circuit in the drain and odd-harmonic should appear as open-circuit. For the case of eliminating up to the 4th harmonic with a classical approach, three stubs are required, as it is shown in Fig. 2.30(a). Each open-ended stub fixes a short-circuit condition in a common point that is transformed by a 90-deg line into the desired

short-circuit for the even-harmonics and open-circuit for the odd-harmonics. By taking advantage of the non-linear response of the CRLH transmission lines, the number of stubs can be reduced. This implies a simpler and more compact implementation (Fig. 2.30(b)). Two approaches are proposed. By using a simple CRLH stub, both harmonics $2f_0$ and $3f_0$ can be eliminated. Another topology based on two stubs can suppress up to the harmonic $4f_0$ as well as it provides impedance matching at f_0 without the need of an external matching network.

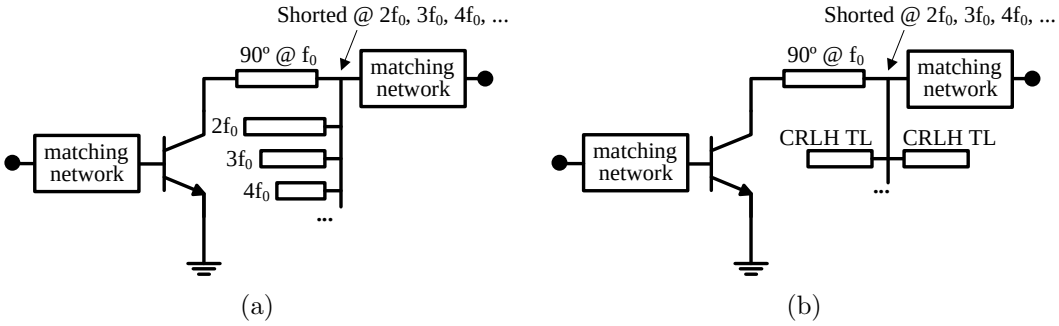

Figure 2.30: Class-F power amplifier presented in [12]: classical approach (a) and proposed topology based on CRLH stubs (b).

A different power amplifier approach is presented in [13]. In this case, the non-linear phase response of the CRLH transmission lines is used to achieve dual-band performance in a class-E amplifier. This type of amplifier requires some specific impedance conditions seen from the input and output of the transistor in order to maximize the efficiency at a certain frequency. If a conventional simple-stub matching network is considered, the desired impedance conditions can be satisfied only at one frequency. However, using a matching network implemented by means of CRLH transmission lines allows synthesizing the optimal conditions simultaneously at two frequencies. The circuit schematic of the proposed dual-band class-E power amplifier is shown in Fig. 2.31. It achieves a power-added efficiency of 42.5 % and 42.6 % at 800 MHz and 1800 MHz respectively.

Finally, a third type of power amplifier based on CRLH transmission lines is presented in [14]. For this case, the topology is a dual-band power amplifier based on two parallel stages, as shown in Fig. 2.32(a). Two class-CE amplifiers are placed in each branch, operating at two different frequencies f_1 and f_2. The signals are combined into a common input and output ports by means of two identical diplexers based on dual CRLH transmission lines (Fig. 2.32(b)) [58]. The input diplexer splits the input signal at frequencies f_1 and f_2 into the corresponding branch. The output combination is done by using the other diplexer. The prototype presented in [14] operates at 380 MHz and 960 MHz, and provides

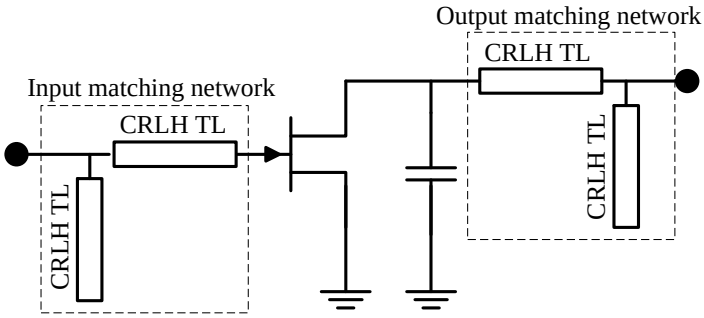

Figure 2.31: Circuit schematic of the dual-band class-E power amplifier presented in [13].

measured power-added efficiencies of 62 % and 60 % respectively. This topology provides an easier design and better behavior with the component tolerances than other dual-band topologies, at the cost of a larger size.

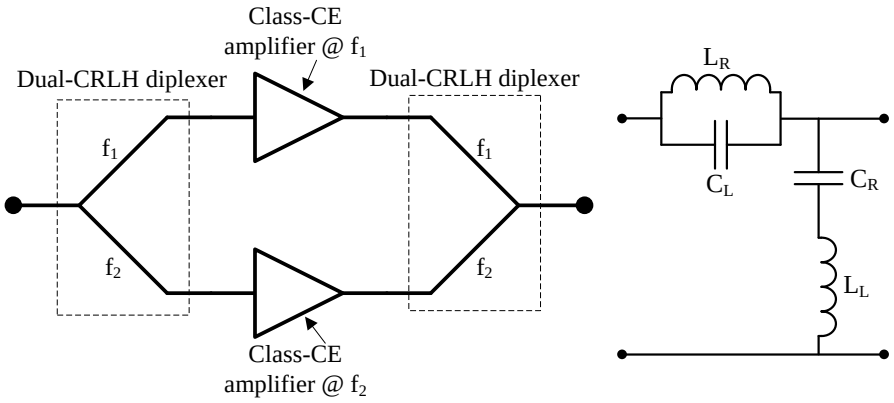

Figure 2.32: Class-CE power amplifier based on diplexers with dual-CRLH transmission lines presented in [14]: circuit schematic (a) and unit cell of a dual-CRLH transmission line (b).

2.2.3.3 Active leaky-wave antennas

In subsection 2.2.1, it was mentioned that transmission lines based on interdigital capacitors and shunt inductors (Fig. 2.27(a)) could be applied to the design of leaky-wave antennas with improved radiating capabilities. Leaky-wave antennas are transmission lines in which the signals are applied at one port while the other port is ended with a matched load. Thus, the power is radiated at the same time

that the wave travels along the line, with an antenna gain that is proportional to the length of such line. However, one of the main constraints is that beyond the length at which the 90 % of the power is radiated, no significant increment in the gain is observed when making the line longer. The solution proposed in [60] consists on regenerating the signal by periodically connecting amplifiers along the line. This approach avoids the previous limitation and theoretically allows achieving any antenna gain level. In addition, unlike in the case of using conventional transmission lines, this CRLH approach allows broadside radiation. The normalized power distribution along the active CRLH transmission line when placing amplifiers every k CRLH cells is shown in Fig. 2.33(a). The comparison between the radiation diagrams and the directivity for the different cases is shown in Fig. 2.33(b). It can be seen that in the passive case ($k = \infty$) the directivity is limited up to 11.1 dB. However, the directivity of the antenna can be significantly increased by including amplifiers in a way directly proportional to the density of active devices. In addition, this approach also allows adjusting the gain of the amplifiers to provide different power distributions along the line (i.e., equivalent to the case of antenna arrays), such as uniform to increase the directivity or binomial to reduce the side-lobe level.

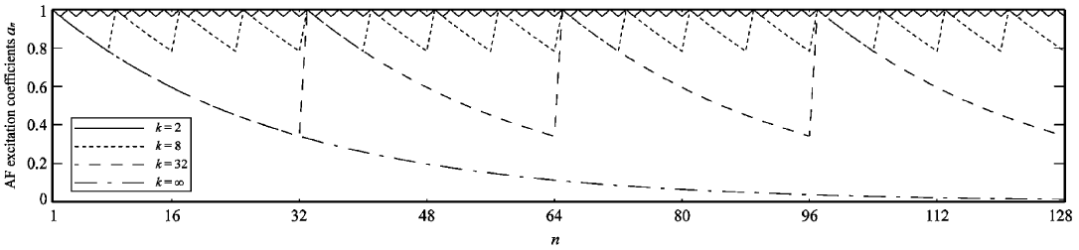

(a)

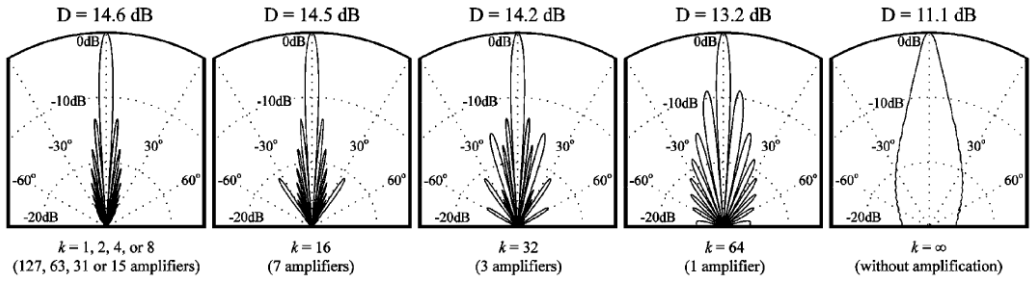

(b)

Figure 2.33: Normalized power distribution along the CRLH line with amplifiers every k cells (a), and radiation diagram and directivity of the antenna for different values of k (b) [60].

2.2.3.4 Meta-distributed amplifiers

One application of particular interest is the design of distributed amplifiers with CRLH transmission lines [16], due to the similarities with the recursive active filter topologies proposed in this thesis. A general distributed amplifier scheme is shown in Fig. 2.34. The input signal is applied through an input line, also known as gate line, which is typically loaded with a matched impedance in the opposite end. A battery of transistors, usually FETs, is connected through their gates to the input line and by their drains to an output line (also known as drain line). This drain line provides two outputs associated to its two ends, which are known as forward and reverse outputs respectively. As it can be seen from the schematic, this circuit is very similar to the topology of a transversal filter, which was previously presented in Fig. 2.8(a).

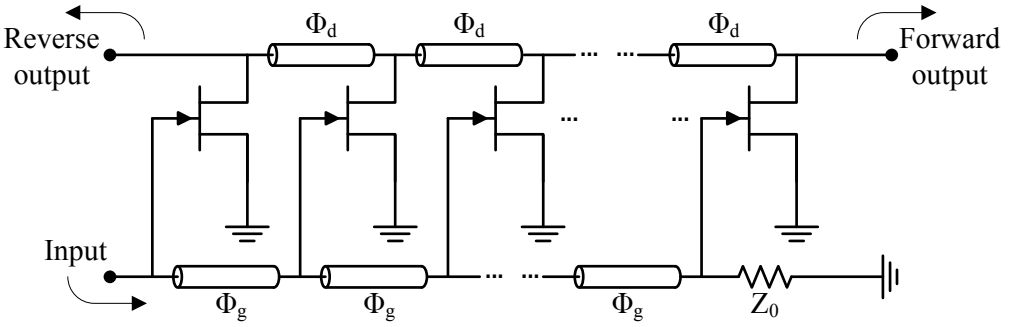

Figure 2.34: Generic circuit schematic of a distributed amplifier.

The corresponding forward and reverse gains, associated to the forward and reverse outputs, can be respectively defined as

$$\begin{aligned} G_f &= \frac{g_m^2 Z_0^2}{4}\left(\frac{sin(N(\Phi_g-\Phi_d)/2)}{sin((\Phi_g-\Phi_d)/2)}\right)^2 \\ G_r &= \frac{g_m^2 Z_0^2}{4}\left(\frac{sin(N(\Phi_g+\Phi_d)/2)}{sin((\Phi_g+\Phi_d)/2)}\right)^2 \end{aligned} \tag{2.37}$$

where g_m is the transconductance of the FETs, N is the number of transistors, Z_0 is the reference impedance, and Φ_g and Φ_d are the phase delays introduced by each section in the gate and drain lines respectively. With regard to (2.37), the conditions at which the maximum gain levels are achieved correspond to

$$\begin{aligned} &\Phi_g - \Phi_d = 0 \pm n2\pi, \text{ for the forward gain} \\ &\Phi_g + \Phi_d = 0 \pm n2\pi, \text{ for the reverse gain} \end{aligned} \tag{2.38}$$

where n denotes any integer number.

Thus, depending on the choice of the gate and drain line sections, three different cases can be considered. The first situation corresponds to the use of identical gate and drain transmission line sections, i.e., $\Phi_g = \Phi_d$. In this case, the signals always combine in phase as they travel to the forward output. That means that the forward gain provides a broadband response. On the other hand, the maximum in the reverse gain is given only at the frequency at which the sum of phases is zero (or multiple of 2π). In the classical approach, identical conventional transmission line sections are used to obtain a broadband forward gain response. Since the line sections are usually as short as possible to reduce the losses, the reverse gain provides a useless low-pass response, so this output is usually ended with a matched load. Instead, for the case of using identical balanced CRLH structures for the gate and drain line sections, the maximum of the reverse gain can be arbitrarily controlled by means of the transition frequency ω_0 of such CRLH lines, as seen in Fig. 2.35(a). The second case corresponds to the use of different gate and drain line sections, but both with the same transition frequency. In this case, the maximum of both forward and reverse gains appears at the transition frequency of the CRLH sections since it is the only frequency at which both conditions in (2.38) are satisfied. This response is plotted in Fig. 2.35(b). Finally, the third

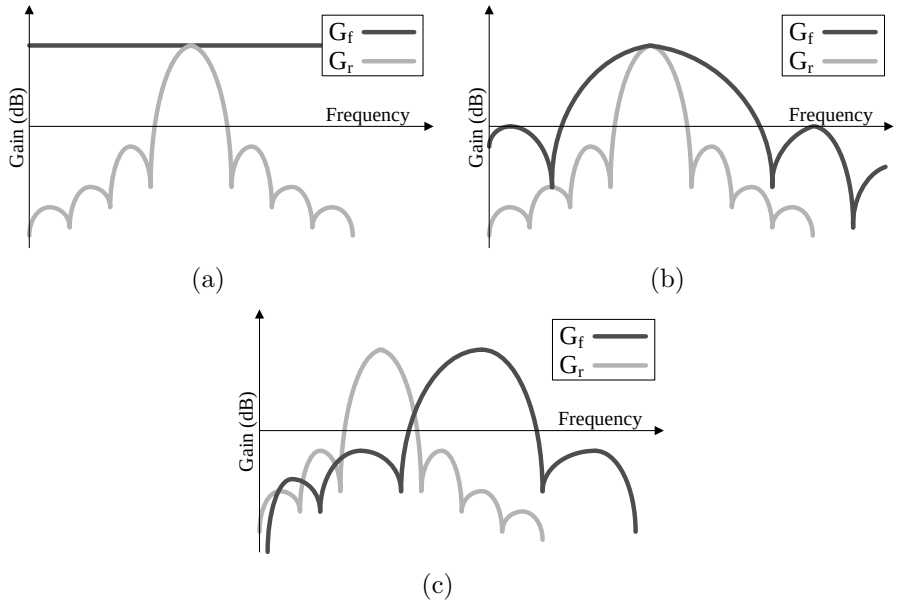

Figure 2.35: Typical forward and reverse gain responses (G_f, G_r) of a meta-distributed amplifier: using identical gate and drain line sections (a), using different gate and drain line sections with the same transition frequency (b), and using different gate and drain line sections with different transition frequencies (c).

situation corresponds to the general case in which different gate and drain sections with different transition frequencies are used. The maximum of both gains appears at two different frequencies in this case, as it is shown in Fig. 2.35(c).

Several applications have been proposed related with the meta-distributed amplifier topology proposed in [16]. The main potentialities are provided by the general case shown in Fig. 2.35(c). It presents two separated filtering outputs at two frequencies. This can be used in the implementation of active diplexers [60]. The main constraint, as it occurs with transversal filters, is that it requires many stages and, therefore, high power consumption to provide high selectivity in both filtering responses. Another application consists on using the scheme whose response is shown in Fig. 2.35(b) to implement power amplifiers [62]. This power amplifier topology uses the four ports of the distributed device, combining both inputs and both outputs by means of two power combiners. Finally, other structures that combine distributed amplifiers and CRLH leaky-wave antennas have also been proposed in the literature [63].

2.3 Proposed Dual-Band Active Filter Designs

2.3.1 Dual-band operation with recursive filters

Concerning the active filter classification done in subsection 2.1.2, the first three types (i.e., negative resistances, active inductors and actively coupled resonators) correspond to topologies in which the filtering response is given by a passive resonator (e.g., LC tank and/or coupled lines) and the active components are included to provide losses compensation or isolation. However, the operation of the transversal/recursive filters is somehow different. In this last case, the filtering response is provided by the combination of different samples of the input signal that travels along different paths (usually based on transmission lines and amplifiers). This distributed nature makes transversal and recursive active filters be very suitable to be implemented by means of CRLH transmission lines to achieve dual-band operation. In fact, the same design philosophy has been successfully proved in passive devices [5] and in distributed amplifiers [16].

As in the case of many passive circuits, the ideal scheme of a recursive active filter provides operation at a certain design frequency and, in turn, at some of the harmonics of such frequency. As it was described in subsection 2.1.3, the operation frequencies of a first-order recursive filter are determined as the frequencies at which the phase of the loop is multiple of 2π (2.11). If conventional lines are used, and assuming that the amplifier response is ideal and does not introduce any phase delay, the phase of the loop presents a linear response with respect to frequency of the form

$$\Phi_{loop} = -kf \tag{2.39}$$

where f denotes the frequency and k represents the slope. Since the y-axis intercept point is already fixed to zero (i.e., loop phase is zero at 0 Hz), there is only one degree of freedom to adjust the slope of the line (e.g., by adjusting the length of the transmission lines) to provide the desired phase value (in this case multiple of 2π) at one operation frequency f_1. In fact, due to the linear nature of the phase responses, condition (2.11) will also be satisfied at other harmonic frequencies, but without any possible control from the circuit designer. It leads to an ideally periodic filter transmission response in the frequency domain. In practice, the phase response of the active devices may be non-linear, which would give a pseudo-periodic filtering transmission response as the one represented in Fig. 2.36, but still without any additional control over a hypothetic second operation frequency.

This thesis proposes to use CRLH transmission lines in order to provide additional degrees of freedom in the recursive active filter design. Thus, the phase in

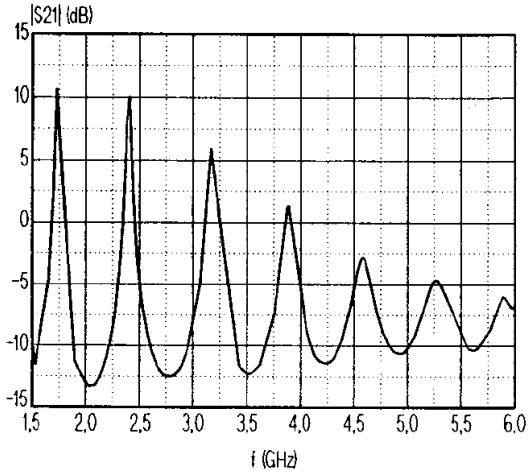

Figure 2.36: Pseudo-periodical transmission response of a microwave recursive active filter [64].

the loop can be independently controlled at two arbitrary frequencies f_1 and f_2, in order to provide the desired dual-band performance. The CRLH transmission line design that will be used in our case is the one shown in Fig. 2.37(a). It consists of two transmission line sections and several intermediate LH cells based on lumped capacitors and inductors. Assuming that the phase delay introduced by each LC unit cell is much smaller than $\pi/2$ (keeping the infinitesimal approach assumption), the overall phase response of the CRLH line can be approximated by

$$\Phi_{CRLH} \approx 2\Phi_{RH} + N\frac{1}{2\pi f\sqrt{L'_L C'_L}} \tag{2.40}$$

where Φ_{RH} is the phase delay introduced by each transmission line section, N is

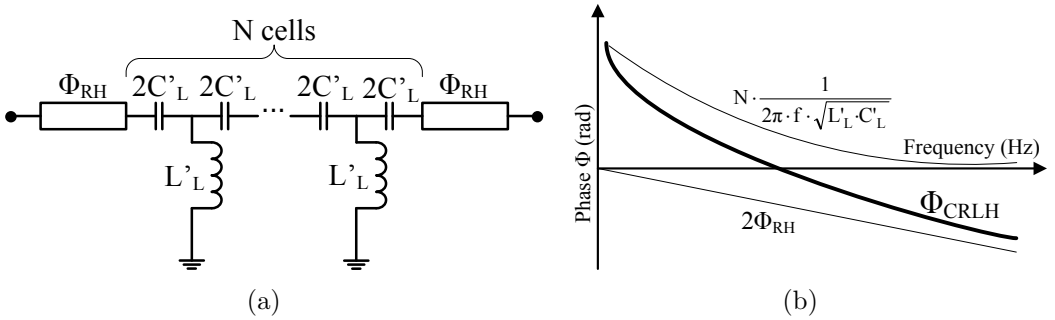

Figure 2.37: Circuit schematic of the lumped-element based CRLH transmission line (a) and its corresponding phase response (b).

the number of LH cells, f is the frequency, and L'_L and C'_L are the inductance and capacitance values of the lumped components. As it can be seen, the overall phase response is formed by the separated contribution from the transmission lines (RH response) and the lumped components (LH response). The RH phase term is linear and it can be adjusted by modifying the physical length of the transmission lines. On the other hand, the LH phase term can be controlled by changing the number of cells N and the value of the components. In addition, impedance conditions should also be satisfied. In the case of the transmission line sections, the characteristic impedance should be adjusted (by modifying the width of the line) to the same value than the desired in the CRLH transmission line. In the case of the LH cells, the characteristic impedance is fixed by means of the lumped components as

$$Z_0 = \sqrt{\frac{L'_L}{C'_L}} \tag{2.41}$$

The first design goal is to achieve dual-band performance by using the first-order recursive filter scheme shown in Fig. 2.38. Based on the first-order design, the further step toward higher-order structures is then immediate. One of the requirements for dual-band operation is the use of power combiners simultaneously working at the two desired frequencies. Thus, two design alternatives can be considered: dual-band or broadband combiners. Other important issue is related to stability, since the gain in the loop should be limited under a certain threshold condition (see subsection 2.1.3). Assuming a lossless implementation of the feedback line, the gain in the loop is then determined by the power balance in the combiners and by the gain of the amplifier. Thus, one of the two parameters should be fixed to a certain value and the other should be later adjusted

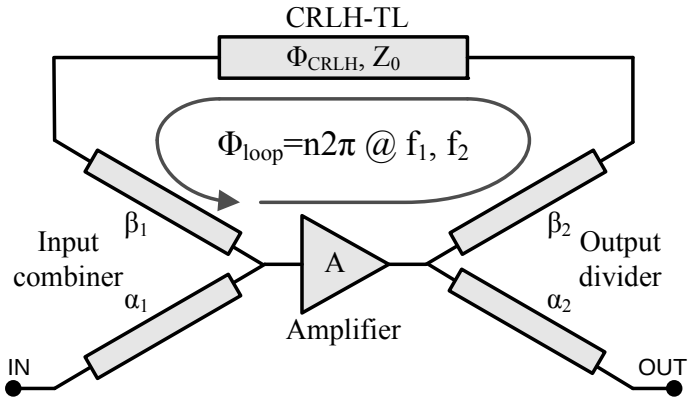

Figure 2.38: Circuit schematic of the proposed dual-band first-order recursive active filter.

to limit the gain in the loop. The balance in the combiners can be controlled by a proper choice of the topology, although asymmetrical combiners are usually more complicated and larger structures in comparison with symmetrical ones. For the amplifier, the transmission parameter can be adjusted by means of a series attenuator, since commercial devices usually provide relatively high gain values. In general, it is desirable to use a gain block with flat gain response, in order to obtain the same transmission in both pass-bands. The last step consists on designing the CRLH feedback lines. These lines should be synthesized to compensate the sum of arbitrary phases provided by the amplifier and the power combiners, in order to obtain an overall loop phase response multiple of 2π at the two desired bandpass frequencies, i.e.,

$$\Phi_{CRLH} = n2\pi - (\angle(A) + \angle(\beta_1) + \angle(\beta_2)) \tag{2.42}$$

where n is any integer number, $\angle(\bullet)$ denotes the angle, A is the gain of the amplifier, and β_1 and β_2 are the transmission parameters of the upper branches of the two combiners. It must also be noticed that the impedance of the line should be chosen equal to the reference impedance in order to avoid undesired reflections between the blocks.

2.3.2 First-order dual-band active filters

This subsection presents the design and characterization process of a dual-band first-order recursive active filter [9]. The intended bandpass frequencies are 850 MHz and 1750 MHz. The simplified circuit schematic of the active filter is shown in Fig. 2.39. For the design of the power combiners, the dual-band

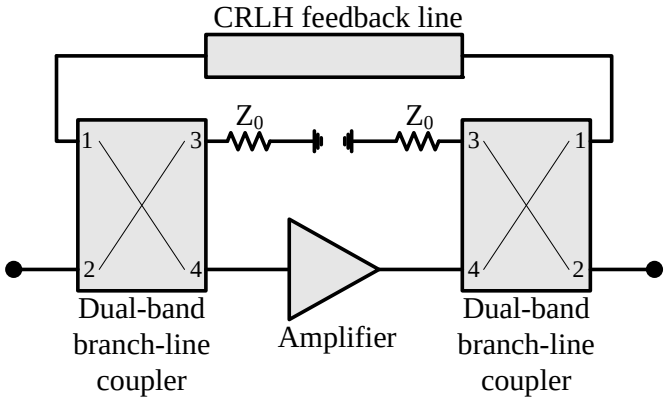

Figure 2.39: Circuit schematic of the proposed first-order dual-band recursive active filter using dual-band branch-line couplers.

stub-loaded branch-line topology proposed in [65] has been chosen. This choice is motivated by two reasons. The first one is that branch line couplers present narrower bandwidth in comparison with other combiners (e.g., Wilkinson). The other one is the strong rejection presented by this concrete branch-line topology in the transmission response in the middle between the two operation frequencies. It allows to improve the selectivity of the filter as well as it helps to mitigate the intermediate spurious bands. The electrical schematic of the combiners and their simulated amplitude and phase response are shown in Fig. 2.40(a) and Fig. 2.40(b)

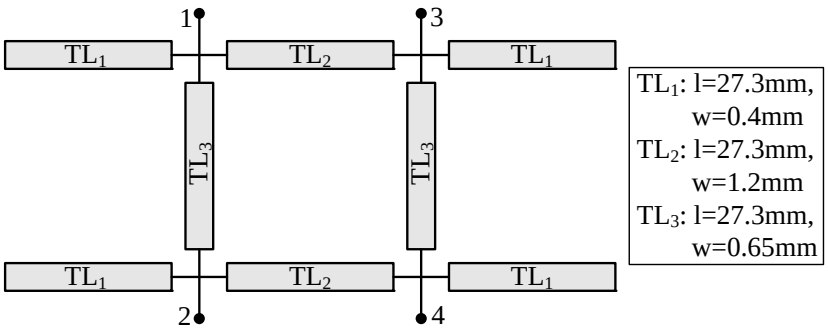

(a)

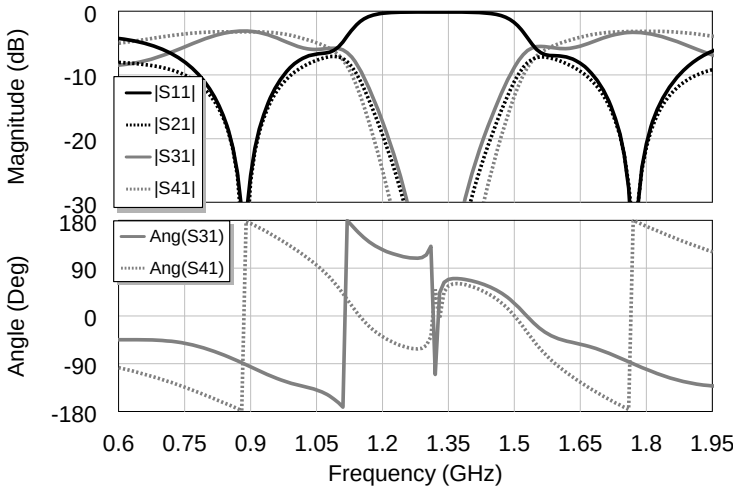

(b)

Figure 2.40: (a) Circuit schematic of the dual-band branch-line coupler based on stub-loaded transmission lines (Terms l and w indicate the length and the width of the transmission lines respectively. Substrate is Arlon600 (height H=0.6 mm, permittivity ϵ_r=6.15)). (b) Simulated S-parameters (magnitude and phase) of the dual-band branch-line coupler.

respectively. A rejected bandwidth around 1350 MHz can be appreciated in the amplitude response.

Concerning to the active stage, a single-stage distributed amplifier [66] has been implemented to achieve broadband and flat gain response. The transistor is a FET, model ATF-34143 from *Avago Technologies*. A series resistive network is used to reduce the gain of the amplifier and, therefore, to avoid instabilities in the active filter. One of the limitations of the distributed amplifiers is that it is

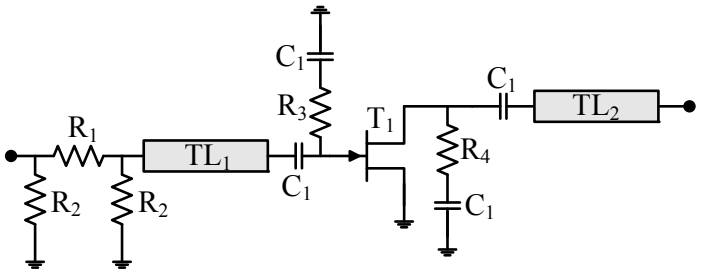

TL_1: l=19mm,	R_2=110Ω
w=0.9mm	R_3=75Ω
TL_2: l=10mm,	R_4=100Ω
w=0.9mm	C_1=100pF
R_1=91Ω	T_1=ATF-34143

(a)

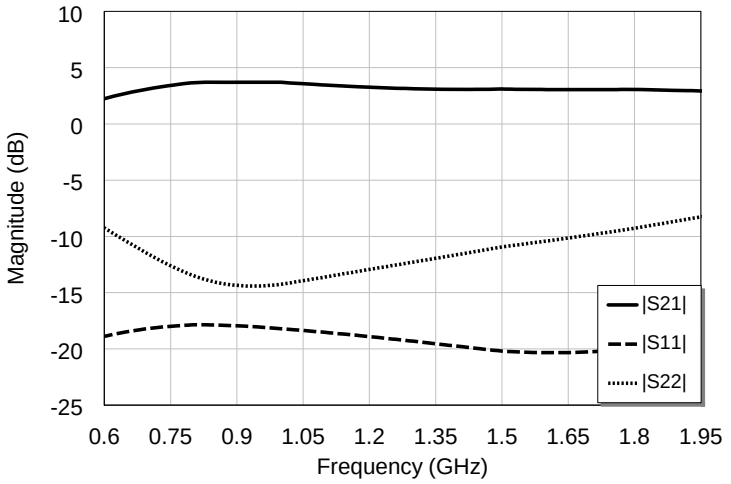

(b)

Figure 2.41: (a) Circuit schematic of the gain block (Biasing has been omitted for simplicity. Substrate is Arlon600 (height H=0.6 mm, permittivity ϵ_r=6.15)). (b) Simulated S-parameters of the gain block.

difficult to achieve very good input matching over the whole bandwidth. Thus, the attenuator can be placed at the input to reduce the input reflection, or at the output so as not to degrade the noise. The circuit schematic with the attenuator at the input and the corresponding simulated S-parameters of the gain block are shown in Fig. 2.41(a) and Fig. 2.41(b) respectively. As it can be seen from the graph, the simulated gain is around 3.7 dB in the lower and 3.1 dB in the upper design frequencies respectively.

The design of the CRLH feedback transmission line is shown in Fig. 2.42(a). It consists of two transmission line sections, and two LC left-handed unit cells. The characteristic impedance has been fixed to 50 Ω, which is the reference impedance of the filter. As it can be seen in Fig. 2.42(b), the insertion losses are

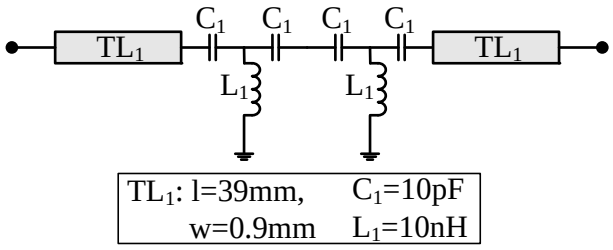

(a)

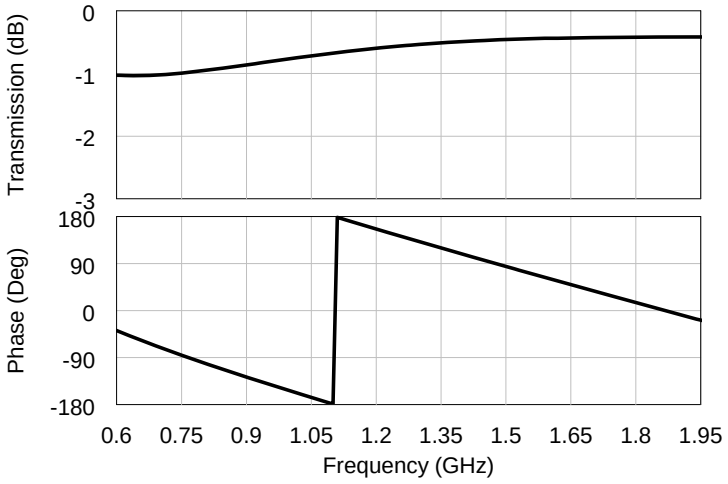

(b)

Figure 2.42: (a) Circuit schematic of the CRLH feedback transmission line (Terms l and w indicate the length and the width of the transmission lines respectively. Substrate is Arlon600 (height H=0.6 mm, permittivity ϵ_r=6.15)). (b) Simulated S-parameters (magnitude and phase) of the CRLH transmission line.

lower than 1 dB in the two bands of interest. The phase of the feedback line has been synthesized in order to compensate the phase delay provided by the gain block and the power combiners in the filter loop (2.42). As it can be seen from Fig. 2.43, the phase in the loop of the filter has been successfully tuned to be 0 deg at the two desired bandpass frequencies (marked with squares in the graph). On the other hand, the amplitude response has been tuned to be below 0 dB, in order to ensure the stability of the filter. It must be noticed that there are some intermediate frequencies at which the condition (2.42) is also fulfilled, which may lead to undesired spurious peaks in the filter response. These frequencies are marked with a circle in the phase graph shown in Fig. 2.43. In this case, these peaks can be mitigated by the transmission response of the stub-loaded branch line couplers. A more detailed analysis about these spurious bands and how to avoid them using broadband combiners will be discussed in subsection 2.3.3.

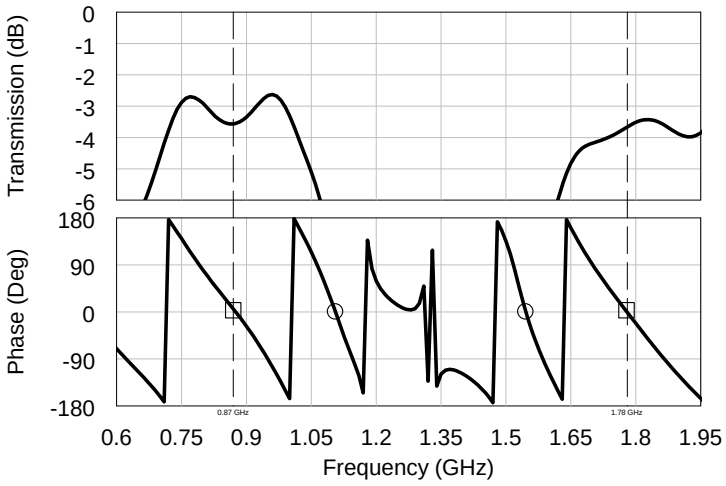

Figure 2.43: Simulated amplitude and phase response of the active filter loop. The desired pass bands are marked with a square and the undesired spurious bands are marked with a circle.

The simulated and measured response of the implemented active filter is shown in Fig. 2.44. The gain level in the lower and higher frequency pass bands is 6.9 dB and 3.3 dB respectively. The absolute 3 dB-bandwidths are 55 MHz and 46 MHz respectively. The higher frequency pass band has suffered a considerable reduction of the transmission level in comparison with the simulations. Nevertheless, the transmission level at both operating frequencies is still higher than the gain level provided by the gain block alone because of the feedback. The gain reduction in the higher band is probably due to the parasitics in the lumped elements, which would not be properly modeled in the simulation and whose effect is more

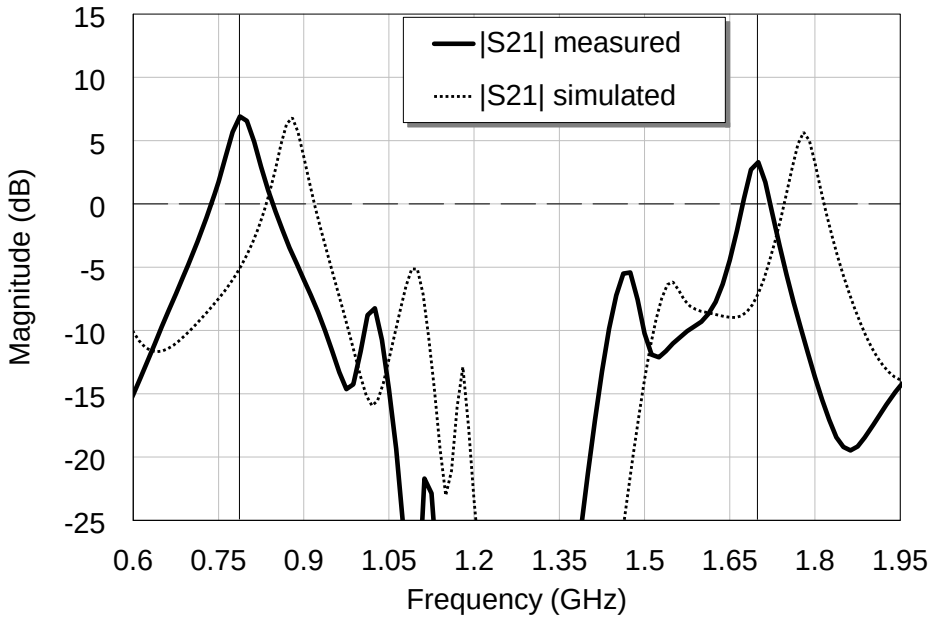

(a)

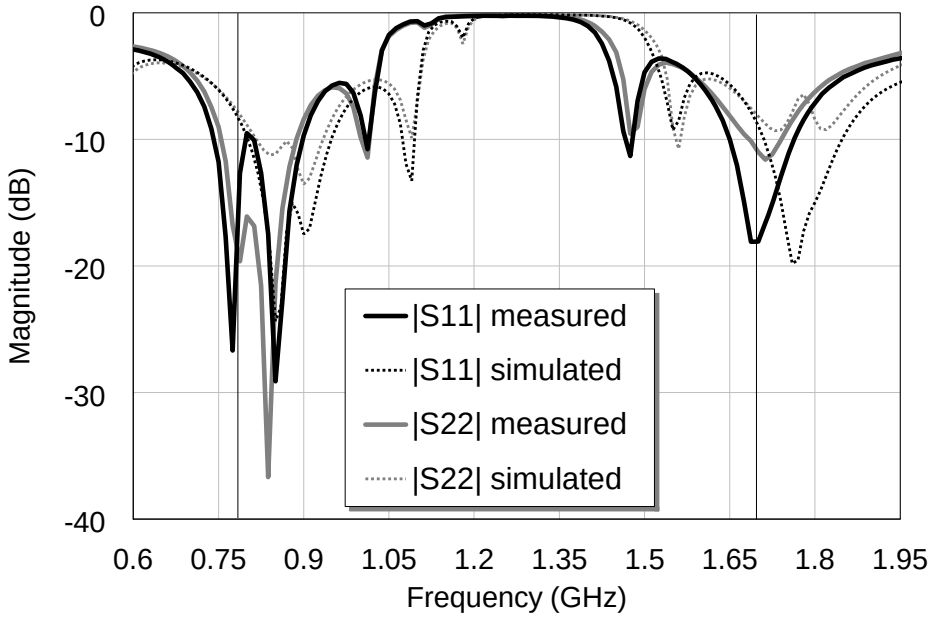

(b)

Figure 2.44: Measured (solid line) and simulated (dashed line) S-parameters of the dual-band active filter based on branch-line couplers.

critical at higher frequencies. Another observable effect is a global frequency shift of the measured response towards lower frequencies. This discrepancy can be attributed to the substrate permittivity and transistor phase tolerances.

Both the simulated and measured responses show, at least, two spike-shaped spurious pass bands at the inner stop-band. These peaks appear as undesired solutions of (2.11), and were already predicted from the graph of the phase response of the filter loop shown in Fig. 2.43. As it was explained before, their effect is mitigated in this case by means of the stop-band response provided by the branch-line couplers at intermediate frequencies. Thus, the maximum level of the two spikes closer to the pass bands is around -8 dB for the one at 1025 MHz and -6 dB for the one at 1470 MHz. Additional attenuation can be achieved by including notch filtering elements in the active filter structure (e.g., filtering lines with SRRs).

Due to the trade-off between the input matching and the noise figure in the gain block, two different implementations have been developed: one with the attenuator at the input of the distributed amplifier and the other with the attenuator at the output. For the one with the attenuator before the amplifier, the measured noise figures present a poor performance with values of 17.9 dB and 17.3 dB in both pass bands. However, the input matching is around -20 dB at both frequencies. When placing the attenuator at the output of the amplifier, the noise figure is reduced down to 7.1 dB and 6.6 dB at the two working frequencies. However, the matching level is worsened at the second frequency, resulting in 6 dB return losses. The summary with the measured results is shown in Table 2.1. The photograph of the implemented active filter prototype is shown in Fig. 2.45.

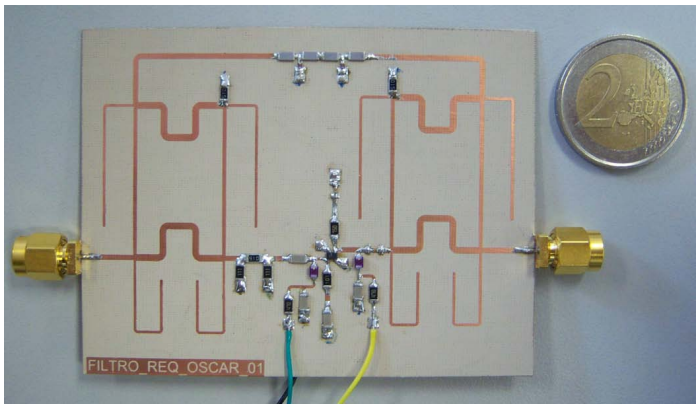

Figure 2.45: Photograph of the dual-band recursive active filter based on branch-line couplers.

Table 2.1: Measured results of the first-order dual-band active filter based on branch-line couplers.

Parameter	**1st band: 788 MHz**	**2nd band: 1700 MHz**
$\|S_{21}\|$	6.9 dB	3.3 dB
$\|S_{22}\|$	-19 dB	-11 dB
BW_{-3dB}	55 MHz	46 MHz
$BW_{\%}$	7.0 %	2.7 %
Attenuator before the amplifier		
$\|S_{11}\|$	-19 dB	-18 dB
NF	17.9 dB	17.3 dB
Attenuator after the amplifier		
$\|S_{11}\|$	-19 dB	-6 dB
NF	7.1 dB	6.6 dB

2.3.3 Multiple-order dual-band active filters

As it was seen in Fig. 2.17, several approaches can be considered for the design of multiple-order recursive active filter structures. Paying attention to aspects such as simplicity, compactness and modularity, the more adequate solution seems to be the one based on coupled ring resonators, whose scheme is shown in Fig. 2.17(c). This subsection presents the design and characterization process of a first-, a second-, and a third-order active filters based on cascading multiple passive and/or active rings [10].

The three filter prototypes are intended to provide two different pass bands, around f_1=800 MHz and f_2=1700 MHz. The circuit schematic of the first-order design is shown in Fig. 2.46. The active stage has been designed by using a monolithic broadband amplifier, model ERA-5+ from *Minicircuits*, which is already matched to 50 Ω. This amplifier is placed in the direct branch. The CRLH transmission line is placed in the feedback branch of the filter. The gain in the ring is controlled by means of a resistive attenuator also connected in the feedback branch. The design procedure is equivalent to the one followed for the first-order filter based on branch-line couplers presented in the previous subsection.

The simulated gain of the amplifier is around 17.6 dB and 14.9 dB in the lower and upper bands respectively. On the other hand, the simulated parameters of the coupled lines are shown in Fig. 2.47. In order to compensate the descending-slope in the amplifier gain response, the center frequency of the coupled lines is tuned to a frequency slightly higher than the middle frequency between f_1 and f_2. It allows obtaining a more symmetrical filtering response with similar gains in both

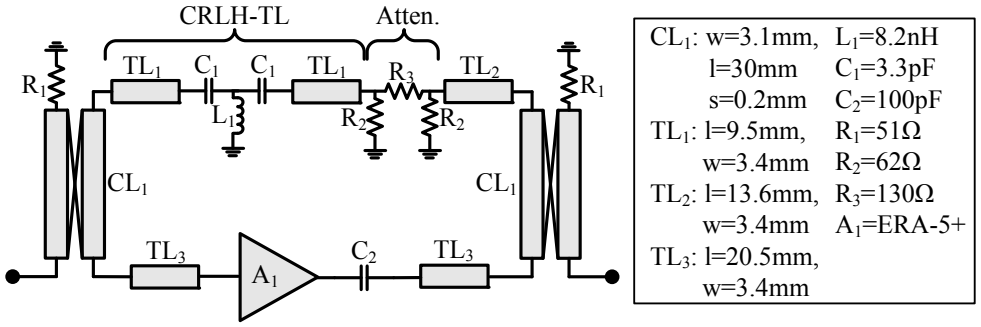

Figure 2.46: Circuit schematic of the first-order dual-band active ring filter (Terms l and w indicate the length and the width of the transmission lines respectively. The coupled lines are also characterized by the separation gap s. Substrate is Arlon25N (height H=1.5 mm, permittivity ϵ_r=3.38)).

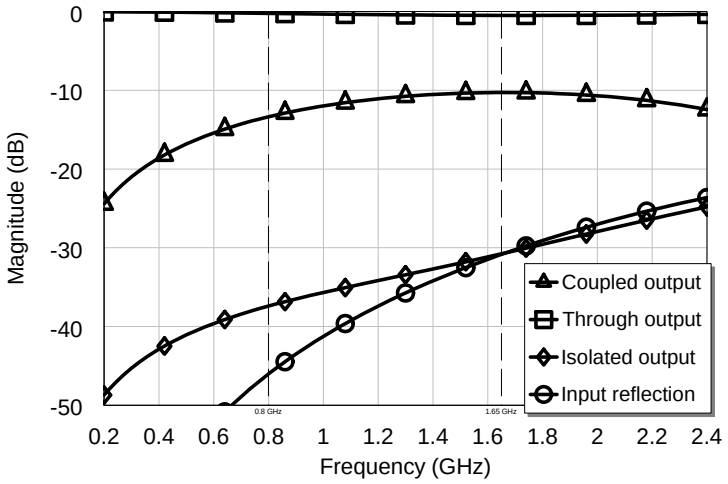

Figure 2.47: Simulated response of the coupled lines combiners.

pass bands. As it was done in the previous filter design, the CRLH transmission line is designed in order to provide 0-deg phase response in the ring at the two desired bandpass frequencies. Both, the phase and the magnitude response of the filter loop are shown in Fig. 2.48. It can be seen that the condition (2.11) is fulfilled at the two bandpass frequencies. Furthermore, the gain in the loop has been limited to values below 0 dB to ensure electrical stability.

The measured response of the first-order filter is shown in Fig. 2.49. There is a good agreement between the simulated and measured results. The transmission response is very symmetrical, with maximum gain values of 3.8 dB and 3.5 dB respectively. The relative bandwidths at each frequency band are 5.8 % and 4.4 %

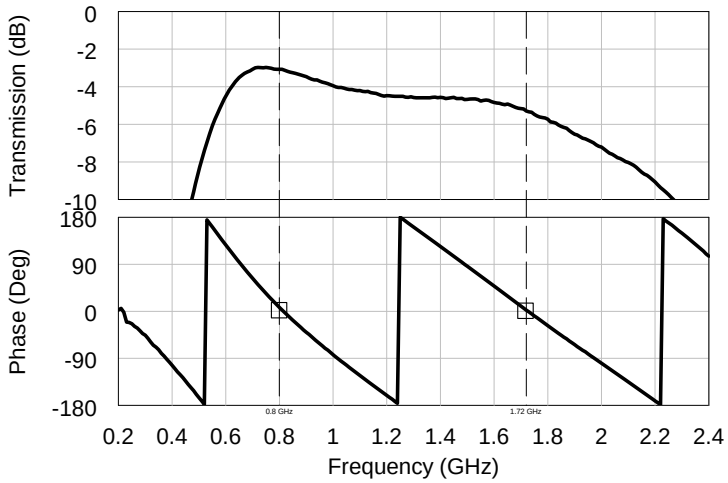

Figure 2.48: Simulated amplitude and phase response of the active filter loop. The desired pass bands are marked with a square.

respectively. All the reflection coefficients are better than -9 dB in the bands of interest.

One of the things that may attract the attention from the current filter response shown in Fig. 2.49 is the absence of spurious peaks around the two desired pass bands. This is due to the broadband nature of the power combiners used in this case. The qualitative comparison between using dual-band or broadband combiners is represented in Fig. 2.50. When using dual-band combiners, they require to replicate the same phase conditions at the two operating frequencies f_1 and f_2 and, therefore, the phase curve has to abruptly change between both frequencies (Fig. 2.50(c)). This response is equivalent to the one obtained with an electrically long transmission line and, therefore, enlarges the electrical length of the filter loop as well (Fig. 2.50(e)). Thus, condition (2.11) is satisfied not only at the two operating frequencies but, unavoidably, at other intermediate frequencies (Fig. 2.50(g)). On the other hand, the slope in the phase curve provided by the broadband combiner (i.e., coupled lines in this case) is flatter (Fig. 2.50(d)), and the electrical length of the filter loop is drastically reduced (Fig. 2.50(f)). Thus, the spurious peaks can be avoided in this case (Fig. 2.50(h)).

With respect to the noise performance, the filter noise figure mainly depends on the first coupling coefficient and on the amplifier noise (2.21). As the input coupled lines present a low coupling coefficient (from Fig. 2.47, $\alpha_1(f_1)$=-13.5 dB and $\alpha_1(f_2)$=-10.3 dB), one of the ways to reduce the noise is to choose an amplifier with lower noise figure. Three prototypes with three different monolithic

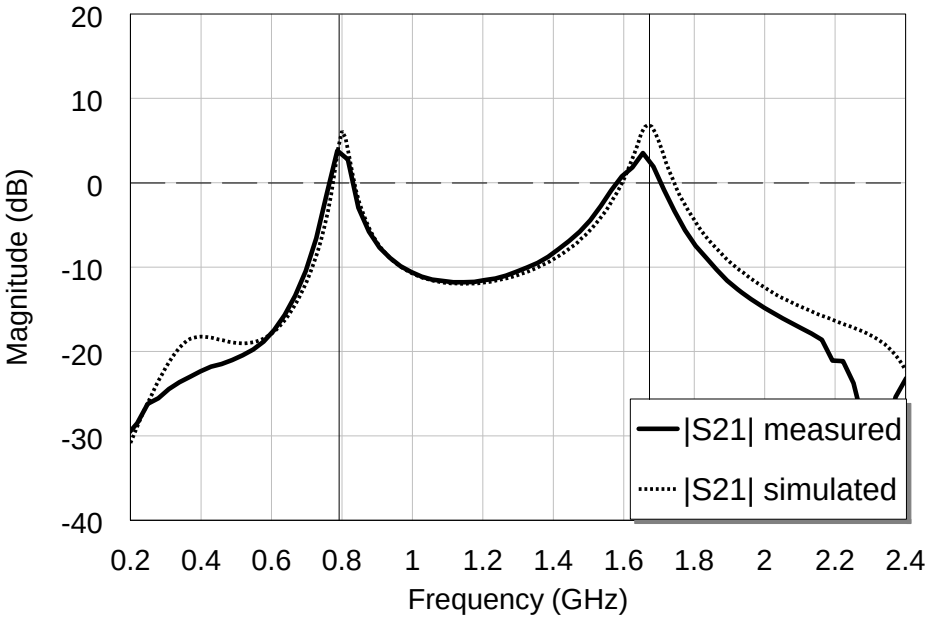

(a)

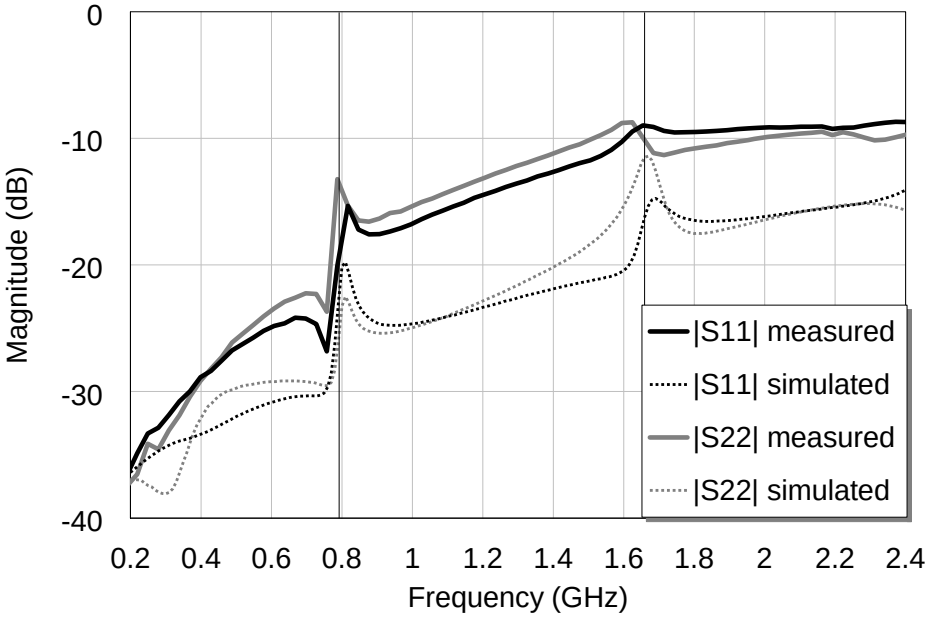

(b)

Figure 2.49: Measured (solid line) and simulated (dashed line) S-parameters of the first-order dual-band active ring filter.

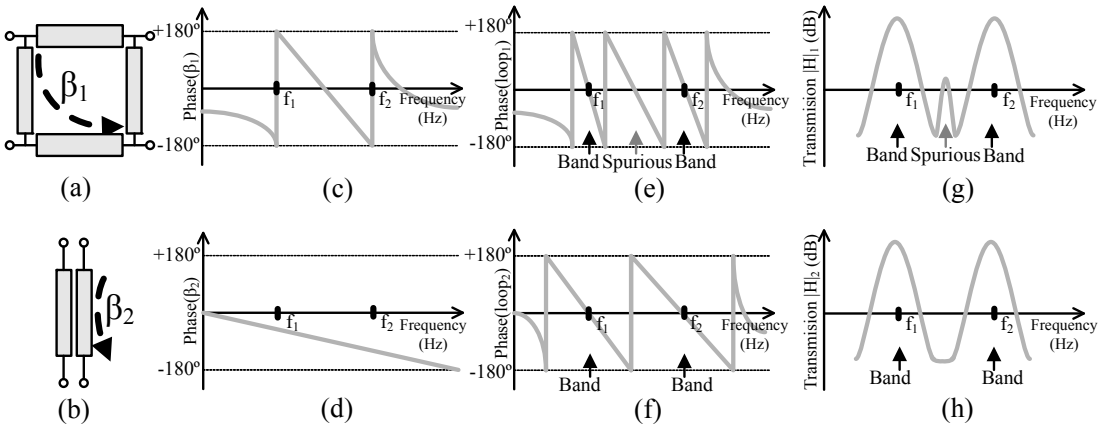

Figure 2.50: Comparison between feedback filters based on dual-band (top) or broadband (bottom) combiners: (a)(b) schematic of the power combiners, (c)(d) phase response of the combiners, (e)(f) phase response of the filter loop, and (g)(h) bandpass filter response.

amplifiers (ERA-5+, ERA-8+ and PMA-545+ from *Minicircuits*) have also been implemented. As it can be seen in Fig. 2.51, the noise figure of the filter can be improved by using amplifiers with lower noise values, as it was expected.

When more stringent requirements in terms of selectivity, bandwidth or ripple are given, higher-order implementations may be needed in order to satisfy all these conditions. In this case, higher-order structures can be easily obtained just by cascading several ring resonators. The design of a second- and a third-order dual-band active filter will be shown below. The common goal is to improve the out-of-band rejection and to increase the bandwidth obtained with the previous first-order implementation by adding additional ring resonators. The circuit schematic of the second-order prototype is shown in Fig. 2.52(a). A passive ring resonator based on two CRLH transmission lines has been coupled to the output of the previous first-order design. On the other hand, the third-order schematic is shown in Fig. 2.52(b). This last design has been formed by adding an extra active ring stage at the output of the second-order filter.

The measured results of the second-order design are plotted in Fig. 2.53. Although the gain has not been significantly increased (due to the passive nature of the additional ring), the rejection at intermediate frequencies has been improved more than 15 dB compared with the first-order implementation. Furthermore, the bandwidth in this case is around 9 % in both bands, which has been widely increased with respect to the previous case. Other characteristics such as the

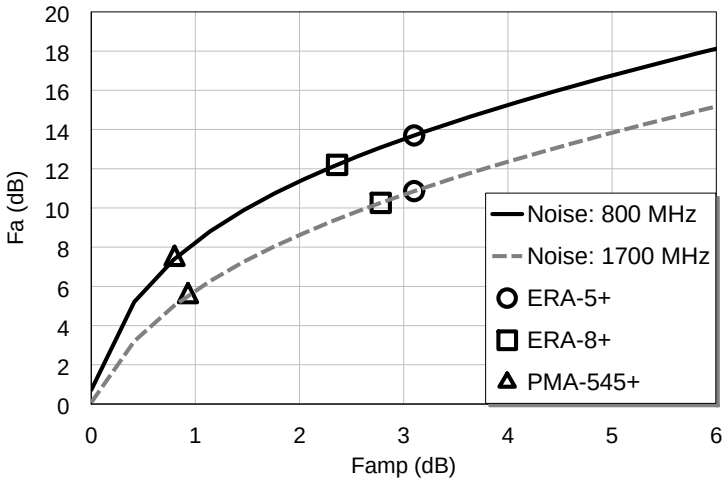

Figure 2.51: Simulated noise curves of the filter F_a as a function of the noise figure of the amplifier F_{amp} (from (2.21)), and measured noise performance obtained with the ERA-5+, ERA-8+ and PMA-545+ amplifiers.

reflection coefficients and the noise figure have not suffered significant variations.

In the case of the third-order design, the measured results are shown in Fig. 2.54. As it is shown in the graph, the gain at both pass bands has been improved around 10 dB with respect to the second-order filter, but with the cost of doubling the power consumption. The fractional bandwidth in this case is around 11 % in both bands. The reflection coefficients and the noise figure are very similar to the previous implementations. All the numerical results are summarized in Table 2.2. The photographs of the three manufactured filter prototypes are shown in Fig. 2.55.

Table 2.2: Measured results of the three dual-band active filter based coupled active rings.

Parameter	**1st order (1 amplifier)**		**2nd order (1 amplifier)**		**3rd order (2 amplifiers)**	
Frequency	800 MHz	1650 MHz	800 MHz	1750 MHz	800 MHz	1750 MHz
$\|S_{21}\|$	3.8 dB	3.5 dB	5.0 dB	2.8 dB	15.5 dB	11.5 dB
$\|S_{11}\|$	-13 dB	-10 dB	-22 dB	-11 dB	-23 dB	-8 dB
$\|S_{22}\|$	-17 dB	-9 dB	-11 dB	-11 dB	-26 dB	-10 dB
BW_{-3dB}	47 MHz	72 MHz	70 MHz	160 MHz	83 MHz	202 MHz
$BW_{\%}$	5.8 %	4.8 %	8.8 %	9.1 %	10.4 %	11.5 %

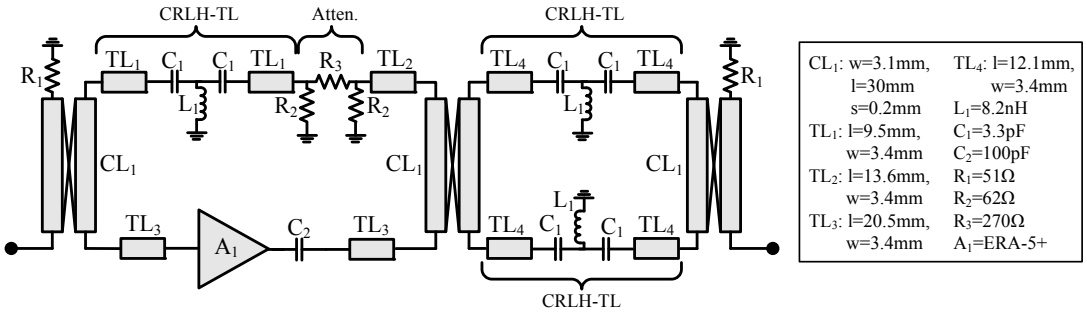

(a)

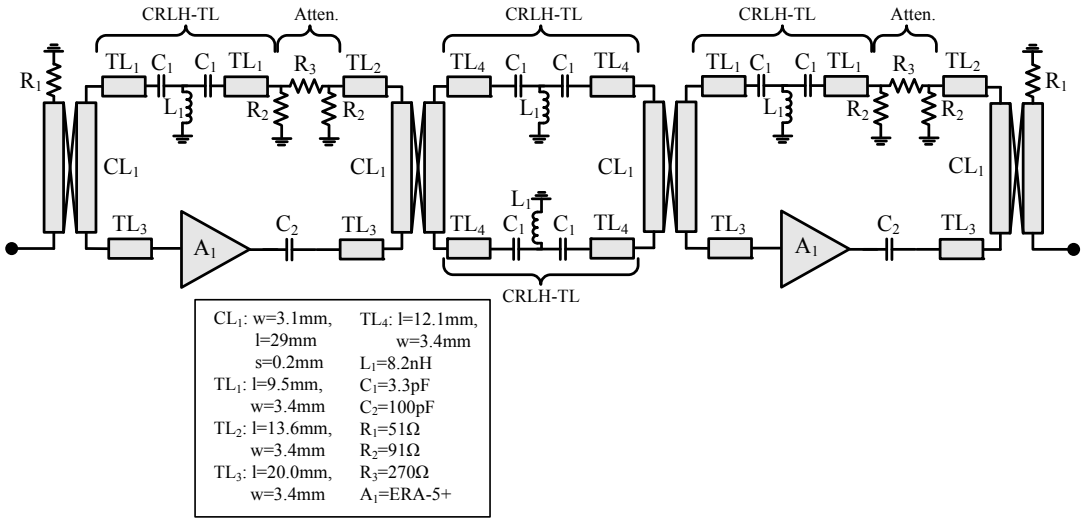

(b)

Figure 2.52: Circuit schematics of the second-order (a) and third-order (b) dual-band active ring filters (Terms l and w indicate the length and the width of the transmission lines respectively. The coupled lines are also characterized by the separation gap s Substrate is Arlon25N (height H=1.5 mm, permittivity ϵ_r=3.38)).

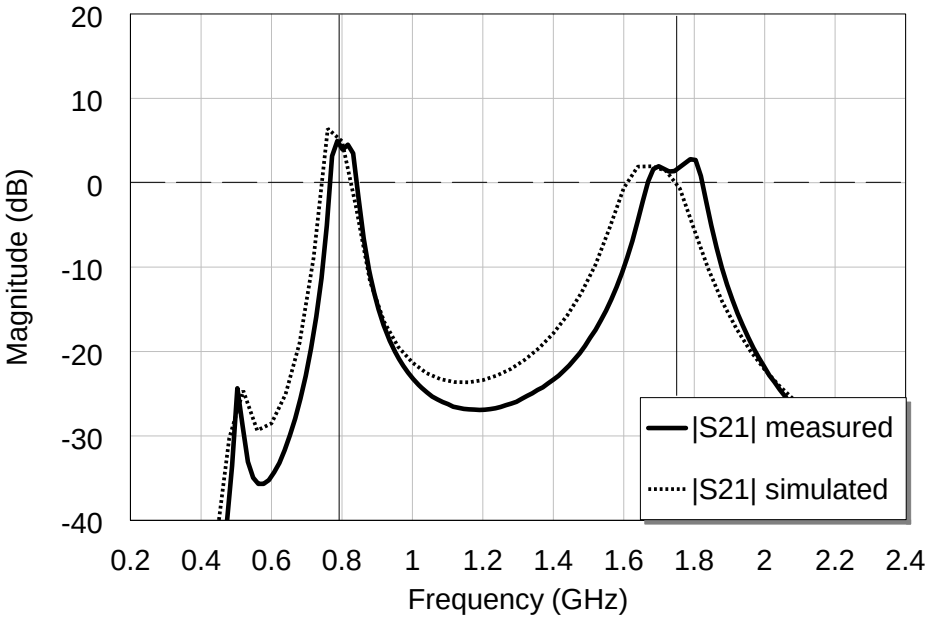

(a)

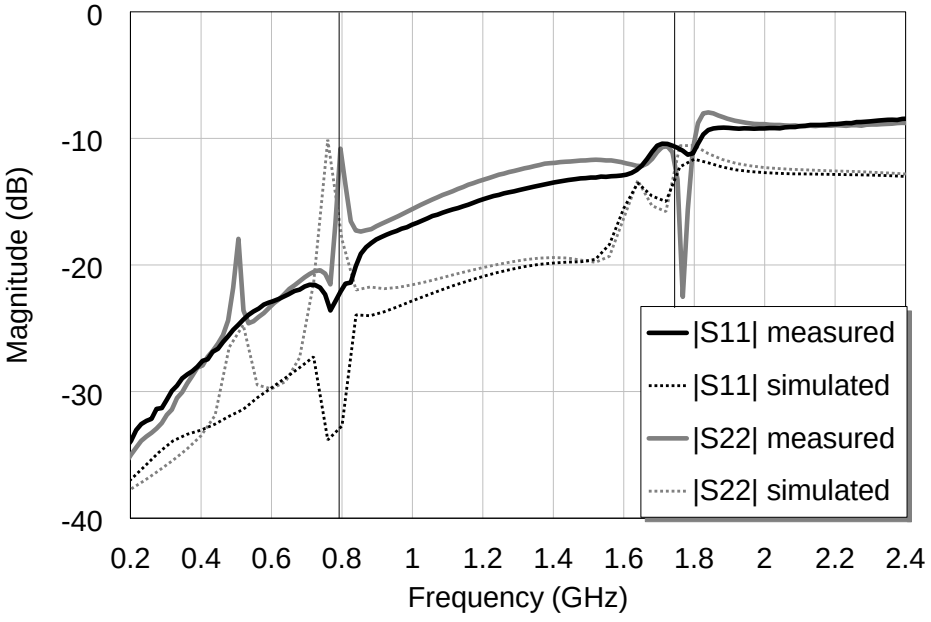

(b)

Figure 2.53: Measured (solid line) and simulated (dashed line) S-parameters of the second-order dual-band active ring filter.

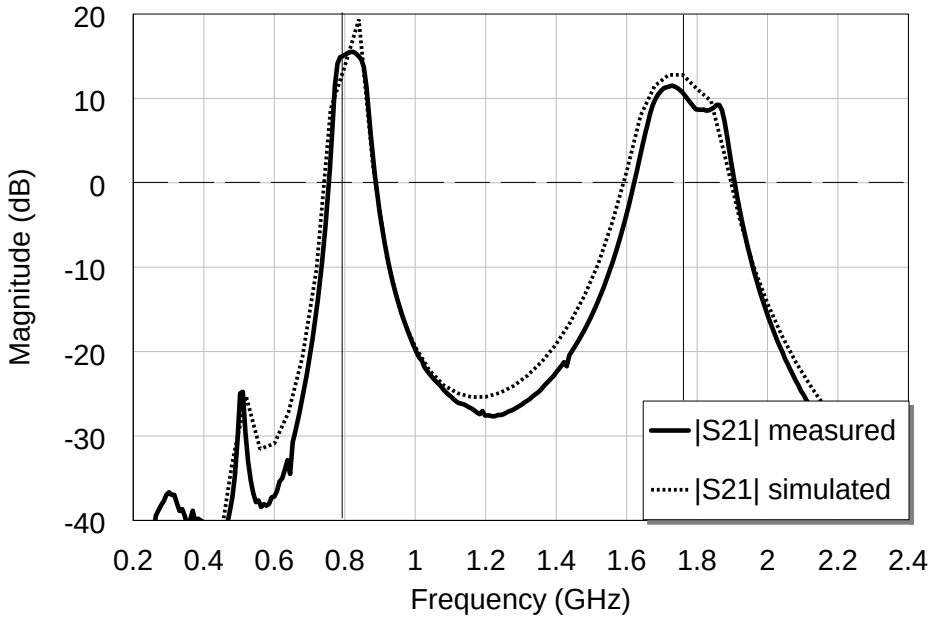

(a)

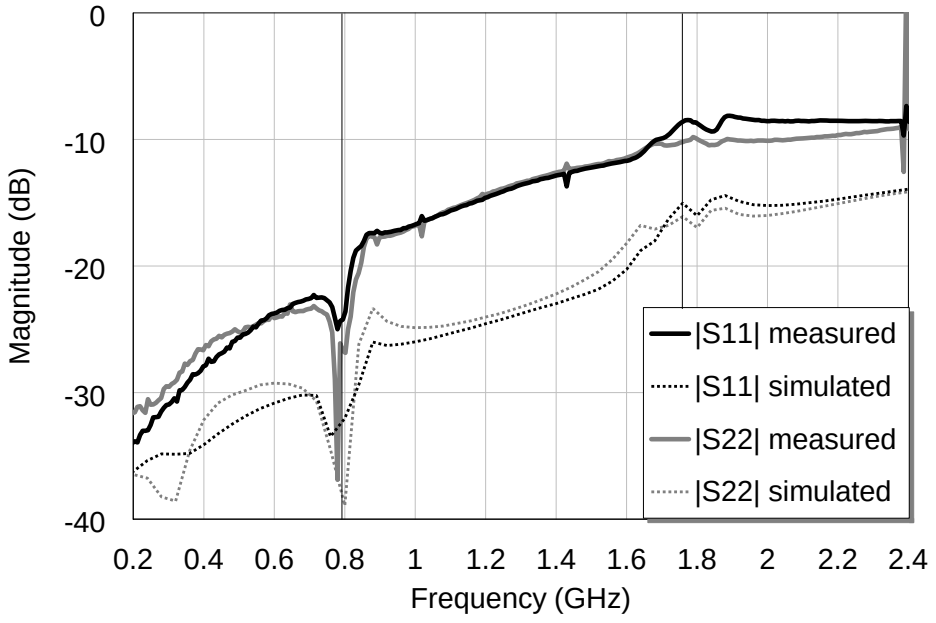

(b)

Figure 2.54: Measured (solid line) and simulated (dashed line) S-parameters of the third-order dual-band active ring filter.

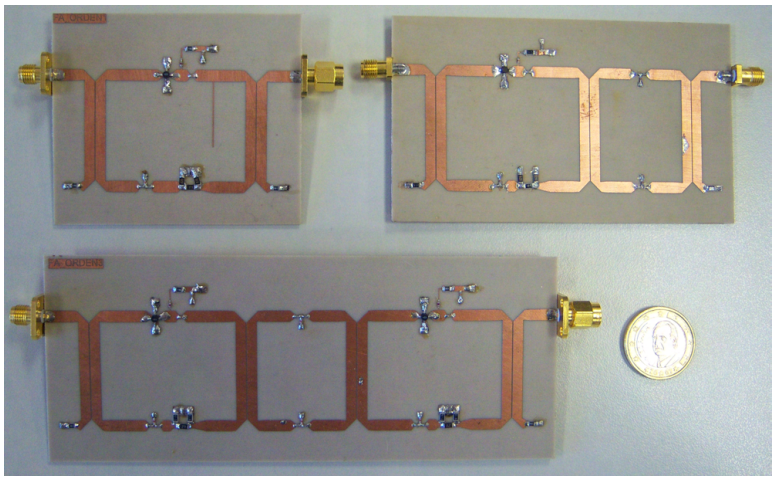

Figure 2.55: Photograph of the three active ring filters.

2.3.4 Tunable dual-band active filters

A natural step in active filters is to obtain a voltage-controlled frequency-tunable circuit, since voltage supply is already present in the structure. It improves the versatility of the filter to be used in any general-purpose application. Tuning is particularly simple to obtain in first-order recursive structures, just by including a phase shifter in the feedback line. It allows obtaining a very linear response of the center frequency with respect to the phase shift. Thus, several single-band tunable recursive active filters have been proposed in the literature (e.g., [30]). This subsection presents the design and characterization process of a novel first-order recursive active filter with two independently tunable pass bands [11].

Future telecommunication systems, such as cognitive radio devices, will require multipurpose and highly versatile radio frequency components. Thus, combining both multi-frequency and tuning capabilities in active filter designs would be a very adequate solution for this type of applications. However, no active filter design with several tunable bands has been presented before. One of the main features of the solutions presented in the previous subsections is that a single feedback line is used to provide the dual-band performance. However it presents a constraint for tuning, since any phase shift in this feedback line would affect both frequency bands. Therefore, a novel approach based on a recursive topology with two feedback lines is presented in this subsection. It allows providing dual-band performance with independent tuning capability in the two pass bands. Highly linear phase shifters based on left-handed cells have been included in both branches [67]. They allow a quite linear response of the center frequencies with respect to the corresponding control voltages.

The basic scheme of the proposed dual-band tunable active filter is shown in Fig. 2.56. It is equivalent to the structure used in the previous first-order designs, but using two feedback branches instead of one. Each feedback structure operates at low and high frequencies respectively, and they are isolated by means of low/high-pass filters. Thus, the phase condition (2.11) can be independently satisfied in the lower band just by adjusting the phase in line γ_L, and in the higher band by adjusting the phase of γ_H. In this case, the lines γ_L and γ_H are based on left-handed phase shifters, so the center frequency can be independently controlled in the two pass-bands. The design philosophy is somehow different to the previous designs, since they provided dual-band performance by using a single feedback transmission line and now it is necessary to use several feedback lines. Thus, the CRLH transmission lines are used for different purposes in each case. In the previous case, the nonlinear phase response of a CRLH line was used to adjust the phase in the loop at two different frequencies. In this case, the use of LH structures is used to provide highly-linear phase-shift capabilities, and dual-band performance is obtained by using several feedback sections.

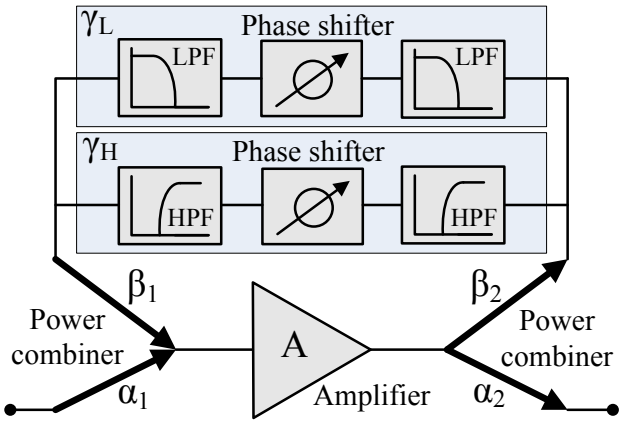

Figure 2.56: General scheme of the dual-band tunable active filter.

A dual-band tunable active filter working in bands around 765 MHz and 1680 MHz has been designed and measured. The circuit board and the schematic are shown in Fig. 2.57 and Fig. 2.58. The gain block has been implemented by cascading a commercial amplifier (ERA-5+ from *Minicircuits*) and a resistive attenuator to limit the gain and avoid instabilities. The measured gain of this block is around 4.9 dB and 4.7 dB, and the noise figure is around 3.5 dB and 3.8 dB in the lower and higher bands respectively. The low/high-pass filters have been implemented by two cascaded LC sections. The rejection of the undesired frequency range is better than 24 dB and 21 dB respectively. The power combiners are dual-band Wilkinson hybrids, designed by means of stub-loaded 90-deg trans-

mission lines [68]. A Wilkinson design has been chosen instead of others (e.g., branch-line) because of its broader bandwidth and its flatter transmission, which is very useful to obtain a response with a more constant gain during the tuning. Finally, the phase shifters are designed following the topology presented in [67]. This phase shifter design is based on left handed cells (i.e., series capacitors and shunt inductors) and is inspired by the model of a metamaterial transmission line. In this case, two T-cells have been used, and the variable capacitance is synthesized by using varactor diodes (model BBY-31 from *Philips*). Two control voltages (V_{DC1} and V_{DC2}) are used to independently control the center frequency of both low/high frequency pass bands respectively. Additionally, two transmission line sections are included in the feedback structure in order to center the tunable band at the desired value. The simulated amplitude and phase response of the two phase shifters is shown in Fig. 2.59. The insertion losses are lower than 1.5 dB and 2.5 dB in the lower and higher frequency ranges.

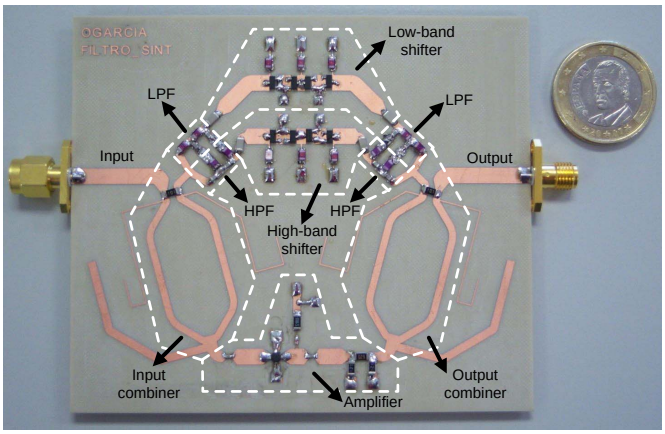

Figure 2.57: Photograph of the dual-band tunable active filter.

The measured filter response for a fixed value of the control voltages is shown in Fig. 2.60. There is a good agreement with the simulated response. A necessary condition for stability is to ensure that the loop gain remains below 0 dB. Fig. 2.61 shows that this condition is fulfilled in the in-band and out-of-band regions. The measured filter response in the two bands for different values of the corresponding control voltages is shown in Fig. 2.62 and Fig. 2.63. The tunable frequency range with less than 3 dB gain ripple covers a range of 312 MHz around 765 MHz in the lower band, and covers 100 MHz around 1680 MHz. The higher frequency band has been shifted around 100 MHz nearer to the notch with respect to the simulation, so it has been attenuated in the lower part. It should be noted that the gain of this filter topology is very sensitive to variations in the transmission in the loop (see Fig. 2.16), which makes difficult to achieve very flat responses.

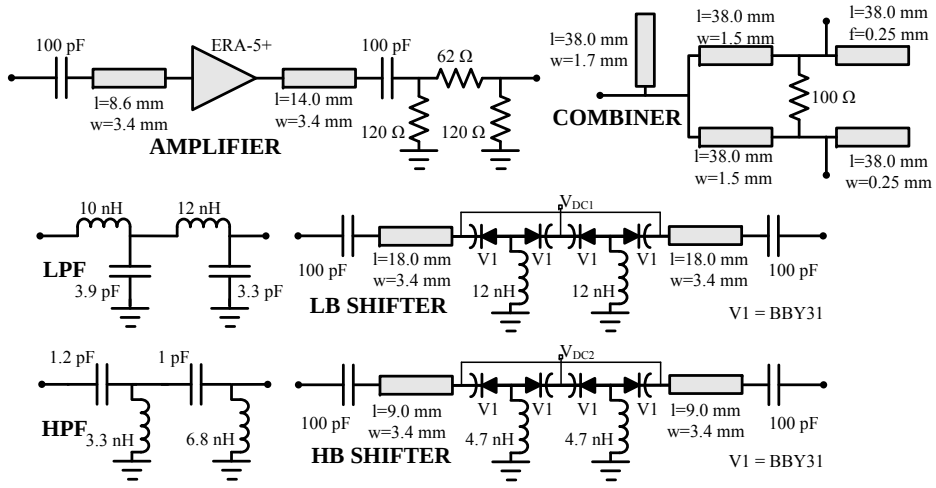

Figure 2.58: Circuit schematic of the different parts of the manufactured tunable dual-band active filter.

Some spurious peaks appear in the response as undesired solutions of (2.11). They could be eliminated by adding additional filtering or by using broadband combiners. Broader tuning regions can be obtained by increasing the number of cells of the shifters. The typical 3-dB bandwidths of the different bands are around 40 MHz. The curves of the center frequency as a function of the control voltages are almost linear for most the voltage range, as shown in Fig. 2.64. The in-band reflection coefficients are better than -6 dB in all the cases. The typical noise figure is around 7.2 dB and 8.0 dB in both bands. It should be noted that half-power combiners increment the noise of the filter more than 3 dB with respect to the isolated gain block. The main measured results are summarized in Table 2.3.

Table 2.3: Measured results of the tunable dual-band active filter.

Parameter	**Low-frequency band**	**High-frequency band**
Tunable frequency range (ripple<3 dB)	698–831 MHz	1630–1730 MHz
Control voltage	0–26 V	6–26 V
Maximum gain	4.1–6.6 dB	3.6–6.6 dB
3-dB bandwidth	40–80 MHz	35–40 MHz
$\|S_{11}\|$	<-6 dB	<-7 dB
$\|S_{22}\|$	<-6 dB	<-6 dB
NF	6.8–7.6 dB	7.5–8.5 dB

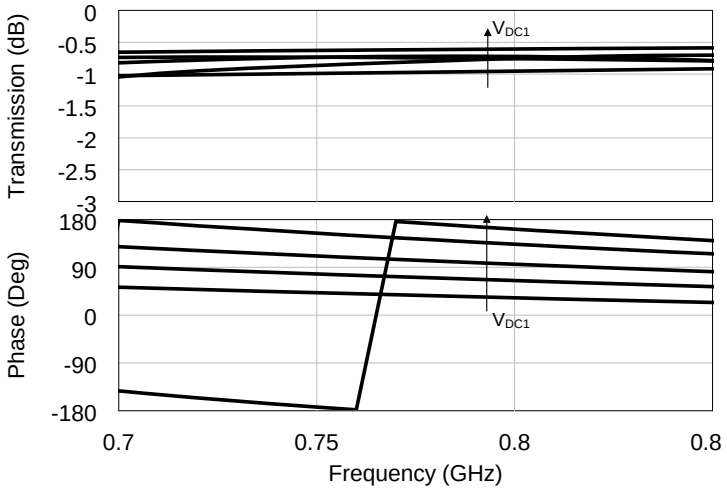

(a)

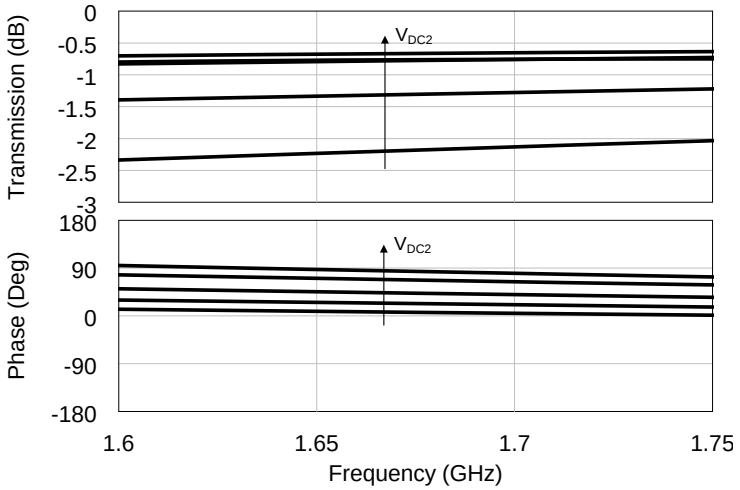

(b)

Figure 2.59: Simulated amplitude and phase response of the low-band (a) and high-band (b) phase shifters based on LH cells. Control voltages V_{DC1} and V_{DC2} take values: 2, 6, 10, 14, 18, and 22 V.

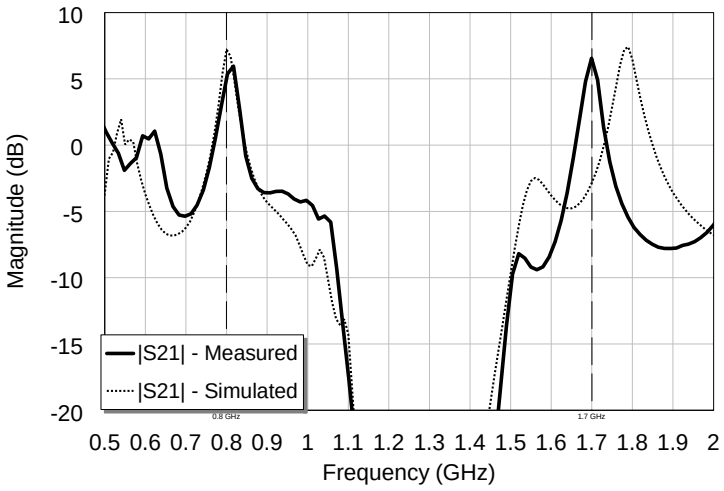

Figure 2.60: Measured (solid line) and simulated (dashed line) transmission response of the filter for V_{DC1}=V_{DC2}=18 V.

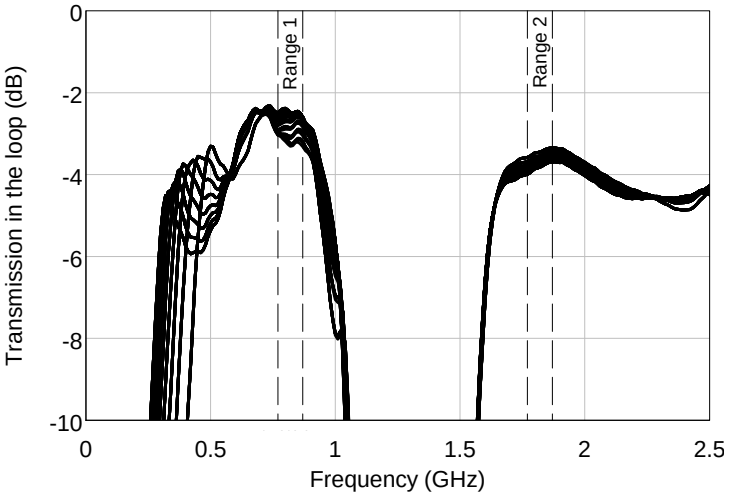

Figure 2.61: Simulated transmission response in the filter loop for V_{DC1}=0–26 V and V_{DC2}=0–26 V.

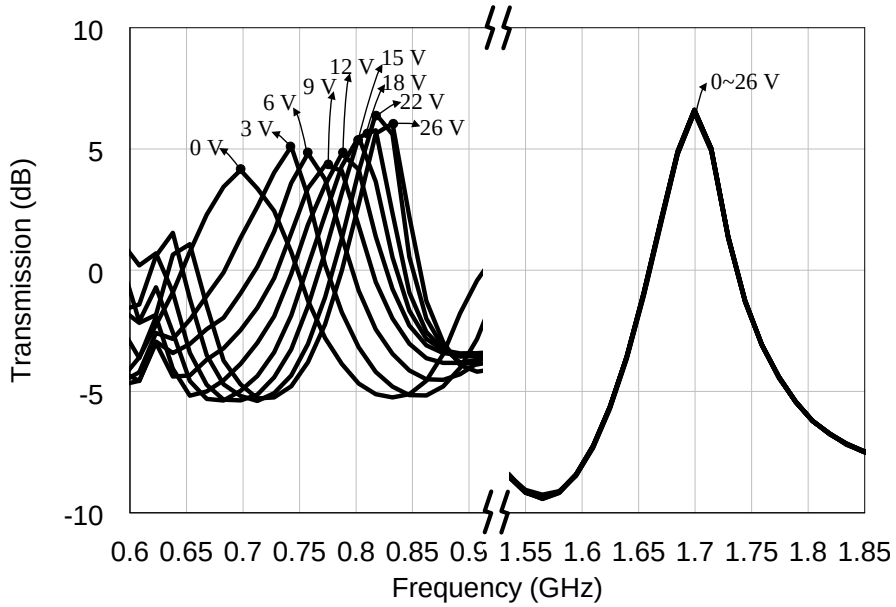

Figure 2.62: Measured transmission response of the filter for a variable value of V_{DC1} (specified over the curves), and a fixed value of V_{DC2}=18 V.

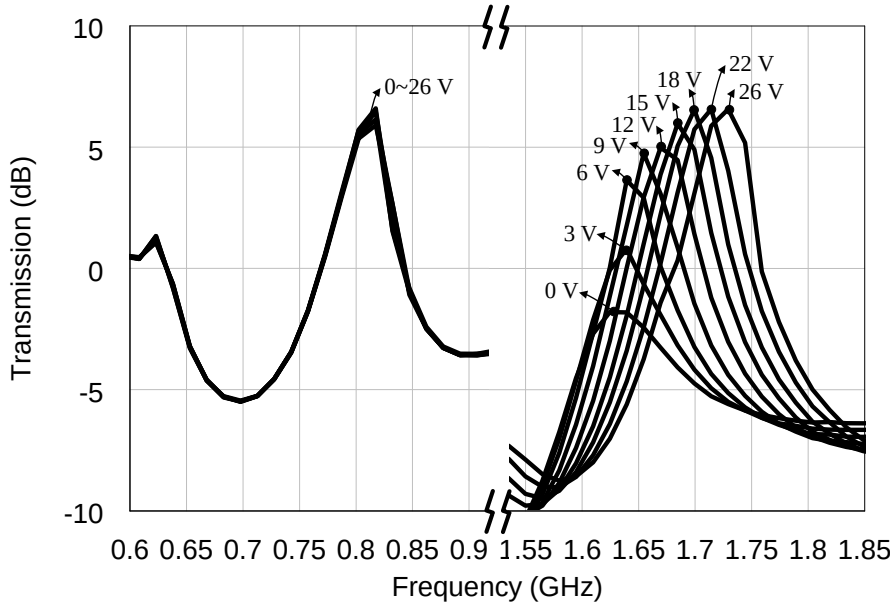

Figure 2.63: Measured transmission response of the filter for a fixed value of V_{DC1}=18 V, and a variable value of V_{DC2} (specified over the curves).

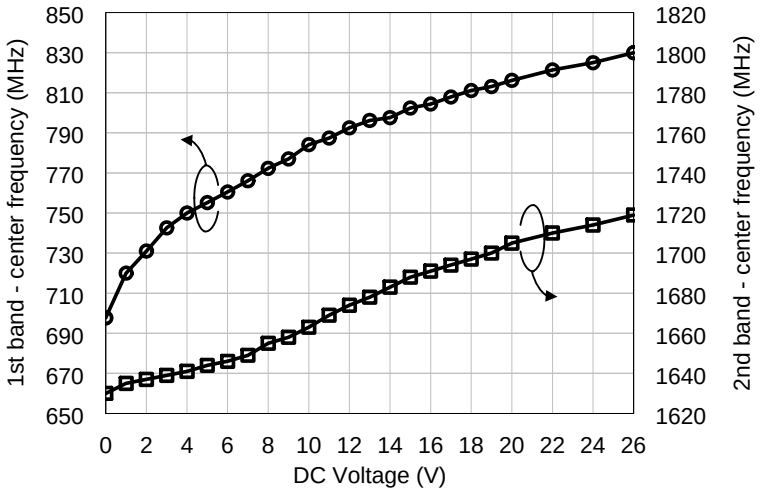

Figure 2.64: Variation of the center frequency as a function of the control voltages V_{DC1} for the first band and V_{DC2} for the second band.

Finally, although a dual-band implementation has been demonstrated, the proposed idea can be reutilized to design filters with arbitrary number of tunable sub-bands, just by including more feedback lines and taking into account some considerations. Firstly, low/high-pass filters should be replaced with band-pass filters, isolating the feedback lines in their corresponding frequency ranges. Additionally, the power combiners and the gain block should cover the different frequency regions at which the filter operates (i.e., multiband or wideband solutions).

2.4 Conclusions

During the last decade, the use of metamaterial structures, and more concretely the use of CRLH transmission lines, has been a key factor in the development of many kind of dual-band microwave circuits. Most of such devices correspond to antennas and passive structures. The work presented in this chapter is an original contribution in which CRLH transmission lines are firstly integrated into a microwave active filter topology to achieve dual-band performance. Moreover, the proposed topology is, as far as we know, the first active filter implementation that provides dual bandpass response at microwave frequencies.

Firstly, the theoretical principles of both, CRLH transmission lines and microwave active filters, have been separately analyzed. Then, a novel recursive active filter design in which CRLH transmission lines are used as feedback sections has been proposed. It has been demonstrated that the non-linear phase response provided by such lines allows obtaining two pass bands at two arbitrary frequencies. Finally, several dual-band active filter prototypes have been implemented and measured. The experimental results acceptably agree with the simulated results, so the viability of this type of devices has been successfully proved. Different filter designs have been investigated, including first-order, multiple-order and tunable topologies.

The advantages of the proposed topology compared with other approaches (e.g., amplifier in series with a dual-band passive resonator) include higher gain, low power consumption and improved selectivity. The high gain is provided by the feedback topology, which allows obtaining filter gain values potentially larger than with the isolated amplifier. It also allows reducing the power consumption, since lower gain (and therefore with lower bias currents) active devices can be used to achieve the same gain levels than other approaches with an amplifier in series. Of course, in multiband applications this dual-band approach is more efficient than the use of single-band active filters since, in the dual-band case, a single active device is enough to cover the double of bands. On the other hand, the feedback structure also allows improving the selectivity of the filter. In contrast, the main disadvantage of the proposed topology is the higher noise figure, in particular compared with passive resonators. Nevertheless, this limitation can be in part mitigated by using low-noise gain blocks and by a proper choice of the power balance in the combiners.

Nowadays, there is an increasing trend in developing telecommunication devices providing several communication services in different frequency bands. Therefore, the development of multiband microwave components is particularly interesting to cover this demand, and active filters are not an exception. Thus, the

number of potential applications of the proposed dual-band active filter designs is quite large. The investigation of more compact versions of the proposed filtering structures is a key factor to make these components more suitable to be used in commercial communication equipments. The feasibility of the implementation in MMIC technology, as well as other future research lines, will be presented in Chapter 4.

2.5 References

[1] A. Lai, T. Itoh, and C. Caloz, "Composite right/left-handed transmission line metamaterials," *IEEE Microwave Magazine*, vol. 5, no. 3, pp. 34–50, Sep. 2004.

[2] X. Jie, C. Luo, and X. Zhao, "A dual-frequency microstrip antenna based on an unbalanced composite right/left-handed transmission line," *Microwave and Optical Technology Letters*, vol. 50, no. 3, pp. 767–771, Jan. 2008.

[3] F. J. Herraiz-Martinez, V. Gonzalez-Posadas, L. E. Garcia-Muñoz, and D. Segovia-Vargas, "Multifrequency and dual-mode patch antennas partially filled with left-handed structures," *IEEE Transactions on Antennas and Propagation*, vol. 56, no. 8, pp. 2527–2539, Aug. 2008.

[4] A. Yu, F. Yang, and A. Elsherbeni, "A dual-band circularly polarized ring antenna based on composite right and left handed metamaterials," *Progress In Electromagnetics Research*, vol. 78, pp. 73–81, 2008.

[5] L. I. Hsiang, M. De Vicentis, C. Caloz, and T. Itoh, "Arbitrary dual-band components using composite right/left-handed transmission lines," *IEEE Transactions on Microwave Theory and Techniques*, vol. 52, no. 4, pp. 1142–1149, Apr. 2004.

[6] X. Q. Lin, R. P. Liu, X. M. Yang, J. X. Chen, X. X. Yin, Q. Cheng, and T. J. Cui, "Arbitrarily dual-band components using simplified structures of conventional CRLH TLs," *IEEE Transactions on Microwave Theory and Techniques*, vol. 54, no. 7, pp. 2902–2909, Jul. 2006.

[7] D. Castro-Galan, L. E. Garcia-Muñoz, D. Segovia-Vargas, and V. Gonzalez-Posadas, "Diversity monopulse antenna based on a dual-frequency and dual-mode CRLH rat-race coupler," *Progress In Electromagnetics Research B*, vol. 14, pp. 87–106, 2009.

[8] M. Hayati, and M. Nosrati, "Loaded coupled transmission line approach of left-handed (LH) structures and realization of a highly compact dual-band branch-line coupler," *Progress In Electromagnetics Research C*, vol. 10, pp. 75–86, 2009.

[9] O. Garcia-Perez, A. Garcia-Lamperez, V. Gonzalez-Posadas, M. Salazar-Palma, and D. Segovia-Vargas, "Dual-band recursive active filters with composite right/left-handed transmission lines," *IEEE Transactions on Microwave Theory and Techniques*, vol. 57, no. 5, pp. 1180–1187, May 2009.

[10] O. Garcia-Perez, L. E. Garcia-Muñoz, D. Segovia-Vargas, and V. Gonzalez-Posadas, "Multiple order dual-band active ring filters with composite right-/left-handed cells," *Progress in Electromagnetics Research*, vol. 104, pp. 201–219, 2010.

[11] D. Segovia-Vargas, O. Garcia-Perez, V. Gonzalez-Posadas, and F. Aznar-Ballesta, "Dual-band tunable active filter based on phase shifters with left-handed cells," *IEEE Microwave and Wireless Components Letters*, vol. 21, no. 2, pp. 92–94, Feb. 2011.

[12] A. A. Dupuy, K. M. Leong, and T. Itoh, "Class-F power amplifier using a multi-frequency composite right/left-handed transmission line harmonic tuner," *IEEE MTT-S International Microwave Symposium Digest*, Jun. 2005.

[13] S. H. Ji, C. S. Cho, J. W. Lee, and J. Kim, "Concurrent dual-band class-E power amplifier using composite right/left-handed transmission lines," *IEEE Transactions on Microwave Theory and Techniques*, vol. 55, no. 66, pp. 1341–1347, Jun. 2007.

[14] J. L. Jimenez-Martin, V. Gonzalez-Posadas, F. J. Arques-Orobon, L. E. Garcia-Muñoz, and D. Segovia-Vargas, "Dual band high efficiency power amplifier based on CRLH lines," *Radioengineering*, vol. 18, no. 4, pp. 567–578, Dec. 2009.

[15] J. L. Jimenez Martin, V. Gonzalez-Posadas, J. E. Gonzalez-Garcia, F. J. Arques-Orobon, L. E. Garcia-Munoz, and D. Segovia-Vargas, "Dual band high efficiency class CE power amplifier based on CRLH diplexer," *Progress In Electromagnetics Research*, vol. 97, pp. 217–240, 2009.

[16] J. Mata-Contreras, T. M. Martin-Guerrero, and C. Camacho-Peñalosa, "Distributed amplifiers with composite left/right-handed transmission lines," *Microwave and Optical Technology Letters*, vol. 48, no. 3, pp. 609–613, Jan. 2006.

[17] C.-Y. Chang, and T. Itoh, "Microwave active filters based on coupled negative resistance method," *IEEE Transactions on Microwave Theory and Techniques*, vol. 38, no. 12, pp. 1879–1884, Dec. 1990.

[18] S. Lucyszyn, and I. D. Robertson, "Monolithic narrow-band filter using ultrahigh-Q tunable active inductors," *IEEE Transactions on Microwave Theory and Techniques*, vol. 42, no. 12, pp. 2617–2622, Dec. 1994.

[19] F. Sabouri, C. Christensen, and T. Larsen, "A single-chip GaAs MMIC image-rejection front-end for digital European cordless telecommunications," *IEEE Transactions on Microwave Theory and Techniques*, vol. 48, no. 8, pp. 1318–1325, Aug. 2000.

[20] C. Rauscher, "Microwave active filters based on transversal and recursive principles," *IEEE Transactions on Microwave Theory and Techniques*, vol. 33, no. 12, pp. 1350–1360, Dec. 1985.

[21] L.-C. Tsai, and C.-W. Hsue, "Dual-band bandpass filters using equal-length coupled-serial-shunted lines and Z-transform technique," *IEEE Transactions on Microwave Theory and Techniques*, vol. 52, no. 4, pp. 1111–1117, Apr. 2004.

[22] V. Palazzari, S. Pinel, J. Laskar, L. Roselli, and M. M. Tentzeris, "Design of an asymmetrical dual-band WLAN filter in liquid crystal polymer (LCP) system-on-package technology," *IEEE Microwave and Wireless Components Letters*, vol. 15, no. 3, pp. 165–167, Mar. 2005.

[23] S. Lee, and Y. Lee, "A planar dual-band filter based on reduced-length parallel coupled lines," *IEEE Microwave and Wireless Components Letters*, vol. 20, no. 1, pp. 16–18, Jan. 2010.

[24] Z. Q. Zhang, X. P. Liao, and R. Wu, "RF on-chip LC passive bandpass filter based on GaAs MMIC technology," *Electronics Letters*, vol. 46, no. 3, Feb. 2010.

[25] D. K. Adams, and R. Y. C. Ho, "Active filters for UHF and microwave frequencies," *IEEE Transactions on Microwave Theory and Techniques*, vol. 17, no. 9, pp. 662–670, Sep. 1969.

[26] L. Billonnet, and B. Jarry, "Active filters: an overview of active filter structures," in *RF and Microwave Engineering*. John Wiley & Sons, 2005.

[27] S. Hara, T. Tokumitsu, and M. Aikawa, "Lossless, broadband monolithic microwave active inductors," *IEEE MTT-S International Microwave Symposium Digest*, pp. 955–958, Jun. 1989.

[28] L. Darcel, P. Dueme, R. Funck, and G. Alquie, "New MMIC approach for low noise high order active filters," *IEEE MTT-S International Microwave Symposium Digest*, Jun. 2005.

[29] M. Delmond, L. Billonnet, B. Jarry, and P. Guillon, "Microwave tunable active filter design in MMIC technology using recursive concepts," *IEEE*

Microwave and Millimeter-Wave Monolithic Circuits Symposium, pp. 105–108, May 1995.

[30] W. Mouzannar, L. Billonnet, B. Jarry, and P. Guillon, "A new design concept for realising highly tunable microwave filters using recursive principles," *28th European Microwave Conference*, pp. 1–5, Oct. 1998.

[31] M. Delmond, L. Billonnet, B. Jarry, and P. Guillon, "New design approach for high-order recursive filter using MMIC technology," *26th European Microwave Conference*, pp. 405–408, Sep. 1996.

[32] L. Nenert, L. Billonnet, B. Jarry, P. Guillon, C. Quendo, E. Rius, and G. Tanne, "Compact high-order planar ring-resonator filters optimized in noise in coplanar technology," *IEEE MTT-S International Microwave Symposium Digest*, pp. 1441–1444, May 2001.

[33] L. Billonnet, B. Jarry, and P. Guillon, "Stability diagnosis of microwave recursive structures using the NDF methodology," *IEEE MTT-S International Microwave Symposium Digest*, pp. 1419–1422, May 1995.

[34] H. Ezzedine, L. Billonnet, B. Jarry, and P. Guillon, "Optimization of noise performance for various topologies of planar microwave active filters using noise wave techniques," *IEEE Transactions on Microwave Theory and Techniques*, vol. 46, no. 12, pp. 2484–2492, Dec. 1998.

[35] V. Veselago, "The electrodynamics of substances with simultaneously negative values of ϵ and μ," *Soviet Physics Uspekhi*, vol. 10, no. 4, pp. 509–514, Jan. 1968.

[36] J. B. Pendry, A. J. Holden, W. J. Stewart, and I. Youngs, "Extremely low frequency plasmons in metallic mesostructure," *Physical Review Letters*, vol. 76, no. 25, pp. 4473–4776, Jun. 1996.

[37] J. B. Pendry, A. J. Holden, D. J. Robbins, and W. J. Stewart, "Magnetism from conductors and enhanced nonlinear phenomena," *IEEE Transactions on Microwave Theory and Techniques*, vol. 47, no. 11, pp. 2075–2084, Nov. 1999.

[38] D. R. Smith, W. J. Padilla, D. C. Vier, S. C. Nemat-Nasser, and S. Schultz, "Composite medium with simultaneously negative permeability and permittivity," *Physical Review Letters*, vol.84, no. 18, pp. 4184–4187, May 2000.

[39] A. Sanada, C. Caloz, and T. Itoh, "Planar distributed structures with negative refractive index," *IEEE Transactions on Microwave Theory and Techniques*, vol. 52, no. 4, pp. 1252–1263, Apr. 2004.

[40] G. V. Eleftheriades, A. K. Iyer, and P. C. Kremer, "Planar negative refractive index media using periodically L-C loaded transmission lines," *IEEE Transactions on Microwave Theory and Techniques*, vol. 50, no. 12, pp. 2702–2712, Dec. 2002.

[41] C. Caloz, and T. Itoh, *Electromagnetic metamaterials: transmission line theory and microwave applications*. Wiley Interscience, 2006.

[42] C. Caloz, and T. Itoh, "Positive/negative refractive index anisotropic 2-D metamaterials," *Electronics Letters*, vol. 13, no. 12, Dec. 2003.

[43] P. P. M. So, D. Huilian, and W. J. R. Hoefer, "Modeling of metamaterials with negative refractive index using 2-D shunt and 3-D SCN TLM networks," *IEEE Transactions on Microwave Theory and Techniques*, vol. 53, no. 4, pp. 1496–1505, Apr. 2005.

[44] E. Saenz, R. Gonzalo, I. Ederra, J. C. Vardaxoglou, and P. de Maagt, "Resonant meta-surface superstrate for single and multifrequency dipole antenna arrays," *IEEE Transactions on Antennas and Propagation*, vol. 56, no. 4, pp. 951–960, Apr. 2008.

[45] C. A. Allen, K. M. K. H. Leong, and T. Itoh, "Design of a balanced 2D composite right-/left-handed transmission line type continuous scanning leaky-wave antenna," *IET Microwaves, Antennas and Propagation*, vol. 1, no. 3, pp. 746–750, Jun. 2007.

[46] I. Gil, J. Garcia-Garcia, J. Bonache, F. Martin, M. Sorolla, and R. Marques, "Varactor-loaded split ring resonators for tunable notch filters at microwave frequencies," *Electronics Letters*, vol. 40, no. 21, Oct. 2004.

[47] J. Garcia-Garcia, F. Martin, F. Falcone, J. Bonache, I. Gil, T. Lopetegi, M. A. G. Laso, M. Sorolla, and R. Marques, "Spurious passband suppression in microstrip coupled line band pass filters by means of split ring resonators," *IEEE Microwave and Wireless Components Letters*, vol. 14, no. 9, pp. 416–418, Sep. 2004.

[48] A. Lai, K. M. K. H. Leong, and T. Itoh, "Infinite wavelength resonant antennas with monopolar radiation patterns based on periodic structures," *IEEE Transactions on Antennas and Propagation*, vol. 55, no. 3, pp. 868–876, Mar. 2007.

[49] J. Bonache, G. Siso, M. Gil, A. Iniesta, J. Garcia-Rincon, and F. Martin, "Application of composite right/left handed (CRLH) transmission lines

based on complementary split ring resonators (CSRRs) to the design of dual-band microwave components," *IEEE Microwave and Wireless Components Letters*, vol. 18, no. 8, pp. 524–526, Aug. 2008.

[50] M. Gil, I. Gil, J. Bonache, J. Garcia-Garcia, and F. Martin, "Metamaterial transmission lines with extreme impedance values," *Microwave and Optical Technology Letters*, vol. 48, no. 12, pp. 2499–2505, Dec. 2006.

[51] C. Caloz, and T. Itoh, "Transmission line approach of left-handed (LH) materials and microstrip implementation of an artificial LH transmission line," *IEEE Transactions on Antennas and Propagation*, vol. 52, no. 5, pp. 1159–1166, May 2004.

[52] L. Liu, C. Caloz, and T. Itoh, "Dominant mode (DM) leaky-wave antenna with backfire-to-endfire scanning capability," *Electronics Letters*, vol. 38, no. 23, pp. 1414-1416, 2000.

[53] S. Lim, C. Caloz, and T. Itoh, "Metamaterial-based electronically controlled transmission line structure as a novel leaky-wave antenna with tunable radiation angle and beamwidth," *IEEE Transactions on Microwave Theory and Techniques*, vol. 52, no. 12, pp. 2678–2690, Dec. 2004.

[54] S. Lim, C. Caloz, and T. Itoh, "A reflectodirective system using a composite right/left-handed (CRLH) leaky-wave antenna and heterodyne mixing," *IEEE Microwave and Wireless Components Letters*, vol. 14, no. 4, pp. 183–185, Apr. 2004.

[55] C. Caloz, A. Sanada, and T. Itoh, "A novel composite right/left-handed coupled-line directional coupler with arbitrary coupling level and broad bandwidth," *IEEE Transactions on Microwave Theory and Techniques*, vol. 52, no. 3, pp. 980-992, Mar. 2004.

[56] C. Caloz, and H. V. Nguyen, "Novel broadband conventional- and dual-composite right/left-handed (C/D-CRLH) metamaterials: properties, implementation and double-band coupler application," *Applied Physics A*, vol. 87, no. 2, pp. 309–316, 2007.

[57] H. Okabe, C. Caloz, and T. Itoh, "A compact enhanced-bandwidth hybrid ring using an artificial lumped-element left-handed transmission-line section," *IEEE Transactions on Microwave Theory and Techniques*, vol. 52, no. 3, pp. 798–804, Mar. 2004.

[58] V. Gonzalez-Posadas, J. L. Jimenez-Martin, A. Parra-Cerrada, L. E. Garcia-Muñoz, and D. Segovia-Vargas, "Dual-composite right-left-handed transmission lines for the design of compact diplexers," *IET Microwaves, Antennas and Propagation*, vol. 4, no. 8, pp. 982–990, Aug. 2010.

[59] M. Gil, J. Bonache, J. Garcia-Garcia, J. Martel, and F. Martin, "Composite right/left-handed metamaterial transmission lines based on complementary split-rings resonators and their applications to very wideband and compact filter design," *IEEE Transactions on Microwave Theory and Techniques*, vol. 55, no. 6, pp. 1296–1304, Jun. 2007.

[60] F. P. Casares-Miranda, C. Camacho-Peñalosa, and C. Caloz, "High-gain active composite right/left-handed leaky-wave antenna," *IEEE Transactions on Antennas and Propagation*, vol. 54, no. 8, pp. 2292–2300 , Aug. 2006.

[61] J. Mata-Contreras, C. Camacho-Peñalosa, and T. M. Martin-Guerrero, "Active distributed mixers based on composite right/left-handed transmission lines," *IEEE Transactions on Microwave Theory and Techniques*, vol. 57, no. 5, pp. 1091–1101, May 2009.

[62] F. Y. Ng-Molina, T. M. Martin-Guerrero, and C. Camacho-Penñalosa, "Power and gain considerations in distributed amplifiers based on composite right/left handed transmission lines," *IET Microwaves, Antennas and Propagation*, vol. 4, no. 8, pp. 1000–1006, Aug. 2010.

[63] C.-T. M. Wu, and T. Itoh, "A re-radiating CRLH-transmission line leaky wave antenna using distributed amplifiers," *Asia Pacific Microwave Conference*, pp. 1998–2001, Dec. 2009.

[64] L. Billonnet, B. Jarry, and P. Guillon, "Theoretical and experimental analysis of microwave tunable recursive active filters using power dividers," *IEEE MTT-S International Microwave Symposium Digest*, pp. 185–188, Jun. 1993.

[65] K.-K. M. Cheng, and F. L. Wong, "A novel approach to the design and implementation of dual-band compact planar 90 branch-line coupler," *IEEE Transactions on Microwave Theory and Techniques*, vol. 52, no. 11, pp. 2458–2463, Nov. 2004.

[66] J. B. Beyer, S. N. Prasad, R. C. Becker, J. E. Nordman, and G. K. Hohenwarter, "MESFET distributed amplifier design guidelines," *IEEE Transactions on Microwave Theory and Techniques*, vol. 32, no. 3, pp. 268–275, Mar. 1984.

[67] H. Kim, A. B. Kozyrev, A. Karbassi, and D. W. Weide, "Linear tunable phase shifter using a left-handed transmission line," *IEEE Microwave and Wireless Components Letters*, vol. 15, no. 5, pp. 366–368, May 2005.

[68] A. A. S. Mohra, "Compact dual-band Wilkinson power divider," *Microwave and Optical Technology Letters*, vol. 50, no. 6, pp. 1678–1682, Jun. 2008.

Chapter 3

Broadband Differential Low Noise Amplifiers: Application to Active Differential Antennas

During the last decades, differential amplifiers have been widely used in low frequency electronics. More recently, engineers have exploited the interesting properties of differential amplifiers in the microwave range as well. One of the applications in which differential amplifiers are being used is the design of differential active antenna arrays for the next generation of radio-telescopes (e.g., Square Kilometre Array (SKA)) [1],[2]. The SKA telescope is intended to work in a very broad bandwidth, between 70 MHz and 10 GHz, divided in smaller sub-bands. The lower sub-bands are intended to be covered with both sparse and dense aperture arrays, whereas small dish reflectors are intended for higher frequency bands. More precisely, the mid-frequency band, which ranges from 300 MHz to 1 GHz, is intended to be covered by a dense array of millions of cheap tapered slot antenna (TSA) elements. Due to the intrinsic balanced nature of the TSAs, the use of differential low noise amplifiers instead of single-ended ones is fully justified in order to reduce the losses in the receiving RF front-ends. For this purpose, many research groups are currently working in the development of small array demonstrators in order to validate all the technologies that will be necessary for the final implementation of the SKA telescope (e.g., [3]-[12]).

The TSA elements (i.e., Vivaldi or bunny-ear antennas [13]) are balanced antennas that must be fed in a differential way (i.e., two complementary signals traveling on two separated wires). In order to amplify the differential signals coming from each antenna element, either a passive balun with a single-ended LNA or a differential LNA is required. Since including a passive balun as the

first element of the receiver chain can introduce an unnecessary increase in the noise temperature (around 10 K), the option of a differential LNA directly connected to the antenna ports can be a more suitable solution in terms of system noise temperature [14]. Furthermore, differential amplifiers have other inherent advantages in comparison with single-ended ones, which include interference rejection (e.g., noise from the power supply, external interferences, etc.), higher dynamic range, and reduced even-order harmonic distortion [15]. As counterpart, the characterization and measurement of differential devices is not as immediate as with conventional single-ended devices, and it is necessary the use of some ad-hoc measurement techniques at microwave frequencies [16]-[20].

During the last years, several broadband differential LNAs for radio-astronomy applications have been proposed. Three possible solutions for the differential LNA design could be considered: commercial amplifiers, MMICs, and hybrid solutions. For the commercial amplifier case there are not differential devices working in this frequency range with the bandwidth and low noise level required for this application. Secondly, many of the proposed ad-hoc designs are MMIC devices based on different types of transistor technologies (i.e., CMOS [20], SiGe BiCMOS [21]-[23], or GaAs HEMT [24]). However, MMICs present some constraints due to the low Q-factor of the printed inductors and the large size needed for the planar coupling capacitors, especially when working at frequencies of some hundreds of MHz. Thus, they usually require the use of external chip inductors and capacitors. This increases the total size of the circuit, so the advantage of the compactness provided by the MMIC is partially lost. Thirdly, other differential LNA designs based on discrete transistors have been presented as well, but working at higher frequencies and in a narrower relative bandwidth than in the present work [25].

The work presented in this chapter deals with the design and characterization of differential low noise amplifiers for active antenna arrays. This research has been undertaken at different levels, from the characterization and design of differential amplifiers at microwave frequencies up to the study of active antenna array systems.

This chapter is structured as follows. As the application is devoted to the SKA project, Section 3.1 presents some introductory concepts about the SKA telescope. The characterization of active antenna arrays taking into account the mutual coupling between the elements is described in Section 3.2. The main methods that are needed to characterize the differential amplifiers in terms of gain and noise are presented in Section 3.3. In that section, a novel method to measure the noise and gain performance of differential amplifiers using passive baluns is proposed [26],[27]. The design and measurement process of an active antenna array prototype (called FIDA3), including the radiating structure and the differential amplifiers, is presented in Section 3.4 [12]. For the characterization

of the amplifiers of FIDA3, a novel technique to measure the gain and noise curves of the differential devices has been developed [27]. Some improved topologies of differential low noise amplifiers are presented in Section 3.5. Finally, the main conclusions of this chapter are presented in Section 3.6.

3.1 The Square Kilometre Array Telescope

The SKA telescope will be a next-generation radio-telescope with a collecting area of about 1 km^2. This instrument is intended to cover the frequency range between 70 MHz and 10 GHz, and it will be much more sensitive than current telescopes (Fig. 3.1). The SKA technology will allow breakthroughs in different areas of science, such as astroparticle physics and cosmology, fundamental physics, galactic and extragalactic astronomy, solar system science, and astrobiology. In the context of the instrumentation, different antenna technologies are proposed in order to cover the entire bandwidth: arrays of dipole-like antennas in random sparse configuration for the lowest frequency band (70-450 MHz), aperture arrays of TSAs for the mid-frequency range (300-1000 MHz), and small dish reflectors at higher frequencies (1-10 GHz). An artistic impression of the array configurations and the different antenna technologies is shown in Fig. 3.2.

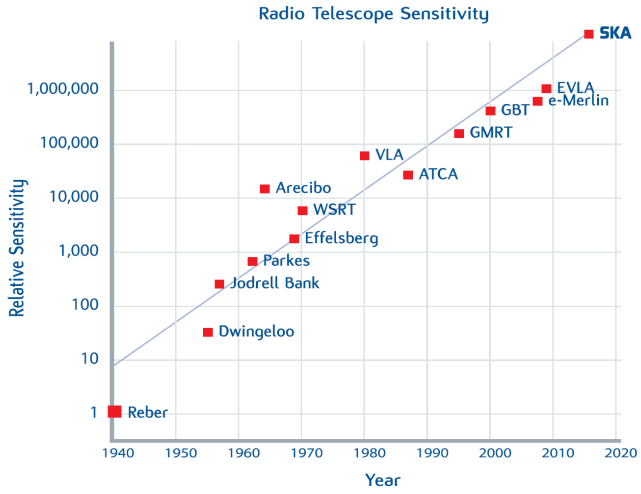

Figure 3.1: Sensitivity of the SKA compared to that of other major radio telescopes at time of construction [2].

Two different sites are being considered for the emplacement of SKA: one in a region of central South Africa, and the other in Western Australia. The southern hemisphere has been chosen since the view of the Milky Way is better and radio frequency interferences (RFIs) are lower. There is a global collaboration of more than 20 countries that are currently working to find the most suitable technologies that will be needed to construct this enormous instrument. The work developed in this thesis has been developed in the framework of the SKADS project, which is a European consortium whose work is mostly focused on the mid-frequency

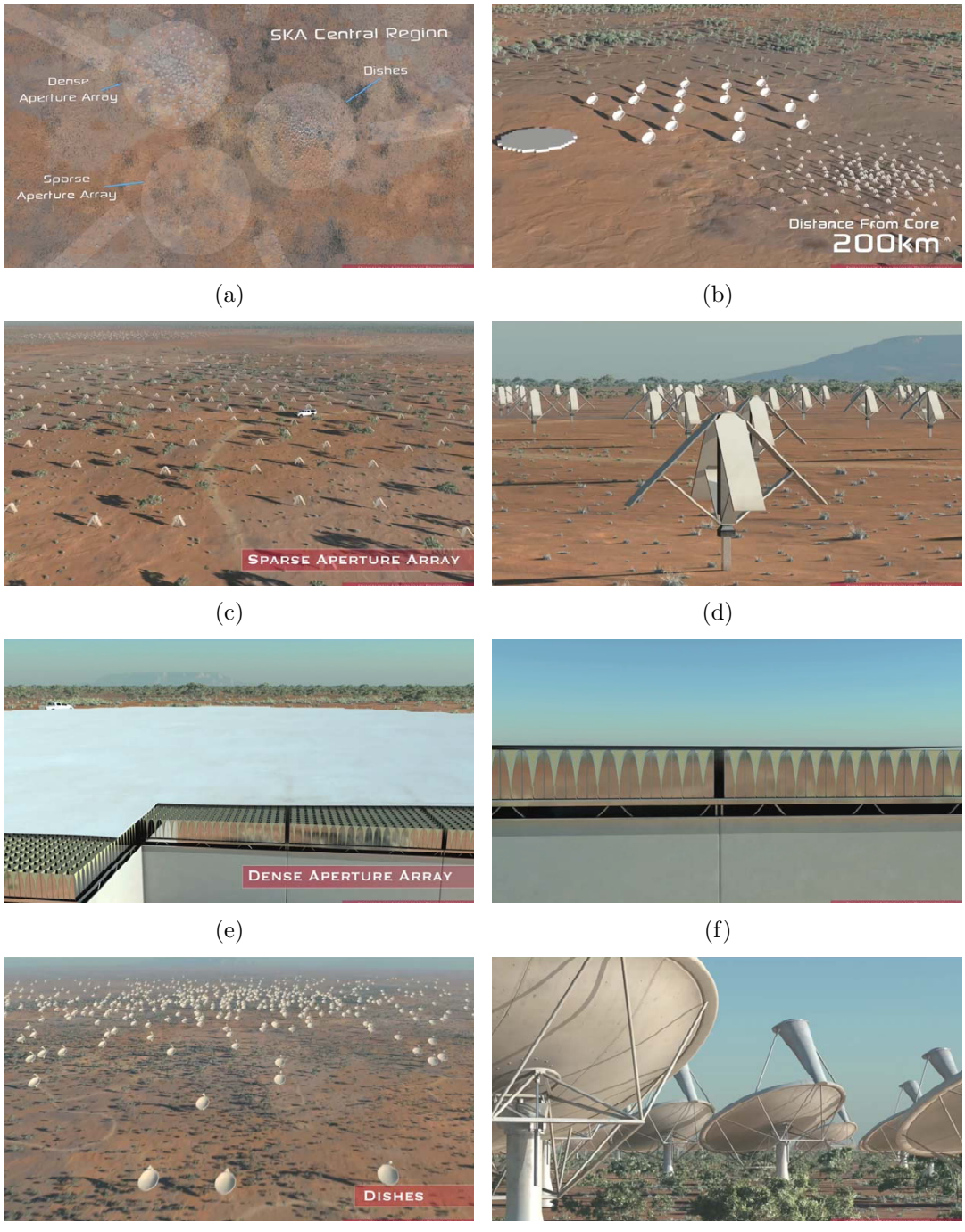

(a) (b)

(c) (d)

(e) (f)

(g) (h)

Figure 3.2: Artistic impression of the SKA: central core (a), sub-station (b), sparse aperture arrays (c)(d), dense aperture arrays (e)(f), and dishes (g)(h) [2] (courtesy of *SPDO/Swinburne Astronomy Productions*).

band of SKA [28]. As it can be seen from Fig. 3.2, SKA will be formed by a central core (a) and by several sub-stations (b) along five spiral arms out to 200 km radius. The summary with the main specifications for the final design of the SKA telescope is shown in Table 3.1. The timeline with the schedule of the project is represented in Fig. 3.3. The construction is scheduled to begin in 2016. Initial observations are projected to begin in 2019. The instrument is intended to be fully operative in 2024. Nowadays, the project is in the phase of "design and costing", in which the research groups are investigating the technologies that will be necessary to fulfill both the technical and cost requirements.

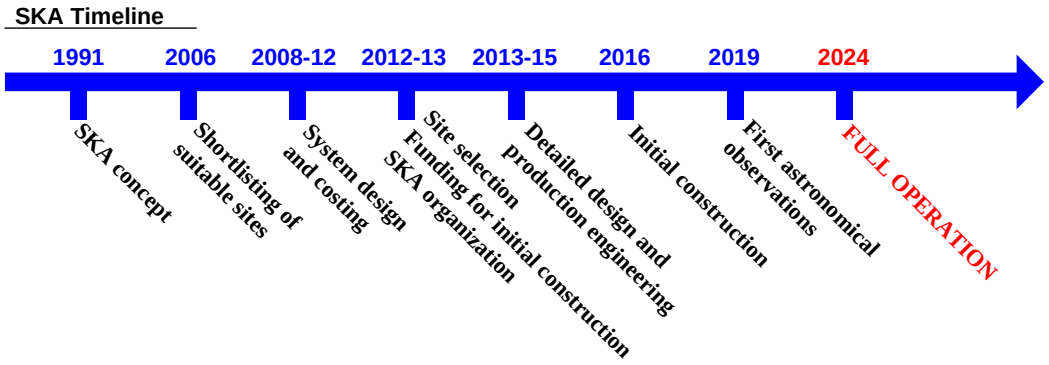

Figure 3.3: SKA project timeline [2].

Table 3.1: Design specifications for the SKA [2].

Parameter	**Specification**
Frequency range	70 MHz to 10 GHz
Sensitivity (area/system temperature)	5000 m^2/K between 70 and 300 MHz 10000 m^2/K between 0.3 and 10 GHz
Survey figure-of-merit	4×10^7 – 2×10^{10} $m^4K^{-2}deg^2$
Field of view	200 deg^2 between 70 and 300 MHz 1–200 deg^2 between 0.3 and 1 GHz 1 deg^2 between 1 and 10 GHz
Angular resolution	<0.1 arcsec
Instantaneous bandwidth	Band center ± 50 %
Spectral frequency channels	16384 per band and per baseline
Calibrated polarization purity	10000:1
Synthesized image dynamic range	>1000000
Imaging processor computation rate	10^{15} operations/sec
Telescope output data rate	1 Tbyte/min (typ.)

In the case of the mid-frequency arrays, the 66 % of the antennas will be placed in the central core, and the rest will be placed along the spiral arms. Above 300 MHz, the sky noise is relatively low and flat, so the system noise temperature is mainly determined by the array's technical performance. Thus, a dense configuration (i.e., distance between elements is shorter than half a wavelength) seems the most adequate choice for the highest dynamic range. Additionally, a dense configuration provides fixed effective aperture across the band, wider beams, faster survey speeds and easier beamforming, and absence of grating lobes. Each mid-frequency aperture sub-array consists of around 75000 dual polarization elements and will have 180 m diameter. The entire telescope will consist of around 250 mid-frequency sub-arrays. The main front-end technical parameter requirements are [14]

- System noise temperature: $\leq$38 K
- Power consumption: $\leq$30 mW/element
- Polarization: double-polarization
- Scan angle: up to $\pm$45 deg

During the recent years, several dense-array demonstrators have been proposed for the mid-frequency band of the SKA. One of the pioneering prototypes was the *THousand Element Array* (THEA) [3], which was developed by ASTRON (Netherlands) in the late 90's. Each THEA tile consisted of 64 Vivaldi antenna elements placed for single linear polarization, and could be used to detect (strong) radio sources in the frequency band from 600 to 1700 MHz. Other recent array designs have also been based on Vivaldi or bunny-ear antenna elements, but providing dual-polarization and avoiding the use of expensive and lossy substrate boards to print the antennas. Some examples are the *Electronic Multi-Beam Radio Astronomy ConcEpt* (EMBRACE) [4], and the *Vivaldi ALuminium ARRaY* (VALARRY) [5], both developed by ASTRON, and the *Bunny Ear Combline Antenna* (BECA) [6], developed by the University of Manchester (UK). Since cost reduction is a key factor in the success of SKA, some very low-cost designs have also been proposed. One example is the *Foil-based LOW-cost PAcman Differential Dual-polarized Demonstrator* (FLOWPAD3) [7], developed by ASTRON. This design consists on Vivaldi-like antennas, in which the radiating elements are printed on a very thin foil of polyester or kapton. In addition, these foils are kept straight by using a cheap foam structure. Apart of TSAs (i.e., Vivaldi or bunny-ear antennas), other types of antenna elements have also been proposed. Some examples are the *Octagon Ring Antennas* (ORA) [8], developed by University of Manchester, or the *checkerboard* array [9] developed as a focal

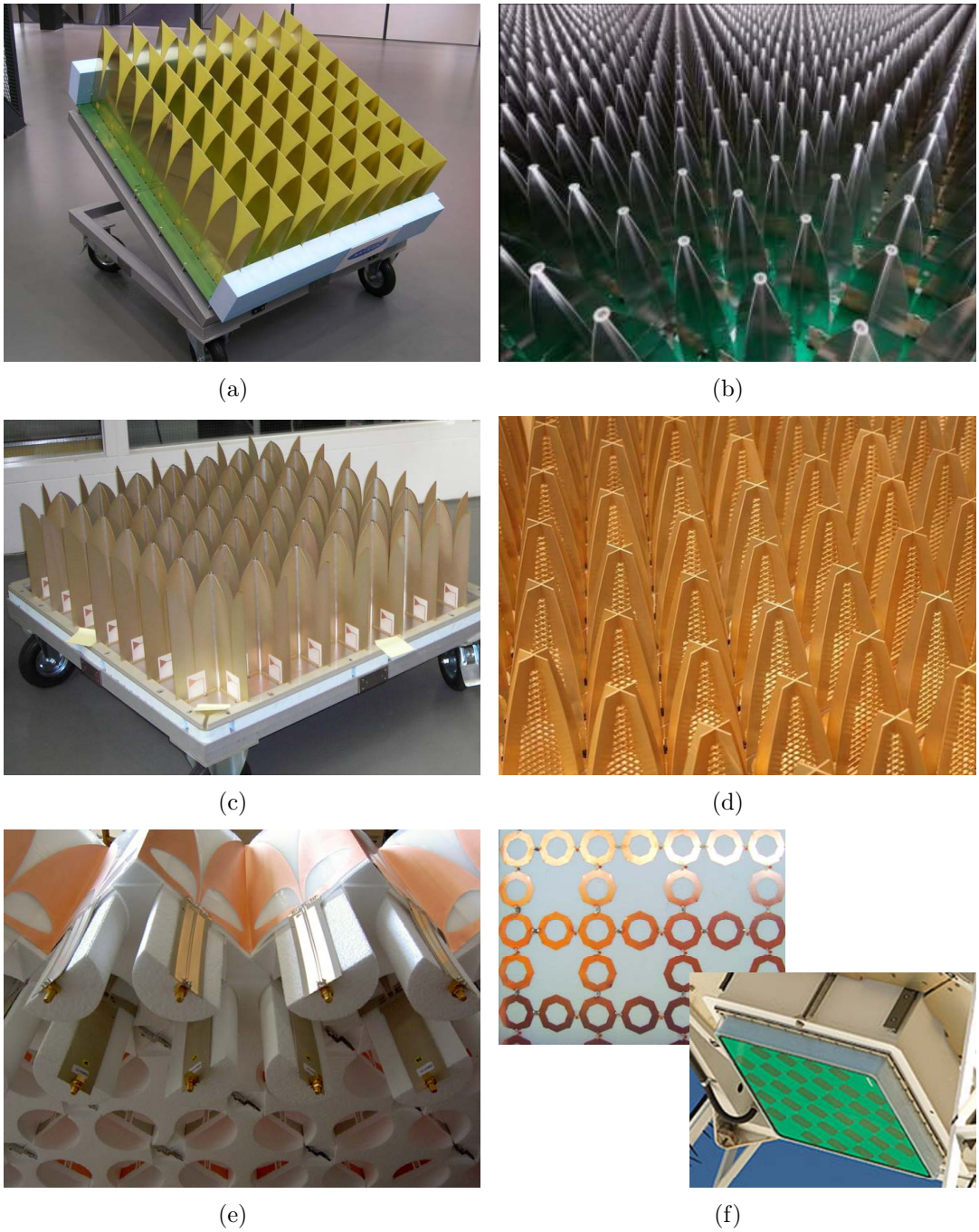

(a) (b)

(c) (d)

(e) (f)

Figure 3.4: Different array prototypes developed for the mid-frequency range of the SKA telescope: (a) THEA [3], (b) EMBRACE [4], (c) VALARRY [5], (d) BECA [6], (e) FLOWPAD3 [7], and (f) ORA [8] and checkerboard [9].

plane array for the *Australian SKA Pathfinder* (ASKAP). The photographs of the manufactured prototypes are shown in Fig. 3.4.

The main characteristics of the dense array demonstrators cited before are listed in Table 3.2. This list presents some logical evolutions in certain aspects of the array design if the newer prototypes are compared with the older ones. The first aspect deals with the array polarization. The primitive THEA prototype provided single linear polarization. Newer prototypes can provide two orthogonal linear polarizations just by placing the antenna elements in a grid configuration. Although some novel antenna designs have been recently proposed (i.e., ORA or *checkerboard* array), TSA elements (i.e., Vivaldi or bunny-ear antennas) are mostly preferred due to their demonstrated good performance in dense array configurations. Another aspect is the balanced-unbalanced nature of the antenna connection, which in turn determines the nature of the LNAs. The intrinsic nature of all the proposed antenna elements is balanced. However, first prototypes used a balancing feeding board (balun) to convert the balanced signal coming from the antenna into a ground-referred (single-ended) signal (i.e., THEA, EMBRACE, VALARRY). Therefore, it allowed using conventional single-ended amplifiers to amplify the signals. This approach has been seen to be inefficient, since the losses of the passive balun directly contribute to increase the system noise temperature. Novel approaches consider a fully-differential front-end, based on a differential

Table 3.2: Main characteristics of some dense array demonstrators for radio-astronomy.

Prototype	**THEA**	**EMBRACE**	**VALARRY**
Antenna type	Vivaldi	Vivaldi	Vivaldi
Polarization	Single	Dual	Dual
Output	Single-ended	Single-ended	Single-ended
Frequency band	600–1700 MHz	400–1500 MHz	600–1500 MHz
Materials	FR4	Metal (antenna) Rogers (feed board)	Metal (antenna) Rogers (feed board)
Nominal impedance	100 Ω	70 Ω	50 Ω
Prototype	**BECA**	**FLOWPAD3**	**ORA**
Antenna type	Bunny-ear	Vivaldi	Ring patches
Polarization	Dual	Dual	Dual
Output	Differential	Differential	Differential
Frequency band	300–1000 MHz	300–1000 MHz	300–1000 MHz
Materials	Metal	Polyester foil	Foil
Nominal impedance	120 Ω	150 Ω	120 Ω

amplifier directly connected to the antenna (i.e., BECA, FLOWPAD3, ORA). One issue to take into account is that the nominal impedance in differential mode for this type of antennas is typically high (i.e., between 100–200 Ω). The final aspect is the cost, which is directly related with the materials and the fabrication process of the antennas. THEA design was based on printed antennas on FR4 substrate boards, due to the easiness of fabrication. Novel designs avoid the use of substrate boards to print the antennas due to their high cost. In contrast, they are directly manufactured in aluminum (i.e., EMBRACE, VALARRY, BECA), or they make use of cheap foils or foam structures (i.e., FLOWPAD3, ORA).

As it was pointed out before, a common feature of all the proposed antenna elements is that they are intrinsically fed with balanced signals (i.e., they are fed by two conductors of the same type, each of which have equal impedances along their lengths and equal impedances to ground and to other circuits). Thus, the use of a differential amplifier directly attached to the antenna seems more adequate to reduce the overall system noise temperature, instead of using a passive balancing circuit and a conventional single-ended amplifier. The results presented in this chapter deals with the research of differential low noise amplifier structures at different levels: design, measurement, and active array integration. Apart of the hypothetical use of differential amplifying circuits, SKA presents several additional challenges for the design of the LNAs:

- **Low noise temperature**: The final goal for the mid-frequency band of SKA is to achieve less than 38 K system noise temperature. Considering the contributions of the sky, antenna connections, spillover, etc., the noise contribution of the LNA alone should be better than 25–30 K.
- **Broadband performance**: Mid-frequency range of SKA implies a 3.3:1 relative bandwidth (i.e., 300-1000 MHz).
- **Cooling**: Unlike in conventional single-dish radio-telescopes, in which cryostats are used to reduce the physical temperature of the receiver (typically ≈20 K), SKA does not consider the use of cooling systems due to the huge number of receivers. Therefore, LNAs are assumed to operate at room temperature (i.e., 290 K), with the consequent poorer noise performance.
- **Antenna impedance**: Due to the broadband performance of the array, the matching condition for the antenna elements can be relaxed up to VSWR<2.5. It implies a relatively wide antenna impedance range over the Smith chart in which the LNA should provide the desired low noise performance. In addition, due to the mutual coupling, the active antenna impedance[1] provided by each element will depend on the current scanning

[1]The *active impedance* concept will be defined in Section 3.2.

angle of the array. Finally, the reference impedance of the TSAs is typically different from 50 Ω, which should be considered for the LNA design.

3.2 Characterization of Dense Antenna Arrays

3.2.1 Classical antenna array theory

In some applications it is required the use of highly directive antennas. This can be accomplished by increasing the size of the antenna. In radio-astronomy, it has been typically achieved by using larger parabolic dish antennas. Another way to achieve high directivity, without necessarily increasing the size of the individual elements, is to form an assembly of multiple radiating elements (i.e., antenna array). The latter approach is the one proposed for the SKA telescope implementation. Apart of high directivity, the use of antenna arrays in radio-astronomy provides several additional advantages compared with classical dish antennas, such as electronic beam-scanning (instead of mechanical one) or the possibility of using multiple beams scanning the sky simultaneously.

The classical approach in the analysis of antenna arrays consists on assuming independent antenna elements. We can consider the case of a linear array formed by N identical isotropic elements, with a separation d between adjacent elements. This scenario is represented in Fig. 3.5. Assuming a far-field source emitting a signal $s(t)$ impinging on the array with an inclination angle θ, the signal received

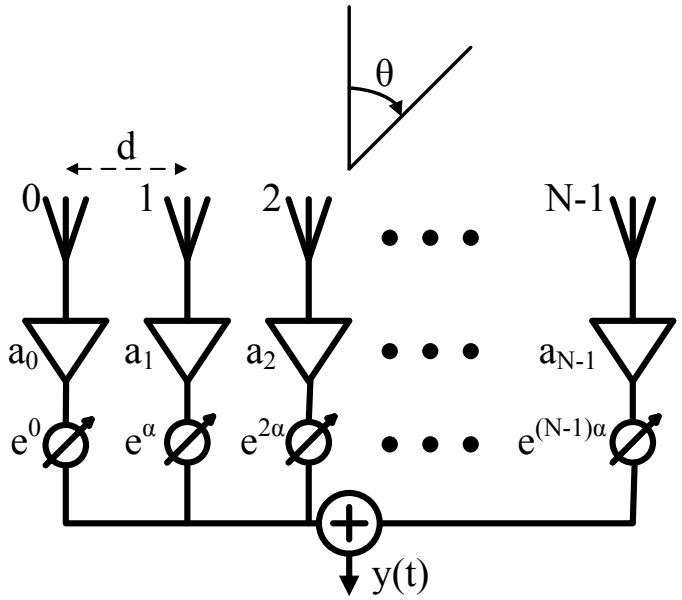

Figure 3.5: General scheme of a N-elements antenna array.

by the n-th element in the array is proportional to

$$x_n(t) = s(t)\frac{e^{-jkr_n}}{r_n}$$

where k is the wave number ($k = 2\pi/\lambda$), λ is the the free space wavelength, and r_n is the distance between the source and the n-th element. In the array structure, the signals coming from the antenna elements are weighted by a (real) amplitude factor a_n and by a phase delay $n\alpha$, where n is the index of each element. Therefore, the output signal $y(t)$ is obtained as the weighted combination of the incoming signals $x_n(t)$ as

$$y(t) = \sum_{n=0}^{N-1} a_n e^{-j\alpha n} x_n(t)$$

The difference of paths between the source and two adjacent elements can be obtained as

$$|r_n - r_{n+1}| = d\,sin(\theta)$$

If the source is far enough, it can be assumed that the previous difference of paths only affects to the phase difference between the signals arriving to different elements, but its effect can be neglected in terms of amplitude. Thus, the output signal can be written as

$$y(t) = \frac{s(t)}{D}\sum_{n=0}^{N-1} a_n e^{-jn(kd\,sin(\theta)+\alpha)}$$

where D is the average distance between source and the array. In the case of real antenna elements, the far-field radiation pattern of the array is given by

$$E(\theta) = E_0(\theta)AF(\theta) \tag{3.1}$$

where E_0 is the far-field radiation pattern of the isolated element and $AF(\theta)$ is the array factor. The array factor AF is obtained as

$$AF(\theta) = \sum_{n=0}^{N-1} a_n e^{-jn(kd\,sin(\theta)+\alpha)} = \sum_{n=0}^{N-1} a_n e^{-jn\Psi} \tag{3.2}$$

where $\Psi = kdsin(\theta)+\alpha$. The term Ψ represents the phase correction for adjacent antennas.

Regarding to (3.2), it can be seen that the radiation pattern of the array independently depends on both the radiation pattern of the isolated antenna

element and the array factor of the structure. It should be noticed that, in the ideal case of using isotropic elements, the radiation pattern of the array and the array factor coincide. When the array is uniformly excited in amplitude (i.e., $a_n = a_0$, $\forall n$), the weight factor can be taken out from the sum, resulting in

$$AF(\Psi) = a_0 \sum_{n=0}^{N-1} e^{-jn\Psi}$$

The absolute value of the previous expression can be written as

$$|AF(\Psi)| = a_0 \frac{sin(N\Psi/2)}{sin(\Psi/2)}$$

The maximum of $|AF(\Psi)|$ in the case of uniform excitation is given when $\Psi = 0$ and the maximum value is $|AF|_{max} = a_0 N$. Last result shows how the directivity of the antenna array is directly proportional to the number of elements N.

3.2.2 Mutual coupling in antenna arrays

In the previous analysis it was seen how the radiation pattern of an antenna array depended on both, the radiation pattern of the individual elements and on the array topology itself (3.1). For this analysis, it was assumed that the individual elements were perfectly matched to the corresponding reference impedance, and therefore the return losses in the antennas were not considered. The non-ideal antenna impedance matching can be considered as a factor that reduces the power transmitted/received by the array. This factor is the return loss, which can be calculated as

$$RL = 1 - |\Gamma_{ant}|^2 = 1 - \left| \frac{Z_{ant} - Z_0}{Z_{ant} + Z_0} \right|^2 \tag{3.3}$$

where Γ_{ant} is the reflection coefficient of the antenna, Z_{ant} is the (complex) input impedance of the antenna, and Z_0 is the corresponding reference impedance. For the case of an array with isolated elements (i.e., there is no power transfer between the antennas), the antenna impedance Z_{ant} coincides with the impedance provided by the isolated elements. Thus, the RL factor corresponds to the power reflected in each antenna element with independence of the scanning angle, so the normalized radiation pattern of the array is not affected by the antenna impedance matching.

For any practical array, mutual coupling between elements is present. This effect is, in general, undesired and several techniques to reduce the power transfer between elements have been proposed in the literature (e.g., [29]). The advantage when mutual coupling is negligible is that the antenna elements can be

independently designed. The philosophy in the SKA is the opposite, since the high density of antennas (and therefore the high mutual coupling) facilitates the broadband performance of the array, the beamforming and the absence of grating lobes. However, as it will be shown below, mutual coupling in the antenna arrays should be carefully taken into account.

The easiest way to illustrate how the mutual coupling mechanism affects to the array performance is by analyzing the simple case of a two-element array [30]. With regard to the scheme that is shown in Fig. 3.6(a), let us assume that the two amplifiers are identical and are perfectly matched to Z_0 (i.e., $s_{11}^{LNA} = 0$). Otherwise, if $s_{11}^{LNA} \neq 0$, the (complex) reference impedance has to be adjusted such that s_{11}^{LNA} becomes zero. The same reference impedance Z_0 is used for all the S-parameters matrices. We can model the noise of the amplifiers by two correlated noise waves that are propagated from the input and output of the amplifier (i.e., c_1 and c_2 respectively in Fig. 3.6(a)) [31]. Thus, these two waves propagates to the output of the array and are combined as

$$\begin{aligned} c_{tot} &= \text{direct part} + \text{reflected part} + \text{coupled part} \\ &= c_2 e^{j\varphi_1} + c_1 s_{11}^{ant} s_{21}^{LNA} e^{j\varphi_1} + c_1 s_{21}^{ant} s_{21}^{LNA} e^{j\varphi_2} \\ &= c_2 e^{j\varphi_1} + c_1 s_{21}^{LNA} (s_{11}^{ant} e^{j\varphi_1} + s_{21}^{LNA} e^{j\varphi_2}) \\ &= c_2 e^{j\varphi_1} + c_1 s_{21}^{LNA} \Gamma_{act}^1 \end{aligned} \tag{3.4}$$

where $\Gamma_{act}^1 = s_{11}^{ant} e^{j\varphi_1} + s_{21}^{LNA} e^{j\varphi_2}$ denotes the *active reflection coefficient* [32],[33] of the first antenna element. In general, the active reflection coefficient of the n-th element of an N-element array can be obtained, with the same reasoning, as

$$\Gamma_{act}^n = \sum_{m=1}^{N} s_{mn}^{ant} e^{j(\varphi_m - \varphi_n)} \tag{3.5}$$

where the elements of the array are numbered from 1 to N, and φ_i denotes the phase delay of the i-th channel. As with any conventional reflection coefficient, it is possible to obtain an equivalent value in terms of impedance. This parameter is known as *active antenna impedance* and can be calculated as

$$Z_{act}^n = \frac{{Z_0}^* + Z_0 \Gamma_{act}^n}{1 - \Gamma_{act}^n} \tag{3.6}$$

where Z_0 denotes the (complex) reference impedance. For the particular case of non-coupled elements, this value coincides with the input impedance of the isolated element.

By using the result in (3.5), it is possible to obtain an equivalent representation of the array in which the elements are decoupled, as it is represented in

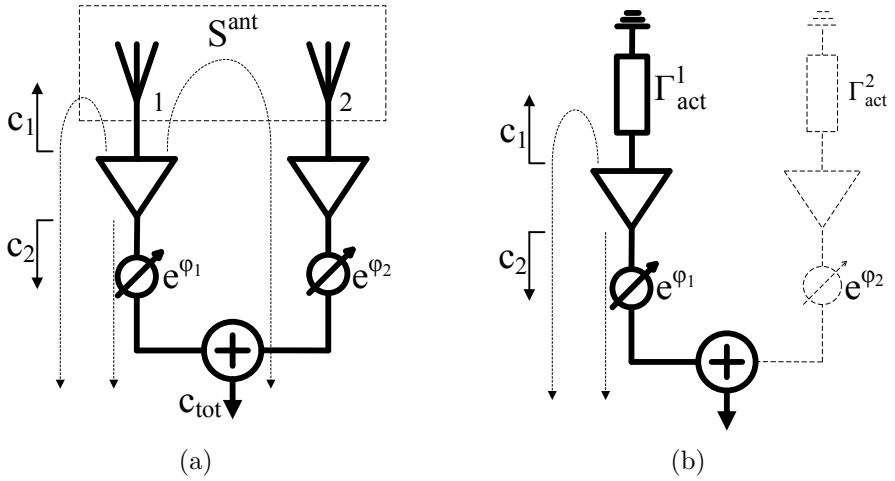

Figure 3.6: General scheme of a two-element array (a), and equivalent representation using the *active reflection coefficient* concept (b).

Fig. 3.6(b). This equivalent representation basically consists on transforming the S-parameters matrix of the antenna structure into a diagonal matrix with the respective active reflection coefficients in the diagonal. The case in which there is no coupling between elements (i.e., $s_{ji}^{ant} = 0$, $\forall\, j, i \in [1, N]$ and $j \neq i$) is a particular case in which the active reflection coefficients are directly given by $|\Gamma_{act}^{i}| = |s_{ii}^{ant}|$.

The active reflection coefficient in arrays presents some peculiarities compared with the conventional reflection coefficient of a single antenna. In the case of an antenna array with mutual coupling, the return losses of each antenna element depends on the phase delays φ_i and, therefore, on the scanning angle θ of the array. Thus, the radiated power of each antenna element at different scanning angles is weighted by the scanning-dependent element return losses. Also, the presence of scanning angles at which the radiated power can fall to zero is feasible [32]. In the case of infinite arrays, in which the active impedance of every element is identical, this effect is known as *scan blindness* and is given at the angles θ at which $|\Gamma_{ant}(\theta)| = |\Gamma_{act}(\theta)| = 1$.

Another important aspect is the noise performance of the amplifiers connected to the antennas. For single-antenna receivers, the noise performance of a given amplifier design depends on the source impedance condition that, in this case, is directly provided by the input antenna impedance (i.e., $Z_S = Z_{ant}$ in (1.11)). In arrays, the source impedance condition in each channel is provided by the corresponding Z_{act}^{i}, and the noise performance of the system is minimized by achieving the optimal noise performance in each channel (i.e., $Z_{opt}^{LNA_i} = Z_{act}^{i}$),

where i is the index of the channel. Since Z_{act}^{i} is scanning-dependent, the noise performance of the receiving array will also depend on the corresponding scanning angle. It makes difficult to obtain the minimum noise temperature for a range of scanning angles, since it is not possible to match the varying scanning-dependent active impedance with the unique optimum impedance of the LNAs (at a given frequency). Thus, the challenge is to design the radiating structure to provide reasonably well-matched elements for a given range of scan angles and, later, optimize the amplifier for the average antenna element impedance. The SKA requirements need to go further since it is necessary to achieve these conditions in a broad range of frequencies.

3.2.3 Impedance mismatching effects

The trade-off between low input return losses and low noise temperature is a well known limitation in the design of LNAs. For some designs, with strong requirements in terms of noise, obtaining a noise performance close to the optimum is only feasible at a price of increasing the impedance mismatching factor between the antenna and the amplifier. In the case of broadband LNAs working from some hundreds of MHz, many of the designs proposed in the literature present poor input reflection coefficients, mainly due to the high input impedance provided by the FETs in this frequency range [34],[35].

Concerning the previous analysis, the active reflection coefficient provided by certain element in an array structure is obtained as a function of the coupling coefficients between this element and the others (3.5). However, the power coupled between the different elements depends on the loading conditions of the array which, in this case, are provided by the LNA input impedances. This may become a limitation, since LNAs with extreme input impedance values can mismatch the active antenna impedances and, in turn, degrade the system noise performance.

Equation (3.5) provides an expression to calculate the active reflection coefficient of certain array element from the S-parameters matrix of the radiating structure. One of the conditions under which this expression is valid is that s_{11}^{LNA}=0 [30]. Otherwise, the S-parameters of the antenna structure should be taken from a renormalized matrix using a reference impedance equal to the LNA input impedance. For a more illustrative explanation, let us consider the simple case of a two element antenna array. From (3.5), the active reflection coefficient of the first antenna can be obtained as

$$\Gamma_{act}^{1} = s_{11}^{ant}{}_{(Z_0=Z_{in}^{LNA})} + s_{21}^{ant}{}_{(Z_0=Z_{in}^{LNA})} e^{j(\varphi_2-\varphi_1)} \tag{3.7}$$

where the terms s_{ij}^{ant} denotes the terms from the S-parameters matrix of the antenna with a reference impedance Z_0 equal to the input impedance of the

LNAs Z_{in}^{LNA}. In order to explicitly show the dependence of the active antenna impedance with respect to the LNA input impedance, (3.7) can be written in terms of impedance parameters Z^{ant} (whose matrix is unique, since it is not normalized by the port impedances), just by applying a simple parameter-matrix conversion [36]

$$\Gamma_{act}^{1} = \frac{(z_{11}^{ant} - Z_{in}^{LNA})(z_{22}^{ant} + Z_{in}^{LNA}) - z_{12}^{ant} z_{21}^{ant} + 2 z_{21}^{ant} Z_{in}^{LNA} e^{j(\varphi_2 - \varphi_1)}}{(z_{11}^{ant} + Z_{in}^{LNA})(z_{22}^{ant} + Z_{in}^{LNA}) - z_{12}^{ant} z_{21}^{ant}} \tag{3.8}$$

By using (3.6), it is possible to obtain the expression of the corresponding active antenna impedance of the first antenna in a two-element array as

$$Z_{act}^{1} = \frac{(z_{11}^{ant})^2 + z_{11}^{ant} Z_{in}^{LNA} - (z_{21}^{ant})^2 + z_{21}^{ant} Z_{in}^{LNA} e^{j(\varphi_2 - \varphi_1)}}{Z_{in}^{LNA} + z_{11}^{ant} + z_{21}^{ant} e^{j(\varphi_2 - \varphi_1)}} \tag{3.9}$$

The previous result explicitly shows that the active antenna impedance provided from the first port of a two element array depends on the physical parameters of the array (i.e., Z^{ant}) and on the amplifier input impedance (i.e., Z_{in}^{LNA}).

An equivalent expression for Z_{act}, but for the general case of an N-element array is given in [37]. This expression can be written in vector notation as

$$Z_{act}^{n} = \frac{\mathbf{i_{\bullet n}}^{T} \mathbf{Z^{ant}} (\mathbf{Z^{ant}} + Z_{in}^{LNA} \mathbf{I})^{-1} \mathbf{w}}{\mathbf{i_{\bullet n}}^{T} (\mathbf{Z^{ant}} + Z_{in}^{LNA} \mathbf{I})^{-1} \mathbf{w}} \tag{3.10}$$

where Z_{act}^{n} is the active antenna impedance of the n-th element in the array, Z_{in}^{LNA} is the LNA input impedance, $\mathbf{Z^{ant}}$ is the NxN impedance matrix of the antenna structure, $\mathbf{I}$ is the NxN identity matrix, $\mathbf{i_{\bullet n}}$ is the n-th column-vector of the identity matrix (i.e., all-zero vector except a 1 in position n), and $\mathbf{w}$ is the beam-forming vector (i.e., $\mathbf{w} = [0 \ \alpha \ 2\alpha \ ... \ (N-1)\alpha]^T$ in the scheme shown in Fig. 3.5). From (3.10), it can be see again that the active antenna impedance of the different array elements depends on the input impedance of the amplifiers.

For the trivial case of a single-antenna receiver, the antenna impedance is directly given by

$$Z_{act(N=1)}^{1} = z_{11}^{ant} \tag{3.11}$$

which only depends on the geometry of the antenna. Thus, any LNA connected to the antenna has the same source impedance condition Z_S. Consequently, if two amplifiers with the same set of noise parameters (i.e., F_{min}, Z_{opt} and R_n) are connected to an antenna, the noise performance of both amplifiers will be identical, with independence on their input impedances (Fig. 3.7(a)). This analysis is equivalent for the case of an ideal array without mutual coupling, and it could be a valid approximation when the coupling coefficients are low in module.

Another case of interest is the infinite array configuration. This approximation is particularly interesting, since it is commonly used to estimate the performance of very large arrays with low computational cost. Since every element in an infinite array of identical elements has the same boundary conditions, the problem can be reduced to the analysis of a single antenna element with periodic boundary conditions. This approximation is well-known since many decades ago (i.e., waveguide simulators [38],[39]), and it is commonly available in modern electromagnetic software. Thus, this situation is equivalent to the single-antenna case and, therefore, the active antenna impedance of an infinite array is also independent of the loading conditions. As in the previous case, two amplifiers with the same set of noise parameters connected to an infinite array provide the same system noise temperature (Fig. 3.7(b)).

For the general case of an N-element array, two amplifiers with different input impedances will see different source impedance conditions from a given array element, as it is expressed in (3.10). Therefore, even if they have the same set of noise parameters their noise contribution will be different (Fig. 3.7(c)). In the case of a single-antenna receiver, the amplifier can be optimized in terms of noise for a given antenna impedance that can be assumed to be constant at a given frequency. However, the dependence of the active antenna impedance of the array elements with respect to the LNA input impedance gives an additional difficulty in the design process, since any modification in the LNA design can affect the antenna impedance and, therefore, the source matching condition under which the noise performance is calculated.

Modeling the mutual coupling between two antenna elements is complicated, and usually requires the use of electromagnetic simulators. Nevertheless, there are some canonical expressions developed in the literature. In [40], an analytical expression of the mutual impedance between two dipoles is given. This expression has been used to easily calculate the performance of an array of dipoles, with an arbitrary number of elements. More concretely, the characterization of an array of half-wavelength ($\lambda/2$) dipoles with different LNA conditions has been undertaken, in order to illustrate the effect of the impedance mismatching between the array elements and the amplifiers. The simulated results are shown in Fig. 3.8. Firstly, the performance of the center element of the array has been studied. The array configuration is shown in Fig. 3.8(a). The array consists of $2N + 1$ parallel $\lambda/2$ dipoles, with separation of 0.2λ between adjacent elements. The Z-matrix of the structure has been calculated by using the expressions provided in [40]. The corresponding antenna impedance has been obtained using (3.10). The active antenna impedance of the center element, as a function of the dimension of the array, and for two different LNA input impedances (i.e., 50 Ω and 300 Ω, assuming that the LNA output is matched to Z_0) is shown in Fig. 3.8(c). It can be observed

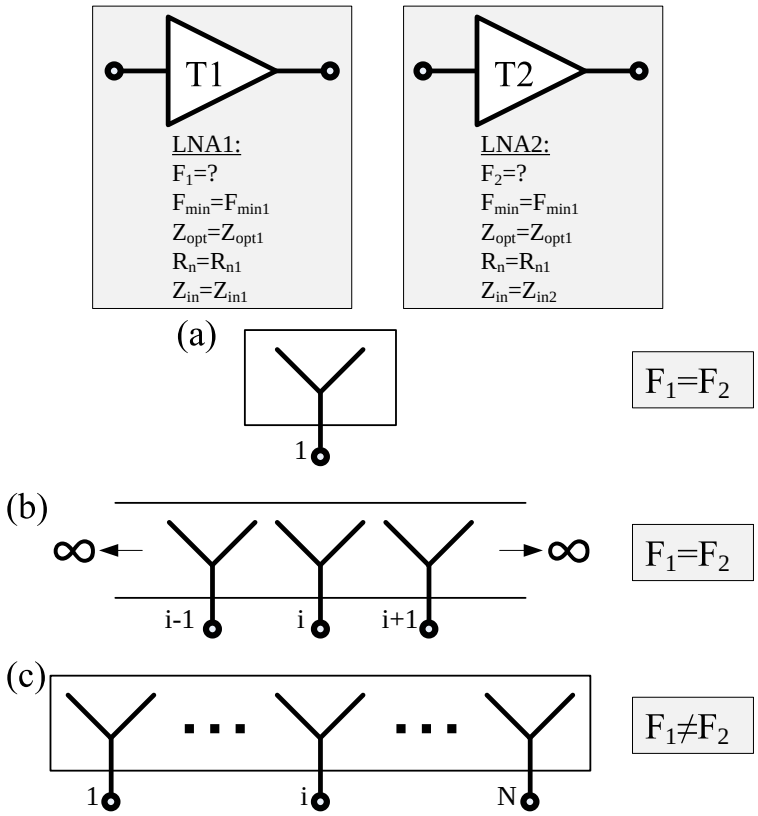

Figure 3.7: Noise performance of two LNA designs, with equal set of noise parameters (F_{min}, Z_{opt} and R_n) but different input impedances Z_{in}, in different receiving array configurations: (a) single-antenna, (b) infinite array, and (c) N-element array.

that, for low number of elements, the active impedance of the center element is greatly affected by the LNA impedance (as expected from (3.10)). However, as the array becomes larger, the active impedance converges to a unique value, which corresponds with the active antenna impedance that could be obtained from the infinite array simulation. Thus, in large enough arrays, the active antenna impedance of the center element can be considered as a fixed value (for a given scan condition), as it occurs in single-antenna receivers, since the effect of the LNA impedance decreases with the array dimension. This result seems logical since, as it was stated before, the analysis of the infinite array case is somehow equivalent to the analysis of a single antenna.

Once the case of the center element has been analyzed, the next point of interest is to analyze the behavior of the edge elements. The array scheme used in this case is shown in Fig. 3.8(b). It consists of $N+1$ parallel $\lambda/2$ dipoles, with

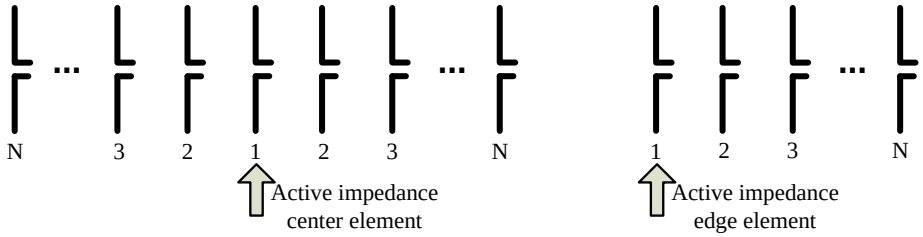

(a) (b)

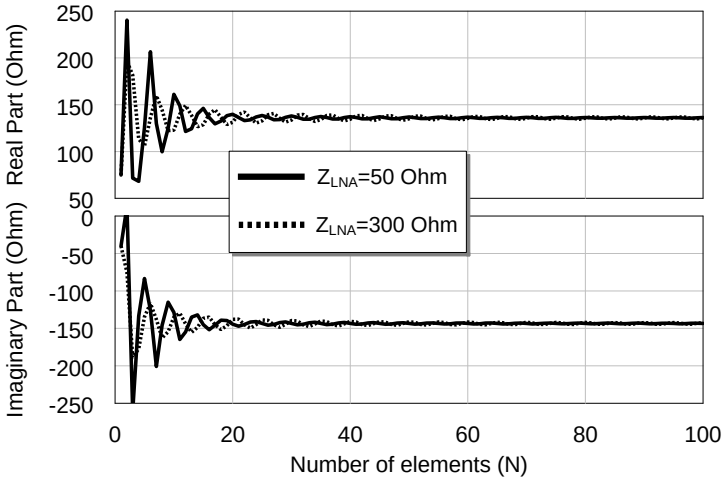

(c)

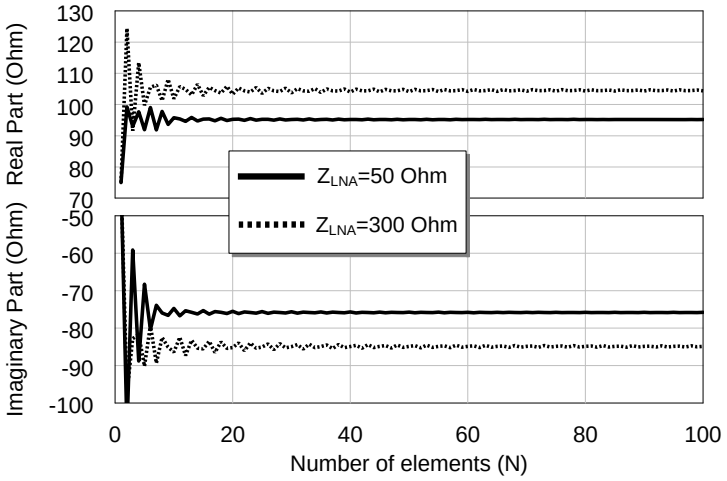

(d)

Figure 3.8: Array configuration and active antenna impedance characterization of the center (a)(c) and edge (b)(d) elements of an array of parallel dipoles, for two different LNA input impedances.

separation of 0.2λ between adjacent elements. As in the previous case, the active antenna impedance of the edge element has been obtained for two different LNA impedances. The results are shown in Fig. 3.8(d). It can be seen that, in this case, the active impedance completely depends on the LNA impedance, and the curves converge to different values when the number of elements is large. Unlike in the case of the center elements, whose dependence on the loading conditions (i.e., Z_{in}^{LNA}) is mitigated in large structures, the active antenna impedance for the edge elements is different for different realizations of the LNA, even in large array structures.

For the case of large array implementations, such as the mid-frequency SKA stations, some interesting conclusions can be extracted from the previous analysis. Since most antennas in large arrays are inner elements, the infinite array approach can be a good approximation to model the performance of the radiating structure. Furthermore, this model is independent from the LNA design, and the obtained active antenna impedance can be used as a fixed source impedance condition to optimize the LNA designs. Such design procedure has been the one used in the design of the differential LNAs presented in the subsequent sections.

In practice, any array implementation has edge elements, which will unavoidably provide different impedances than the inner elements. It usually degrades the system noise performance, since the LNAs (optimized for the center elements) in the edge channels are not properly matched to this different antenna condition. Before implementing the complete array, it can be important to quantify how much these edge elements degrade the overall system performance. In order to answer the previous question, the impedance mismatching factor of such edge elements (which is usually difficult to estimate, since it requires an analysis of the whole array structure) has to be known. In any case, the hypothetical analysis of the edge effects is fully conditioned by the amplifier, and needs to consider a precise LNA implementation.

3.3 Characterization of Differential Amplifiers at Microwave Frequencies

The measurement of differential devices is not as obvious as the measurement of single ended ones since they require some specific methods [19]. The use of the so-called mixed-mode S-parameters instead of the conventional ones has served to obtain a direct, and therefore more practical, interpretation of differential devices driven by differential/common-mode excitations. On the other hand, for the measurement of the differential noise figure several methods have been proposed [18],[20],[24],[26] although it is still an open problem. This section presents a summary of such differential measurement methods, including gain, noise and source-pull characterizations.

3.3.1 S-parameters characterization

3.3.1.1 Mixed-mode S-parameters theory

Scattering parameters or power-wave analysis tools have been a tremendous aid in designing linear two-port amplifiers. Although differential amplifiers are four-port devices, they can be seen as an equivalent two-port amplifier driven by common/differential-mode input/output signals. Thus, a specific interpretation of the conventional S-parameters is needed to characterize this type of differential circuits. This interpretation are the so-called mixed-mode S-parameters [16].

For the case of a four-port circuit, the conventional (i.e., single-ended) S-parameter matrix relation is defined as

$$\begin{bmatrix} b_1 \\ b_2 \\ b_3 \\ b_4 \end{bmatrix} = \begin{bmatrix} s_{11} & s_{12} & s_{13} & s_{14} \\ s_{21} & s_{22} & s_{23} & s_{24} \\ s_{31} & s_{32} & s_{33} & s_{34} \\ s_{41} & s_{42} & s_{43} & s_{44} \end{bmatrix} \begin{bmatrix} a_1 \\ a_2 \\ a_3 \\ a_4 \end{bmatrix} \tag{3.12}$$

The last expression can also be written in vector notation as $\bar{b} = [S]\bar{a}$, where $[S]$ is the four-port S-parameters matrix and $\bar{b}$ and $\bar{a}$ are the reflected and input power wave vectors at the four ports. The expression in (3.12) can be expanded into algebraic relations as

$$\begin{aligned} b_1 &= s_{11}a_1 + s_{12}a_2 + s_{13}a_3 + s_{14}a_4 \\ b_2 &= s_{21}a_1 + s_{22}a_2 + s_{23}a_3 + s_{24}a_4 \\ b_3 &= s_{31}a_1 + s_{32}a_2 + s_{33}a_3 + s_{34}a_4 \\ b_4 &= s_{41}a_1 + s_{42}a_2 + s_{43}a_3 + s_{44}a_4 \end{aligned} \tag{3.13}$$

From (3.12) and (3.13), the individual S-parameter matrix elements can be calculated or measured under the following conditions

$$s_{xy} = \left.\frac{b_x}{a_y}\right|_{a_{i\neq y}=0} \tag{3.14}$$

For the case of using mixed-mode power-waves, the same relationships can be used to develop the mixed mode S-parameters as

$$\begin{bmatrix} b_{d1} \\ b_{d2} \\ b_{c1} \\ b_{c2} \end{bmatrix} = \begin{bmatrix} s_{dd11} & s_{dd12} & s_{dc11} & s_{14} \\ s_{dd21} & s_{dd22} & s_{dc21} & s_{dc22} \\ s_{cd21} & s_{cd12} & s_{cc11} & s_{cc12} \\ s_{cd21} & s_{cd22} & s_{cc21} & s_{cc22} \end{bmatrix} \begin{bmatrix} a_{d1} \\ a_{d2} \\ a_{c1} \\ a_{c2} \end{bmatrix} \tag{3.15}$$

or in algebraic notation as

$$\begin{aligned} b_{d1} &= s_{dd11}a_{d1} + s_{dd12}a_{d2} + s_{dc11}a_{c1} + s_{dc12}a_{c2} \\ b_{d2} &= s_{dd21}a_{d1} + s_{dd22}a_{d2} + s_{dc21}a_{c1} + s_{dc22}a_{c2} \\ b_{c1} &= s_{cd11}a_{d1} + s_{cd12}a_{d2} + s_{cc11}a_{c1} + s_{cc12}a_{c2} \\ b_{c2} &= s_{cd21}a_{d1} + s_{cd22}a_{d2} + s_{cc21}a_{c1} + s_{cc22}a_{c2} \end{aligned} \tag{3.16}$$

The subscript naming convention in this case is

$$s_{m_o m_i p_o p_i} = s_{(output-mode)(input-mode)(output-port)(input-port)} \tag{3.17}$$

where the modes can be common (c) or differential (d). The common mode corresponds with the case in which two signals with equal magnitude and phase travels along a two-conductor system. In a differential-mode system, two signals with equal magnitude but opposite phase relative to reference ground potential are transmitted along a pair of conductors. In the ideal differential circuit, the ground is not the path for the return signal currents, as it occurs in single-ended systems. In the differential case, the reference ground terminal is ideally at a constant midpotential level between the voltage potential associated with the differential input signal. Finally, it must be remarked that any arbitrary signal transmitted along two conductors can be represented as a combination of both purely common and differential-mode signals.

The difference between the conventional (single-ended) S-parameters and the mixed-mode S-parameters is illustrated in Fig. 3.9. This figure represents the excitations needed to obtain the first column of the corresponding S-parameter matrices in a differential amplifier. For the case of the conventional S-parameters (Fig. 3.9(a)), an incident power wave a_1 is applied to port 1, and four output power waves are generated from the four ports (i.e., b_1, b_2, b_3 and b_4). In this

case, all the single-ended ports are defined with respect to a common ground. On the other hand, for the mixed-mode parameters (Fig. 3.9(b)) an equivalent two-port representation of the circuit has been obtained. This representation is more coherent for an amplifier, since it usually provides amplification between an input and an output port. The mixed-mode input port is now defined as a signal sum or difference of signals between the single-ended ports 1 and 2, depending on the excitation mode (common or differential). Equivalently, the output port is defined between the single-ended ports 3 and 4. In the example of the figure, a differential-mode incident power wave a_{d1} is applied at mixed-mode port 1, and four reflected waves are generated (i.e., b_{d1}, b_{c1}, b_{d2} and b_{c2}).

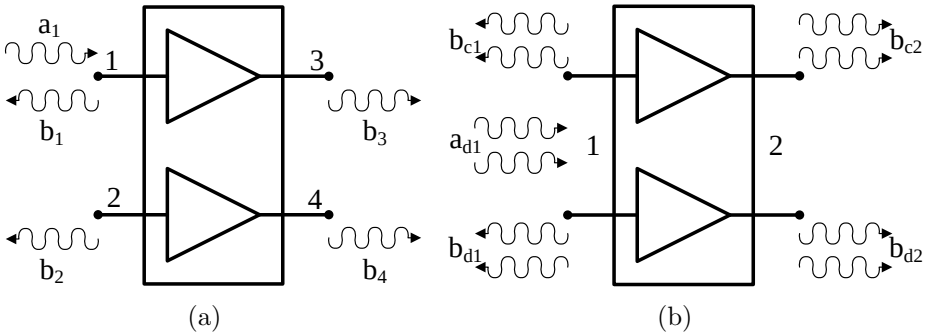

Figure 3.9: Representation of a four-port circuit driven by single-ended (a) and mixed-mode (b) excitations.

As it was seen in (3.15), the mixed-mode S-parameters matrix of a four-port device contains 16 terms. This matrix can be divided into four 2x2 sub-matrices as

$$\left[\begin{array}{cc|cc} s_{dd11} & s_{dd12} & s_{dc11} & s_{dc12} \\ s_{dd21} & s_{dd22} & s_{dc21} & s_{dc22} \\ \hline s_{cd21} & s_{cd12} & s_{cc11} & s_{cc12} \\ s_{cd21} & s_{cd22} & s_{cc21} & s_{cc22} \end{array}\right] = \left[\begin{array}{cc} S_{dd} & S_{dc} \\ S_{cd} & S_{cc} \end{array}\right] \tag{3.18}$$

in which each sub-matrix represents the parameters of the equivalent two-port representation of the circuit for common/differential-mode input/output excitations. This is illustrated in Fig. 3.10 by means of a differential amplifier. The cross-mode terms (i.e., S_{dc} and S_{cd}) would be zero for an ideal differential amplifier. The differential-to-differential sub-matrix S_{dd} represents the conventional performance of the amplifier, and gives the parameters of interest in most cases. The common-to-common matrix S_{cc} depends on the topology of the differential amplifier.

There exist two classical differential amplifier implementations: balanced and fully-differential [15]. The balanced configuration consists on two separated am-

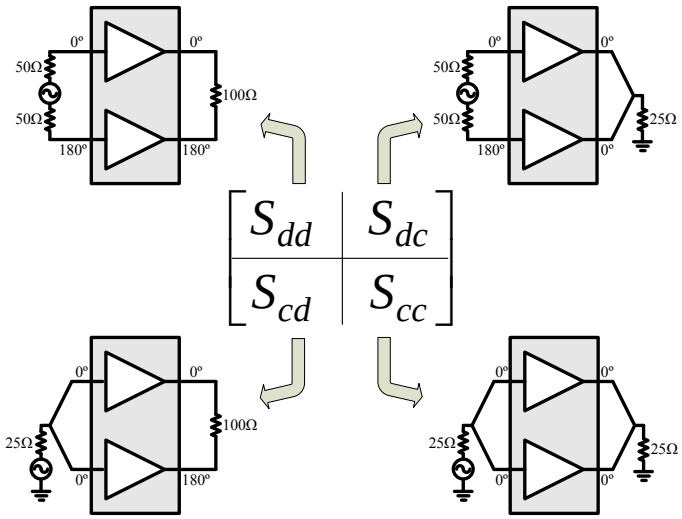

Figure 3.10: Partitioned mixed-mode S-parameter matrix.

plifiers that are independent and identical (Fig. 3.11(a)). The fully-differential amplifier or differential pair consists on two amplifying devices with a common bias current sink or source (Fig. 3.11(b)). Both implementations are feasible for RF or microwave applications and mixed-mode S-parameter tools can evaluate both implementations. For both cases, the differential-mode gain $|s_{dd21}|$ is the same, and corresponds to the gain of each individual single-ended amplifier A. The basic difference between the two differential amplifier implementations is the common-mode gain $|s_{cc21}|$. For the balanced amplifier, the common-mode gain and the differential gain are equal, i.e., $|s_{dd21}| = |s_{cc21}| = A$. For the case of the fully-differential amplifier, the common-mode gain is zero, i.e., $|s_{cc21}| = 0$. In the differential-to-differential model of the fully-differential amplifier, the common-emitter node acts as a virtual ground, and the input signal is amplified at the output. However, in the common-to-common model, the common-emitter node acts as an open circuit or high-impedance and the input signal is not propagated to the output. The relationship between both gains is known as common-mode rejection ratio (CMRR), and it is a standard differential amplifier parameter which indicates how much of the common-mode signal (e.g., interferences) will appear at the output of the amplifier. The CMRR can be obtained from

$$\text{CMRR(dB)} = 20log\left(\frac{|s_{dd21}|}{|s_{cc21}|}\right) \tag{3.19}$$

It must be noted that the CMRR of the ideal balanced design is equal to 0 dB, since it exhibits equal common-mode and differential-mode gains. For the case of the fully-differential amplifier, CMRR is ideally infinite. In practice, this value is

finite, and it is desirable to obtain a high value to mitigate as much as possible all the undesirable common-mode signals.

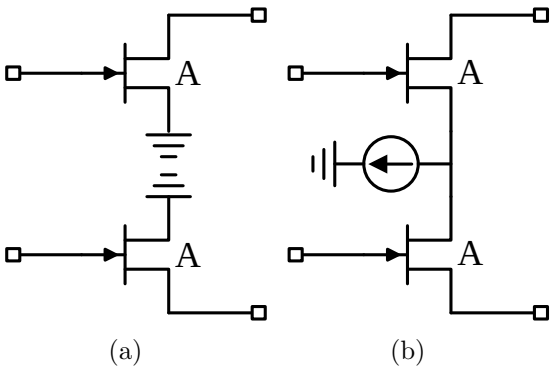

Figure 3.11: Simplified schematic of a balanced (a) and a fully-differential (b) amplifier.

Mixed-mode S-parameters are not restricted only for differential amplifiers. They can also be used to characterize power combiners or baluns. The mixed-mode S-parameters matrix of the three-port power combiner shown in Fig. 3.12 can be written as

$$[S] = \begin{bmatrix} s_{ss11} & s_{sd12} & s_{sc12} \\ s_{ds21} & s_{dd22} & s_{dc22} \\ s_{cs21} & s_{cd22} & s_{cc22} \end{bmatrix} \tag{3.20}$$

where sub-index s denotes single-ended mode. In this case, the input port 1 is defined as single-ended, and the mixed-mode output port 2 is defined between the two single-ended output ports of the combiner. In the case of an in-phase power combiner (e.g., Wilkinson), the single-ended output signals have 0 deg phase difference. Thus, the common-mode transmission parameter is equal to one (i.e., $|s_{cs21}| = 1$), and the differential-mode transmission is zero (i.e., $|s_{ds21}| = 0$). On

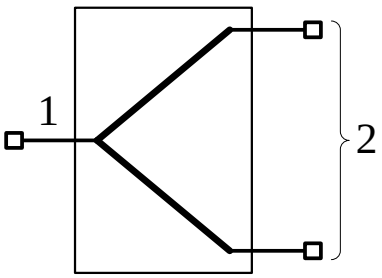

Figure 3.12: Circuit schematic of a three-port power combiner.

the other hand, for the case of an out-of-phase combiner (e.g., rat-race) occurs the opposite, i.e., $|s_{ds21}| = 1$ and $|s_{cs21}| = 0$.

3.3.1.2 Mixed-mode S-parameters measurement

The direct way to measure the mixed-mode S-parameters of differential devices is by using a pure-mode vector network analyzer (PMVNA) [17]. The problem is that this type of equipment is not always available, since it is a network analyzer for a very specific use. Furthermore, the differential noise measurements are not solved yet with this type of equipment.

Conventional network analyzers usually provide single-ended two-port measurement capabilities. By taking measurements from pairs of ports (and matching the others unused ports) it is possible to measure the complete S-parameter matrix of any N-port device. As it is well-known, the standard S-parameters matrix gives the complete information about the power transfers between all the circuit ports. Thus, if all the information is contained in this matrix, it seems reasonable to think that it is possible to extract the mixed-mode parameters with some kind of transformation from the standard ones. This transformation exists, and allows converting the standard S-parameters to the mixed-mode ones and vice versa [16]. The transformation for four-port devices can be written as

$$S^{mm} = M S^{std} M^{-1} \tag{3.21}$$

where S^{mm} is the mixed-mode S-parameters matrix, S^{std} is the standard S-parameters matrix, and M is the following matrix

$$M = \frac{1}{\sqrt{2}} \begin{bmatrix} 1 & -1 & 0 & 0 \\ 0 & 0 & 1 & -1 \\ 1 & 1 & 0 & 0 \\ 0 & 0 & 1 & 1 \end{bmatrix} \tag{3.22}$$

Using the sub-matrix division in (3.18), expression (3.21) can be expanded as

$$\begin{aligned}
S_{dd} &= \begin{bmatrix} s_{dd11} & s_{dd12} \\ s_{dd21} & s_{dd22} \end{bmatrix} = \frac{1}{2} \begin{bmatrix} (s_{11} - s_{12} - s_{21} + s_{22}) & (s_{13} - s_{14} - s_{23} + s_{24}) \\ (s_{31} - s_{32} - s_{41} + s_{42}) & (s_{33} - s_{34} - s_{43} + s_{44}) \end{bmatrix} \\
S_{dc} &= \begin{bmatrix} s_{dc11} & s_{dc12} \\ s_{dc21} & s_{dc22} \end{bmatrix} = \frac{1}{2} \begin{bmatrix} (s_{11} + s_{12} - s_{21} - s_{22}) & (s_{13} + s_{14} - s_{23} - s_{24}) \\ (s_{31} + s_{32} - s_{41} - s_{42}) & (s_{33} + s_{34} - s_{43} - s_{44}) \end{bmatrix} \\
S_{cd} &= \begin{bmatrix} s_{cd11} & s_{cd12} \\ s_{cd21} & s_{cd22} \end{bmatrix} = \frac{1}{2} \begin{bmatrix} (s_{11} - s_{12} + s_{21} - s_{22}) & (s_{13} - s_{14} + s_{23} - s_{24}) \\ (s_{31} - s_{32} + s_{41} - s_{42}) & (s_{33} - s_{34} + s_{43} - s_{44}) \end{bmatrix} \\
S_{cc} &= \begin{bmatrix} s_{cc11} & s_{cc12} \\ s_{cc21} & s_{cc22} \end{bmatrix} = \frac{1}{2} \begin{bmatrix} (s_{11} + s_{12} + s_{21} + s_{22}) & (s_{13} + s_{14} + s_{23} + s_{24}) \\ (s_{31} + s_{32} + s_{41} + s_{42}) & (s_{33} + s_{34} + s_{43} + s_{44}) \end{bmatrix}
\end{aligned} \tag{3.23}$$

As it can be seen from (3.23), it is possible to obtain any mixed-mode parameter from a given combination of single-ended parameters, which can be obtained with any conventional network analyzer. A similar transformation can also be obtained for three-port combiners. For example, the mixed-mode S-parameters matrix of a circuit such as the one shown in Fig. 3.12 can be expanded as

$$\begin{aligned} S^{mm} &= \begin{bmatrix} s_{ss11} & s_{sd12} & s_{sc12} \\ s_{ds21} & s_{dd22} & s_{dc22} \\ s_{cs21} & s_{cd22} & s_{cc22} \end{bmatrix} \\ &= \frac{1}{2}\begin{bmatrix} 2s_{11} & \sqrt{2}(s_{12}-s_{13}) & \sqrt{2}(s_{12}+s_{13}) \\ \sqrt{2}(s_{21}-s_{31}) & (s_{22}-s_{23}-s_{32}+s_{33}) & (s_{22}+s_{23}-s_{32}-s_{33}) \\ \sqrt{2}(s_{21}+s_{31}) & (s_{22}-s_{23}+s_{32}-s_{33}) & (s_{22}+s_{23}+s_{32}+s_{33}) \end{bmatrix} \end{aligned} \tag{3.24}$$

Another procedure to measure the mixed-mode S-parameters of a differential device is by using baluns and/or combiners connected at the input and output of the device. The idea is to convert the four-port circuit into a two-port one, and directly measure the four parameters of each one of the sub-matrices in (3.18). The different configurations are shown in Fig. 3.10. Thus, baluns are used to transform from single-ended mode into differential-mode (180 deg phase difference), and in-phase combiners are used to transform from single-ended mode into common-mode (0 deg phase difference). The most common procedure is by using two baluns, with which one can obtain the differential-to-differential sub-matrix S_{dd} that is usually the main operation mode of a differential amplifier. The main disadvantages of this procedure come from the frequency and losses limitations introduced by the external passive circuits. A de-embedding method to obtain the actual gain and noise performance of the differential amplifier from a measurement with external baluns will be described in the next subsection.

3.3.2 Noise characterization

The noise figure is used to quantify the degradation of the signal-to-noise ratio that suffers an input signal when crossing through an electronic component or system, and that is due to the noise generated by the own electronic devices (1.9). This parameter needs to be defined and, therefore, measured between a pair of ports (input and output). Thus, noise measurement equipments usually provide two connectors to do the measurement of the device-under-test (DUT). For the case of using the Y-factor method (Fig. 1.15), one connector provides the signal coming from a calibrated noise source, and the other connector senses the output signal coming from the DUT.

In the case of a single-ended amplifier the measurement procedure is immedi-

ate (Fig. 3.13). However, in the case of differential amplifiers, this measurement is not as obvious. Practical implementations of differential amplifiers have four ports, so the noise figure definition is not unique. Nevertheless, as it was seen in subsection 3.3.1, an equivalent two-port representation of the differential device supporting different combinations of input/output excitation modes is feasible (Fig. 3.10). Assuming that the differential-to-differential configuration is usually the case of interest, the noise figure of a differential amplifier can be defined in an equivalent way that the one of a conventional single-ended amplifier, as it is represented in Fig. 3.14. Although this theoretical reasoning is completely consistent, most noise measurement equipments used in practice are not prepared to generate pure differential excitations and, therefore, the differential noise figure cannot be directly measured in four-port differential amplifiers. Several measurement protocols proposed to overcome this limitation are described below.

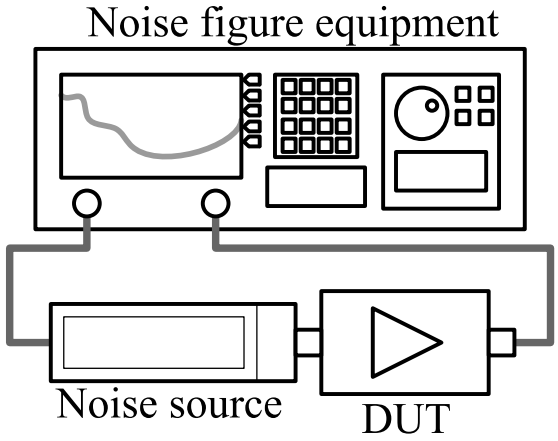

Figure 3.13: Typical noise figure measurement setup.

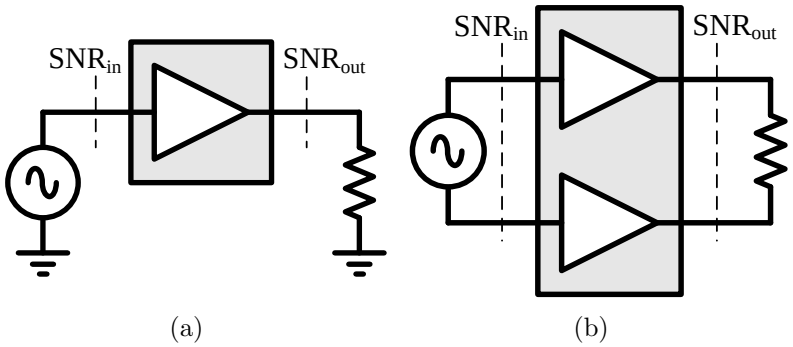

Figure 3.14: Noise figure definition of a single-ended (a) and a differential (b) amplifier.

3.3.2.1 Differential noise measurement with baluns

The use of passive baluns is the simplest method to characterize a differential amplifier. These components are used to drive the differential device with differential input/output excitations, and allow characterizing the device in any conventional two-port measurement equipment. However, since external baluns affect the measurement procedure, it is necessary to de-embed the gain and noise values of the isolated DUT from the measurement of the cascaded system (i.e., input balun, differential amplifier and output balun).

A method to de-embed the noise figure and the gain of differential amplifiers measured by using external baluns is described in [18]. The cited work assumes a simplified model of the balun, in which losses are symmetrical (i.e., equal in both branches) and there is an ideal 180 deg phase difference between the output ports. This may be far from the behavior of real baluns used in practice. With this simplified model, only differential-mode signals are propagated, so the effect of common-mode signals is not taken into account. There was not a procedure in the literature to de-embed the noise figure of a differential device when phase unbalances or asymmetrical amplitude responses appear in the baluns. Thus, one of the original contributions presented in this chapter deals with the development of a method to de-embed the noise figure of a differential amplifier using a more complete model of the baluns [26]. It would allow improving the accuracy of the noise figure measurement of the differential low noise amplifiers developed in subsequent sections, which is quite critical in the proposed application.

The method that will be analyzed in this section is shown in Fig. 3.15. Ideally, the input balun equally splits the signal along two 180 deg out-of-phase output branches. The behavior of the output balun is equivalent, so it also combines the output signals from the amplifiers. Thus, the measured noise figure of the system with ideal baluns equals the noise figure of the isolated amplifier with differential excitations [18].

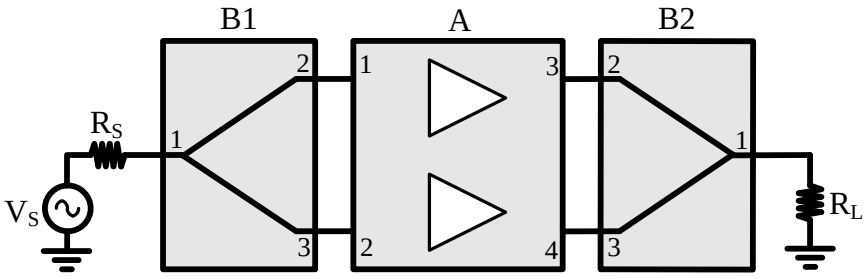

Figure 3.15: Measurement of a differential amplifier A by using two baluns $B1$ and $B2$.

Differential amplifiers can be classified into two groups: balanced and fully-differential (Fig. 3.11) [15]. Although the response when using differential excitations is equivalent in both cases, it is not so for common-mode excitations. Balanced amplifiers equally amplify both differential- and common-mode signals, which means CMRR=1. However, fully-differential amplifiers only amplify differential signals, since common-mode excitations are mitigated by the structure (i.e., CMRR=∞). If a simplified model of the balun with symmetrical losses and no phase unbalance were used, only differential signals would propagate along the system, and a single general model of the amplifier could be considered [18]. In this case, both losses and phase/magnitude unbalances are considered in the baluns. Therefore, since both differential- and common-mode signals may appear, a separate analysis for the balanced and the fully-differential amplifier should be undertaken.

- **Balanced amplifier**

Balanced amplifiers consist of two independent amplifiers working in parallel (Fig. 3.11(a)). In this case, all the S-parameters of the amplifier are assumed to be zero, except the transmission parameters between ports 1-3 and 2-4 (Fig. 3.15)

$$s_{31}^{A} = s_{42}^{A} = A \tag{3.25}$$

where A is the gain factor of the amplifier. For the case of the baluns, it is assumed that all the S-parameters are zero (perfect impedance matching and output ports isolation), except the transmission coefficients between ports 1-2 and 1-3 (arbitrary losses and phase/magnitude unbalances), i.e.,

$$\begin{aligned} s_{12}^{B1} = s_{21}^{B1}, s_{13}^{B1} = s_{31}^{B1} \\ s_{12}^{B2} = s_{21}^{B2}, s_{13}^{B2} = s_{31}^{B2} \end{aligned} \tag{3.26}$$

where super-indices $B1$ and $B2$ indicate the input and output baluns respectively. Assuming perfect output ports isolation and impedance matching in the balun is necessary to ensure that the amplifier loading conditions are the same as in the case of a 50 Ω isolated environment. Otherwise, the amplifier would not be correctly excited and the de-embedding would not be feasible. For the case of the S-parameters, one can re-normalize the parameters matrix obtained for certain port impedance conditions and extract the corresponding matrix for any other port impedance conditions. However, this is not so for noise measurements. Measuring the noise figure (even knowing the S-parameters) of a device under certain port-impedance conditions does not give enough information to analytically obtain the corresponding noise figure for other matching conditions. It would require to have the complete set of noise parameters available (i.e., minimum noise

figure (F_{min}), optimum noise matching (Γ_{opt}) and noise resistance (R_n)), which is assumed to be unknown a priori in this case. The noise factor of a two-port device can be written as

$$f = \frac{\text{Total noise at the output}}{\text{Noise power at the output due to the source resistor}} \tag{3.27}$$

In this case, the noise power at the output port is due to the contributions from the source resistor, from the two baluns, and from the amplifier. For the input balun, it can be assumed that the two branches generate uncorrelated noise signals [18]. Since the noise factor of a passive device equals its losses, the noise spectral density at its output is kT (W^2/Hz), where k is the Boltzmann constant (i.e., k=$1.38 \cdot 10^{-23}$ JK^{-1}) and T is the system temperature. For the case of the 1-2 and 1-3 branches of the input balun, this power density propagates to the output through the amplifier and the output balun as

$$\begin{aligned} N_{1-2}^{B1,a} &= kT|s_{31}^{A} s_{12}^{B2}|^2 \\ N_{1-3}^{B1,a} &= kT|s_{42}^{A} s_{13}^{B2}|^2 \end{aligned} \tag{3.28}$$

where sub-indices 1-2 and 1-3 indicate the corresponding branch of the balun, super-index a is used for the balanced topology and super-indices $B1$, A, $B2$ denote the corresponding input balun or amplifier or output balun parameter. Terms in (3.28) contain the combined contribution from the source resistor and the input balun. For the balanced amplifier, it can be assumed that the noise generated by the two independent branches is uncorrelated. By definition, the noise power at the output of an amplifier is kTf_AG_A, where f_A is the noise factor of the amplifier and G_A is the power gain [18]. In order to calculate the contribution of the amplifier alone, the contribution from the source must be eliminated (i.e., kTG_A). Thus, the noise power of each stage of the balanced amplifier propagated to the output of the system is respectively

$$\begin{aligned} N_1^{A,a} &= (kTf_A|s_{31}^{A}|^2 - kT|s_{31}^{A}|^2)|s_{12}^{B2}|^2 \\ &= kT(f_A - 1)|s_{31}^{A} s_{12}^{B2}|^2 \\ N_2^{A,a} &= kT(f_A - 1)|s_{42}^{A} s_{13}^{B2}|^2 \end{aligned} \tag{3.29}$$

where sub-indices 1 and 2 indicate the corresponding input port of the amplifier. The noise spectral density at the output of the balun $B2$ is kT (W^2/Hz). Since two independent source resistors launch noise at the 2nd and 3rd output balun ports, the noise generated by the balun alone can be obtained as

$$\begin{aligned} N^{B2,a} &= kT - kT|s_{12}^{B2}|^2 - kT|s_{13}^{B2}|^2 \\ &= kT\left[1 - \left(|s_{12}^{B2}|^2 + |s_{13}^{B2}|^2\right)\right] \end{aligned} \tag{3.30}$$

Finally, the noise contribution from the source resistor at the output of the system is obtained as

$$N^{S,a} = kT|s_{21}^{B1}s_{31}^{A}s_{12}^{B2} + s_{31}^{B1}s_{42}^{A}s_{13}^{B2}|^2 \tag{3.31}$$

From the last expression, the power gain of the cascaded system when using a balanced amplifier can be extracted as

$$G_{casc}^{(a)} = |s_{21}^{B1}s_{31}^{A}s_{12}^{B2} + s_{31}^{B1}s_{42}^{A}s_{13}^{B2}|^2 \tag{3.32}$$

The noise figure of the cascaded system can be obtained from (3.27)-(3.31) as

$$\begin{aligned} f_{casc}^{(a)} &= \frac{N_{1-2}^{B1,a} + N_{1-3}^{B1,a} + N_{1}^{A,a} + N_{2}^{A,a} + N^{B2,a}}{N^{S,a}} \\ &= \frac{f_A(|s_{31}^{A}s_{12}^{B2}|^2 + |s_{42}^{A}s_{13}^{B2}|^2) + 1 - (|s_{12}^{B2}|^2 + |s_{13}^{B2}|^2)}{|s_{21}^{B1}s_{31}^{A}s_{12}^{B2} + s_{31}^{B1}s_{42}^{A}s_{13}^{B2}|^2} \end{aligned} \tag{3.33}$$

The mixed-mode parameters of the baluns can be used instead of the conventional ones [15],

$$\begin{aligned} s_{ds21}^{B1} &= (s_{21}^{B1} - s_{31}^{B1})/\sqrt{2} \\ s_{cs21}^{B1} &= (s_{21}^{B1} + s_{31}^{B1})/\sqrt{2} \\ s_{sd21}^{B2} &= (s_{12}^{B2} - s_{13}^{B2})/\sqrt{2} \\ s_{sc21}^{B2} &= (s_{12}^{B2} + s_{13}^{B2})/\sqrt{2} \end{aligned} \tag{3.34}$$

where the sub-indices c, d and s denote common-mode, differential-mode and single-ended excitations respectively. In addition, the sub-index order in the mixed mode parameters considers the differential or common-mode outputs for the first balun and single-ended output for the second balun. Then, assuming an ideal balanced amplifier (3.25) and using the mixed-mode S-parameter notation (3.34), (3.33) can be simplified to

$$f_{casc}^{(a)} = \frac{(f_A|A|^2 - 1)(|s_{sd21}^{B2}|^2 + |s_{sc21}^{B2}|^2) + 1}{|s_{ds21}^{B1}As_{sd21}^{B2} + s_{cs21}^{B1}As_{sc21}^{B2}|^2} \tag{3.35}$$

It can be seen that for the case of ideal baluns, i.e.,

$$\begin{aligned} s_{21}^{B1} = 1/\sqrt{2},\ s_{31}^{B1} = -1/\sqrt{2}, \\ s_{12}^{B2} = 1/\sqrt{2},\ s_{13}^{B2} = -1/\sqrt{2} \end{aligned} \tag{3.36}$$

the noise figure and the gain of the cascaded system is equal to the performance of the isolated amplifier

$$f_{casc}^{(a)} = f_A \text{ and } G_{casc}^{(a)} = G_A \tag{3.37}$$

- **Fully-differential amplifier**

A fully-differential amplifier, also known as differential pair, is an amplifier in which the sources of two transistors are both connected to a common current source (Fig. 3.11(b)). Unlike the previous case, the differential pair cannot be analyzed as two independent stages. Thus, for the ideal case, all the S-parameters of the amplifier are zero except the transmission parameters between the input ports and the output ports (Fig. 3.15)

$$\begin{aligned} s_{31}^{A} &= s_{42}^{A} = A/2 \\ s_{32}^{A} &= s_{41}^{A} = -A/2 \end{aligned} \tag{3.38}$$

In this case, the noise power present in one of the inputs of the amplifier is propagated through the two outputs. Thus, the noise coming from one branch of the input balun is divided into two paths in the amplifier and combined in the output balun as

$$\begin{aligned} N_{1-2}^{B1,b} &= kT|s_{31}^{A}s_{12}^{B2} + s_{41}^{A}s_{13}^{B2}|^2 \\ N_{1-3}^{B1,b} &= kT|s_{32}^{A}s_{12}^{B2} + s_{42}^{A}s_{13}^{B2}|^2 \end{aligned} \tag{3.39}$$

where sub-indices 1-2 and 1-3 indicate the corresponding branch of the balun, and sub-index b refers to the fully-differential topology. The noise contribution of the differential amplifier can be calculated assuming two independent noise sources at both input ports. Therefore, the noise launched by each source is propagated through the two outputs of the amplifier and finally combined by the output balun as

$$\begin{aligned} N_{1}^{A,b} &= kT(f_A - 1)|s_{31}^{A}s_{12}^{B2} + s_{41}^{A}s_{13}^{B2}|^2 \\ N_{2}^{A,b} &= kT(f_A - 1)|s_{32}^{A}s_{12}^{B2} + s_{42}^{A}s_{13}^{B2}|^2 \end{aligned} \tag{3.40}$$

where sub-indices 1 and 2 indicate the corresponding input port of the amplifier. For the output balun, the noise coming from ports 2 and 3 cannot be considered uncorrelated in this case, since there are not two independent paths in the overall scheme. As the differential pair only propagates differential signals (common-mode gain is zero), the noise can be modeled as a differential source connected between ports 2 and 3. Then, the output balun can be interpreted as a two-port passive device, with a differential input port and a single-ended output port, whose transmission parameter s_{sd21}^{B2} can be obtained from (3.34). Since the output noise power density is kT (W^2/Hz), the contribution of the balun alone is obtained as

$$N^{B2,b} = kT(1 - 0.5|s_{12}^{B2} - s_{13}^{B2}|^2) \tag{3.41}$$

Finally, the noise contribution from the source resistor propagated to the output can be calculated from the combination of the different paths along which the

source signal propagates

$$N^{S,b} = kT|(s_{21}^{B1}s_{31}^{A} + s_{31}^{B1}s_{32}^{A})s_{12}^{B2} + (s_{21}^{B1}s_{41}^{A} + s_{31}^{B1}s_{42}^{A})s_{13}^{B2}|^2 \tag{3.42}$$

The gain of the cascaded system in this case is directly obtained from (18) as

$$G_{casc}^{(b)} = |(s_{21}^{B1}s_{31}^{A} + s_{31}^{B1}s_{32}^{A})s_{12}^{B2} + (s_{21}^{B1}s_{41}^{A} + s_{31}^{B1}s_{42}^{A})s_{13}^{B2}|^2 \tag{3.43}$$

and the corresponding noise figure is

$$\begin{aligned} f_{casc}^{(b)} &= \frac{N_{1-2}^{B1,b} + N_{1-3}^{B1,b} + N_{1}^{A,b} + N_{2}^{A,b} + N^{B2,b}}{N^{S,b}} \\ &= \frac{f_A(|s_{31}^{A}s_{12}^{B2} + s_{41}^{A}s_{13}^{B2}|^2 + |s_{32}^{A}s_{12}^{B2} + s_{42}^{A}s_{13}^{B2}|^2) + 1 - 0.5|s_{12}^{B2} - s_{13}^{B2}|^2}{|(s_{21}^{B1}s_{31}^{A} + s_{31}^{B1}s_{32}^{A})s_{12}^{B2} + (s_{21}^{B1}s_{41}^{A} + s_{31}^{B1}s_{42}^{A})s_{13}^{B2}|^2} \end{aligned} \tag{3.44}$$

For an ideal, fully-differential amplifier (3.38) and using notation of mixed-mode S-parameters for the baluns (3.34), (3.44) can be simplified to

$$f_{casc}^{(b)} = \frac{(f_A|A|^2 - 1)|s_{ds21}|^2 + 1}{|s_{ds21}^{B1}As_{sd21}^{B2}|} \tag{3.45}$$

It can be seen that (3.45) is analogous to (3.35), but removing the common-mode terms. That conclusion is logical, since the fully-differential amplifiers mitigate the common-mode signals.

- **Step-by-step gain and noise measurement procedure**

The step-by-step gain and noise measurement procedure for both balanced and fully-differential amplifier topologies is summarized below:

1. Characterization of the balun:
   Measure the transmission parameters (3.26) of the baluns $B1$ and $B2$ by using a conventional network analyzer. Also, it should be checked that the reflection coefficients and the output ports isolations are significantly low (e.g., lower than -15 dB) in the band of interest.

2. Gain measurement:
   Connect the baluns and the differential amplifier following the scheme shown in Fig. 3.15. Measure the gain G_{casc} of the two-port cascaded system by means of a conventional two-port network or gain analyzer. Assuming that condition (3.25) is satisfied in the case of the balanced amplifier or (3.38) in the case of the fully-differential amplifier, de-embed the gain A of the amplifier making use of the expressions (3.32) or (3.43) respectively.

3. Noise measurement:
   Measure the noise figure f_{casc} of the cascaded system by using a conventional two-port noise analyzer. De-embed the noise figure f_A of the amplifier by making use of (3.33) in the case of the balanced amplifier or (3.44) for the case of the fully-differential amplifier.

- **Numerical example**

Equations (3.33) and (3.44) give analytical expressions that can be used to de-embed the noise figure of a balanced or a fully-differential amplifier using non-ideal baluns. Nevertheless, the choice of a proper configuration of a given set of baluns can diminish the noise increase in f_{casc} and, therefore, reduce the uncertainty and errors during the de-embedding due to the limitations of the measurement equipments. A numerical example has been computed by using the formulas presented in the previous section, in order to illustrate the effects of the baluns over the measurement of a balanced and a fully-differential amplifier. For both cases, an amplifier with a gain A=6 dB, and a noise figure F_A=1 dB is assumed. Additionally, the same examples have been validated by means of the software *AWR Microwave Office* obtaining the same results.

Fig. 3.16 shows the effect of the phase unbalances in the baluns. It should be noted that phase unbalances are not treated in the de-embedding analysis developed in the literature [18]. The unbalances ϵ_{B1} and ϵ_{B2} are defined as the increase in the phase difference between the output ports of both baluns with respect to the ideal 180 deg as

$$\begin{aligned} \angle s_{21}^{B1} - \angle s_{31}^{B1} &= 180 \text{ deg} + \epsilon_{B1} \\ \angle s_{12}^{B2} - \angle s_{13}^{B2} &= 180 \text{ deg} + \epsilon_{B2} \end{aligned} \tag{3.46}$$

Several scenarios have been simulated, with unbalances in one or both baluns and assuming that they do not present losses (see legend of Fig. 3.16). The first scenario (a) only considers a phase unbalance in the input balun $B1$ ($\epsilon_{B1} = \epsilon$); the second scenario (b) only considers a phase unbalance in the output balun ($\epsilon_{B2} = \epsilon$); the third scenario (c) considers equal phase unbalances in the input and output balun ($\epsilon_{B1} = \epsilon_{B2} = \epsilon$); finally the fourth scenario (d) considers equal but opposite phase unbalance in both the input and output baluns ($\epsilon_{B1} = \epsilon$, $\epsilon_{B2} = -\epsilon$). For the case of the balanced amplifier, the scenarios (a) and (b) (the same unbalanced balun connected at the input or the output) equally affects in the measurement. For the third scenario (c) the increase in the noise figure for the balanced configuration is the largest since there is no compensation between the input and output baluns. However, for the fourth scenario (d), there is no increment in the noise figure since the unbalances of $B1$ and $B2$ compensate

each other. Thus, for the balanced configuration, if two identical baluns are used to characterize a balanced amplifier, it is a good practice to connect them anti-symmetrically (port 2 of $B1$ and port 3 of $B2$ in the upper path and vice versa). For the case of the fully-differential amplifier, the effect of the input balun is the same as the one with the balanced amplifier (a), but the effect of the output balun is mitigated by the gain factor of the amplifier (b). For the case of unbalances in the two baluns, it is indifferent whether the unbalances appear in phase or anti-phase (c,d).

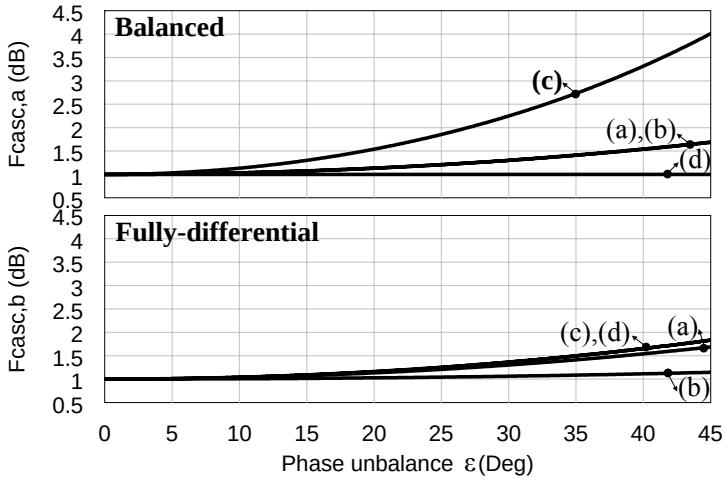

Figure 3.16: Phase unbalance effect in different scenarios: (a) unbalance in $B1$ ($\epsilon_{B1} = \epsilon$), (b) unbalance in $B2$ ($\epsilon_{B2} = \epsilon$), (c) unbalances in phase in $B1$ and $B2$ ($\epsilon_{B1} = \epsilon_{B2} = \epsilon$), and (d) unbalances in anti-phase in $B1$ and $B2$ ($\epsilon_{B1} = \epsilon$, $\epsilon_{B2} = -\epsilon$).

The losses and amplitude unbalance effects are now analyzed. Fig. 3.17 shows the impact of the losses and magnitude unbalances of the balun in the noise figure measurement. The loss factors are defined from

$$\begin{aligned} |s_{21}^{B1}| = 1/(\alpha_{B1}^{'}\sqrt{2}),\ |s_{31}^{B1}| = 1/(\alpha_{B1}^{''}\sqrt{2}), \\ |s_{12}^{B2}| = 1/(\alpha_{B2}^{'}\sqrt{2}),\ |s_{13}^{B2}| = 1/(\alpha_{B2}^{''}\sqrt{2}) \end{aligned} \tag{3.47}$$

It can be seen that the effect is very similar for the two types of amplifier. As it is expected from the Friis formula, the losses in the output balun (b,d) are less critical than the losses in the input balun (a,c), since they are mitigated by the gain factor of the amplifier. It should be noticed that [18] only considers symmetrical losses in the baluns (i.e., scenarios (c,d) in this case) but does not explain how to deal with the amplitude unbalances (i.e., scenarios (a,b)).

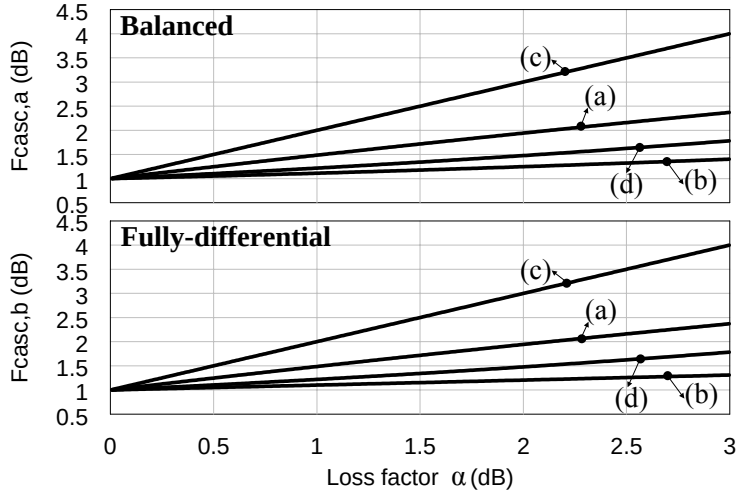

Figure 3.17: Losses effect in different scenarios: (a) unbalance only in $B1$ ($\alpha'_{B1} = \alpha$, $\alpha''_{B1} = 1$), (b) unbalance only in $B2$ ($\alpha'_{B2} = \alpha$, $\alpha''_{B2} = 1$), (c) symmetric losses only in $B1$ ($\alpha'_{B1} = \alpha''_{B1} = \alpha$), and (d) symmetric losses only in $B2$ ($\alpha'_{B2} = \alpha''_{B2} = \alpha$).

- **Experimental results**

In order to test the noise measurement procedure described before, some experimental measurements have been undertaken using two differential amplifier prototypes. Fig. 3.18 shows a photograph of the manufactured prototypes. The baluns have been implemented using the well-known topology of a rat-race coupler (loading the isolated port with 50 Ω), which intrinsically gives half-power splitting with 180 deg phase difference at the center frequency. The circuit schematic of the baluns is shown in Fig. 3.19(c). The center frequency of the baluns is 2100 MHz. Fig. 3.20 shows the measured transmission parameters and phase unbalance of both baluns. It should be noticed that the phase unbalance is computed as the difference with respect to the ideal 180 deg phase difference. The frequency range between 1600 and 2600 MHz is the bandwidth in which all the reflection coefficients (s_{11}, s_{22} and s_{33}) and the isolation parameters (s_{23}, s_{32}) of the baluns are lower than -15 dB, which ensures that the source and load conditions are considerably closer to the desired 50 Ω. The active devices have been implemented by using commercial single-ended amplifiers, model ERA-5+ from *Minicircuits*. This gain block provides a broadband amplifying device, already matched to 50 Ω. Fig. 3.19 shows the circuit schematic of the manufactured balanced and fully-differential amplifiers. The balanced amplifier has been designed just by connecting two independent ERA-5+ amplifiers in parallel (Fig. 3.19(a)). The fully-differential amplifier has been implemented using two ERA-5+ am-

plifiers, in which the sources are connected to ground by means of a common high-Q lumped inductor acting as current source (Fig. 3.19(b)). Capacitors $C1$ are just DC block devices, so their value is chosen to be high enough to provide low impedance (ideally an open circuit for DC and short-circuit for AC). In the case of the inductor $L1$, it should act as an open-circuit for AC and short-circuit for DC, which means a high inductance value. However, very high inductance values lead to undesired parasitic resistances in physical inductors, so a trade-off value of 68 nH has been chosen.

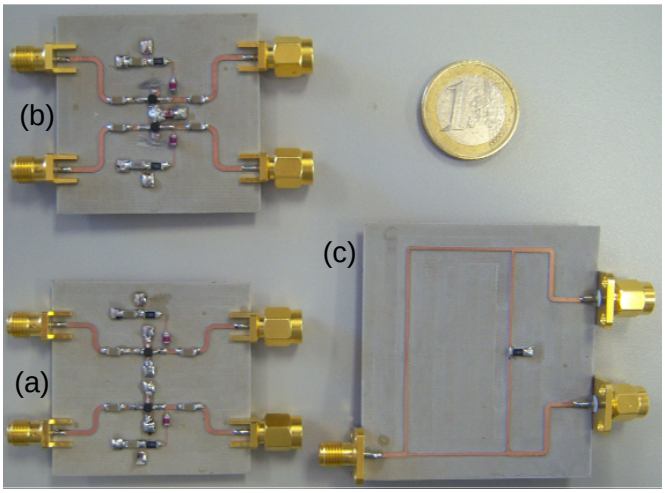

Figure 3.18: Photographs of the balanced (a) and the fully-differential (b) amplifiers, and one of the baluns (c).

The measured results for the gain and for the noise have been plotted in Fig. 3.21. The gain and noise measurements have been obtained using the noise analyzer N8975A from *Agilent*. Two sets of curves have been represented in each graph. The continuous lines represent the gain and noise curves obtained from the single-ended amplifier. A set of lines that are labeled as G_{casc} and F_{casc} respectively represents the measured gain and noise curves directly obtained from the cascaded system formed by the baluns and the corresponding balanced/fully-differential amplifier. The actual performance of the differential amplifiers should be the same as the performance of the single-ended amplifier of the two branches (for equivalent loading conditions). Thus, if no de-embedding procedure is applied to the measurement, the gain would be underestimated up to 1.5 dB and the noise would be overestimated up to 1 dB with respect to the actual value (i.e., single-ended measurement) in the worst cases. In the edges of the band, the error is higher due to the larger phase and magnitude unbalances in the baluns. In the center of the band, although the unbalances are not significant, the error

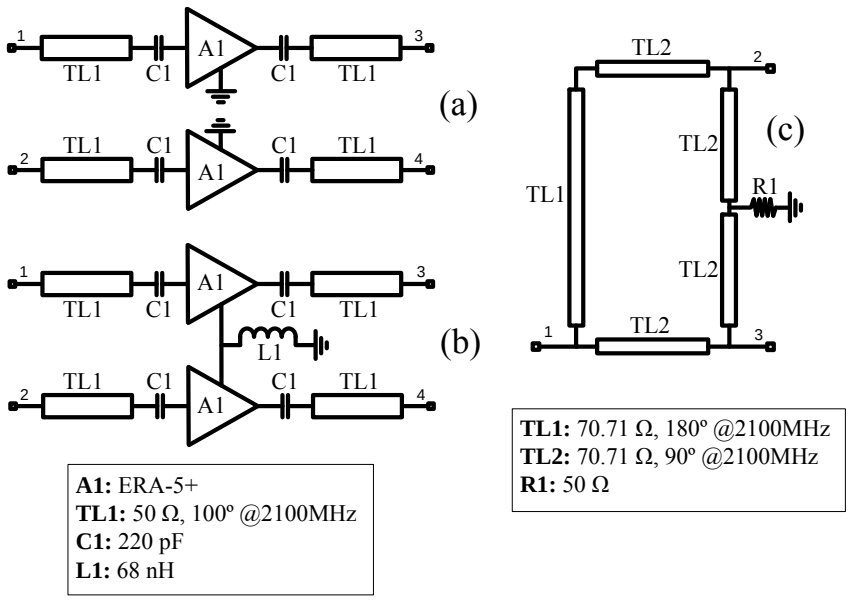

Figure 3.19: Circuit schematics of the balanced (a) and fully-differential (b) amplifiers, and the balun based on a rat-race hybrid (c).

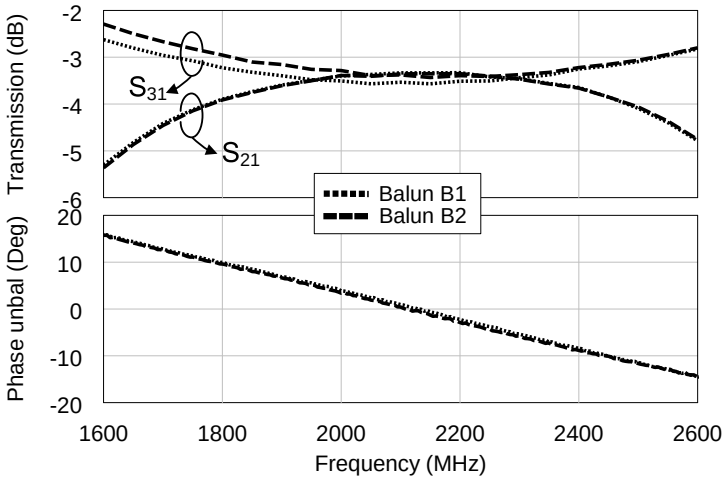

Figure 3.20: Measured transmission parameters and phase unbalance of the baluns.

is still high due to the balun losses. The gain and noise curves after the de-embedding procedures are labeled as *Estimated Gain* and *Estimated Noise* in the graph. Such de-embedded gain and noise curves have been compared with the curves measured from the single-ended amplifier, obtaining a good agreement. It can be seen that both losses and phase/magnitude unbalance effects have been significantly corrected following the proposed de-embedding methodology.

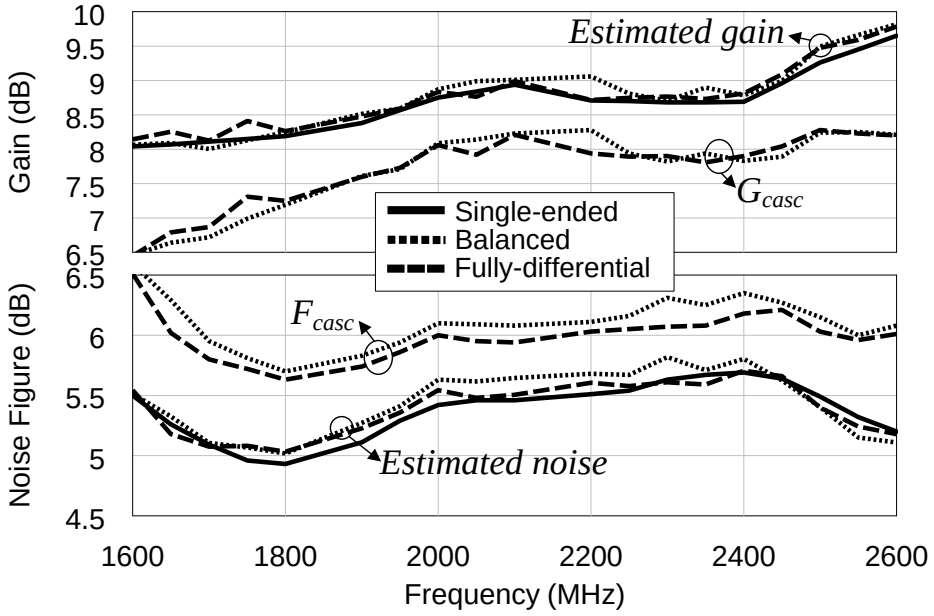

Figure 3.21: Measured results with the balanced and fully-differential amplifiers, before and after the de-embedding process, and comparison with the performance of the single-ended amplifier.

It is remarked that other de-embedding procedures do not deal with magnitude and phase unbalances in the baluns. In [18], it is assumed that the outputs of the balun are 180 deg out of phase and the transmission between ports 1-2 and 1-3 are equal in module. Thus, only the value of $|s_{21}|$ is used to characterize each balun. A comparison between the de-embedding method described in [18] (based on the 1-2 branch of the balun, as specified in the Fig. 2 of [18]) and the one proposed in the present thesis [26] is done in Fig. 3.22. This graph represents the error after the de-embedding of the gain and the noise figure of the two differential amplifiers by using the two methods. This error is defined as the difference (in magnitude) between the actual performance of the amplifier (i.e., single-ended measurement) and the performance obtained after the de-embedding procedure. It can be seen that the present method presents much better results, especially at the frequencies at the edge of the band, in which the unbalances in the baluns are

more significant. Since the proposed analysis does not only consider the losses in the balun (as in [18]), but also the phase and magnitude unbalances, the present method covers a more general case and, therefore, it is inherently more accurate.

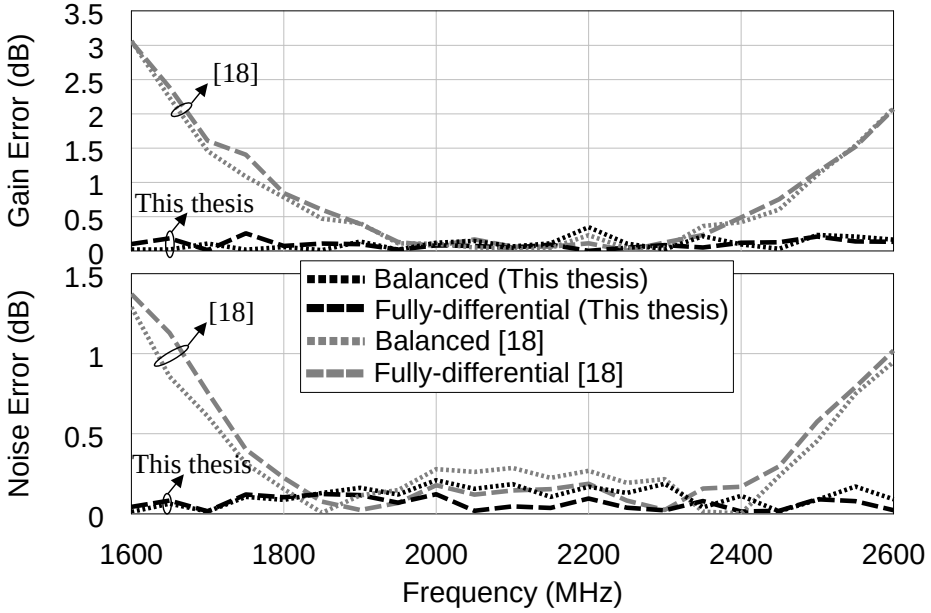

Figure 3.22: Measured gain a noise figure errors obtained with the method developed in this thesis [26] and with the method described in [18], for both differential amplifier implementations.

3.3.2.2 Hot/cold measurement with differential loads

An alternative to the noise measurement method based on baluns is to use a hot/cold differential load, as it is explained in [24]. As it was presented in Fig. 1.15, the Y-factor method is a very common procedure to determine the noise figure of a LNA. With a conventional noise figure equipment (Fig. 3.13), a noise source is typically used to synthesize two input noise signals, acting as a load at two different temperatures. However, the standard single-ended noise sources cannot be connected to a differential device. The method proposed in [24] makes use of a differential load connected to the input of the differential amplifier, as it is represented in Fig. 3.23. Thus, the load is exposed at two different temperatures, usually at room temperature T_0 (i.e., T_{hot}) and immersed into liquid nitrogen (i.e., T_{cold}). The output power is measured for both conditions (i.e., P_{hot} and P_{cold}). It is assumed that the DUT is at constant T_0 temperature

in both cases. Finally, by making use of the Y-factor formula (1.15), the noise temperature T_n of the DUT can be obtained as

$$T_n = \frac{T_{hot} + YT_{cold}}{Y - 1} \tag{3.48}$$

where the Y-factor is obtained from $Y = P_{hot}/P_{cold}$. The load usually consists of a resistance connected to the amplifier board by means of a ladder line. The output power is usually obtained in single-ended mode by using a balun.

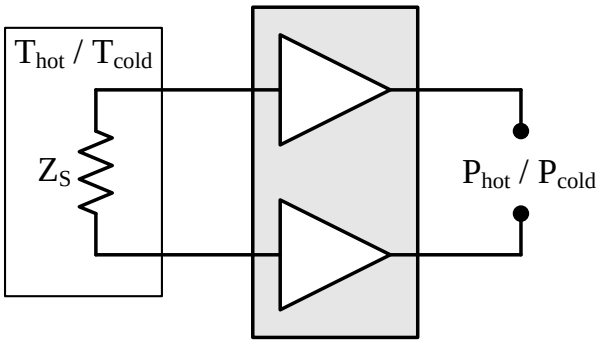

Figure 3.23: Measurement setup for the hot/cold differential noise measurement.

The advantage with this method is that it allows measuring the noise performance of the differential device for any real source impedance value, just by using a resistor as a differential load. Furthermore, it allows obtaining a continuous frequency-dependent noise response with a single measurement. For the case of using baluns, it is necessary to use an additional impedance tuner connected to the input so that a single frequency point is obtained at a time due to the narrowband response of the tuner. As a counterpart, this method requires a mechanism to cool the load (e.g., liquid nitrogen) that may be not easily available. In addition, although resistive load impedances can be easily used, arbitrary complex source impedances are difficult to synthesize. Thus, this method has been used to obtain the noise figure of the DUT for a given source impedance, while the source-pull method based on baluns presented in subsection 3.3.3 has been used in subsequent sections to obtain the gain and noise circles at some frequencies.

3.3.2.3 Other differential noise measurement techniques

A challenge in differential noise characterization is to measure the desired noise performance using the available noise measurement equipments and avoiding the use of external components that may disturb the measurement (e.g., passive baluns). A novel measurement method to characterize differential devices using

standard single-ended noise measurements has been recently presented in [20]. This method consists on doing several gain and noise single-ended measurements between different pairs of ports of the differential amplifier. It is demonstrated that using such single-ended measurements it is possible to analytically calculate the corresponding differential-mode gain and noise performance of the DUT. The philosophy is similar to the method used to convert from the conventional S-parameters to the mixed-mode ones, as it was explained in subsection 3.3.1. The advantage with this procedure is that it only requires a conventional noise figure equipment, and it avoids the use of additional components (e.g., baluns). Thus, for 50 Ω port impedances this method seems more adequate than the method based on baluns. However, it is limited when non-50 Ω port impedances are required. For the case of using baluns, an equivalent two-port circuit is obtained, and a conventional single-ended impedance tuner can be used to change the impedance conditions seen from the input or the output port. However, the method proposed in [20] would require something like a differential impedance tuner in order to synthesize the same impedance condition in the couple of input ports and respect the (anti-)symmetry of the circuit [41]. Nevertheless, this kind of impedance tuners is not usually available. Since the antenna impedances used for the mid-frequency range of the SKA project commonly differs from 50 Ω, this method has been discarded to evaluate the performance of the implemented differential amplifiers.

3.3.3 Source-pull characterization

For the case of the S-parameters, the measurement of a DUT with certain Z_0 port impedance conditions gives enough information to calculate the same performance for any other port impedances, just by applying a renormalization over the original S-parameter matrix. However, it does not occur with the noise parameters. The noise figure F of a two-port amplifier depends on the set of noise parameters of the amplifier (i.e., F_{min}, Z_{opt} and R_n), and on the input port impedance (i.e., Z_S) (1.11). The measurement of the noise figure F of a DUT for certain Z_S source impedance does not allow extrapolating the noise figure for a different source impedance, due to the lack of information about the set of noise parameters of the amplifier (F_{min}, Z_{opt} and R_n).

Obtaining the complete noise model of an amplifier requires a battery of noise figure measurements for different Z_S impedances. This procedure is known as *source-pull* characterization and allows estimating the noise circles of the amplifier. These measured circles allow, in turn, estimating the set of noise parameters F_{min}, Z_{opt} and R_n, which already provides all the information needed to obtain the noise figure of the device for any arbitrary source impedance.

In practice, the source-pull measurement is undertaken by means of a series impedance tuner connected to the input of the DUT, which transforms from the fixed port impedance (usually 50 Ω) of the measurement equipment into the desired source impedance Z_S. Commercial impedance tuners include from manual double-stub networks up to computer-controlled automatic equipments. As it occurs with most microwave equipments, these tuners are conceived for single-ended measurements. Thus, some kind of specific setup should be developed to be used in a differential characterization. Fig. 3.24 shows two possible configurations to obtain a differential source-pull characterization [41]. The case shown in Fig. 3.24(a) is based on two parallel tuners connected at the two inputs of the differential amplifier. This configuration could be compatible with the noise measurement method developed in [20]. Since the two branches of the amplifier need to see the same impedance conditions, the two tuners should synthesize the same impedance value at the same time, in order to keep the (anti-)symmetry of the structure. In practice, this kind of balanced operation is not available with conventional automatic impedance tuners, so specific tools are required [42]. It could be possible to use two manual tuners, but the procedure can be very tedious and prone to errors, due to the double tuning structure (usually voluminous) and

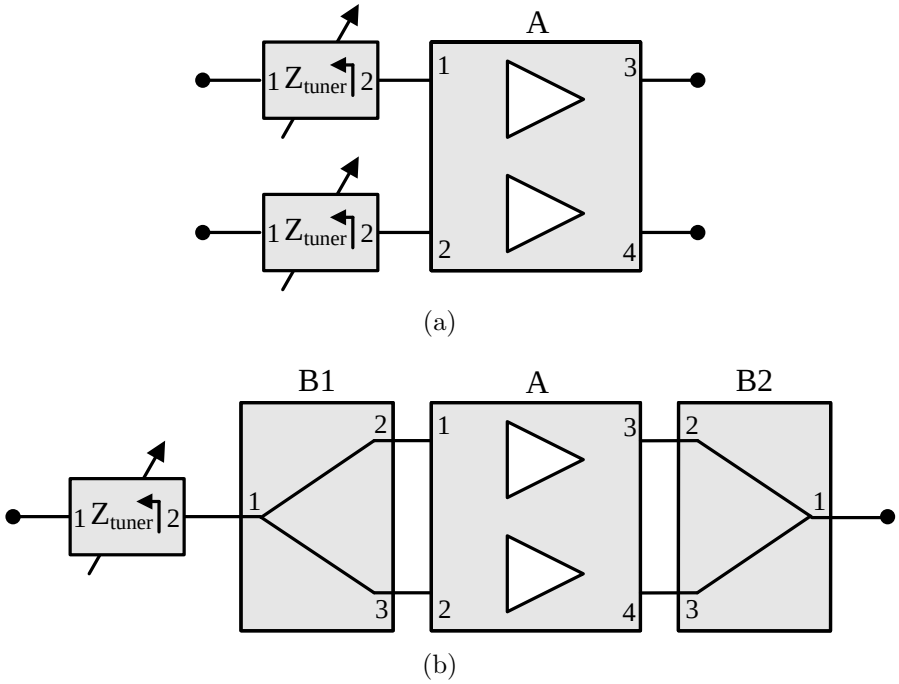

Figure 3.24: Two possible differential source-pull measurements schemes: (a) based on a balanced impedance tuner, and (b) based on baluns.

the number of measurements that the method in [20] already requires by itself. Because of these reasons, this configuration has been rejected to be used in this case.

The other alternative is the one shown in Fig. 3.24(b). It consists on connecting baluns at the input and output of the differential amplifier, and a single impedance tuner at the input of the structure. Since the balun-based topology provides a two-port equivalent circuit, the source-pull characterization is similar to the one that would be done with a conventional single-ended amplifier. This alternative has been studied in detail, and the procedure to realize the source-pull characterization of differential devices is explained below [27].

The impedance tuner is used to synthesize different impedances, transforming from the Z_0 given by the measurement equipment into a different impedance Z_{tuner} (Fig. 3.25(a)). Actually, the impedance seen from the input ports of the DUT will not be directly the impedance synthesized by the tuner, but the impedance seen through the input balun used in the measurement (Fig. 3.25(b)). If this balun is completely characterized (i.e., S-parameters matrix), obtaining the differential input impedance is easy. It must be noticed that, in the case of automatic source-pull equipments, the losses of the tuner are automatically de-embedded. However, for the case of a manual tuner, the losses should be de-embedded by the designer. This loss factor can be calculated from the S-parameters of the tuner as [43]

$$L_{tuner} = \frac{1 - |s^t_{22}|^2}{|s^t_{21}|^2} \tag{3.49}$$

where super-index t indicates the tuner.

Let us assume that the input balun in Fig. 3.24(b) is characterized by means of its mixed-mode S-parameters, with a differential-mode excitation in the output port. The mixed-mode S-matrix can be obtained from the conventional S-parameters as

$$S^{B1}_{ds} = \begin{bmatrix} s^{B1}_{ss11} & s^{B1}_{sd12} \\ s^{B1}_{ds21} & s^{B1}_{dd22} \end{bmatrix} = \frac{1}{2} \begin{bmatrix} 2s^{B1}_{11} & \sqrt{2}(s^{B1}_{12} - s^{B1}_{13}) \\ \sqrt{2}(s^{B1}_{21} - s^{B1}_{31}) & s^{B1}_{22} - s^{B1}_{23} - s^{B1}_{32} + s^{B1}_{33} \end{bmatrix} \tag{3.50}$$

where sub-index s denotes the single-ended port 1, sub-index d indicates the differential-mode excitation between ports 2 and 3 of the balun, and super-index $B1$ denotes the input balun. Once the S_{ds} matrix has been obtained, the corre-

sponding impedance (Z-) parameters can be calculated as [36]

$$\begin{aligned}
z_{ss11}^{B1} &= Z_0 \frac{(1+s_{ss11}^{B1})(1-s_{dd22}^{B1})+s_{sd12}^{B1}s_{ds21}^{B1}}{(1-s_{ss11}^{B1})(1-s_{dd22}^{B1})-s_{sd12}^{B1}s_{ds21}^{B1}} \\
z_{sd12}^{B1} &= Z_0 \frac{2s_{sd12}^{B1}}{(1-s_{ss11}^{B1})(1-s_{dd22}^{B1})-s_{sd12}^{B1}s_{ds21}^{B1}} \\
z_{ds21}^{B1} &= Z_0 \frac{2s_{ds21}^{B1}}{(1-s_{ss11}^{B1})(1-s_{dd22}^{B1})-s_{sd12}^{B1}s_{ds21}^{B1}} \\
z_{dd22}^{B1} &= Z_0 \frac{(1-s_{ss11}^{B1})(1+s_{dd22}^{B1})+s_{sd12}^{B1}s_{ds21}^{B1}}{(1-s_{ss11}^{B1})(1-s_{dd22}^{B1})-s_{sd12}^{B1}s_{ds21}^{B1}}
\end{aligned} \tag{3.51}$$

where Z_0 is the reference impedance. Finally, the last step is to calculate the differential input impedance Z_S seen from ports 2 and 3 of the balun when connecting the impedance tuner at port 1. This impedance is given by

$$Z_S = z_{dd22}^{B1} - \frac{z_{sd12}^{b1} z_{ds21}^{B1}}{z_{ss11}^{B1} + Z_{tuner}} \tag{3.52}$$

where Z_{tuner} is the impedance synthesized by the tuner (seen from the input balun).

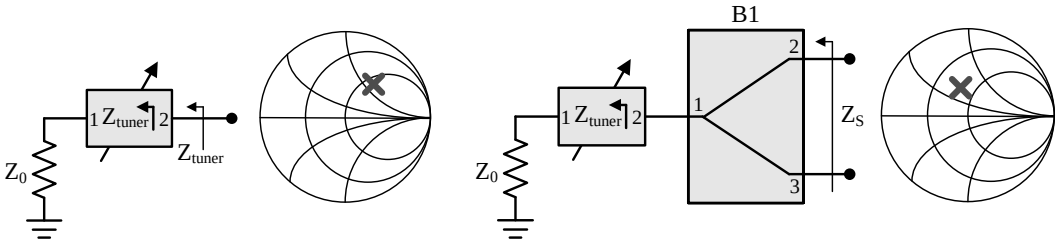

(a) (b)

Figure 3.25: Impedance synthesized by the tuner (a) and impedance transformed when including the input balun (b).

The measurement scheme, including the impedance tuner, both input and output baluns and the differential DUT is the one shown in Fig. 3.24(b). The differential source-pull characterization procedure can be summarized as follows:

1. Characterization of the impedance tuner:
   Synthesize several impedances Z_{tuner} at each frequency of interest (see Fig. 3.25(a)).

2. Characterization of the baluns:
   Measure the S-parameters of both baluns.

3. Measurement of the cascaded system:
   Measure the gain and the noise of the system shown in Fig. 3.24(b) with the different impedance conditions Z_{tuner} at the different frequencies.

4. De-embedding of the impedance tuner:
   Obtain the losses of the tuner L_{tuner} for the different synthesized impedances Z_{tuner} using (3.49). From the measurements of the complete system obtained in step 3, extract the performance of the subsystem formed by the baluns and the amplifier eliminating the influence of the tuner (it can be easily done using the well-known Friis formula (1.12).

5. De-embedding the baluns:
   This process is the same as the one explained in subsection 3.3.2.1. It allows obtaining the gain A and the noise figure F of the amplifier.

6. Synthesized source impedances:
   For the different tuner impedances Z_{tuner}, obtain the actual source impedances Z_S seen from the amplifier by using (3.50)-(3.52) (see Fig. 3.25(b)).

7. Representation:
   From the synthesized source impedances Z_S and the measured gain A and noise figure F of the amplifier, the gain and noise circles of the amplifier can be represented over the Smith chart. It usually needs a specific software to interpolate the discrete measured data (e.g., Load-pull tool in *AWR Microwave Office*).

8. Parameter extraction:
   From the level map obtained in step 7, it is possible to estimate the gain and the noise figure of the amplifier for any source impedance at each frequency. Moreover, other parameters of interest, such as the set of noise parameters of the amplifier (F_{min}, Γ_{opt} and R_n), can also be extracted.

3.4 Implementation of a Differential Active Antenna Array: FIDA3

3.4.1 Description of FIDA3

FIDA3 (*FG-IGN Differential Active Antenna Array*) is an array prototype developed by IGN-UC3M for the SKADS project [28]. This technology is proposed as a potential candidate for the mid-frequency band of SKA. This array design should operate in the 300–1000 MHz band and should be able to scan from broadside up to 45 deg. The active antenna impedance should be well-matched to the reference impedance in the band of interest and along the whole scanning angle range. The amplifiers should be integrated with each antenna element and should be optimized, especially in terms of noise, for the given active antenna impedance. Other aspects, such as low cost and ease of fabrication should also be considered.

Due to the large array dimensions of the final SKA design, the proposed radiating structure has been optimized assuming infinite by infinite dimensions. However, the final prototype will have restricted dimensions. For this case, the area

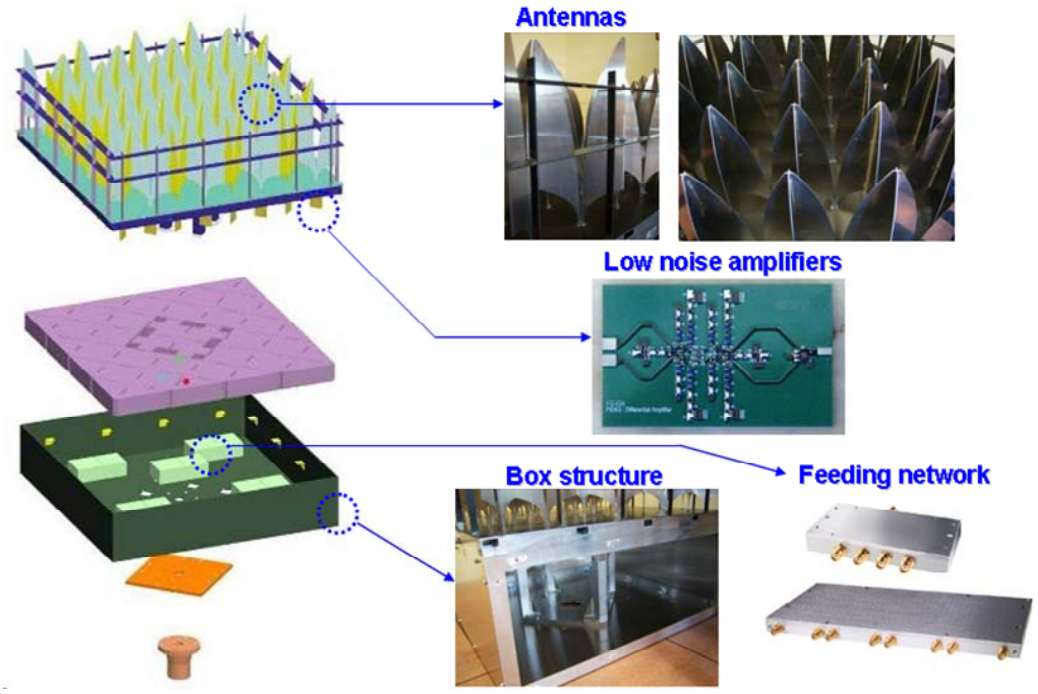

Figure 3.26: Artistic representation of the FIDA3 antenna array prototype and detail of its different parts.

of the array is 1 m^2. An artistic representation of the proposed FIDA3 prototype is shown in Fig. 3.26. The upper part consists of 64 bunny-ear antenna elements, placed in a grid for dual linear polarization (32 per polarization). The radiating structure is placed over a ground plane, and the antennas are attached with PVC rods to the structure edges. The differential LNAs are directly connected to the antenna elements just below the ground plane. Finally, the single-ended LNA outputs are combined by means of broadband power combiners. The connection between the LNAs and the power combiners is done by means of flexible coaxial cables. Thus, two coaxial outputs provide the amplified signals received from the antennas in the two orthogonal polarizations. All the DC and RF circuits (i.e., amplifiers, combiners, cables, DC circuits, etc.) are placed inside a metallic box below the ground plane. Details about the design and characterization of the different parts and the final system integration will be presented in the subsequent subsections.

3.4.2 Radiating structure

The proposed radiating structure for the FIDA3 array is based on bunny-ear antenna elements. The antenna element and the array structure are depicted in Fig. 3.27. For the array configuration, the elements are orthogonally placed in a grid in order to provide the desired dual linear polarization. The design and optimization of the antennas is described in detail in [13], so just the main results will be presented here. The goal is to achieve elements with low return losses (with respect to 150 Ω) in the band of interest (i.e., 300-1000 MHz), and assuming an array scanning range from broadside up to 45 deg. Since large array structures are difficult to simulate in conventional electromagnetic software, an infinite-by-infinite array approximation has been considered. It allows assuming that all the elements in the array have the same boundary conditions and, therefore, the

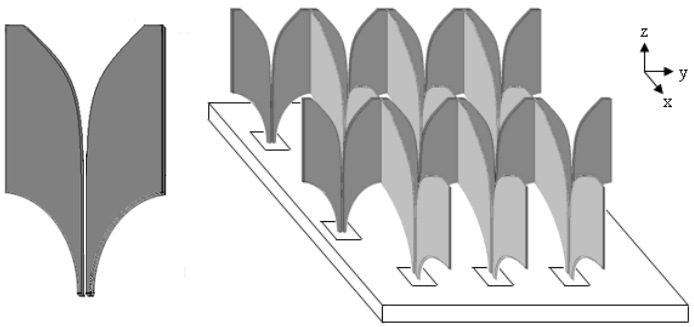

Figure 3.27: Scheme of a bunny-ear antenna element and array configuration.

problem is reduced to a single antenna element analysis. Thus, the simulations have been carried out using periodic boundary conditions with *Ansoft HFSS* software. One of the main contributions in [13] is the analysis and discussion of a new type of anomaly related to the propagation of even-mode currents in the differential array structure, which may degrade the impedance matching of the antennas when the array is scanning at off-broadside angles. These anomalies are corrected in [13] by using two resistors between the feeding lines of the antennas and the ground plane in order to dissipate the undesired signals. Thus, the final

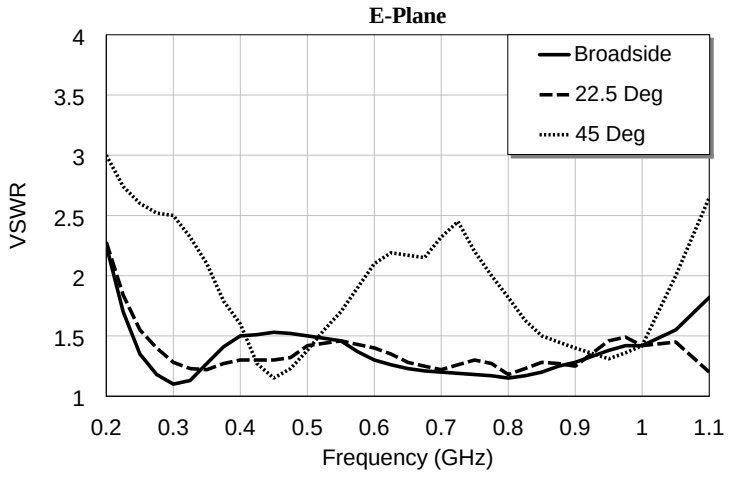

(a)

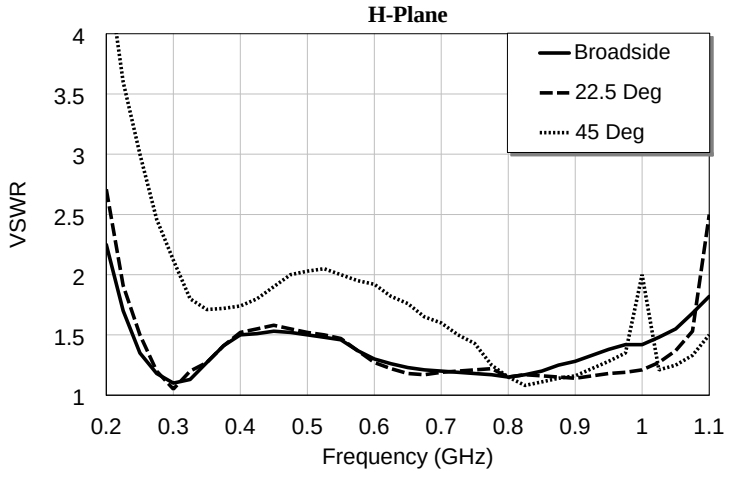

(b)

Figure 3.28: Simulated active reflection coefficient of the array for different E- and H-plane scanning angles.

optimized active reflection coefficient, for both the E- and H-plane array scanning is shown in Fig. 3.28. It can be seen that the VSWR does not exceed the value of 2.5:1 (i.e., $|s_{11}|$ <-7.36 dB), which is acceptable for this application considering the broadband performance of the array.

A photograph of the manufactured array tile is shown in Fig. 3.29. It consists of 64 bunny-ear antennas, with 32 elements per each polarization. The antenna structure, the ground plane and the metallic box have been built in aluminum. The area of the radiating structure is around 1 m^2. The S-parameter matrix of the array has been measured by using passive baluns in order to obtain a coaxial output per antenna. The effect of the baluns has been properly de-embedded, in order to obtain the performance of the array with 150 Ω loading conditions. The active reflection coefficient of each element in the tile has been computed from the measured S-parameter matrix using (3.5). Since the optimization of the array has been done assuming an infinite-by-infinite structure, the best performance is expected for the center elements in a physical implementation of the array. Thus, the measured active reflection of the center element for different E- and H-plane scanning angles from broadside to 45 deg is represented in Fig. 3.30. It can be observed that even for such a small array, the prototype presents good performance. The VSWR is mostly below 3:1 in the band of interest, which corresponds to $|s_{11}|$ <-6 dB. The active reflection coefficient of every element in the array at 800 MHz for broadside operation is shown in Fig. 3.31. As it was expected, the performance of the elements nearer to the edge is significantly worse

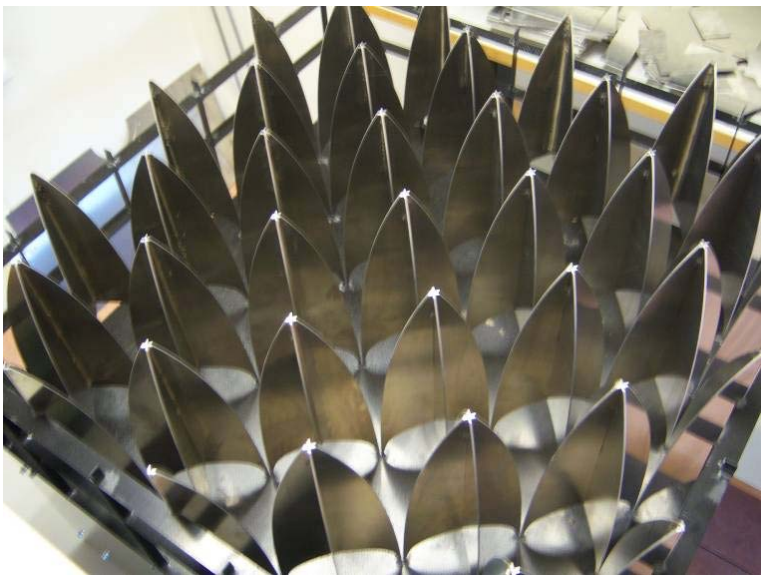

Figure 3.29: Photograph of the manufactured FIDA3 array prototype.

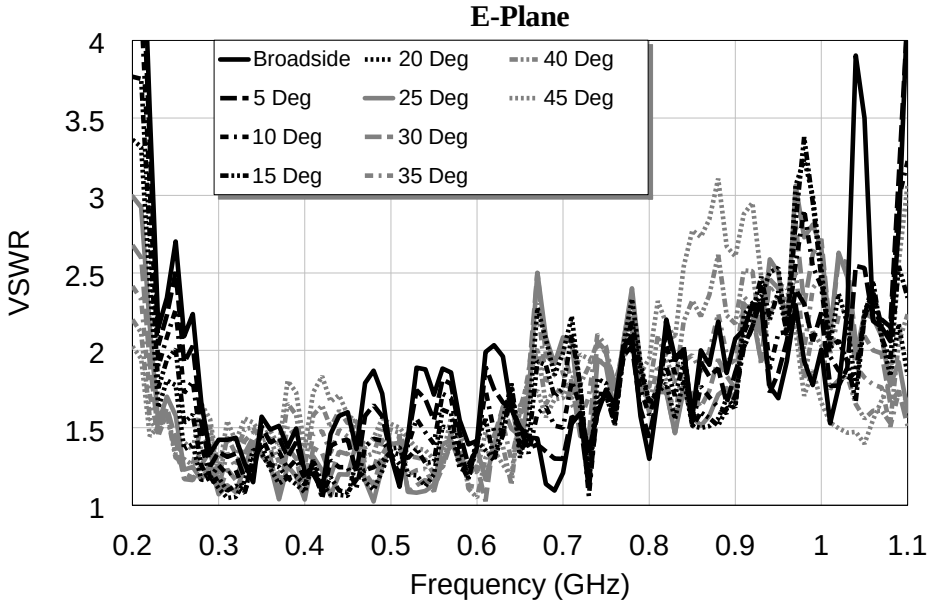

(a)

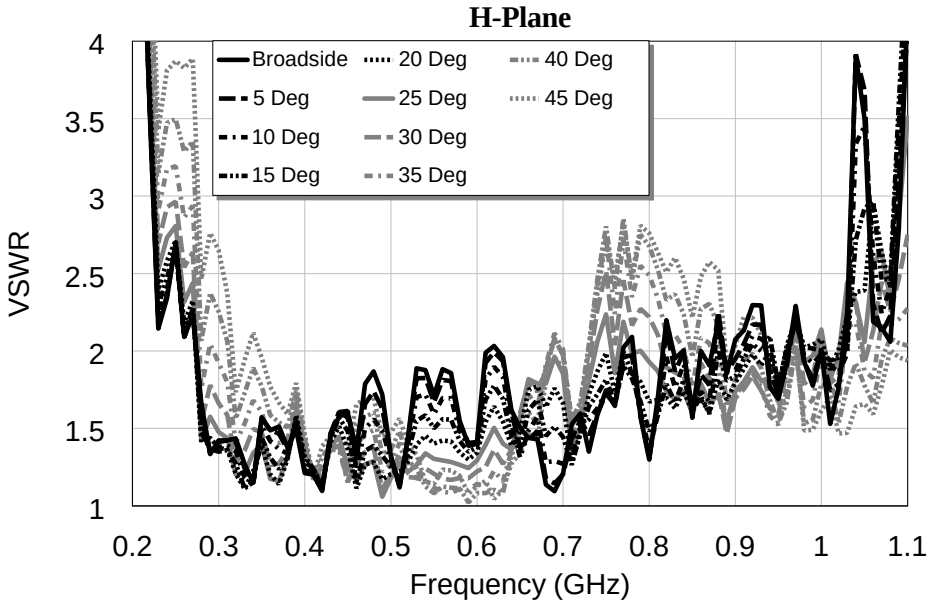

(b)

Figure 3.30: Measured active reflection coefficient of the center element of the array prototype for different E- and H-plane scanning angles.

than in the center elements. This edge-effect is unavoidable, but it becomes less critical with a larger implementation of the array, as in the case of the final SKA substations, due to the lower relative amount of edge elements.

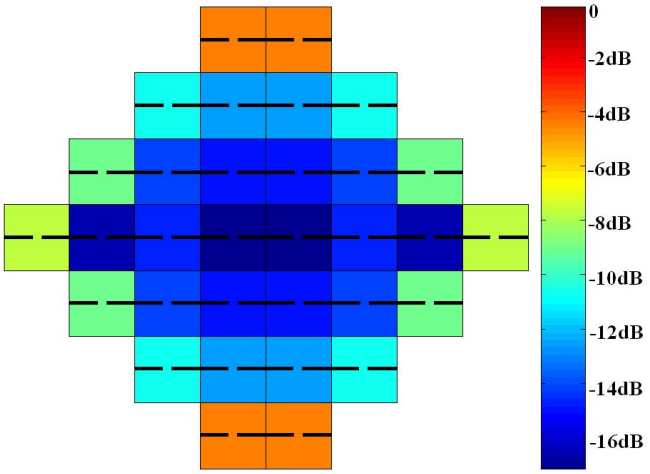

Figure 3.31: Measured active reflection coefficient of the 32 elements of one of the polarizations of the array at 800 MHz.

3.4.3 Differential amplifiers

This subsection presents the design and characterization of the differential LNAs for FIDA3 [27]. The varying impedance of the antenna elements previously presented should be taken into account. The design of a broadband differential low noise amplifier based on discrete elements, covering the bandwidth from 300 MHz to 1 GHz is proposed. In this way, chip components like high Q-factor inductors and high value capacitors can be easily utilized. Although, two different topologies, balanced and fully-differential, were initially studied [44], only the results with the fully-differential one will be presented due to its better performance. As it was presented before, the array antenna elements provide a mean 150 Ω active impedance in differential mode. However, the active antenna impedance curves cover a relatively wide area in the Smith chart due to the relaxed matching condition (i.e., VSWR<2.5) and to the scanning-dependent behavior. Thus, the noise and gain circles of the LNA are indispensable to evaluate the performance of the amplifier in the worst cases. They will be obtained by means of a differential source-pull characterization (subsection 3.3.3). The preliminary design requirements for the present LNA design are summarized in Table 3.3 [45].

Simultaneously obtaining low noise, high gain and unconditional stability is

Table 3.3: Preliminary LNA design requirements.

Parameter	**Value**
Bandwidth	300 MHz - 1 GHz
Noise	< 50 K
Gain	> 20 dB
Stability	Unconditionally stable
Antenna impedance	$\approx 150\ \ \Omega$ (differential)

a difficult task, especially in broadband LNA designs, and different trade-offs should be addressed. The minimum noise figure of a FET is proportional to the drain current, from a threshold level [46]. This implies using low current values to reduce the noise contribution from the FET at a price of degrading the gain response. A batch of measurements with the manufactured prototypes using different transistor currents is a good way to find the most adequate voltage supply levels. On the other hand, stabilization usually requires reducing the gain by the use of resistors, which degrades the noise figure of the amplifier [47]. A parametric study is very helpful in order to obtain the padding resistor values which ensure the stability with the lowest cost in terms of noise figure.

One important additional remark is that the proposed amplifier cannot be considered as isolated from the radiating element and has to work as a unique entity with the antenna forming a differential active antenna. In this way, no matching network would be needed since the differential broadband amplifier would directly match the antenna impedance. This implies that the antenna must provide a near-optimal impedance for the corresponding circuit function to constitute, in this case, a low noise broadband differential amplifying active antenna. Very few broadband active antennas have been proposed till now, and most of them have been based on single-ended amplifiers. One exception to the previous comment are the transmitting active antennas based on push-pull power amplifiers (balanced configuration) [48]. However, the previous topology has been only used for transmitting systems. In addition, the solution proposed for FIDA3 is a differential pair that provides improved common-mode suppression, which is quite advantageous due the inherent protection against external interferences.

3.4.3.1 Proposed fully-differential topology

The circuit schematic of the proposed fully-differential LNA is shown in Fig. 3.32. This prototype is a cascade of two differential amplifiers interconnected with a RC matching network, in which the padding resistors ($R2$ and $R3$ in Fig. 3.32)

are chosen for stability along the whole bandwidth without compromising the noise figure.

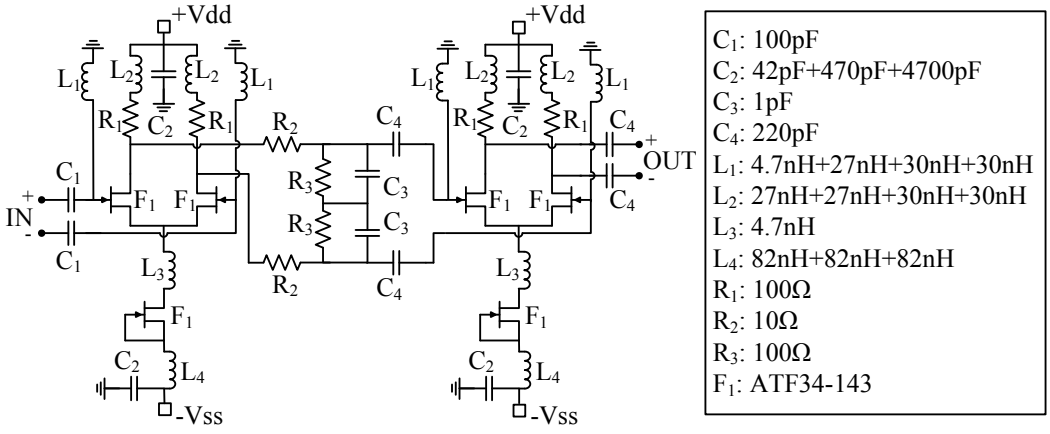

Figure 3.32: Electric schematic of the fully-differential amplifier prototype.

The stability parameter used in this analysis is the input geometric stability factor (1.8). This factor can be obtained as a function of the mixed-mode S-parameters s^A_{ddij} (differential excitations in the input and output planes) of the amplifier as

$$\mu_1 = \frac{1 - |s^A_{dd11}|^2}{|s^A_{dd22} - s^A_{dd11}{}^*(s^A_{dd11}s^A_{dd22} - s^A_{dd12}s^A_{dd21})| + |s^A_{dd21}s^A_{dd12}|} \tag{3.53}$$

The necessary and sufficient condition for unconditional stability of this equivalent two port device is that $\mu_1 > 1$. The parametric study of the amplifier response as a function of $R2$ and $R3$ is shown in Fig. 3.33 and Fig. 3.38 respectively. From our experience, this topology seems somewhat more sensitive to instabilities than a single-ended one. This is due to the fact that the FETs of both branches are interconnected, which may cause power transfer between the branches. A value for the series resistor $R2$ of 10 Ω has been chosen. However, this resistor, $R2$, is not enough to stabilize the circuit, so a shunt resistor $R3$ has been also added. This type of padding reduces the gain as well as improves the output matching, contributing to the stabilization of the circuit [47]. Additionally, the response of $R3$ is equalized by means of the capacitor $C3$. A value for $R3$ of 100 Ω is chosen in the prototype.

The transistors used in this design are the ATF34-143 low noise PHEMT from *Avago Technologies*. The design of the current sources has been done by making use of a FET. Two series inductors ($L3$ and $L4$ in Fig. 3.32) have been included to increase the impedance of the current source. Additionally, several grounded

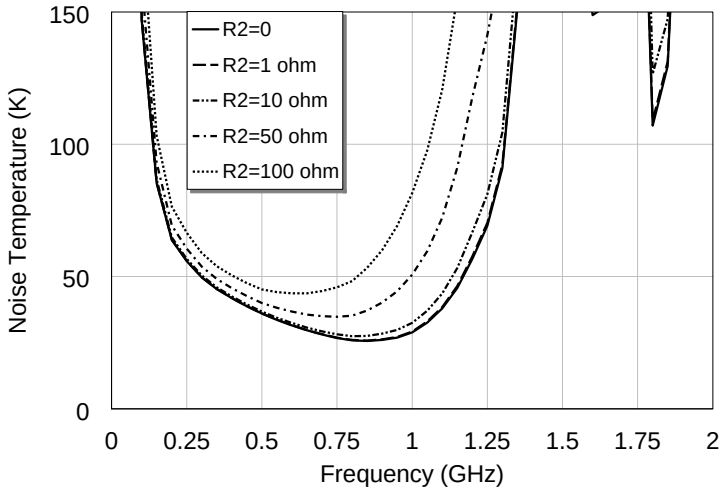

(a)

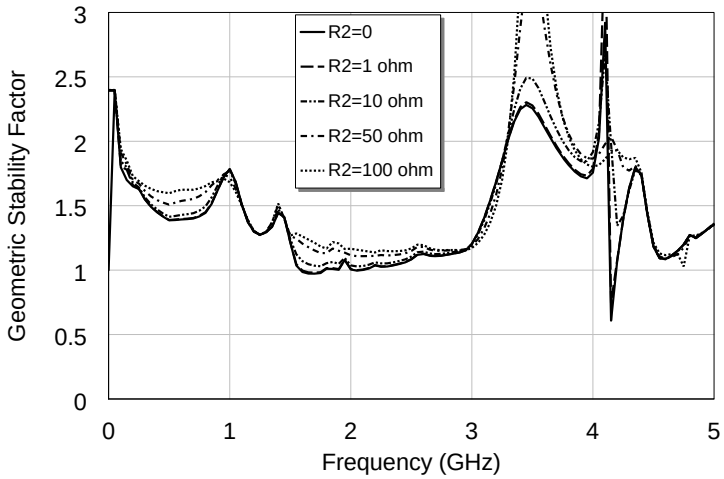

(b)

Figure 3.33: Simulated noise temperature (a) and input geometric stability factor (b) of the differential amplifier for several $R2$ values and $R3$=100 Ω.

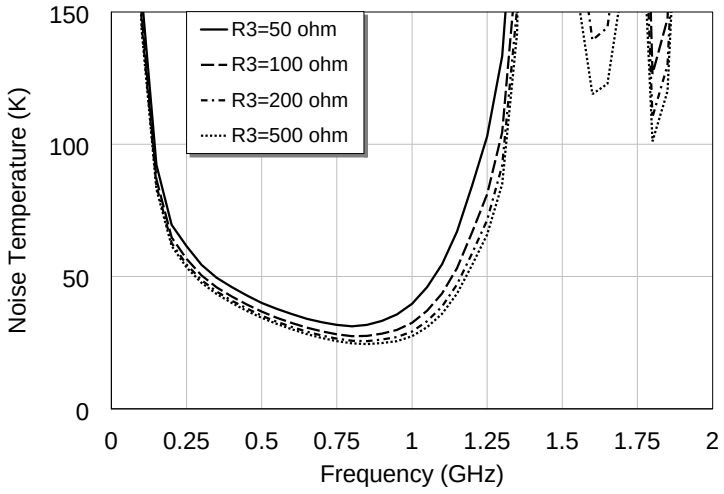

(a)

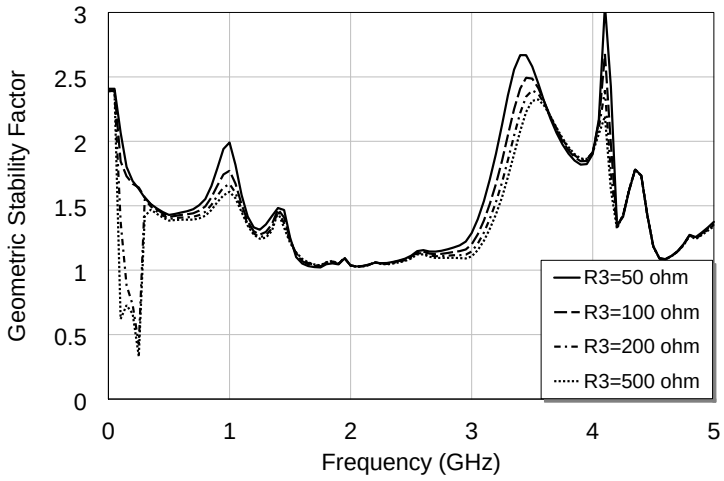

(b)

Figure 3.34: Simulated noise temperature (a) and input geometric stability factor (b) of the differential amplifier for several $R3$ values and $R2$=10 Ω.

shunt capacitors have been used to protect the RF circuit from different DC transient peaks ($C2$ in Fig. 3.32).

With regard to the physical implementation of the circuit, all the components are surface mount devices (SMD). The circuit board is shown in Fig. 3.35. It has been built in microstrip technology with an Arlon 25N substrate (height H=1.5 mm, permittivity ϵ_r=3.38). A thicker substrate has been used in order to reduce the influence of the parasitic feedback capacitances, which may cause instabilities in the amplifier. The dimensions of the manufactured circuit are 60 mm by 50 mm.

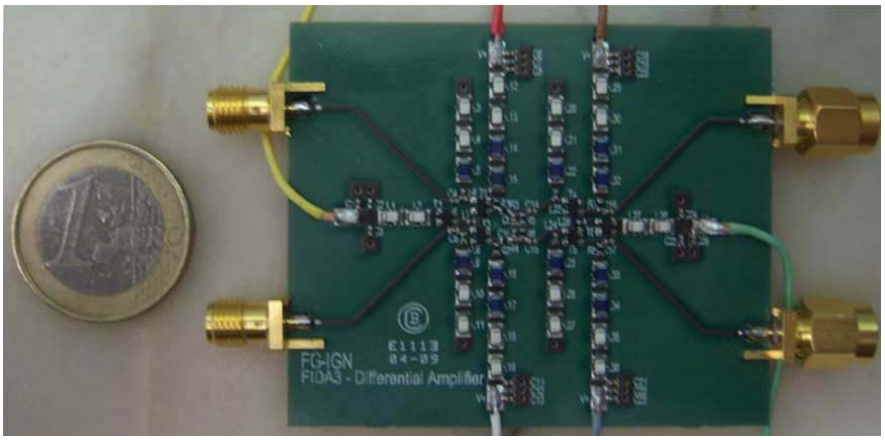

Figure 3.35: Photograph of the differential LNA prototype.

3.4.3.2 50-Ω measurements

This subsection shows the gain and noise measurements of the amplifier, using two baluns at the input and the output. It allows exciting the circuit in differential mode, and provides a two-port equivalent circuit that can be directly measured in a conventional noise or network analyzer. These results have limited significance, since the matching conditions of the amplifier are not the desired ones, but they allow obtaining a first impression about the general performance of the amplifier in the band of interest. The measurements have been taken by using broadband baluns, model ETC1-1-13 of *M/A-COM*, which can work from 4.5 to 3000 MHz (Fig. 3.36). A previous characterization of these baluns has been done, obtaining insertion losses lower than 1 dB, and amplitude and phase unbalances of 0±0.7 dB and 180±8 deg respectively along all the frequency range. The de-embedding method described in subsection 3.3.2.1 has been used to eliminate the loss and unbalance effects introduced by the baluns in the measurement. The gain and noise curves obtained by the fully-differential amplifier are shown in Fig. 3.37. A

gain value larger than 25 dB and a noise temperature below 125 K (NF=1.6 dB) can be seen in the 300-1000 MHz bandwidth. Good agreement between simulation and measurement is obtained with the gain curve, and not so good with the noise curve. In this case, it has also been obtained a CMRR better than 26.5 dB in the band of interest. These 50 Ω measurements have been taken in order to make a comparison between simulations and measurements and see the goodness of the simulations in the entire working band. It must be emphasized that the 50 Ω conditions will not be the ones when the antenna is connected to the differential amplifier.

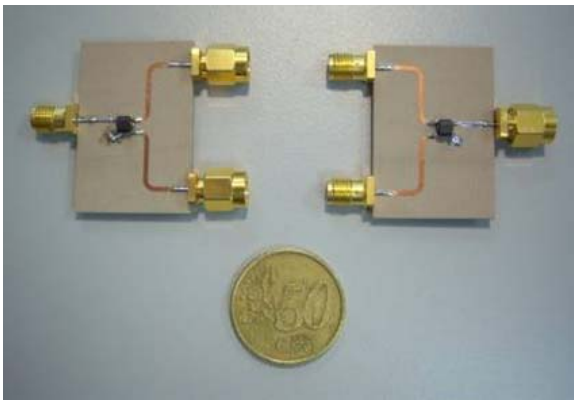

Figure 3.36: Photograph of the transformer-based broadband baluns.

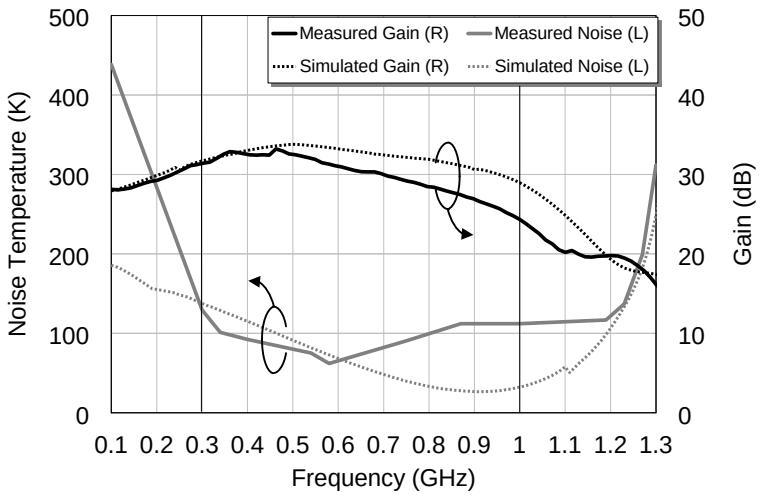

Figure 3.37: Gain and noise measurements in a 50-Ω environment of the fully-differential amplifier with baluns.

Concerning to the analysis undertaken in subsection 3.3.1, the complete mixed-mode characterization can be done from the conventional single-ended measurements. Furthermore, a subsequent post-processing allows obtaining such parameters for any arbitrary port impedances, just by renormalizing the matrix. For this case, we are interesting in obtaining the amplifier parameters for 150 Ω differential source impedance (the average antenna impedance) and for 50 Ω differential load impedance. The measured differential S-parameters (i.e., S_{dd} sub-matrix) are plotted in Fig. 3.38. The gain (s_{dd21}) is higher than 27 dB in the band of interest. The output matching is better than -13 dB, and the input matching is better than -1.8 dB in the band. The poor input impedance matching in the lower part of the band id due to the high impedance presented by the FETs, whose equivalent circuit has a small capacitance connected to ground at the input. All these results are summarized in Table 3.4.

Table 3.4: Measured S-parameters results of the differential low noise amplifier.

Parameter	**Value**
Bandwidth	300 - 1000 MHz
Source impedance	150 Ω (diff.)
Gain	>27 dB
$\|s_{dd11}\|$	<-1.8 dB
$\|s_{dd22}\|$	<-13.0 dB
CMRR	>26.5 dB

3.4.3.3 Source-pull measurements

The source-pull measurements have been undertaken by evaluating the gain and the noise at three frequencies (300 MHz, 650 MHz and 1000 MHz), with thirty-five different impedance points at each frequency. The different source impedances have been synthesized by means of a manual coaxial impedance tuner, model 1819A from *Maury Microwave Corporation* (Fig. 3.39). It consists of a coaxial line with three shunt stubs, whose length can be modified to synthesize the desired input impedances. The measurement scheme consists of the differential amplifier, which is transformed into an equivalent two-port amplifier by means of two baluns (the same that were used in subsection 3.4.3.2), and the impedance tuner connected at the input of the cascaded system. The de-embedding methods for the baluns and the tuner were already discussed in subsections 3.3.2.1 and 3.3.2.3 respectively.

Considering the previous results at 50 Ω (Fig. 3.37), no abrupt variations with

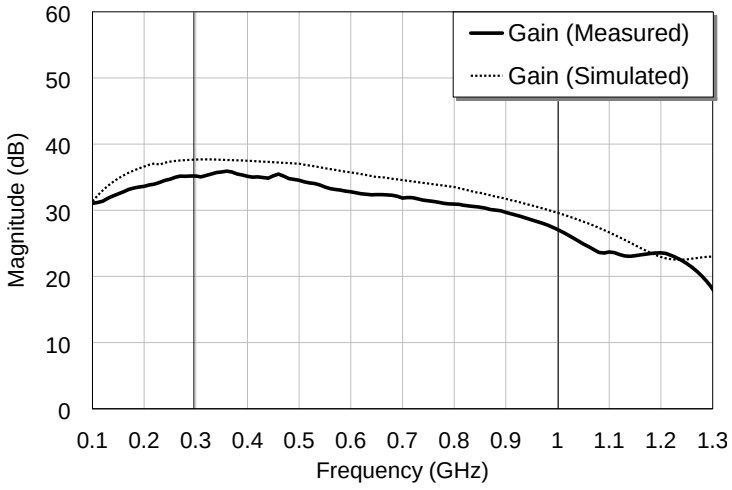

(a)

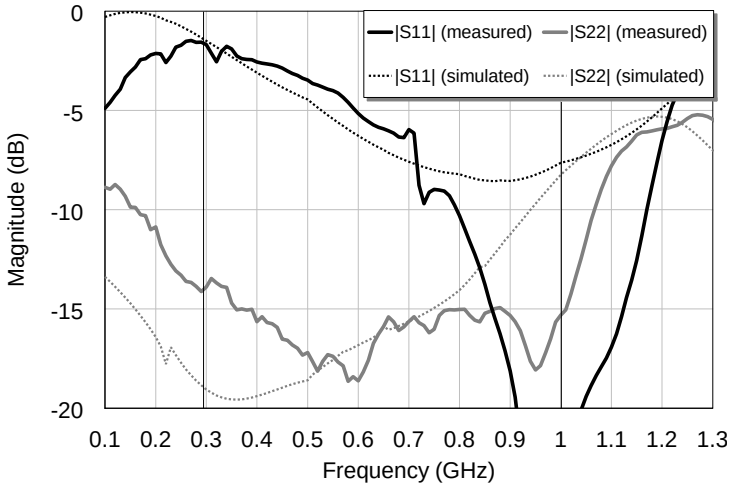

(b)

Figure 3.38: Measured (solid line) and simulated (dashed line) differential S-parameters ($|s_{dd21}|$, $|s_{dd11}|$ and $|s_{dd22}|$) of the differential low noise amplifier.

Figure 3.39: Photograph of the coaxial impedance tuner.

frequency are expected, so three frequency points are considered to be enough for this analysis. The obtained gain and noise circles at the three different frequencies have been represented in Fig. 3.40. By means of such circles, the characteristics of the amplifier (working with an ideal 150 Ω differential source impedance and with the bunny-ear active impedance of Fig. 3.28(a)) have been estimated.

The gain and noise results are summarized in Table 3.5. The results presented in this table correspond to two different situations: a fixed source impedance of 150 Ω, and the simulated active antenna impedance for different array scanning angles. For that last case, three different scanning angles have been considered: 0, 22.5 and 45 deg. For the case of fixed 150 Ω impedance it can be seen that the variation of both the gain and noise values is not very large. A gain higher 26 dB and a noise temperature lower than 55 K (NF=0.75 dB) is obtained. For the scanning case, the gain varies between 35 dB and 25 dB for the worst case while the noise temperature varies between 45 K and 65 K in the worst case. One of the advantages of the source-pull measurement is that it is also possible to extract the complete set of noise parameters (i.e., Γ_{opt}, F_{min} and R_n). In this case, the noise circles from the ideal model of a FET-based amplifier (1.11) have been superposed over the circles obtained from the measurements, and the parameters with which the circles acceptably matched were estimated. This process was "manually" done in this case. A possible improvement can include the development of a software to automatically extract these parameters by minimizing some kind of cost function. The values of Γ_{opt} and F_{min} are indicated in Fig. 3.40. The value of R_n, which indicates how fast the noise performance degrades when the source

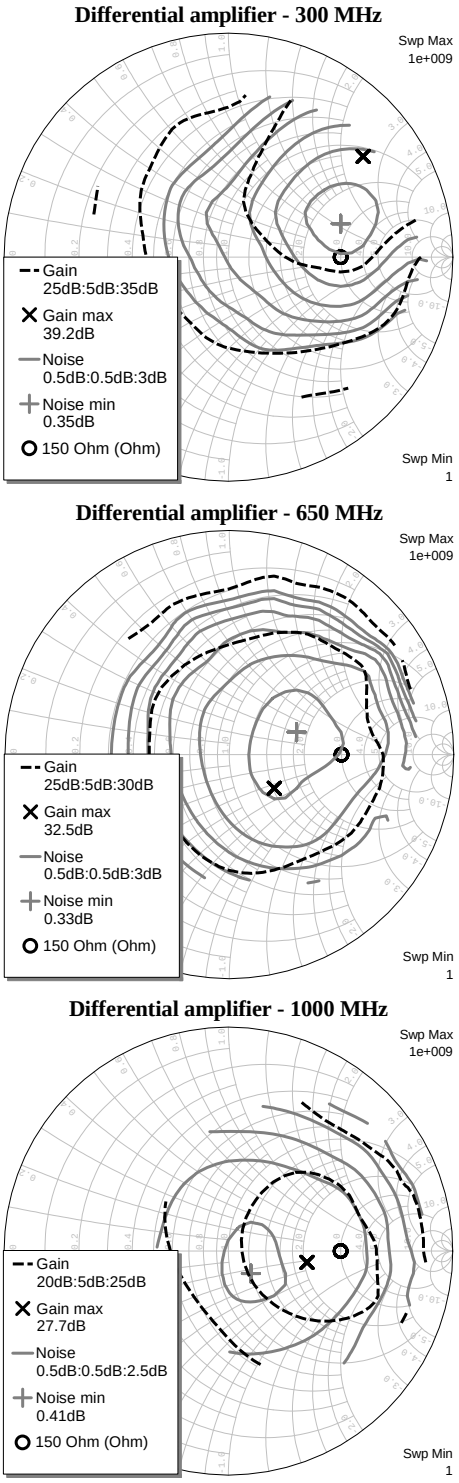

Figure 3.40: Measured gain and noise source-pull curves at 360, 650 and 1000 MHz. The reference impedance of the Smith chart is 50 Ω.

impedance is different from the optimum, is estimated to be 37 Ω in the worst case. This value is sensibly higher than the 23 Ω expected from the simulation.

Finally, in order to have a comparison for the entire frequency bandwidth, a hot/cold noise measurement has been done using the method described in subsection 3.3.2.2. This method is used only for an impedance of 150 Ω, due to the limitations to synthesize arbitrary complex load impedances. The gain has also been obtained from the mixed-mode S-parameters with a 150 Ω differential source impedance. Fig. 3.41 shows the obtained noise temperature with the hot/cold procedure and the gain obtained with the mixed mode method. In addition, all the values obtained from the source-pull method have also been drawn. A good agreement between the different methods is observed.

Table 3.5: Measured source-pull results of the differential low noise amplifier.

Parameter		**Value**			
Source impedance (diff.)		150 Ω	$Z_{antenna}$ (θ=0 deg)	$Z_{antenna}$ (θ=22.5 deg)	$Z_{antenna}$ (θ=45 deg)
Gain ($\lvert s_{dd21}\rvert$)	300 MHz	36 dB	35 dB	35 dB	34 dB
	650 MHz	31 dB	31 dB	31 dB	30 dB
	1000 MHz	26 dB	27 dB	27 dB	25 dB
Noise (T)	300 MHz	43 K	51 K	55 K	65 K
	650 MHz	40 K	59 K	59 K	55 K
	1000 MHz	55 K	51 K	45 K	45 K
F_{min} (T_{min})	300 MHz	0.35 dB (24 K)			
	650 MHz	0.33 dB (23 K)			
	1000 MHz	0.41 dB (29 K)			
R_n	300 MHz	37 Ω			
	650 MHz	20 Ω			
	1000 MHz	9 Ω			

3.4.4 System integration

In the previous subsections, the design and characterization of both the radiating structure and the differential LNAs was presented. This subsection shows the system integration process, and the characterization of the complete active antenna array prototype. The integration of the system parts follows the scheme previously presented in Fig. 3.26. The antennas are placed over a metallic layer, which works as the ground plane of the array. The differential ports of the antennas pass through the ground plane through holes in such plane. The differential

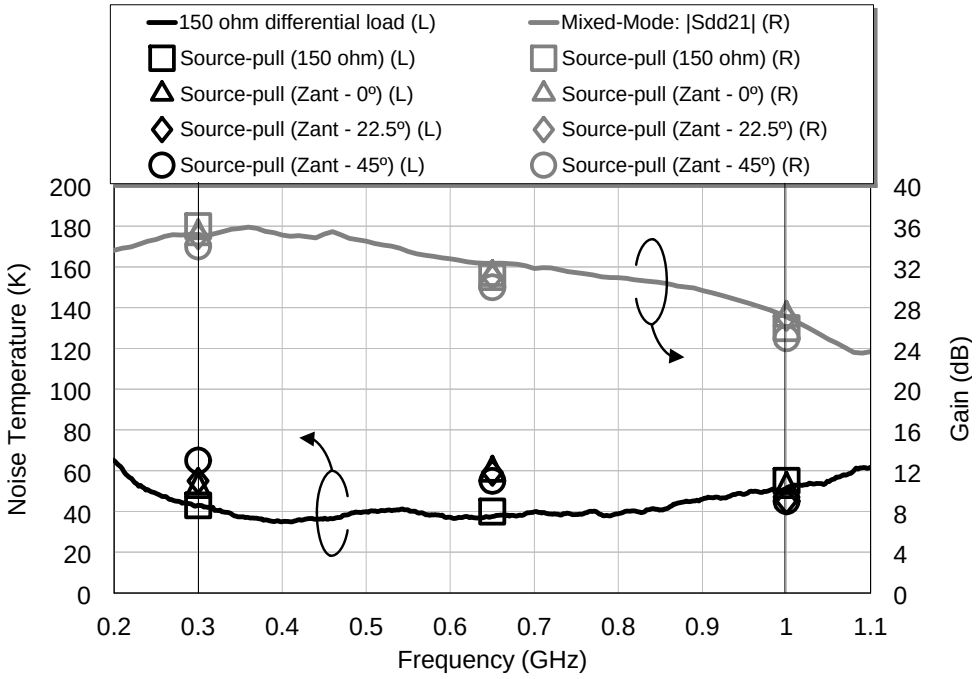

Figure 3.41: Measured results of the differential amplifier: noise temperature obtained from the hot/cold method and gain from the mixed-mode S-parameters compared with the discrete noise and gain source-pull results.

LNAs are soldered to each antenna below the ground plane, as it is shown in Fig. 3.42(a). Each differential LNA provides single-ended output (passive balun at the output). Thus, the outputs of the 32 elements for each polarization are combined by using commercial broadband combiners (i.e., four 8-to-1 and one 4-to-1 boards), so one single coaxial output is given per polarization. The connection between the amplifiers and the combiners is done by means of flexible coaxial cables. A photograph of the array box, including the combiners, the DC circuits and the coaxial cables is shown in Fig. 3.42(b).

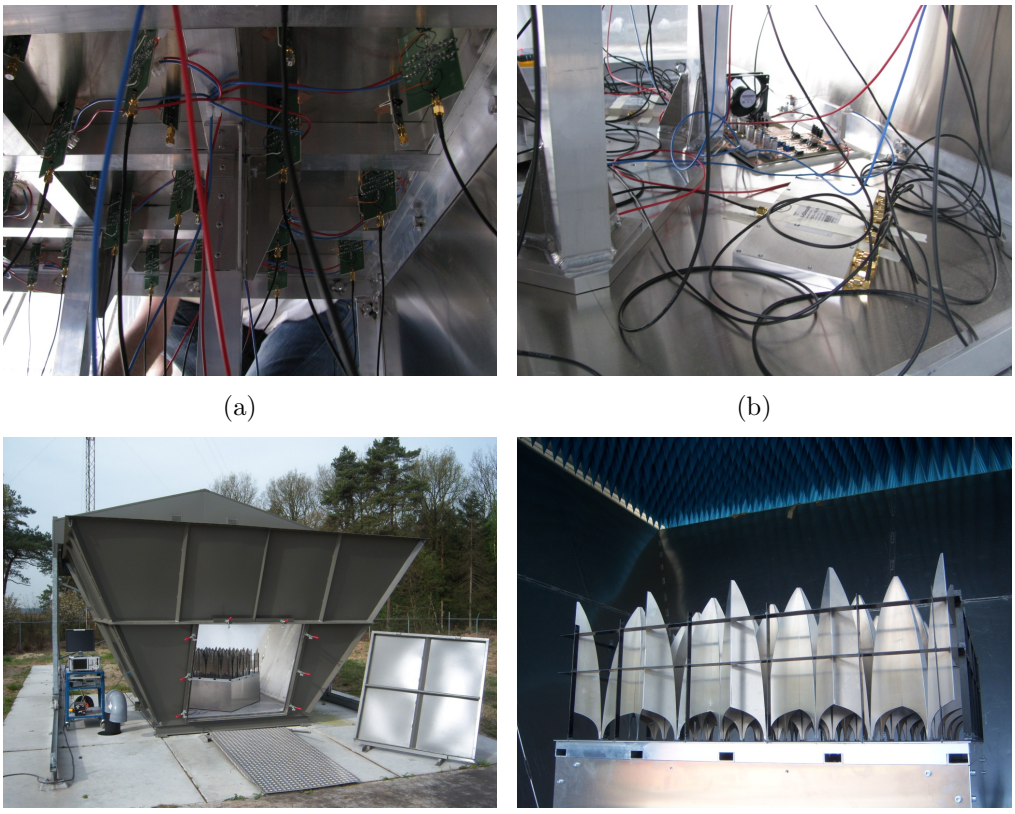

(a) (b)

(c) (d)

Figure 3.42: Photographs of the system integration and measurement process: (a) differential LNAs connected to the antennas, (b) power combiners and power supply circuits, (c) FIDA3 array inside THACO test facility, and (d) measurement setup for *hot* characterization.

The noise characterization of the array system has been done in THACO, the hot/cold system facility developed by ASTRON (The Netherlands) [49]. THACO is a large metallic box with removable roof that allows characterizing the noise temperature of many types of receiving systems. The photograph of the FIDA3

prototype inside the THACO system is shown in Fig. 3.42(c). The aim with the lateral metallic walls is to isolate the system under test from the undesired terrestrial interferences. The characterization of the system is based on the Y-factor method (Fig. 1.15). The output power of the system is measured when the system is excited through two different source temperatures. For this case, the *cold* test is done when the system is looking at the sky, and the *hot* test is obtained when the array is looking toward an absorbing material, which is placed in the removable roof. The photograph of the FIDA3 prototype during the *hot* characterization is shown in Fig. 3.42(d). The *cold* temperature is given by the average sky noise temperature, whose curve is represented in Fig. 3.43, and the *hot* temperature is T_0, which is the ambient temperature. With the two temperatures and the two corresponding output powers, the system noise temperature can be calculated by using (1.14) and (1.15).

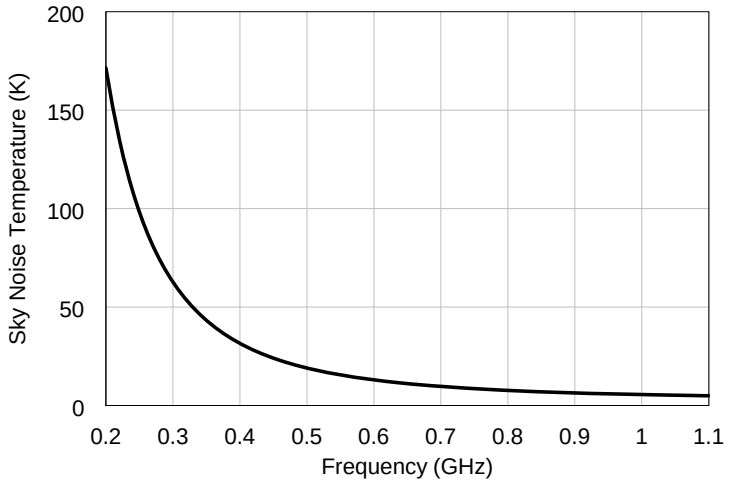

Figure 3.43: Sky noise temperature in the band of interest.

The measurement setup of the FIDA3 array in THACO is shown in Fig. 3.44. In order to obtain higher levels of power with the spectrum analyzer, a broadband low noise amplifier is connected to the output. In addition, a tunable band-pass filter is connected before the output amplifier, in order to avoid out-of-band interferences that can saturate such amplifier. Thus, the measurement along the band of interest is undertaken by means of spectrum captures in sub-bands of 20 MHz, with frequency steps of 10 MHz.

Fig. 3.45 shows the measured noise temperature of the implemented FIDA3 array tile. This system noise value is the average noise temperature of the 32 elements [51]. The grey curve shows the noise temperature curves obtained from each one of the sub-bands in which the measurement has been done. The continu-

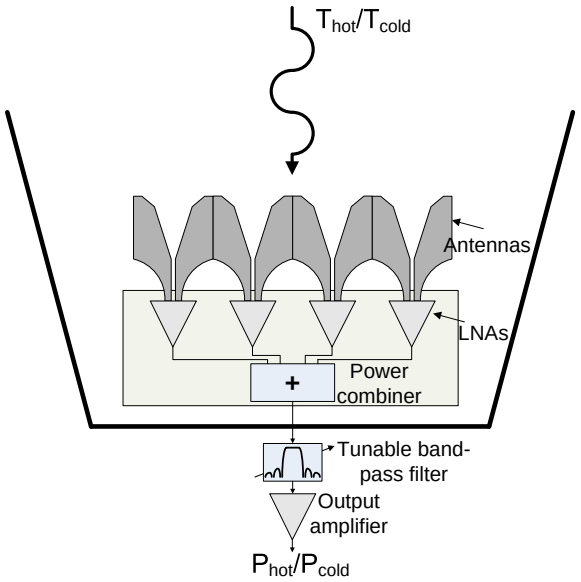

Figure 3.44: Measurement configuration of FIDA3 in THACO.

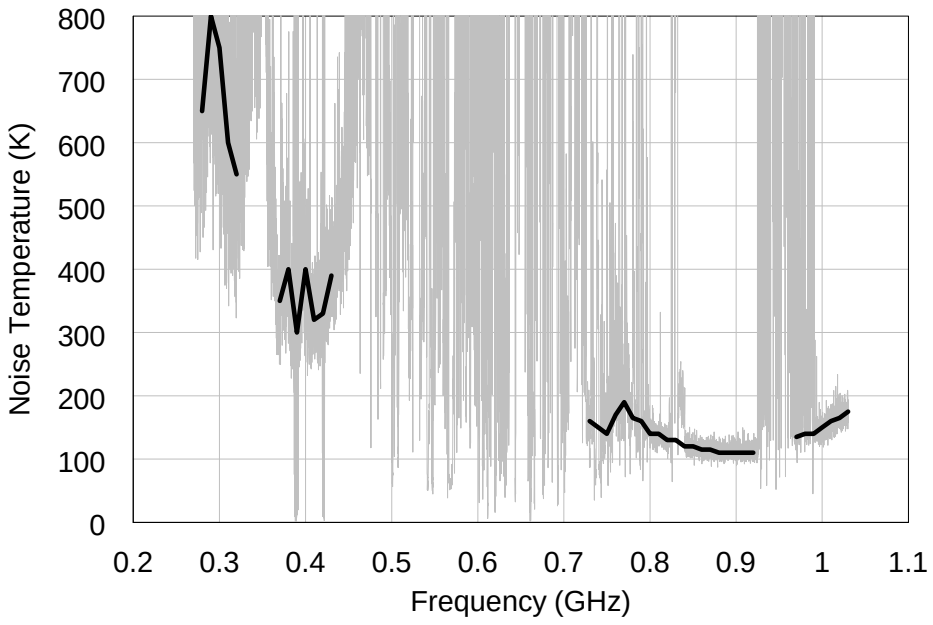

Figure 3.45: Measured noise temperature of the FIDA3 array tile: grey curve shows the raw data, and the black line represents the average value in the frequency ranges with low interferences.

ous black line corresponds to the average noise temperature value in the frequency ranges in which the absence of interferences allows a reliable acquisition of the noise temperature level. There are three frequency ranges, (i.e., 330-360 MHz, 440-720 MHz and 930-960 MHz), in which the interferences, presumably coming from TETRA, TV, GSM900 and other services [50], make impossible a correct measurement of the system noise temperature. This effect is illustrated in Fig. 3.46. It shows the measured *hot* and *cold* output power traces, and the corresponding calculated system noise temperature in four different sub-bands. The first two cases (i.e., 440 MHz (a) and 900 MHz (b)) are obtained in ranges with low interference distortions, and the noise temperature value can be obtained with certain reliability. The next two cases (i.e., 600 MHz (c) and 940 MHz (d))

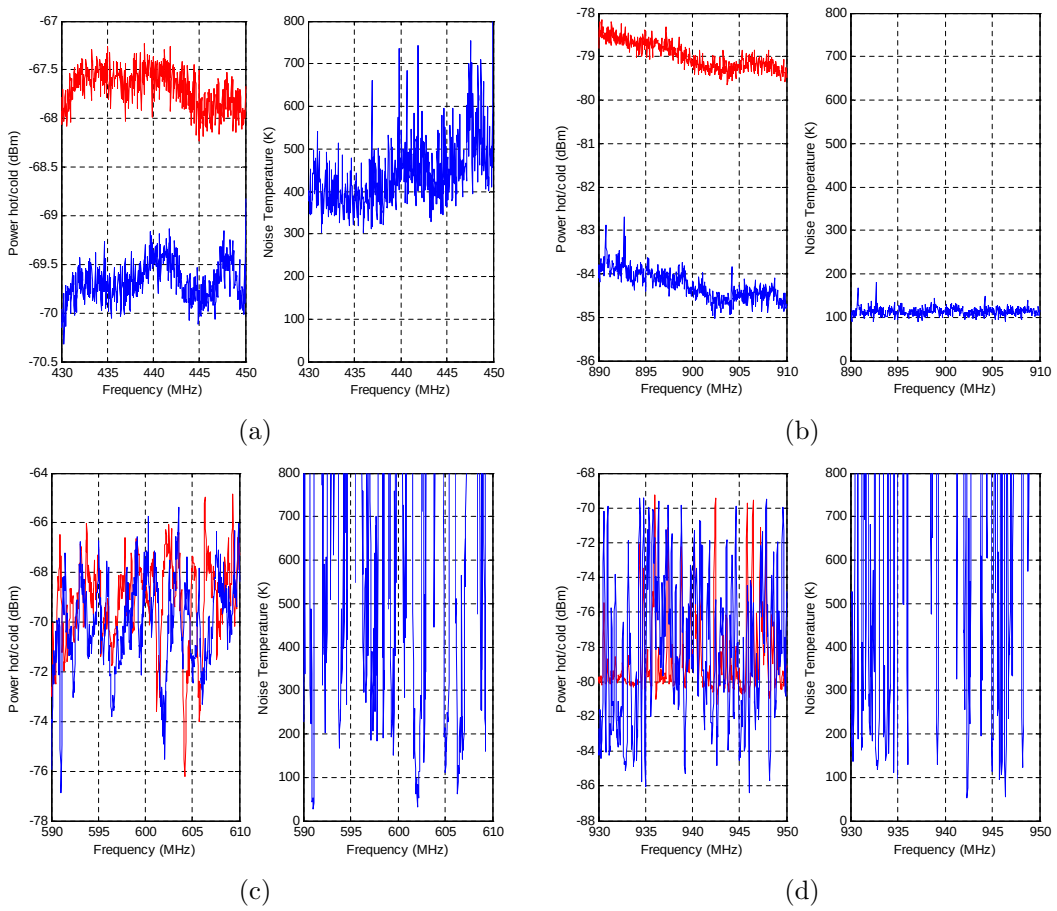

Figure 3.46: Measured hot (red) and cold (blue) output power traces (left) and system noise temperature (right) from the characterization of the FIDA3 array tile in THACO at four different frequencies.

show the measured data at two frequencies with strong interferences that do not allow obtaining a reliable noise temperature level. The complete set of measured results is detailed in [52].

Regarding to the measured performance of the implemented FIDA3 array tile (Fig. 3.45), the system noise temperature is around 700 K in the lower part of the band, and decreases down to around 100 K in the higher part of the band. These noise values significantly differ with respect to the 55 K measured from the isolated amplifier and 150 Ω source impedance matching (Fig. 3.41). This disagreement can be attributed to different effects. In the higher part of the band, the system noise temperature was around 100-150 K and the noise temperature of the LNA was around 50 K. In this range, the discrepancy can be attributed to the mismatching introduced by the edge elements, whose LNAs see a source impedance far from the desired 150 Ω. It must be noticed that 14 of the 32 elements are placed in the edge of the grid. In the case of the lower part of the band, the discrepancy is much more significant, since the system noise temperature reaches up to 800 K in the worst case. One of the reasons of the larger system noise temperature at low frequencies is that the array is electrically smaller (in terms of wavelength), and therefore further from the infinite array assumption (at which the array has been optimized). Furthermore, the noise resistance R_n of the amplifiers of FIDA3 is higher at low frequencies, so the LNAs are less robust against antenna impedance variations in this range.

Beyond the previous effects, the influence of the input impedance of the LNA should also be considered for the 32-element array characterization. The measured active antenna impedances of the 32 elements of the FIDA3 array tile, assuming ideal 150 Ω loading conditions and broadside radiation, are shown in Fig. 3.47(a). The reflection coefficient (assuming Z_0=150 Ω) of the center element is lower than -8 dB in the band of interest, and in the case of the other elements this parameter increases up to -2.5 dB in the worst case. This degradation was expected, due to the poorer performance provided by the edge elements. However, as it was analyzed in subsection 3.2.3, the active antenna impedance seen by the amplifier needs to consider the effect of the own amplifier. Thus, the actual active reflection coefficients (also normalized for Z_0=150 Ω) of the antenna elements considering that the array is loaded by the differential LNAs used in the FIDA3 prototype are shown in Fig. 3.47(b). As it can be observed from the graph, the poor input reflection coefficient given by the amplifier in the lower part of the band causes a strong mismatching in some of the antenna elements in this frequency range. This effect is even more pronounced at low frequencies, due to the higher mutual coupling levels. In fact, some of the active reflection coefficients get values higher than 0 dB, which provides a source impedance condition with unpredictable consequences in the LNAs. This value may result surprising, since

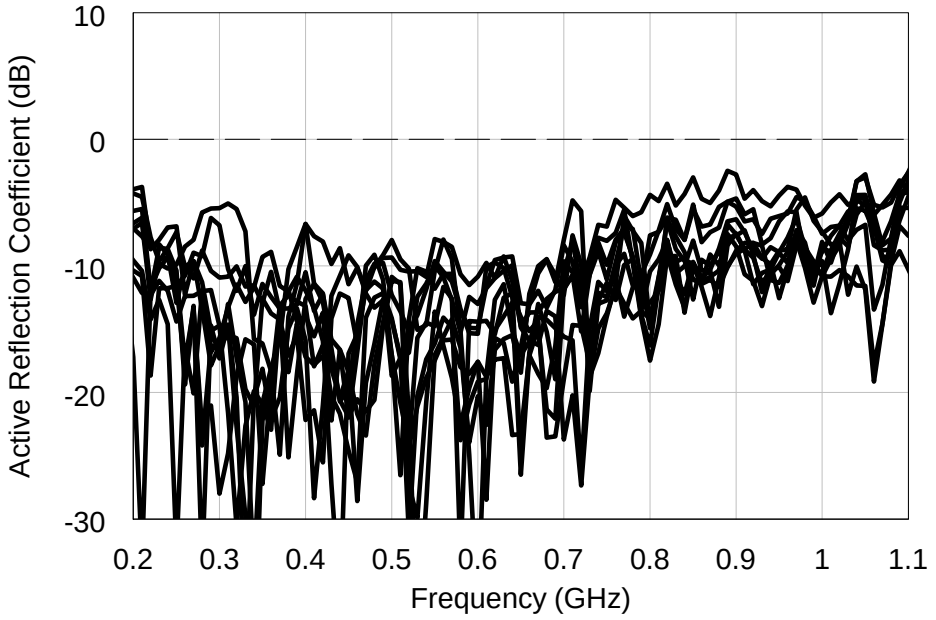

(a)

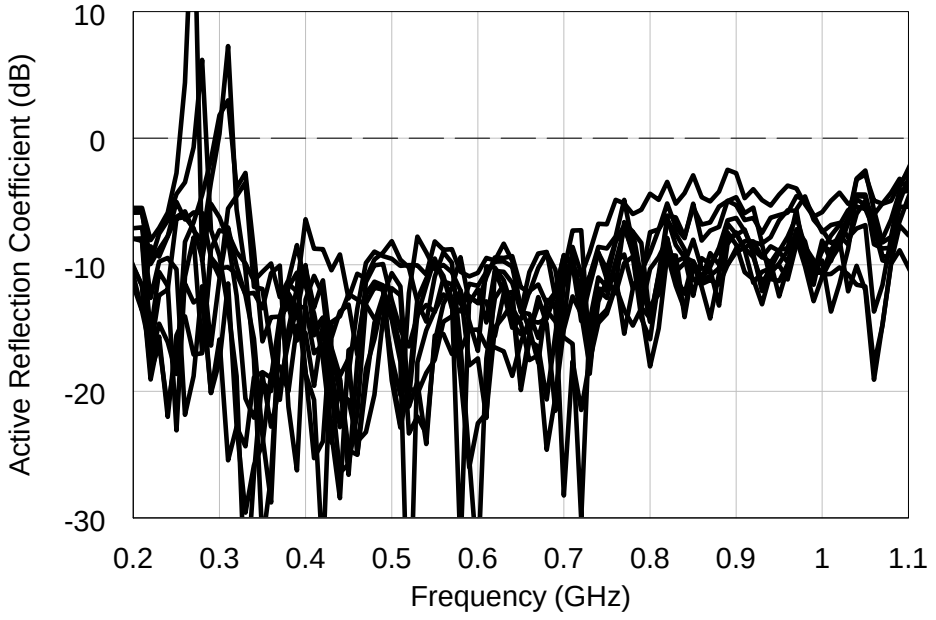

(b)

Figure 3.47: Measured active reflection coefficient of the 32 elements of FIDA3 array tile assuming ideal 150 Ω loading conditions (a) and loading with the implemented differential LNAs (b).

a conventional reflection coefficient higher than 0 dB do not correspond to a passive circuit, but it is feasible for the active reflection coefficient of a finite passive array[2]. With this source impedance condition, corresponding to $|\Gamma_{act}| > 1$, the noise performance of the LNA is unpredictable. Furthermore, the stability is not guaranteed, since the unconditionally stable amplifier ensures stability for source impedances that are inside the Smith chart. The combination of both effects, antenna mismatching and potential instabilities, seems a convincing explanation for the extremely high noise level present at low frequencies in the measurement of the FIDA3 array tile (Fig. 3.45). With a larger implementation of the array, as in the case of the final SKA stations, these effects caused by the poor input power matching of the LNAs are expected to be mitigated (as it was concluded in subsection 3.2.3), at least for the inner elements. However, it is not so clear for the edge elements, since they provide different performance depending on the LNA design and with independence on the dimensions of the array (Fig. 3.8(d)). This discussion is considered to be out of the scope of this thesis and will not be analyzed in detail. Nevertheless, it is presented as an important future line to be studied and taken into account for the final SKA implementation.

As a summary, the information that can be extracted from the implemented array tile is limited due to the reduced size of the prototype. Only in the higher part of the band, the array begins to be large enough to obtain noise values comparable to the expected from the isolated LNA measurements (i.e., between 110-180 K). Thus, a significantly larger array implementation is necessary to obtain a more reliable idea of the expected noise temperature with the final SKA stations. It presents some restrictions, such as cost, assembly or characterization issues, that should be considered. For example, for the case of the THACO system, it is not prepared for systems much larger than the implemented 1 m^2 tile. On the other hand, the difficulties to characterize a system in the 300-1000 MHz band have been evident from the measured results, due to the effects of the external interferences generated by the many communication services operating in this frequency range. In the present case, it avoided to acquire reliable data in more than a half of the band of interest.

[2]Let's imagine a two-element antenna array. Assuming that the antennas are identical, we have that s_{11}^{ant}=s_{22}^{ant} and s_{21}^{ant}=s_{12}^{ant}. A passive antenna network with s_{11}^{ant}=0.6 and s_{21}^{ant}=0.6 is completely feasible ($|s_{11}|^2 + |s_{21}|^2 \leq 1$). However, the module of the active reflection coefficient at broadside is higher than 1 ($|\Gamma_{act}| = |s_{11}^{ant} + s_{21}^{ant}| = 1.2 > 1$)

3.5 Improved Differential LNA Designs

As it was shown in Section 3.4, the differential LNA prototype designed for the FIDA3 array prototype presented an acceptable performance. This first approach provided a gain higher than 26 dB and a noise temperature lower than 55 K for 150 Ω differential source impedance, and working between 300 and 1000 MHz. However, this noise temperature is still far from the 25-30 K that are desirable for the final SKA stations, since they are intended to achieve a system noise temperature below 38 K [14]. Another important aspect that could be improved is the noise resistance R_n, since the antenna impedance matching is not very restrictive, and therefore the LNAs should provide low noise performance for a relatively wide region of source impedances in the Smith chart. On the other hand, other aspect that could be improved is the input power matching s_{dd11} of the LNAs, whose potential effects over the array performance have been analyzed in Section 3.2 and Section 3.4. This section shows two differential LNA implementations with improved performance compared with the LNA prototype developed in Section 3.4.

3.5.1 Inductively degenerated design

The *inductive degeneration* is a technique widely used in the design of single-ended LNAs (e.g., [53],[54]), which consists on connecting two inductors in series with the gate and the source of the transistor, as it is shown in Fig. 3.48. This configuration allows compensating the input capacitance of the transistor and, therefore, obtaining real input impedance at a certain resonance frequency. Assuming ideal inductors, it is feasible to obtain perfect input matching without any cost in terms of noise. The input impedance of the inductively degenerated FET shown in Fig. 3.48 can be obtained as

$$Z_{in} = g_m \frac{L_s}{C_t} + j\left(\omega L_t - \frac{1}{\omega C_t}\right) \tag{3.54}$$

where $L_t = L_g + L_s$, $C_t = C_{gs} + C_{gd}(1 + g_m(R_{ds}Z_0/(R_{ds} + Z_0)))$ and Z_0 is the reference impedance. On the other hand, the optimum noise matching of the structure can be approximated by

$$Z_{opt} \approx Z_{opt}^{FET} - j\omega L_g \tag{3.55}$$

where Z_{opt}^{FET} is the optimum noise matching impedance that provides the minimum noise figure of the FET in common-source configuration (without any external component). The previous approximation is valid for low values of L_s.

Regarding to (3.54), the inductor L_s can be used to independently adjust the desired real part of Z_{in} (usually Z_0). For this value of L_s, the other inductor L_g can be used to cancel out the imaginary part of Z_{in} and, therefore, achieve perfect matching at this frequency. Since the value of L_g also affects the noise matching (3.55), a trade-off value is necessary to achieve both low return losses and low noise performance.

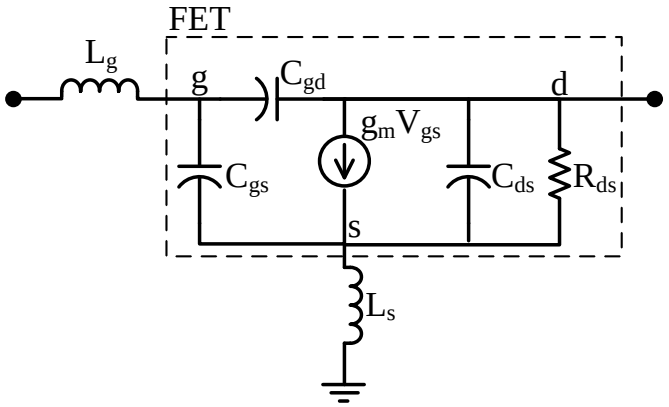

Figure 3.48: Circuit schematic of an inductively degenerated FET. The components inside the box represent the equivalent circuit of the transistor.

The objective with the previous topology is to improve the performance of the differential LNA design presented in Section 3.4. More precisely, the inductive degeneration will be used with the aim of reducing both the return losses and the noise temperature of a fully-differential topology based on the same *Avago* ATF-34143 transistors. The simulated real part of the input impedance of the inductively degenerated transistor, for different values of the source inductor L_s (assuming L_g=0), is shown in Fig. 3.49. As it was predicted by (3.54), the resistive part of the input impedance of the inductively degenerated FET is almost constant and directly proportional to the inductance L_s. Since the nominal source impedance is 75 Ω in single-ended mode (i.e., 150 Ω in differential mode), a value of L_s around 1.5 nH is necessary to improve the input power matching.

The simulated performance of an ideal two-stage fully-differential amplifier based on inductively degenerated FETs obtained for different values of the inductances L_s and L_g is shown in Fig. 3.50 and Fig. 3.51 respectively. As it was expected from (3.54) and (3.55), inductance L_s greatly affects the input matching (Fig. 3.50(a)) but has low influence over the noise performance (Fig. 3.50(b)). Once the inductance value L_s is fixed to achieve the desired input resistance (i.e., 150 Ω in differential mode), the value of the gate inductance L_g can be adjusted to obtain the desired trade-off between input matching and noise temperature.

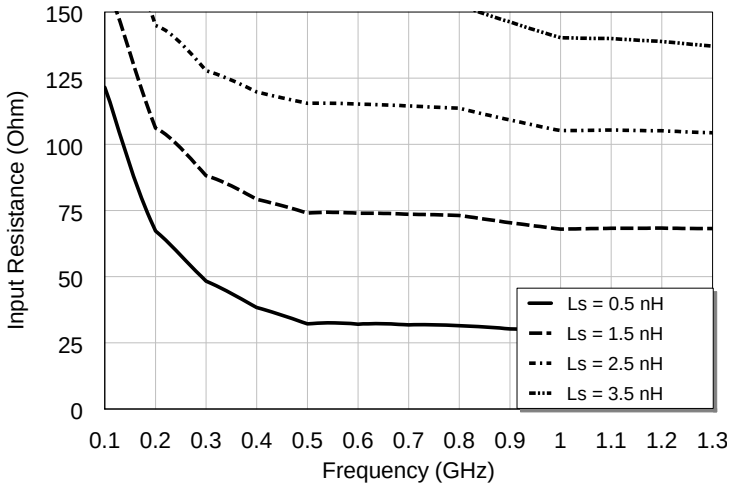

Figure 3.49: Real part of the input impedance of an inductively degenerated FET for different values of the source inductance L_s.

As it can be seen from Fig. 3.51, a value of L_g around 8 nH provides return losses lower than -6 dB and noise temperature below 30 K in the band of interest. An additional degree of freedom could be given by placing an external capacitor in parallel with C_{gs} (Fig. 3.48) [54], but this option was not considered in this case in order to reduce the losses of additional passive components. In addition, although the inductive degeneration technique is conceived a priori for narrow-band designs, acceptable performance has been obtained in this case in a broad bandwidth.

The circuit schematic and the photograph of the inductively degenerated differential LNA prototype are shown in Fig. 3.52 and Fig. 3.53 respectively. It consists on two cascaded fully-differential stages, with differential input and single-ended output. The single-ended output is achieved by using a passive balun, model ETC1-1-13 from *M/A-COM*. The transistors are FETs, model ATF34-143 from *Avago*. Each transistor has two inductors connected at its gate and its source, following the scheme shown in Fig. 3.48. The substrate is Rogers 4003 (height H=0.407 mm, permittivity ϵ_r=3.55).

The simulated input and output geometric stability factors (1.8) are shown in Fig. 3.54. These parameters are both higher than one from 0 to 4 GHz, which ensures unconditional stability in this frequency range. The input and output reflection coefficients, assuming 150 Ω differential source and 50 Ω single-ended load impedances, are shown in Fig. 3.55. The discrepancies between measurement and simulation of the output parameter are attributed to the idealized model of the balun transformer used for the simulation. Both input and output return

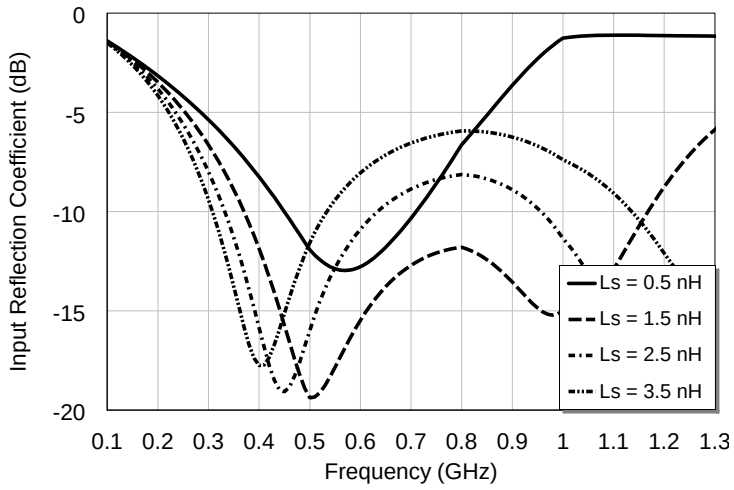

(a)

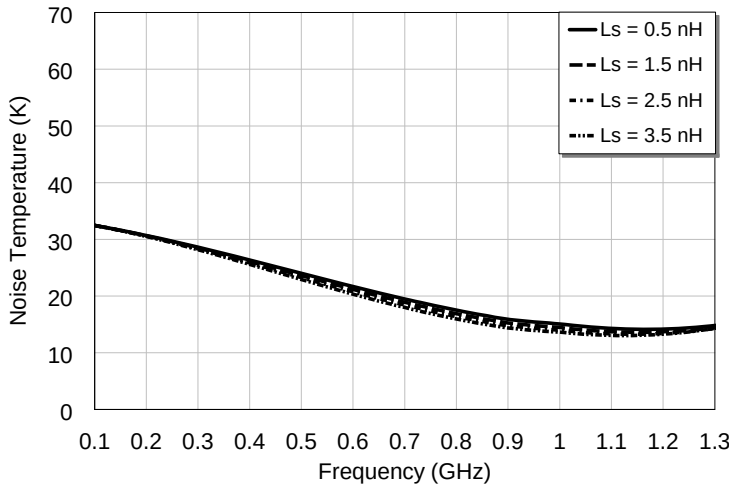

(b)

Figure 3.50: Simulated input matching (a) and noise temperature (b) of a differential amplifier based on inductively degenerated FETs, for different values of L_s and L_g=8.2 nH.

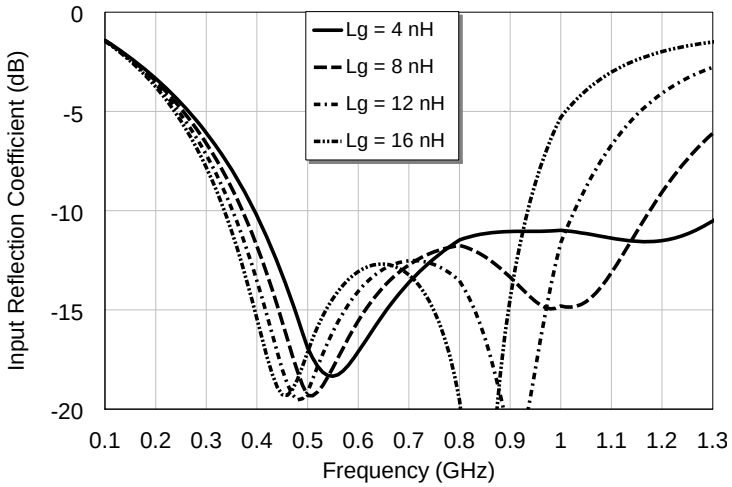

(a)

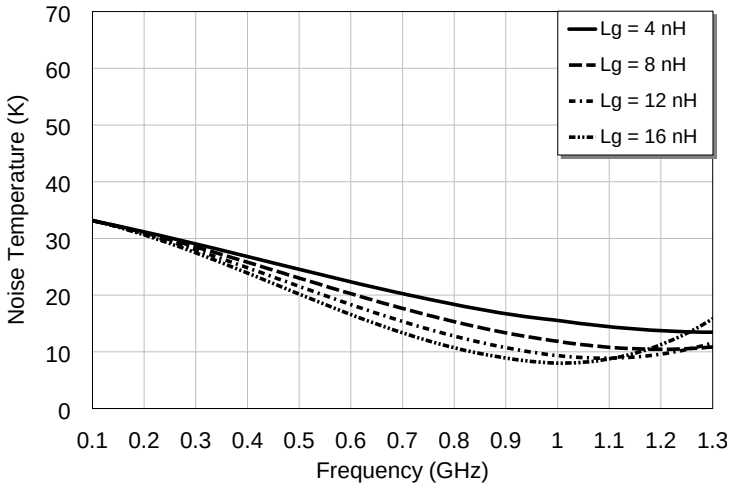

(b)

Figure 3.51: Simulated input matching (a) and noise temperature (b) of a differential amplifier based on inductively degenerated FETs, for different values of L_g and L_s=1.5 nH.

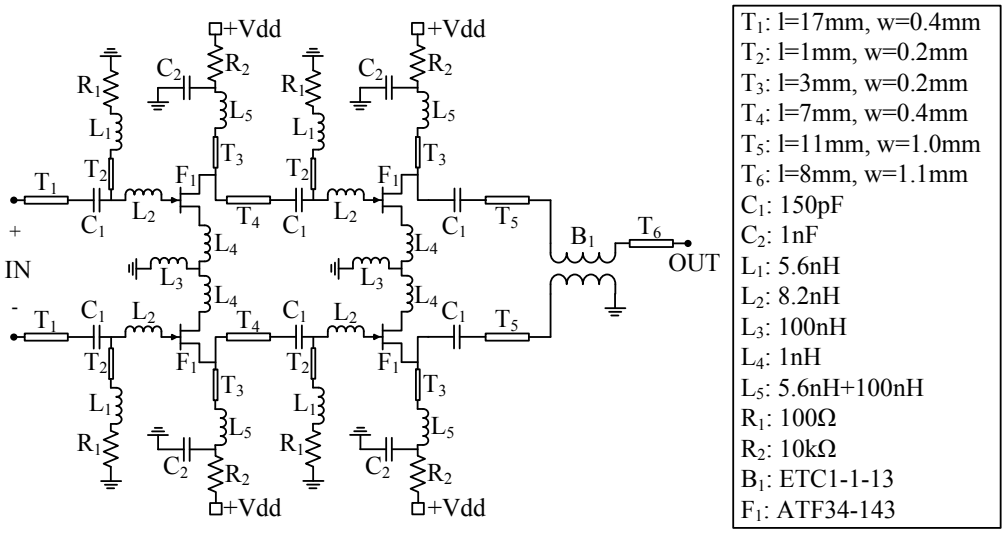

Figure 3.52: Circuit schematic of the inductively degenerated differential LNA.

losses are lower than -6 dB in the 300-1000 MHz bandwidth. It presents a significant improvement compared with the FIDA3 LNA prototype of Section 3.4, which provided an input reflection coefficient of -1.8 dB in the lower part of the band. This poor performance was due to the very high impedance seen at the input of the transistors at hundreds of MHz (small gate-to-source capacitance C_{gs}). In this case, the source inductance is used to cancel out the effect of this capacitance and, therefore, achieve better input power matching. The gain and the noise performance of the prototype is shown in Fig. 3.56. The gain is higher than 26 dB in the band of interest, which is similar to the one obtained with the

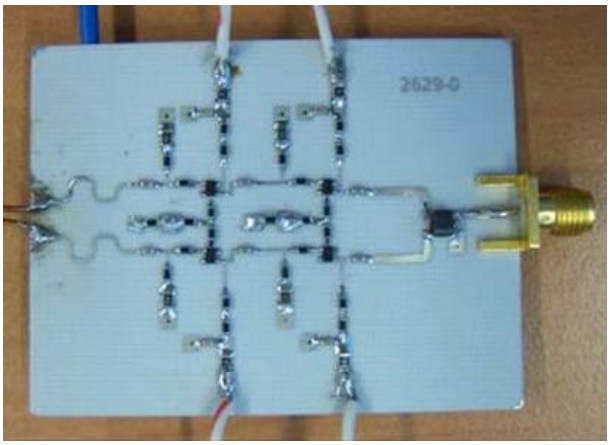

Figure 3.53: Photograph of the inductively degenerated differential LNA board.

FIDA3 prototype. The noise performance has been measured using the method based on the hot/cold differential load [24]. Both simulated and measured curves acceptably agree in the band of interest. It can be seen that the measured noise temperature is lower than 40 K in the band. It implies a noise temperature reduction of around 15 K in comparison with the differential LNA implementation presented in Section 3.4.

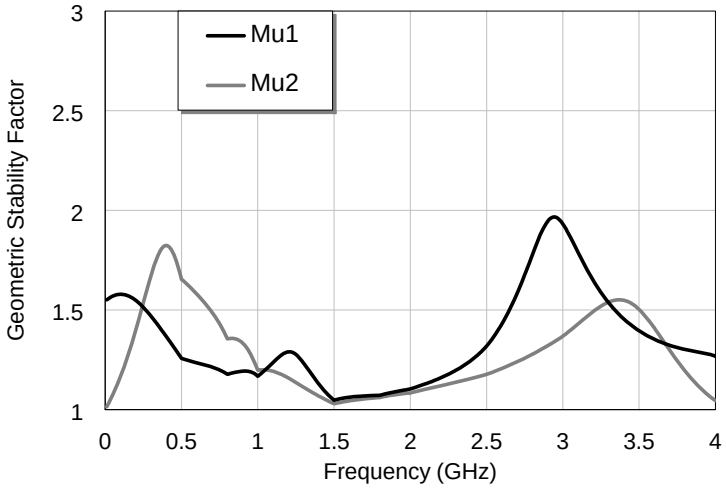

Figure 3.54: Simulated input and output geometric stability factors of the inductively degenerated differential LNA.

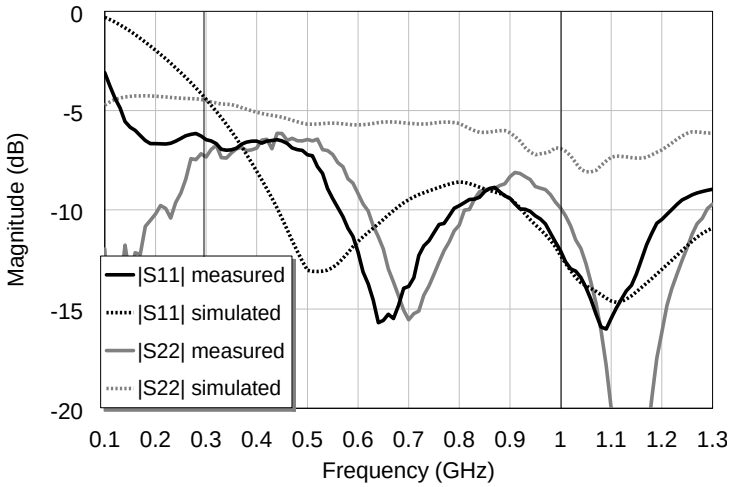

Figure 3.55: Simulated and measured reflection coefficients of the inductively degenerated differential LNA.

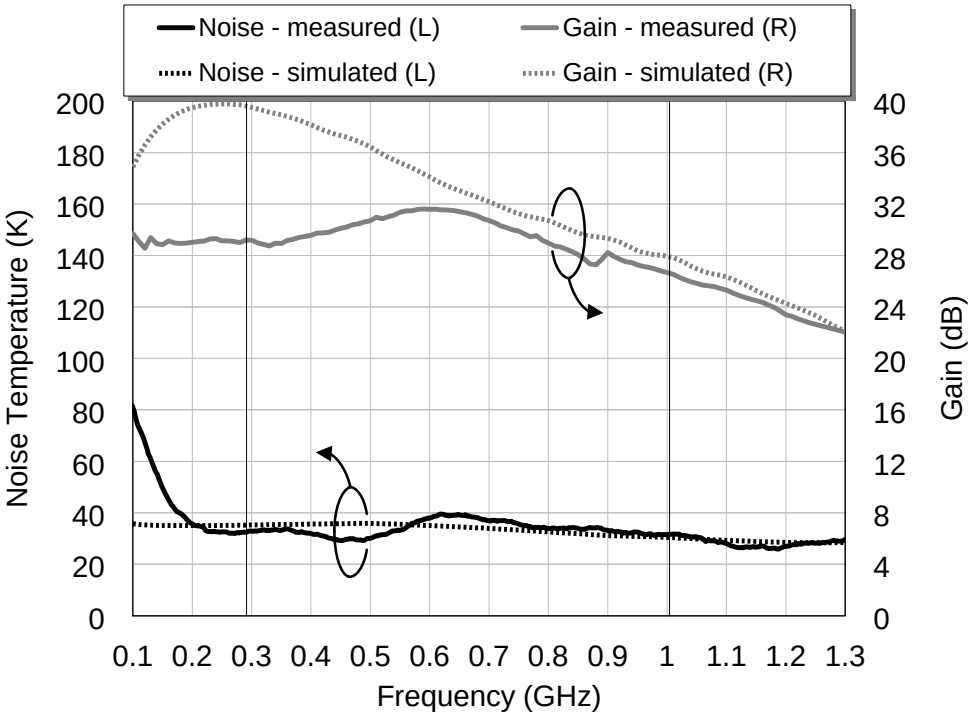

Figure 3.56: Simulated and measured gain and noise temperature of the inductively degenerated differential LNA.

3.5.2 Balanced design

The objective with this second design is to obtain lower noise temperature, using a state-of-the-art transistor technology. The active device in this case is a dual amplifier (two parallel transistors into the same chip), model CGY2105XHV from *OMMIC*. The device technology is also PHEMT, as in the case of the *Avago* ATF-34143, but this new device provides less than a half of the noise resistance value R_n. It is very interesting for broadband applications, in which perfect noise matching is difficult to achieve in the entire band, but the noise degradation is lower for source impedances different to the optimum one. Since the sources of the two transistors are already interconnected inside the chip, techniques such as the inductive degeneration are not feasible in this case. Consequently, the input power matching will not be a priority in this design. Furthermore, the topology will be balanced instead of fully-differential, since the central pad of the chip (i.e., the sources of the transistors) should be directly connected to ground for stability reasons.

The proposed LNA topology is based on two cascaded balanced stages, as it is shown in Fig. 3.57. The simulated results of the structure (using ideal components) for different values of the series resistance R_s and the gate inductance L_g are shown in Fig. 3.58 and Fig. 3.59 respectively. For the case of R_s, this component is used to stabilize the amplifier. As it can be seen in Fig. 3.58(a), a value of R_s higher than 20 Ω is necessary to achieve unconditional stability up to 4 GHz. However, the higher the value of R_s, the higher the increase in terms of noise temperature, as it is shown in Fig. 3.58(b). Thus, a trade-off value is required to ensure stability with the lower cost in terms of noise. On the other hand, the value of the gate inductance L_g can be used to improve the noise matching of the amplifier, as it is shown in Fig. 3.59. This first approach with ideal components is quite promising, with noise temperatures lower than 25 K in the band of interest.

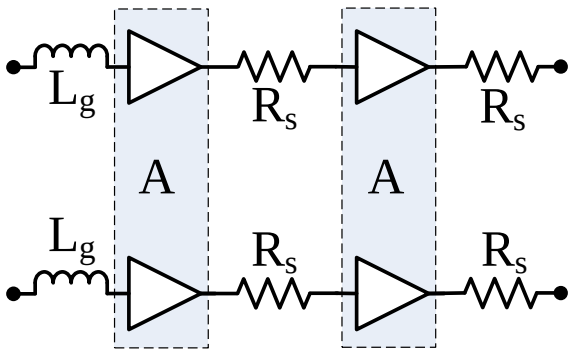

Figure 3.57: Basic balanced LNA configuration.

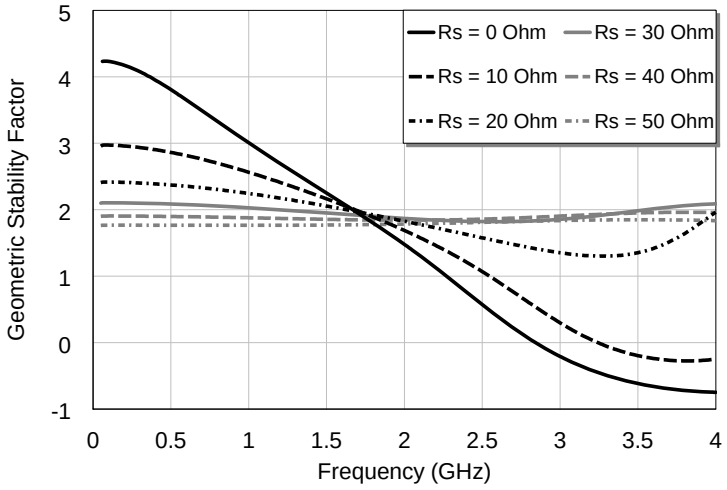

(a)

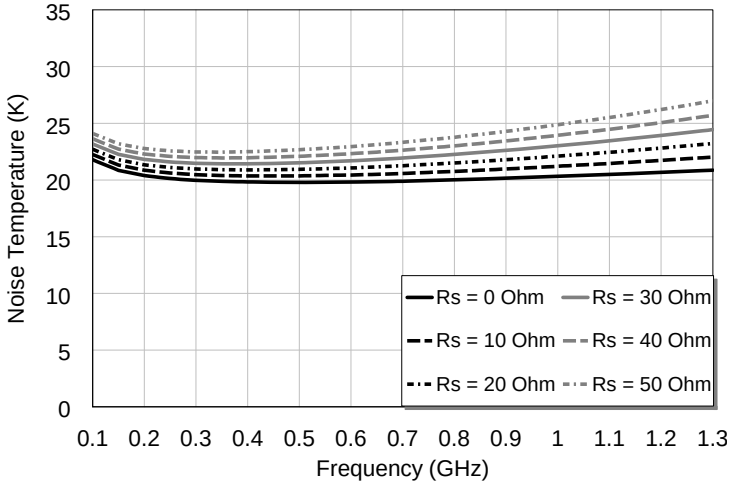

(b)

Figure 3.58: Simulated input geometric stability factor (a) and noise temperature (b) of the balanced amplifier, for different values of R_s and L_g=0 nH.

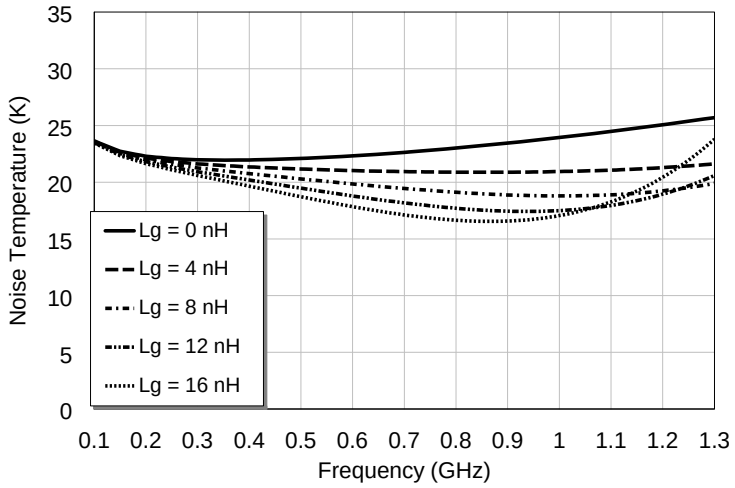

Figure 3.59: Simulated noise temperature of the balanced amplifier, for different values of L_g and R_s=40 Ω.

The circuit schematic and the photograph of the balanced LNA prototype are shown in Fig. 3.52 and Fig. 3.53 respectively. It consists of two cascaded balanced stages, with differential input and single-ended output. As in the previous case, the single-ended output is achieved by using a *M/A-COM* ETC1-1-13 balun. As it was stated before, the active devices are dual amplifiers, model CGY2105XHV from *OMMIC*. The substrate is Rogers 4003 (height H=0.813 mm, permittivity ϵ_r=3.55).

The simulated input and output geometric stability factors (1.8) are shown in Fig. 3.62. Both parameters are higher than one from 0 to 4 GHz, which ensures unconditional stability. The input and output reflection coefficients, assuming differential source impedance of 150 Ω and a load impedance of 50 Ω, are shown in Fig. 3.63. As it could be expected, the input return losses are high, between -1.8 dB and -2.8 dB, due to the absence of power matching structures. The output matching is better, being this parameter below -5 dB in the band of interest. The measured gain and the noise curves of the balanced prototype are shown in Fig. 3.64. Despite the high input return losses, the gain is higher than 36 dB in the band of interest, which is around 10 dB higher than with the previous prototypes. The noise measurement method is the same than in the previous design [24]. Both simulated and measured noise curves agree quite well in the band of interest. There is an out-of-band peak at low frequencies, not present in the simulation. Since no oscillations were observed during the characterization process, and no peaks appeared in the S-parameter results, this anomaly can be attributed to some kind of external interference during the hot/cold measurement.

In any case, it does not seem to affect the performance in the band of interest. Regarding to the graph, the measured noise temperature is better than 30 K in the 300-100 MHz band, which implies an improvement of around 10 K with respect to the previous design, and around 25 K compared with the LNA developed for FIDA3.

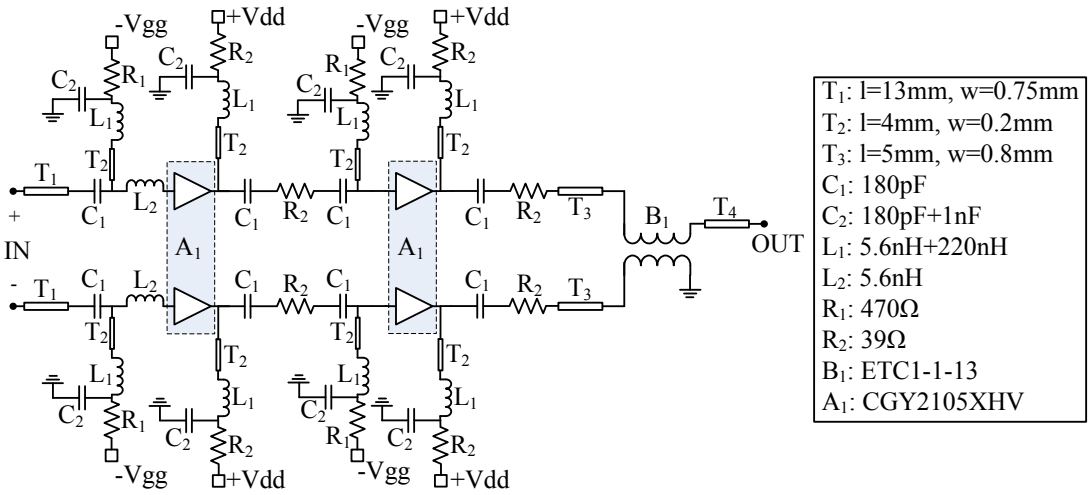

Figure 3.60: Circuit schematic of the balanced LNA.

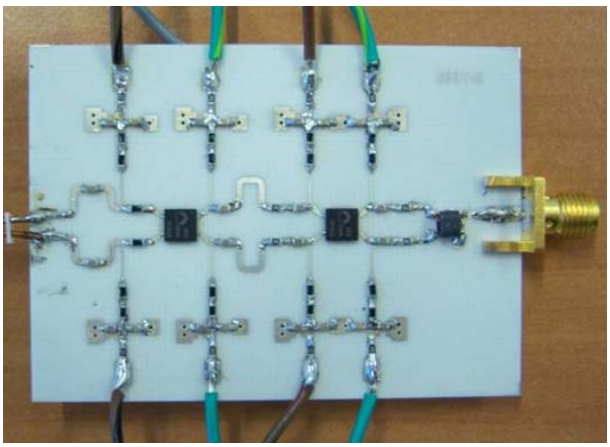

Figure 3.61: Photograph of the balanced LNA board.

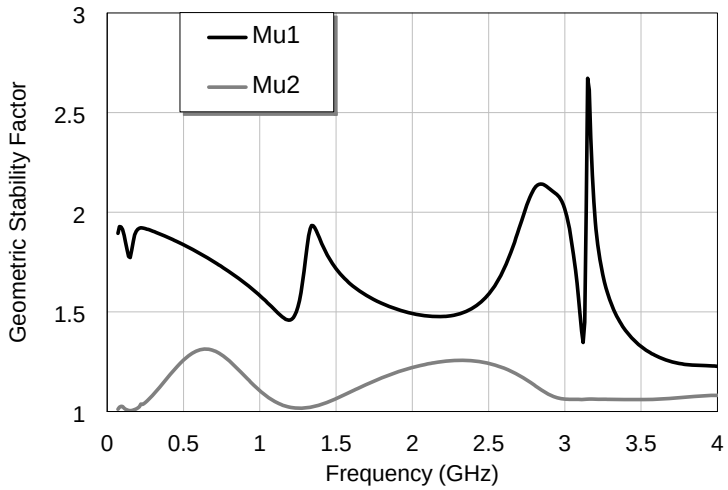

Figure 3.62: Simulated input and output geometric stability factors of the balanced LNA.

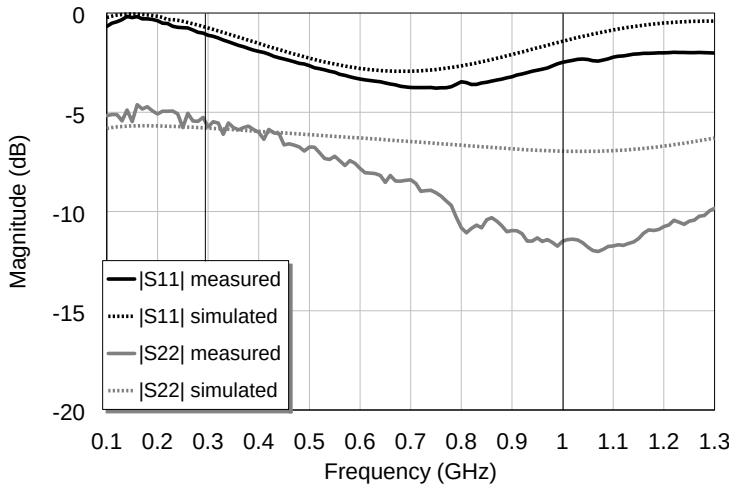

Figure 3.63: Simulated and measured reflection coefficients of the balanced LNA.

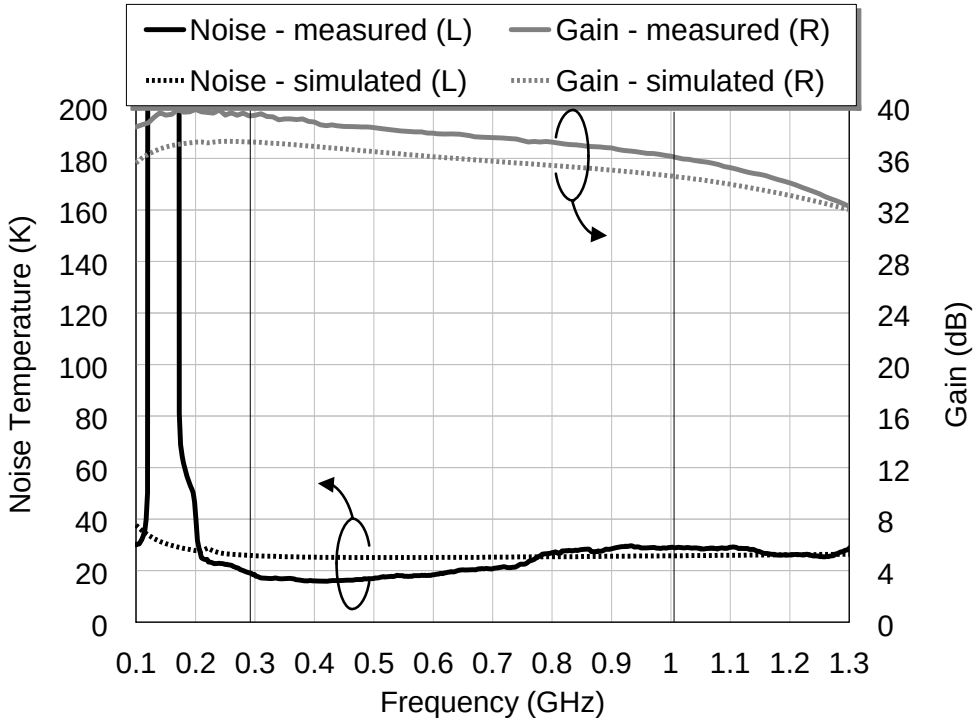

Figure 3.64: Simulated and measured gain and noise temperature of the balanced LNA.

3.5.3 Summary of results

The two differential LNA designs presented in this section have been developed with the aim of improving the performance provided by the LNA prototype designed for FIDA3, which was presented in Section 3.4. A comparison with the main features of the three LNA designs is shown in Table 3.6. The characterization of the three prototypes has been done assuming 150 Ω differential input and 50 Ω single-ended output excitations. The band of interest agrees with the intended mid-frequency range of SKA, which covers from 300 to 1000 MHz. The gain of the balanced LNA is significantly higher than the other two prototypes, due to the higher transconductance of the *OMMIC* CGY2105XHV transistor compared with the *Avago* ATF-34143 transistor. The inductive degeneration technique has been found as an effective way to improve the noise temperature of broadband differential amplifiers. Thus, the noise temperature of the inductively degenerated amplifier is more than 10 K better than the FIDA3 device, using the same transistor model. Also, the input return losses have been reduced with this topology, from -1.8 dB to -6.0 dB in the worst cases. It has been found difficult to significantly improve this value, basically due to the broadband performance and the high capacitive impedance seen from the input of the transistors in the lower part of the band. For the case of the balanced amplifier, the use of an state-of-the-art active device has allowed reducing the noise temperature below 30 K in the band. However, no matching technique has been used to improve the return losses (due to restrictions with the package) and, therefore, the input reflection coefficient is very poor in this last case. In addition, the noise resistance R_n has

Table 3.6: Measured results of the three differential LNA prototypes.

	FIDA3 LNA (subsection 3.4.3)	**Ind. deg. LNA** (subsection 3.5.1)	**Balanced LNA** (subsection 3.5.2)
Bandwidth	300 - 1000 MHz		
Source impedance	150 Ω (diff.)		
Gain	>27 dB	>26 dB	>36 dB
Noise temperature	<53 K	<40 K	<30 K
Noise resistance *	<23 Ω	<13 Ω	<8 Ω
$\lvert s_{dd11}\rvert$	<-1.8 dB	<-6.0 dB	<-1.1 dB
$\lvert s_{ss22}\rvert$	<-13.0 dB	<-6.0 dB	<-5.5 dB
Common-mode rejection	>23 dB	>23 dB	>24 dB

* simulated

been reduced in the last two designs, which means improved robustness against source impedance variations. This parameter is very important in this case, in which the active antenna impedance varies for different array scanning angles. Finally, a measurement of the common-mode rejection has been undertaken. This value has been obtained as the ratio between the gain with common-mode input and single-ended output and the gain with differential input and single-ended output (i.e., $|s_{sd21}|/|s_{sc21}|$). It must be noted that this definition is different to the classical common-mode rejection ratio (3.19), since the output of the last two prototypes is inherently in single-ended mode. In all the cases, the common-mode rejection is better than 23 dB in the entire band.

Regarding to the noise performance of the different LNA prototypes presented in Table 3.6, the balanced amplifier seems to be the most adequate to achieve the lowest system noise temperature in an hypothetical implementation of a mid-frequency range SKA station. In fact, assuming that most antenna elements provide the desired 150 Ω active antenna impedance, the noise temperature provided by such elements can be more than 10 K lower than the one obtained with the inductively degenerated design. This assumption is consistent for the inner elements of the array. However, paying attention to the results shown in Section 3.4, and more precisely to the graphs shown in Fig. 3.47, the choice of the best LNA prototype can be not so obvious due to the edge effects. Thus, the effect of the different LNAs over the antenna array performance should also be evaluated, since extreme LNA input impedance values (as in the case of the balanced prototype) can cause undesired effects in the edge elements. Such edge effects, which can be a priori cataloged as residual in large array implementations (due to the relative lower amount of edge elements), can result critical if, for instance, any of the amplifiers begin to oscillate due to a high active antenna impedance mismatch.

3.6 Conclusions

The Square Kilometre Array breaks with the classical approach of radio-telescope based on single large parabolic dish antennas, and proposes a large array of small individual antennas. This novel concept presents many technology challenges at different levels, including RF front-ends, signal combination, and data-processing. For the case of the RF front-ends, the use of differential low-noise amplifiers has been seen as an interesting solution to significantly reduce the system noise temperature, due to the direct integration with the balanced antennas proposed for the mid-frequency range (i.e., 300-1000 MHz).

The work shown in this chapter presents several original contributions in the measurement and design of differential amplifiers at microwave frequencies. A differential noise figure measurement technique based on passive baluns has been presented. This method is significantly more complete than the de-embedding methods currently available in the literature and, therefore, provides more accurate results in the noise figure measurement of differential amplifiers. This accuracy is very important in this application, since achieving very low noise temperature levels is critical in any radio-astronomy instrument. A complementary source-pull method that allows obtaining the gain and noise circles of a differential amplifier has also been developed. The novelty of this technique is that it uses conventional measurement equipments and impedance tuners, but used in this case to characterize a differential amplifier (instead of a conventional single-ended one). In addition to the measurement techniques, several differential LNAs have been implemented. A preliminary LNA design has achieved less than 55 K noise temperature in the band of interest. This LNA has been used in the implementation of a small array demonstrator, whose technology can be a potential candidate for the mid-frequency range of the future SKA radio-telescope. The measurement of this array in a novel hot/cold test facility has served to extract several interesting conclusions for the implementation and test of the final SKA stations. Finally, other LNA designs that achieve noise temperatures lower than 40 K and 30 K in the band of interest have been presented. These values are at the state-of-the-art noise temperatures achieved with discrete commercial components in this frequency range.

The present work is outlined within the "system design and costing" phase of the SKA project. In such phase, the potential solutions for the final SKA implementation are proposed and their feasibility is evaluated. The presented results serve to affirm that the use of differential amplifiers based on discrete components can be a valid solution to achieve the low noise levels required for the SKA. In fact, both antennas and amplifiers seem to separately fulfill the desired requirements. Nevertheless, there are still some aspects that should be

studied in the future related with the system integration of the different parts of the RF front-end. These aspects, as well as other future research lines, will be proposed in Chapter 4.

3.7 References

[1] P. E. Dewdney, P. J. Hall, R. T. Schilizzi, and T. J. W. Lazio, "The Square Kilometre Array," *Proceedings of the IEEE*, vol. 97, no. 8, pp. 1482–1496, Aug. 2009.

[2] Square Kilometre Array Telescope web page: http://www.skatelescope.org/

[3] A. B. Smolders, and G. W. Kant, "Thousand element array (THEA)," *IEEE Antennas and Propagation Society International Symposium*, vol. 1, pp. 162–165, Jul. 2000.

[4] A. van Ardenne, P. N. Wilkinson, P. D. Patel, and J. G. bij de Vaate, "Electronic multi-beam radio astronomy concept: Embrace a demonstrator for the European SKA program," *Experimental Astronomy*, vol. 17, pp. 65–77, Jun. 2004.

[5] R. Maaskant, M. Popova, and R. van de Brink, "Towards the design of a low cost wideband demonstrator tile for the SKA," *1st European Conference on Antennas and Propagation*, pp. 1–4, Nov. 2006.

[6] Y. Zhang, and A. K. Brown, "Bunny ear combline antennas for compact wide-band dual-polarized aperture array," *SKADS Memo T34*, 2009. [Online]. Available: http://www.skads-eu.org/

[7] M. Arts, R. Maaskant, E. Lera-Acedo, and J. G. bij de Vaate, "Broadband differentially fed tapered slot antenna array for radio astronomy applications," *3rd European Conference on Antennas and Propagation*, pp. 566–570, Mar. 2009.

[8] Y. Zhang, and A. K. Brown, "Octagon rings antennas for compact dual-polarized aperture array," *SKADS Memo T35*, 2009. [Online]. Available: http://www.skads-eu.org/

[9] S. G. Hay, J. D. O'Sullivan, J. S. Kot, C. Granet, A. Grancea, A. R. Forsyth, and D. H. Hayman, "Focal plane array development for ASKAP (Australian SKA Pathfinder)," *2nd European Conference on Antennas and Propagation*, pp. 1–5, Nov. 2007.

[10] J. G. bij de Vaate, L. Bakker, E. E. M. Woestenburg, R. H. Witvers, G. W. Kant, and W. van Cappellen, "Low cost low noise phased-array feeding systems for SKA pathfinders," *13rd International Symposium on Antenna Technology and Applied Electromagnetics*, pp. 1–4, Feb. 2009.

[11] D. DeBoer, *et al.*, "Australian SKA pathfinder: a high dynamic range wide-field of view survey telescope," *Proceedings of the IEEE*, vol. 97, no. 8, pp. 1507–1521, Aug. 2009.

[12] L. E. Garcia-Muñoz, O. Garcia-Perez, V. Gonzalez-Posadas, J. L. Vazquez-Roy, D. Segovia-Vargas, J. M. Serna-Puente, T. Finn, and J. A. Lopez-Fernandez, "FIDA3: A novel active array design for the mid-frequency range of the Square Kilometre Array," *4th European Conference on Antennas and Propagation*, pp. 1–4, Apr. 2010.

[13] E. Lera-Acedo, L. E. Garcia-Muñoz, V. Gonzalez-Posadas, J. L. Vazquez-Roy, R. Maaskant, and D. Segovia-Vargas, "Study and design of a differentially fed tapered slot antenna array," *IEEE Transactions on Antennas and Propagation*, vol. 58, no. 1, pp. 68–78, Jan. 2010.

[14] A. Faulkner, *et al.*, "The aperture arrays for the SKA: the SKADS white paper," *SKA Memo 122*, Apr. 2010. [Online]. Available: http://www.skatelescope.org/

[15] W. R. Eisenstadt, B. Stengel, and B. M. Thomson, *Microwave differential circuit design using mixed-mode S-parameters*. Artech House, 2006.

[16] D. E. Bockelman, and W. R. Eisenstadt, "Combined differential and common-mode scattering parameters: theory and simulation," *IEEE Transactions on Microwave Theory and Techniques*, vol. 43, no 7, pp. 1530–1539, Jul. 1995.

[17] D. E. Bockelman, and W. R. Eisenstadt, "Pure-mode network analyzer for on-wafer measurements of mixed-mode S-parameters of differential circuits," *IEEE Transactions on Microwave Theory and Techniques*, vol. 45, no. 7, pp. 1071–1077, Jul. 1997.

[18] A. A. Abidi, and J. C. Leete, "De-embedding the noise figure of differential amplifiers," *IEEE Transactions on Solid-State Circuits*, vol. 34, no. 6, pp. 882–885, Jun. 1999.

[19] Agilent Technologies, "Balanced Device Characterization," *Application Note*, Feb. 2004. [Online]. Available: http://www.home.agilent.com/upload/cmc_upload/All/EPSG084733.pdf

[20] L. Belostotski, and J. W. Haslett, "A technique for differential noise figure measurement of differential LNAs," *IEEE Transactions on Instrumentation and Measurement*, vol. 57, no. 7, pp. 1298–1303, Jul. 2008.

[21] J. Lintignat, M. L. Grima, S. Darfeuille, B. Barelaud, B. Jarry, S. Barth, S. Bosse, P. Meunier, and P. Gamand, "BiCMOS differential low noise amplifier for radioastronomy application," *SKADS Memo T12*, 2008. [Online]. Available: http://www.skads-eu.org/

[22] M. L. Grima, S. Barth, S. Bosse, B. Jarry, P. Gamand, P. Meunier, and B. Barelaud, "A differential SiP (LNA-filter-mixer) in silicon technology for the SKA project," *European Microwave Integrated Circuits Conference*, pp. 331–334, Oct. 2007.

[23] J. Lintignat, S. Darfeuille, B. Barelaud, L. Billonnet, B. Jarry, P.Meunier, and P. Gamand, "A 0.1-1.7 GHz, 1.1dB NF low noise amplifier for radioastronomy application," *European Microwave Integrated Circuits Conference*, pp. 231–234, Oct. 2007.

[24] J. Morawietz, R. H. Witvers, J. G. B. de Vaate, and E. E. M. Woestenburg, "Noise characterization of ultra low noise differential amplifiers for next generation radiotelescopes," *European Microwave Conference*, pp. 1570–1573, Oct. 2007.

[25] N. Roddis, "Noise measurements for the SKA", *RadioNet Engineering Workshop: Low Noise Figure Measurements at Cryogenic and Room Temperatures*, Jun. 2009.

[26] O. Garcia-Perez, V. Gonzalez-Posadas, and D. Segovia-Vargas, "Noise figure measurement of differential amplifiers using non-ideal baluns," *IEEE Transactions on Microwave Theory and Techniques*, 2011 (accepted for publication).

[27] O. Garcia-Perez, D. Segovia-Vargas, L. E. Garcia-Muñoz, J. L. Jimenez-Martin, and V. Gonzalez-Posadas, "Broadband differential low noise amplifier for active differential arrays," *IEEE Transactions on Microwave Theory and Techniques*, vol. 59, no. 1, pp. 108–115, Jan. 2011.

[28] Square Kilometre Array Design Studies web page:
http://www.skads-eu.org/

[29] S. Zhang, S. N. Khan, and S. He, "Reducing mutual coupling for an extremely closely-packed tunable dual-element PIFA array through a resonant slot antenna formed in-between," *IEEE Transactions on Antennas and Propagation*, vol. 58, no. 8, pp. 2771–2776, Aug. 2010.

[30] R. Maaskant, and E. E. M. Woestenburg, "Applying the active antenna impedance to achieve noise match in receiving array antennas," *IEEE APS Antennas and Propagation Symposium*, pp. 5889–5892, Jun. 2007.

[31] S. W. Wedge, and D. B. Rutledge, "Wave techniques for noise modeling and measurement," *IEEE Transactions on Antennas and Propagation*, vol. 40, no. 11, pp. 2004–2012, Nov. 1992.

[32] D. M. Pozar, "The active element pattern," *IEEE Transactions on Antennas and Propagation*, vol. 42, no. 11, pp. 1171–1178, Nov. 1994.

[33] D. M. Pozar, "A relation between the active input impedance and the active element pattern of a phased array," *IEEE Transactions on Antennas and Propagation*, vol. 51, no. 9, pp. 2486–2489 , Sep. 2003.

[34] E. A. M. Klumperink, Z. Qiaohui, G. J. M. Wienk. R. Witvers, J. G. bij de Vaate, B. Woestenburg, and B. Nauta, "Achieving wideband sub-1dB noise figure and high gain with MOSFETs if input power matching is not required," *IEEE Symposium on RFIC*, pp. 673–676, Jun. 2007.

[35] S. Bhaumik, M. Panahi, and D. Kettle, "Differential LNA considerations for the Square Kilometre Array," *International Symposium on Antenna Technologies ans Applied Electromagnetics and the Canadian Radio Sciences Meeting*, pp. 1–4, Feb. 2009.

[36] J. A. Dobrowolski, *Introduction to Computer Methods for Microwave Circuit Analysis and Design*. Artech House Publishers, 1991.

[37] C. Craeye, B. Parvais, and X. Dardenne, "MoM simulation of signal-to-noise patterns in infinite and finite receiving antenna arrays," *IEEE Transactions on Antennas and Propagation*, vol. 52, no. 12, pp. 3245–3256, Dec. 2004.

[38] H. A. Wheeler, "The radiation resistance of an antenna in an infinite array or waveguide," *Proceedings of the IRE*, vol. 36, no. 4, pp. 478–487, Apr. 1948.

[39] P. Hannan, and M. Balfour, "Simulation of a phased-array antenna in waveguide," *IEEE Transactions on Antennas and Propagation*, vol. 13, no. 3, pp. 342–354, May 1965.

[40] R. Hansen, "Formulation of echelon dipole mutual impedance for computer," *IEEE Transactions on Antennas and Propagation*, vol. 20, no. 6, pp. 780–781, Nov. 1972.

[41] O. Garcia-Perez, L. E. Garcia-Muñoz, V. Gonzalez-Posadas, and D. Segovia-Vargas, "Source-pull characterization of differential active antennas for radio-astronomy applications," *2nd European Wireless Technology Conference*, pp. 84–87, Sep. 2009.

[42] Focus Microwaves, "DLPS, a differential load pull system," *Product Note 75*, May 2003. [Online]. Available: http://focus-microwaves.com/

[43] Focus Microwaves, "Using stub tuners and slide screw tuners," *Application Note 42*, Nov. 1999. [Online]. Available: http://focus-microwaves.com/

[44] O. Garcia-Perez, V. Gonzalez-Posadas, J. L. Jimenez-Martin, J. M. Serna-Puente, L. E. Garcia-Muñoz, and D. Segovia-Vargas, "Design of differential low noise amplifiers for UWB antennas in the low band of the SKA project," *29th General Assembly of the International Union of Radio Science*, Aug. 2008.

[45] R. T. Schilizzi, P. Alexander, J. M. Cordes, P. E. Dewdney, R. D. Ekers, A. J. Faulkner, B. M. Gaensler, P. J. Hall, J. L. Jonas, and K. I. Kellermann, "Preliminary specifications for the Square Kilometre Array," *SKA Memo 100*, Dec. 2007. [Online]. Available: http://www.skatelescope.org/

[46] C. A. Liechti, "Microwave field-effect transistors," *IEEE Transactions on Microwave Theory and Techniques*, vol. 24, no. 6, pp. 279–300, Jun. 1976.

[47] U. Delpy, "Stabilize transistors in low-noise amplifiers," *Microwaves & RF*, vol. 45, no. 5, pp. 81–88, May 2006.

[48] W. R. Deal, V. Radisic, Y. Qian, and T. Itoh, "Integrated-antenna pushpull power amplifiers," *IEEE Transactions on Microwave Theory and Techniques*, vol. 47, no. 8, pp. 1418–1425, Aug. 1999.

[49] R. Maaskant, and B. Enthoven, "Design of a hot-cold test facility," *ASTRON Technical Report SKA-ASTRON-RP-397*, 2009.

[50] European Radiocommunications Committee, "The European table of frequency allocations and utilisations covering the frequency range from 9 kHz to 275 GHz," *ERC Report 25*, 2004.

[51] B. Woestenburg, "Definition of array receiver gain and noise temperature," *SKA Memo 98*, Feb. 2008. [Online]. Available: http://www.skatelescope.org/

[52] O. Garcia-Perez, *et al.*, "Noise characterization of a FIDA3 array tile in THACO," *IGN-UC3M/ASTRON Internal Report*, Apr. 2010.

[53] Y. Koolivand, O. Shoaei, A. Zahabi, and P. J. Maralani, "A complete analysis of noise in inductively source degenerated CMOS LNA's," *IEICE Electronics Express*, vol. 2, no. 1, pp. 25–31, 2005.

[54] L. Belostotski, and J. W. Haslett, "Noise figure optimization of inductively degenerated CMOS LNAs with integrated gate inductors," *IEEE Transactions on Circuits and Systems*, vol. 53, no. 7, pp. 1409–1422, Jul. 2006.

Chapter 4

Final Conclusions and Future Research Lines

4.1 Final Conclusions

Modern telecommunication systems are in continuous evolution, which makes necessary the development of ever-increasing performance components. Of course, the RF front-ends are an essential part in many systems, and the design of microwave components with improved features is fundamental to cover this demand. This Ph.D. dissertation presents the results of 4 years of research in the development of microwave active circuits with novel properties. Two kind of topologies have been investigated: active filters with dual bandpass response based on metamaterial structures, and broadband differential low-noise amplifiers for radio-astronomy applications.

For the case of the dual-band active filters, their development is justified by the increasing demand of multiband components for modern multi-service telecommunication equipments. Although filters are an important part in any electronic system, most effort in the development of multiband filters has been focused on passive resonators. The work presented in the second chapter of this thesis has served to demonstrate the feasibility of achieving a dual-band response also with an active filter topology. This novel advance has been possible thanks to the use of metamaterial-based structures, which are one of the most important emerging technologies of the last decade. A complete theoretical analysis of the proposed filtering structure has been provided in the first part of the chapter. Subsequently, such theoretical principles have been successfully validated by the implementation and characterization of several prototypes. Some future lines related with this topic will be proposed below.

The work related with the differential low-noise amplifiers has been carried out in the framework for the SKA project, in which the technologies needed to construct an enormous radio-telescope are being developed. The use of broadband differential amplifiers has been proposed as a promising technique to achieve the extremely low system noise temperatures required by such instrument. However, the use of differential amplifiers, originally conceived for low-frequency electronics, at microwave frequencies has presented several challenges in terms of design and characterization. One of the contributions presented in the third chapter consists on the development of some specific differential measurement methods, which allows us to accurately characterize differential amplifiers by using conventional measurement equipments. In addition, a complete active array demonstrator has been implemented and measured, whose results have served us to extract important conclusions for the final SKA implementation. For the case of the differential amplifiers, several prototypes have been developed, achieving noise temperatures close to the desired performance for the definitive SKA design. It demonstrates the feasibility of using broadband differential LNA designs based on commercially-available discrete components for this application. Some future research lines will be outlined below.

Finally, it is remarked that the work presented in this Ph.D. dissertation has led to five journal papers and one book chapter, as well as it has been presented in 16 conferences and workshops. The list of contributions is detailed in the *Publications* section at the end of this book.

4.2 Future Research Lines

4.2.1 Metamaterial dual-band active filters

One of the keys to unlock the full potential of the proposed active filter topology is its development in MMIC technology. It would allow integrating the proposed filter with the rest of the circuitry in a single PCB in a very compact fashion. The implementation of both, recursive active filters and CRLH transmission lines, has been separately demonstrated in the literature (e.g., [1],[2]). At frequencies higher than 4 GHz, the use of transmission-line based power combiners is feasible, and the design of the MMIC filter can be very similar to the designs presented in Chapter 2. One of the differences is that the lumped components should be designed in planar technology in this case. A preliminary simulation of a simplified first-order active filter structure based on coupled lines is shown in Fig. 4.1. The device has been simulated in a PHEMT GaAs process, and the chip size is about 2x2 mm^2. The simulated results show acceptable dual-band performance at 4.8 GHz and 13.4 GHz.

At frequencies of few GHz, the size of quarter-wavelength transmission lines needed for the combiners may be too large to be implemented in a MMIC. For this case, other alternatives should be considered. One example is the implementation of power combiners based on lumped components, as the filter design presented in [3]. One of the limitations of this solution can be the difficulty to implement a combiner simultaneously operating at the two desired bandpass frequencies. Another option can be the voltage matching technique [4], in which the power combiners of the classical recursive filter scheme are replaced by transistors. In this way, the potential instabilities are avoided by the non-reciprocal response

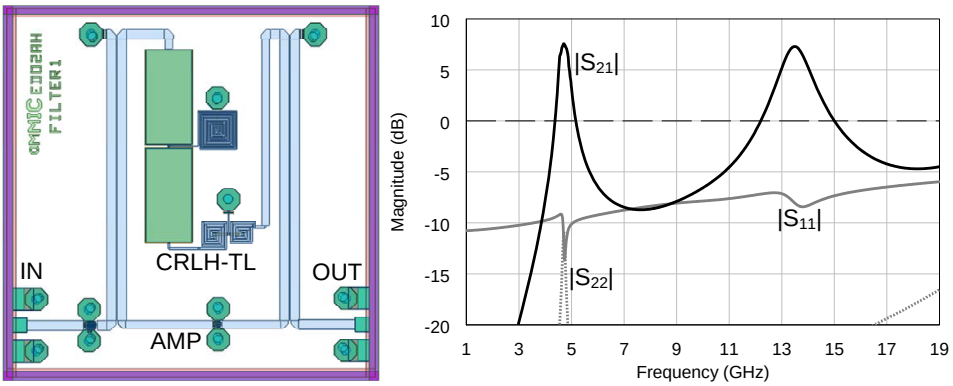

Figure 4.1: Top view of a dual-band MMIC active filter and simulated response.

of the transistors. The advantage of this last approach is that the transistors provide isolation in a relatively broad bandwidth.

In addition to compactness, a MMIC solution would give additional degrees of freedom in the design of the gain block. Low gain blocks are needed to avoid instability problems, and an approach using an attenuator has been used to control the excess of gain, since commercial transistors usually provide gain values higher than the needed for this application. An ad-hoc MMIC amplifier design would allow obtaining low and flat gain values without the use of any external attenuator. Unlike in the implemented designs, in which the drain currents were the corresponding for a relatively high gain level, a low-gain amplifier would require lower drain current values, which makes the MMIC approach more efficient in terms of power consumption. It must be remarked that the gain of the filter can be higher than the gain of the isolated amplifier (due to the feedback), so a low-gain amplifier does not necessarily mean low bandpass gain.

The filter designs presented in this thesis provide pass bands at two arbitrary frequencies. A potential improvement can be to increase the number of frequency bands. One option is to use the scheme presented in subsection 2.3.4, in which several feedback lines are used to provide the dual-band performance. If the feedback sections are CRLH transmission lines, each line can potentially provide two frequencies of operation, and therefore the number of pass bands is twice the number of lines. The challenge of this approach is two isolate the different feedback lines and to achieve combining circuits covering all the frequencies of interest. Another option is to use the so-called extended CRLH (E-CRLH) transmission lines, whose unit cell is based on the combination of a conventional CRLH line and its dual form (D-CRLH) [5]. This configuration allows adjusting the phase of the artificial transmission line at four arbitrary frequencies, so it can be used in the implementation of quad-band devices. Other extended CRLH implementations based on SRRs have also demonstrated quad-band capabilities [6].

Finally, another line of interest is to find effective methods to improve the noise performance of the proposed dual-band filters. In addition to the use of lower noise transistors, the key to reduce the noise contribution, and still maintaining the desired filtering response of the structure, is to find the adequate power distribution between the branches of the input and output power combiners [7]. This would require the use of unequal-split combiners. However, conventional asymmetric combiners may present some limitations, such as narrow-band operation, extreme values of the line impedances for certain power balance ratios, or large size. All the previous limitations can be solved by using, for example, asymmetrical Wilkinsons based on SRR-loaded metamaterial transmission lines, as the one shown in Fig. 4.2. This kind of circuits can provide dual-band performance in a compact design, and extreme line impedance values are more feasible than with

conventional lines [8]. Another advantage of using unequal-split combiners is that the excess of gain in the loop can be directly controlled by the own power balance of the combiners, which avoids the use of attenuators and potentially allows increasing the gain of the filter. Only some preliminary results have been obtained for single-band filter designs for this thesis [9]. Thus, further investigation on dual-band low-noise active filter topologies is a potential future line.

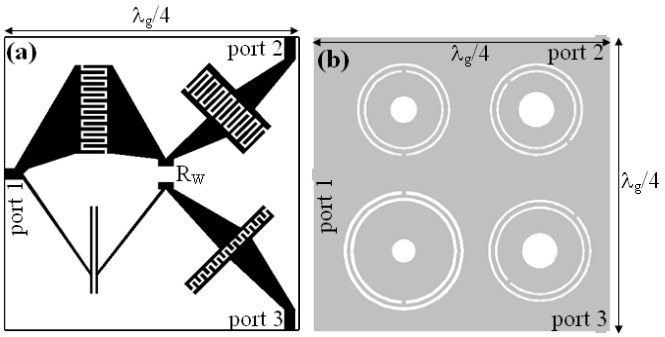

Figure 4.2: Layout (top and bottom view) of an unequal Wilkinson power divider designed with SRR-based unit cells in all of their sections.

4.2.2 Broadband differential low-noise amplifiers

As in the previous case, the research on low-noise differential amplifiers in MMIC technology is a potential future line. Although the development cost of monolithic devices is higher than in the case of discrete implementations, the per-unit cost for large volume of units is usually lower. Thus, a MMIC solution can be a feasible solution to save cost in the final SKA front-ends. A graph showing the noise figure trends of the different transistor technologies during the last years is shown in Fig. 4.3 [10]. As it can be seen from the plot, GaAs or InP solutions seem more adequate to achieve the desired low noise levels required in SKA. However, the noise figure of CMOS technology has been significantly reduced during the last decade. Although GaAs and InP devices are still more adequate to achieve the lower noise figure, CMOS LNAs are also a potential candidate due to the higher integration levels and to the lower per-unit cost. Thus, the device technology (i.e., GaAs, CMOS, InP, SiGe, etc.) and the integration level (i.e., discrete or MMIC) should be carefully chosen for the definitive SKA design considering both aspects: system performance and cost. A priori, a compromise based on a discrete/MMIC GaAs/InP front-end (i.e., LNA) and the rest of the receiver components (i.e., analog-to-digital converters, etc.) implemented in SiGe BiCMOS technology seems to be the most suitable solution [11].

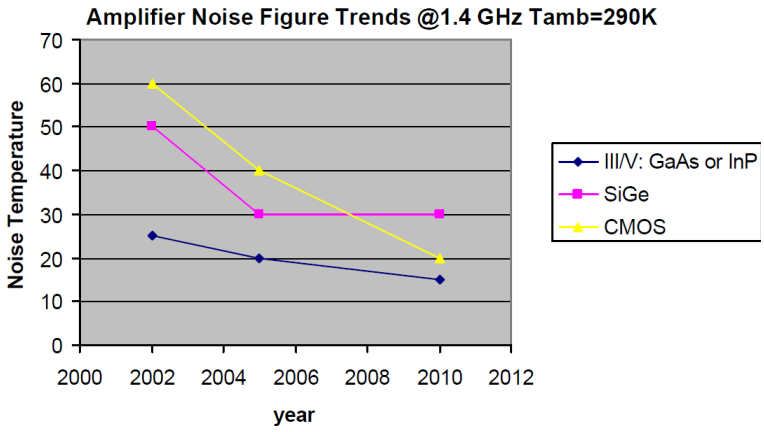

Figure 4.3: Noise figure trends of different transistor technologies [10].

The receivers for the mid-frequency range of SKA are projected to operate at room temperature (≈300 K), since conventional cryostat systems used nowadays for radio-astronomy are impractical to cool the millions of amplifiers needed for the dense aperture arrays. However, a localized solution in which only the LNA is cooled (instead of the whole system) could be a feasible option (Fig. 4.4), as long as the extra power consumption needed for the coolers is compensated by a significant reduction of the system noise temperature [12]. Recently, some miniature cooling systems have been developed with the aim of refrigerating electronic circuits. In [13], a micro-cooler with a net cooling power of about 10 mW at 96 K has been presented. The cold stage consists of a stack of three glass

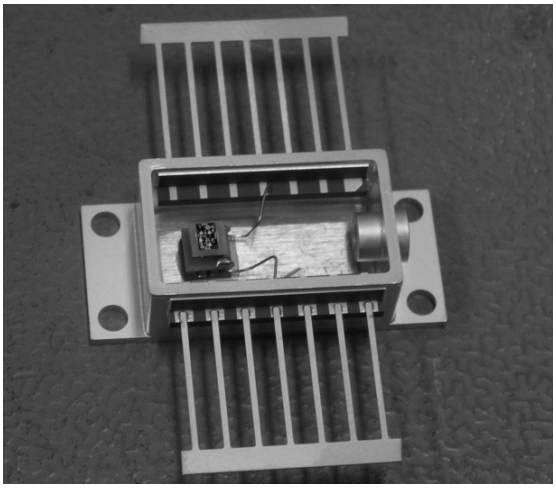

Figure 4.4: LNA chip inside a localized cooling system in vacuum [12].

wafers, in which there is a flux of nitrogen between the wafers. Using the previous system, a LNA can be directly integrated with the cooler, using the glass as circuit substrate [14]. Since the sensitivity of the aperture array is proportional to A_{eff}/T_{sys}, where A_{eff} is the effective area of the array and T_{sys} is the system noise temperature, reducing T_{sys} would allow reducing A_{eff} and, therefore, the cost for a given A_{eff}/T_{sys} value. A reduction of T_{sys} from 50 K to 40 K would allow saving around €200 million [15]. In addition, cooling would also deliver temperature stabilization. The challenges for the LNA designers would be to integrate the amplifier with the cooler, to design the active device to properly operate for the new physical temperature, and to reduce the power consumption of the transistors.

Another point of interest is to analyze with more detail the mismatching effects between the amplifiers and the antennas in the proposed dense array configurations. As it was analyzed in the present thesis, the effects caused by a poorly matched amplifier may affect to the active antenna impedance of the array elements. If the array is large enough, most antenna elements (in the center) can be approximated by the infinite array solution, with independence of the LNAs. However, the LNAs still may affect the edge elements, with independence of the dimensions of the array, since the impedance mismatching of such antenna elements are dependent on the input impedance of the amplifiers. Thus, any future analysis of the array performance degradation caused by the edge elements should consider a precise implementation of the active array system, including both the antenna structure and the amplifiers. This performance degradation may be given by a noise increment generated by the antenna impedance mismatching, or even by oscillations if the active antenna impedances of the edge elements present extreme impedance values. Regarding to the mid-frequency SKA stations, the dimension of each array seems large enough to use the infinite array approximation to model the system. In practice, each dense array may be mounted by placing smaller array tiles together, since small array tiles are easier to fabricate and transport than the complete large array system. It may cause additional edge effects in the interstices between an array tile and the adjacent, since the antennas may be not in physical contact. All these effects should be studied in detail in the subsequent phases of the SKA project.

4.3 References

[1] M. Danestig, H. Johansson, A. Ouacha, and S. Rudner, "Low-noise active recursive MMIC filters," *IEEE MTT-S International Microwave Symposium Digest*, pp. 705–708, Jun. 2007.

[2] Z. Hu, P. D. Curtis, and W. Tong, "A multilayer compact solid state composite right/left-handed metamaterial transmission line," *IEEE Electron Device Letters*, vol. 29, no. 12, pp. 1383–1385, Dec. 2008.

[3] M. Delmond, L. Billonnet, B. Jarry, and P. Guillon, "Microwave tunable active filter design in MMIC technology using recursive concepts," *IEEE Microwave and Millimeter-Wave Monolithic Circuits Symposium*, pp. 105–108, May 1995.

[4] W. Mouzannar, L. Billonnet, B. Jarry, and P. Guillon, "A new design concept for realising highly tunable microwave filters using recursive principles," *28th European Microwave Conference*, pp. 1–5, Oct. 1998.

[5] A. Rennings, S. Otto, J. Mosig, C. Caloz, I. Wolff, "Extended composite right/left-handed (E-CRLH) metamaterial and its application as quadband quarter-wavelength transmission line," *Asia-Pacific Microwave Conference*, pp. 1405–1408, Dec. 2006.

[6] M. Duran-Sindreu, G. Siso, J. Bonache, and F. Martin, "Fully planar implementation of generalized composite right/left handed transmission lines for quad-band applications," *IEEE MTT-S International Microwave Symposium Digest*, pp. 25–28, May 2010.

[7] H. Ezzedine, L. Billonnet, B. Jarry, and P. Guillon, "Optimization of noise performance for various topologies of planar microwave active filters using noise wave techniques," *IEEE Transactions on Microwave Theory and Techniques*, vol. 46, no. 12, pp. 2484–2492, Dec. 1998.

[8] M. Gil, I. Gil, J. Bonache, J. Garcia-Garcia, and F. Martin, "Metamaterial transmission lines with extreme impedance values," *Microwave and Optical Technology Letters*, vol. 48, no. 12, pp. 2499–2505, Dec. 2006.

[9] F. Aznar-Ballesta, O. Garcia-Perez, V. Gonzalez-Posadas, and D. Segovia-Vargas, "Recursive active filter with metamaterial unequal Wilkinson power dividers," *European Microwave Conference*, pp. 930–933, Sep. 2010.

[10] A. van Ardenne, H. Butcher, J. G. bij de Vaate, A. J. Boonstra, J. D. Bregman, B. Woestenburg, K. van der Schaaf, P. N. Wilkinson, and M. A. Garrett, "The aperture array approach for the Square Kilometre Array," *White Paper*, May 2003. [Online]. Available: http://www.skatelescope.org/

[11] A. Faulkner, *et al.*, "The aperture arrays for the SKA: the SKADS white paper," *SKA Memo 122*, Apr. 2010. [Online]. Available: http://www.skatelescope.org/

[12] F. Schreuder, and J. G. bij de Vaate, "Localized LNA cooling in vacuum," *International Workshop on Thermal investigations of ICs*, Sep. 2006.

[13] P. P. P. M. Lerou, G. C. F. Venhorst, T. T. Veenstra, H. V. Jansen, J. F. Burger, H. J. Holland, H. J. M. ter Brake, and H. Rogalla, "All-micromachined Joule-Thomson cold stage," *International Cryocooler Conference*, pp. 437–441, Jul. 2007.

[14] R. Bara, "Low noise front-end design for phased-array radio astronomy systems," M.S. thesis, Universite de Limoges/ASTRON, Limoges, France, Sep. 2009.

[15] P. Alexander, R. Bolton, A. Faulkner, *et al.*, "SKADS benchmark scenario: design and costing," *SKA Memo 93*, Mar. 2007. [Online]. Available: http://www.skatelescope.org/

Publications

The work developed in this Ph.D. dissertation has led to several journal, book and conference contributions. The complete list is detailed below.

Journal papers (5):

Related with Chapter 2:

- D. Segovia-Vargas, O. Garcia-Perez, V. Gonzalez-Posadas, F. Aznar-Ballesta, "Dual-band tunable active filter based on phase shifters with left-handed cells," *IEEE Microwave and Wireless Components Letters*, vol. 21, no. 2, pp. 92–94, Feb. 2011.

- O. Garcia-Perez, L. E. Garcia-Muñoz, D. Segovia-Vargas, V. Gonzalez-Posadas, "Multiple order dual-band active ring filters with composite right/left-handed cells," *Progress in Electromagnetics Research*, PIER 104, 201–219, 2010.

- O. Garcia-Perez, A. Garcia-Lamperez, V. Gonzalez-Posadas, M. Salazar-Palma, D. Segovia-Vargas, "Dual-band recursive active filters with composite right/left-handed transmission lines," *IEEE Transactions on Microwave Theory and Techniques*, vol. 57, no. 5, pp. 1180–1187, May 2009.

Related with Chapter 3:

- O. Garcia-Perez, V. Gonzalez-Posadas, D. Segovia-Vargas, "Noise figure measurement of differential amplifiers using non-ideal baluns," *IEEE Transactions on Microwave Theory and Techniques*, 2011 (accepted for publication).

- O. Garcia-Perez, D. Segovia-Vargas, L. E. Garcia-Muñoz, J. L. Jimenez-Martin, V. Gonzalez-Posadas, "Broadband differential low noise amplifier for active differential arrays," *IEEE Transactions on Microwave Theory and Techniques*, vol. 59, no. 1, pp. 108–115, Jan. 2011.

Book chapters (1):

Related with Chapter 2:

- D. Segovia-Vargas, V. Gonzalez-Posadas, J. L. Jimenez- Martin, L. E. Garcia-Muñoz, O. Garcia-Perez, "Passive diplexers and active filters based on metamaterial particles," in *Passive Microwave Components and Antennas*, V. Zhurbenko (Ed.), Vukovar: INTECH, pp. 451–468, Apr. 2010. (ISBN: 978-953-307-083-4)

Conferences and workshops (16):

Related with Chapter 2:

- F. Aznar-Ballesta, O. Garcia-Perez, V. Gonzalez-Posadas, D. Segovia-Vargas, "Recursive active filter with metamaterial unequal Wilkinson power dividers," *40th European Microwave Conference*, Paris, pp. pp. 930–933, Sep. 2010.

- F. Aznar Ballesta, O. Garcia Perez, V. Gonzalez Posadas, D. Segovia Vargas, "Filtro activo recursivo con divisores de potencia metamaterial asimétricos," *XXV Simposium Nacional de la URSI*, Bilbao, Sep. 2010.

- O. Garcia-Perez, V. Gonzalez-Posadas, D. Segovia-Vargas, "Dual band-pass active filters based on recursive topologies and CRLH transmission lines," *3rd International Congress on Advanced Electromagnetic Materials in Microwaves and Optics*, London, pp. 190–192, Sep. 2009.

- O. Garcia Perez, V. Gonzalez Posadas, D. Segovia Vargas, "Filtros activos de doble banda basados en estructuras recursivas y líneas CRLH," *XXIV Simposium Nacional de la URSI*, Santander, Sep. 2009.

- O. Garcia-Perez, V. Gonzalez-Posadas, D. Segovia-Vargas, "Design of recursive active filters with CRLH lines," *3rd Young Scientist Meeting on Metamaterials*, Leganes, pp. 307–308, Jul. 2009.

- O. Garcia-Perez, J. Herraiz-Martinez, V. Gonzalez-Posadas, D. Segovia-Vargas, "Design of a dual-band active filter using CRLH structures," *19th International Conference on Applied Electromagnetics and Communications*, Dubrovnik, pp. 1–4, Sep. 2007.

- O. Garcia Perez, V. Gonzalez Posadas, D. Segovia Vargas, "Diseño de un filtro activo de doble banda usando estructuras CRLH," *XXII Simposium Nacional de la URSI*, Tenerife, Sep. 2007.

Related with Chapter 3:

- O. Garcia Perez, L. E. Garcia Muñoz, V. Gonzalez Posadas, J. L. Vazquez Roy, D. Segovia Vargas, J. M. Serna Puente, T. Finn, J. A. Lopez Fernandez, "Diseño y caracterización de un array activo de banda ancha para radioastronomía," *XXV Simposium Nacional de la URSI*, Bilbao, Sep. 2010.

- L. E. Garcia-Muñoz, O. Garcia-Perez, V. Gonzalez-Posadas, J. L. Vazquez-Roy, D. Segovia-Vargas, J. M. Serna-Puente, T. Finn, J. A. Lopez-Fernandez, "FIDA3: A novel active array design for the mid-frequency range of the Square Kilometre Array," *4th European Conference on Antennas and Propagation*, Barcelona, pp. 1–4, Apr. 2010.

- O. Garcia-Perez, J. A. Lopez-Fernandez, D. Segovia-Vargas, L. E. Garcia-Muñoz, V. Gonzalez-Posadas, J. L. Vazquez-Roy, J. M. Serna-Puente, E. Lera-Acedo, T. Finn, P. Colomer, R. Bachiller, "FIDA3: a novel active array for the mid-SKA," *5th SKADS Workshop: Widefield Astronomy and Technology for the SKA*, Limelette, pp. 381–386, Nov. 2009.

- O. Garcia-Perez, J. G. bij de Vaate, D. Segovia-Vargas, L. E. Garcia-Muñoz, J. M. Serna-Puente, V. Gonzalez-Posadas, "FIDA3, the Spanish contribution to the Square Kilometre Array," *6th COST Assist IC0603 Workshop*, Wroclaw, Oct. 2009.

- O. Garcia-Perez, L. E. Garcia-Muñoz, V. Gonzalez-Posadas, D. Segovia-Vargas, "Source-pull characterization of differential active antennas for radio-astronomy applications," *2nd European Wireless Technology Conference*, Rome, pp. 84–87, Sep. 2009.

- O. Garcia-Perez, L. E. Garcia-Muñoz, J. M. Serna-Puente, V. Gonzalez-Posadas, J. L. Vazquez-Roy, D. Segovia-Vargas, "Differential active antennas for the SKA project," *3rd European Conference on Antennas and Propagation*, Berlin, pp. 1316–1319, Mar. 2009.

- O. Garcia-Perez, J. A. Lopez-Fernandez, D. Segovia-Vargas, L. E. Garcia-Muñoz, V. Gonzalez-Posadas, J. L. Vazquez-Roy, J. M. Serna-Puente, T. Finn, "Progress in differential amplifiers," *4th SKADS Workshop*, Lisbon, Oct. 2008.

- O. Garcia Perez, V. Gonzalez Posadas, J. L. Jimenez Martin, J. M. Serna Puente, L. E. Garcia Muñoz, D. Segovia Vargas, J. A. Lopez Fernandez, "Diseño de amplificadores diferenciales de bajo ruido para antenas UWB en la banda baja del proyecto SKA," *XXIII Simposium Nacional de la URSI*, Madrid, Sep. 2008.

- O. Garcia-Perez, V. Gonzalez-Posadas, J. L. Jimenez-Martin, J. M. Serna-Puente, L. E. Garcia-Muñoz, D. Segovia-Vargas, "Design of differential low noise amplifiers for UWB antennas in the low band of the SKA project," *29th General Assembly of the International Union of Radio Science*, Chicago, Aug. 2008.

About the Author

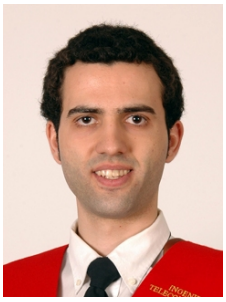

Óscar García-Pérez was born in Madrid, Spain, on December 23, 1984. He received the Engineer degree in telecommunications from the Carlos III University in Madrid, Spain, in 2007. Then, he started working towards the Ph.D. in communications at Carlos III University in Madrid. His main research interests are the study of microwave active circuits with metamaterial structures and broadband differential low noise amplifiers for radio-astronomy applications. Since 2008 he is recipient of a grant from the Yebes Astronomical Center for the research on radio-astronomy instrumentation at low and mid frequencies.